

Probabilistic modeling of short fiber-reinforced composites
taking into account finite deformations
– Numerical modeling and experimental validation –

CUMULATIVE HABILITATION THESIS

approved by the Department of
Mechanical and Civil Engineering

of the Helmut-Schmidt-University
University of the Federal Armed Forces Hamburg

for obtaining the academic degree of
Doktor-Ingenieurin habilitata (Dr.-Ing. habil.)

by

Dr.-Ing. Natalie Rauter

from Essen, Germany

Hamburg 2023

Reviewers:

Prof.'in Dr.-Ing. Kerstin Weinberg

University of Siegen

Prof. Dr.-Ing. Rolf Lammering

Helmut-Schmidt-University /

University of the Federal Armed Forces

Prof. Dr.-Ing. habil. Daniel Balzani

Ruhr-Universität Bochum

Date of colloquium: March 17, 2023

Abstract

Due to the capability of mold injecting manufacturing short fiber-reinforced composites are increasingly in use in the aeronautical and automotive industries. However, a crucial aspect is their spatially distributed material properties induced by the probabilistic characteristics of the microstructure. To predict the structural response of components made of short fiber-reinforced composites by numerical simulation correctly the probabilistic information must be included in the modeling approach. Furthermore, commonly used matrix material is characterized by a distinct plastic deformation even at low stress levels. Therefore, in this work, a modeling approach is proposed that utilizes second-order Gaussian random fields for the representation of the spatially distributed material properties on the component level in the elastic and plastic domain. The modeling approach comprises the cross-correlation analysis of the material parameters describing the elastic-ideal plastic material behavior and a subsequent representation of the parameters by second-order Gaussian random fields. The analysis reveals a complex cross-correlation structure of the parameters, which depends on the window size on the mesoscale and requires the use of suitable numerical methods like the multiple correlated Karhunen-Loève expansion to synthesize the representation of the material parameters. The numerical simulations of tensile test specimens in the elastic and plastic domain predict the structural response under uniaxial loading accurately. The localized plastic deformation of the specimen is observable and meets the experimental validation by tensile tests until failure. Furthermore, the experimental data is used to determine the correlation length. Besides this, the modeling approach is validated by nanoindentation tests on the mesoscale, which reveal the spatial distribution of the material properties. Furthermore, it is shown that the area characterized by nanoindentation tests is 25 times larger than the projected area of the used Berkovich tip. In conclusion, the proposed modeling approach utilizing random fields is capable of representing the localized deformation of short fiber-reinforced composites induced by the probabilistic characteristics of the microstructure. Furthermore, the correlation structure can be derived by numerical simulation on the mesoscale, which can be experimentally analyzed by nanoindentation tests. Finally, the correlation length is an independent material parameter, which can be derived from experimental data.

Kurzfassung

Auf Grund der Eignung von kurzfaserverstärkte Verbundwerkstoffen zur Verarbeitung in Spritzgussbauteilen werden diese zunehmend in der Luftfahrt- und Automobilindustrie eingesetzt. Eine wichtige Eigenschaft dieser Materialien sind ihre räumlich verteilten Materialeigenschaften, die durch die probabilistischen Eigenschaften der Mikrostruktur bedingt sind. Um die Strukturantwort von Bauteilen aus kurzfaserverstärkten Verbundwerkstoffen durch numerische Simulation korrekt voraussagen zu können, müssen diese probabilistischen Informationen in den Modellierungsansatz mit einbezogen werden. Darüber hinaus zeichnet sich das üblicherweise verwendete Matrixmaterial durch eine ausgeprägte plastische Verformung auch bei geringen Belastungen aus. Abgeleitet aus diesen Eigenschaften wird in dieser Arbeit ein Modellierungsansatz vorgestellt, der homogene Gauß'sche Zufallsfelder zweiter Ordnung für die Abbildung der räumlich verteilten Materialeigenschaften auf Komponentenebene im elastischen und plastischen Bereich verwendet. Der Modellierungsansatz umfasst die Kreuzkorrelationsanalyse der Materialparameter, die das elastisch ideale-plastische Materialverhalten beschreiben, und eine anschließende Abbildung der streuenden Parameter durch homogene Gauß'sche Zufallsfelder. Dabei zeigt sich eine komplexe Kreuzkorrelationsstruktur der Materialparameter, die von der Fenstergröße auf der Mesoskala abhängt und somit die Verwendung einer geeigneten numerischen Methode, wie der mehrfach korrelierten Karhunen-Loève-Erweiterung zur Synthese der Zufallsfelder zur Darstellung der Materialparameter erfordert. Diesem Ansatz folgend geben numerische Simulationen von Zugversuchsproben im elastischen und plastischen Bereich die Verformung unter einem einachsigen Belastungszustand wieder. Die lokalisierte plastische Verformung des Probekörpers ist beobachtbar und entspricht der experimentellen Validierung durch Zugversuche bis zum Versagen. Darüber hinaus werden die experimentellen Daten zur Bestimmung der Korrelationslänge verwendet. Weiterhin wird der Modellierungsansatz durch Nanoindentationsversuche auf der Mesoskala validiert, welche die räumliche Verteilung der Materialeigenschaften aufzeigen. Dabei kann nachgewiesen werden, dass die durch Nanoindentationstests charakterisierte Fläche 25 Mal größer ist als die projizierte Fläche der verwendeten Berkovich-Spitze. Zusammenfassend lässt sich sagen, dass der vorgeschlagene Modellierungsansatz unter Verwendung von Zufallsfeldern in der Lage ist, die lokalisierte Verformung von kurzfaserverstärkten Verbundwerkstoffen darzustellen, die durch die probabilistischen Eigenschaften der Mikrostruktur verursacht wird. Ferner kann die Korrelationsstruktur durch numerische Simulation auf der Mesoskala abgeleitet werden, die durch Nanoindentationstests experimentell analysiert werden kann. Schließlich ist die Korrelationslänge ein unabhängiger Materialparameter, der aus experimentellen Daten bestimmt werden kann.

Publications

This thesis is a cumulative thesis collecting the results presented in the following peer-reviewed publications. They are referred to by the term paper and their Roman index in the text. To preserve a consistent layout throughout the thesis the papers are reformatted. This includes a continuous numbering of the figures, tables, and equations as well as a uniform citation style and a combined bibliography at the end. In front of each publication an overview holds the main bibliographic information e.g. the title, authors, current status, journal, and abstract.

- I. **N. Rauter** and R. Lammering. Correlation structure in the elasticity tensor for short fiber-reinforced composites. *Probabilistic Engineering Mechanics*, **62**, pp. 103100, DOI: 10.1016/j.prob engmech.2020.103100, 2020.
- II. **N. Rauter**. A computational modeling approach based on random fields for short fiber-reinforced composites with experimental verification by nanoindentation and tensile tests. *Computational Mechanics*, **67**, pp. 699 – 722, DOI: 10.1007/s00466-020-01958-3, 2021.
- III. **N. Rauter** and R. Lammering. Experimental characterization of short fiber-reinforced composite on the mesoscale by indentation tests. *Applied Composite Materials*, **28**, pp. 1747 – 1765, DOI: 10.1007/s10443-021-09937-4, 2021.
- IV. **N. Rauter**. Correlation analysis of the elastic-ideal plastic material behavior of short fiber-reinforced composites. *International Journal for Numerical Methods in Engineering*, pp. 1-19, DOI: 10.1002/nme.7113, 2022.
- V. **N. Rauter**. Numerical simulation of the elastic-ideal plastic material behavior of short fiber-reinforced composites including its spatial distribution with an experimental validation. *Applied Science*, **12**, pp. 10483, DOI: 10.3390/app122010483, 2022.

Contents

Abstract	i
Kurzfassung	ii
Publications	iii
Part A Research summary	1
1 Introduction	2
1.1 Motivation and state of the art	2
1.2 Objectives and outline	3
2 Fundamentals of probabilistic multi-scale material modeling	5
2.1 Techniques of probabilistic modeling	5
2.1.1 Random variables	5
2.1.2 Random fields	5
2.1.3 Synthesizing random fields	6
2.2 Multi-scale modeling	6
3 Specimen definition and probabilistic characteristics of the microstructure	8
3.1 Specimen definition	8
3.2 Extraction methodology	8
3.3 Probabilistic characteristics of the microstructure	9
3.4 Influence of the probabilistic characteristics on the apparent overall material properties	11
4 Linear-elastic modeling on the mesoscale	15
4.1 Numerical simulations	15
4.2 Experimental verification	15
5 Adaption to the component level with elastic ideal plastic material behavior	21
5.1 Experimental characterization by tensile tests	21
5.2 Modeling approach	22
5.3 Apparent overall material properties and correlation analysis of elastic-ideal plastic material behavior	23
5.3.1 Apparent overall material properties	23
5.3.2 Correlation analysis	23
5.4 Application to tensile test specimens	24
6 Concluding remarks	30

Part B	Publications of the Habilitation thesis	33
I	Correlation structure in the elasticity tensor for short fiber-reinforced composites	34
I.1	Introduction	35
I.2	Theoretical Framework	36
I.2.1	Numerical multi-scale modeling	36
I.2.2	Analytical modeling of SFRC	38
I.2.3	Correlated second-order random fields	39
I.3	Analytical treatment	41
I.3.1	Material properties and their probabilistic characteristics	41
I.3.2	Procedure	42
I.3.3	Results	43
I.4	Numerical analysis	44
I.4.1	Generation of the microstructure	44
I.4.2	Finite Element Model	47
I.4.3	Analysis of the element size	48
I.4.4	Influence of the microstructure	50
I.4.5	Comparison of the analytical and numerical results	54
I.4.6	Correlation analysis	54
I.5	Conclusion	61
I.A	Analytical results	63
I.B	Numerical analysis	67
I.B.1	Determination of the elasticity tensor elements	67
I.B.2	Results based on a plane strain assumption	68
II	A computational modeling approach for SFRC with experimental verification	71
II.1	Introduction	72
II.2	Karhunen-Loève expansion	73
II.2.1	Second-order random fields	73
II.2.2	Auto-correlated random fields	74
II.2.3	Two-dimensional random fields	78
II.2.4	Apparent material properties	78
II.3	Specimen specification	79
II.4	Extraction of the probabilistic characteristics	80
II.4.1	Theoretical description of the fiber orientation	80
II.4.2	Methodology	81
II.4.3	Probabilistic characteristics	82
II.5	Modeling on the mesoscale	86
II.5.1	Numerical simulations	86
II.5.2	Experimental validation	89
II.6	Modeling on the component level	92
II.6.1	Numerical simulation	92
II.6.2	Experimental validation	97
II.6.3	Modeling based on three-dimensional microstructure characteristics	97
II.7	Summary and Conclusion	100
III	Experimental characterization of SFRC on the mesoscale by indentation tests	102
III.1	Introduction	103
III.2	Multiscale approach	103
III.3	Indentation tests	104

III.3.1	Theory	104
III.3.2	Experimental procedure	105
III.4	Results	107
III.5	Discussion	107
III.5.1	Experimental results	107
III.5.2	Numerical simulation	110
III.5.3	Comparison	112
III.6	Conclusion	114
III.7	Declarations	115
III.8	Data availability	115
III.A	Numerical results	115
III.B	Theoretical framework Halpin-Tsai	115
IV	Correlation analysis of the elastic-ideal plastic material behavior of SFRC	118
IV.1	Introduction	119
IV.2	Theoretical background	119
IV.2.1	Stochastic framework	120
IV.2.2	Elasto-plastic material behavior	122
IV.2.3	Homogenization of plastic material properties	123
IV.3	Determination of the apparent material properties	125
IV.3.1	Methodology	125
IV.3.2	Numerical model	126
IV.3.3	Results	126
IV.4	Correlation	128
IV.4.1	Overall behavior	128
IV.4.2	Correlation length	129
IV.5	Summary and Conclusion	133
IV.A	Determination of the apparent hyperelastic material properties	134
IV.B	Results of the coefficient of determination	135
V	Numerical simulation of the elastic-ideal plastic material behavior of SFRC with experimental validation	137
V.1	Introduction	138
V.2	Experiments	139
V.2.1	Specimens	139
V.2.2	Experimental setup and procedure	139
V.2.3	Results	140
V.3	Generation of cross-correlated random fields	140
V.3.1	Methodology	140
V.3.2	Application to the elastic-ideal plastic material behavior of SFRC	144
V.4	Numerical simulation	145
V.4.1	Framework of elastic-ideal plastic material behavior	146
V.4.2	Implementation in COMSOL Multiphysics®	152
V.5	Application to tensile test specimen	156
V.5.1	Numerical model	156
V.5.2	Results	158
V.5.3	Discussion	158
V.6	Summary and conclusion	160
V.A	Supporting routines	161

Bibliography	164
List of Figures	174
List of Tables	177

Part A

Research summary

Chapter 1

Introduction

1.1 Motivation and state of the art

In comparison to well-established homogeneous materials, heterogeneous materials like reinforced composites show a significantly improved specific strength and stiffness. They usually consist of two constituents, the matrix material and reinforcing elements like particles and fibers, respectively. One class of materials in this context are short fiber-reinforced composites (SFRC), where a thermoplastic matrix material like polyamide or polypropylene is combined with glass or carbon fibers of 100 μm to 300 μm length. The short length of the reinforcing elements allows the processing of such materials by injection molding and hence, in large-scale serial production. Due to this, SFRCs are of high interest in e.g. the automotive industry [38]. However, the short length of the reinforcing fibers in combination with the varying melt flow velocities in the cavity causes a spatial distribution of the material properties on the component level [141]. Subsequently, the accurate representation and prediction of the structural response under load lead to complex and expensive numerical simulations. One approach to solve this issue and allow the exploitation of the full lightweight potential is the use of probabilistic, multi-scale methods.

There are many different approaches to model the probabilistic characteristics of SFRC. In [2] an approach based on the orientation tensor is introduced, which can also be directly implemented in the material description [9]. There is also an extension of this approach, which combines the orientation tensor with a coupled micro-mechanical and phenomenological approach [33, 123]. A further technique is provided by the extended finite element method (XFEM), which was developed for application in the field of crack growth and interfaces [122]. It is also applied to reinforced concrete [68] and combined with a cohesive zone model [137]. Finally, in [156] a first attempt of a scale transition is introduced by combining XFEM with a Monte Carlo sampling to estimate the size of the representative volume element (RVE) for random composites.

In addition, a stochastic technique for the representation of spatially distributed data and hence, a suitable approach for the material modeling of SFRC are random fields [75, 108, 176]. This technique enables one to incorporate the probabilistic information on the component level, without the need for explicit modeling of the microstructure. A comprehensive framework of non-Gaussian positive-definite matrix-valued random fields and tensor-valued random fields for mesoscale stochastic models of anisotropic elastic microstructures is provided in [163, 164]. This work is extended to the stochastic fluctuation in fiber-reinforced composites on the mesoscale in [56, 57], to cover, e.g. the continuous mode conversion of guided ultrasonic waves in thin-walled composites [189], multi-scale approaches for heterogeneous materials with non-Gaussian random fields [55], and random interphases from atomistic simulations to polymer nanocomposites [97]. This technique is also applied in the context of geosystems [22], thin-walled composite cylinders [31] and three-dimensional concrete microstructures [167].

To synthesize random fields mostly the Karhunen-Loève expansion (KLE) is used [106], which leads to a separation of the deterministic numerical modeling and the probabilistic representation of the material properties. This concept is also known as the stochastic finite element method (SFEM) [112, 131], which is used for different applications. The combination of SFEM with cohesive zone models to analyze the crack growth in fiber-reinforced cementitious composites is presented in [86]. In [56, 164] the SFEM is combined with an RVE. In addition to this, the fluctuation of the volume fraction is discussed in [57]. Furthermore, the utilization of the KLE requires knowledge about the correlation structure of the underlying random variables. Since the spatial distribution of the material properties is induced by the probabilistic nature of the microstructure, the influence of the microstructural characteristics on the material properties is of interest. In contrast to

continuous fiber-reinforced composites, local effects on the stress and strain state must be considered. The analytical framework of the properties of materials with inclusions or reinforcement like SFRC is based on the mean-field theory combined with Eshelby's work [40]. This work was expanded in [121, 170] leading to the well-known material models by Mori and Tanaka as well as Tandon and Weng. Besides this, Halpin and Tsai developed an additional approach [61, 62], which is a self-consistent method. A detailed overview is provided in [174], which shows that the material model by Tandon and Weng describes the elastic properties best. Using these material models the analysis of the influencing parameters reveals that the fluctuation of the fiber volume fraction and the fiber orientation affects the mechanical properties significantly [45, 60, 78]. However, it is important to note that the probabilistic information of the microstructural characteristics is not included in these analyses.

In addition to this, so far the work provided in literature is limited to the elastic domain. However, most matrix materials used for SFRC show very prominent plastic deformation even at operation loads [77]. A first application of random fields to nonlinear isotropic material behavior is given in [185]. Besides this, most works either deal with the spatial distribution of the linear-elastic material behavior or homogenization methods are utilized in the context of nonlinear material behavior [1, 22, 85, 118] to derive the RVE of the material [17, 18].

1.2 Objectives and outline

The main objective of the presented work is the development of a probabilistic multi-scale material modeling approach covering elastic and plastic deformations. To reduce computational costs, the probabilistic information induced by the microstructural characteristics is included on the component level without the explicit representation of the microscale. Following the state of the art, a probabilistic modeling approach utilizing second-order homogeneous Gaussian random fields is used to achieve this goal, because this technique enables one to incorporate spatially distributed properties into a numerical modeling procedure on the component level. In combination with knowledge about the influence of the probabilistic characteristics of the microstructure and the resulting spatial distribution of the material properties a probabilistic multi-scale material modeling approach can be established.

Hence, the first step of this work is the analysis of the influencing microstructural characteristics and their spatial distribution to the resulting material properties described by the elasticity tensor. This comprehensive investigation covers an analytical treatment based on well-known material models for SFRC developed by Halpin and Tsai [61, 62] and Tandon and Weng [170] as well as numerical analyses. In contrast to the state of the art, both steps incorporate information about the probability density functions (PDF) of the main microstructural characteristics like fiber length, fiber diameter, and fiber volume fraction. To derive the influence of these characteristics on the elasticity tensor and the engineering constants each characteristic is separately varied following its known PDFs before calculating first the engineering constants and subsequently the elasticity tensor elements. To identify which microstructural characteristic influences which elasticity tensor element most, the analytically obtained material properties are compared with each other.

The corresponding numerical analysis is based on two-dimensional numerical simulations. Here, the numerical model is generated by randomly placing fibers concerning their microstructural characteristics and their PDFs in a predefined area. As already done before, the impact of each characteristic is again analyzed separately. In addition, to cover also interfering effects in separate simulations all parameters are varied. The numerical simulations are conducted following Hill's condition by applying Neumann and Dirichlet type boundary conditions to derive an upper (Voigt) and a lower (Reuss) bound [150, 179].

With the knowledge about the microstructural characteristics and their PDFs influencing the resulting material properties most representative artificial microstructures can be generated. This is necessary to analyze the correlation structure of the material properties in a second step because the correlation structure of the material properties is essential for the discretization of the random fields for the representation of the spatially distributed material properties by the KLE. At first, the linear elastic material properties are analyzed before extending the approach to transversely-isotropic elastic-ideal plastic behavior. In both cases, the methodology

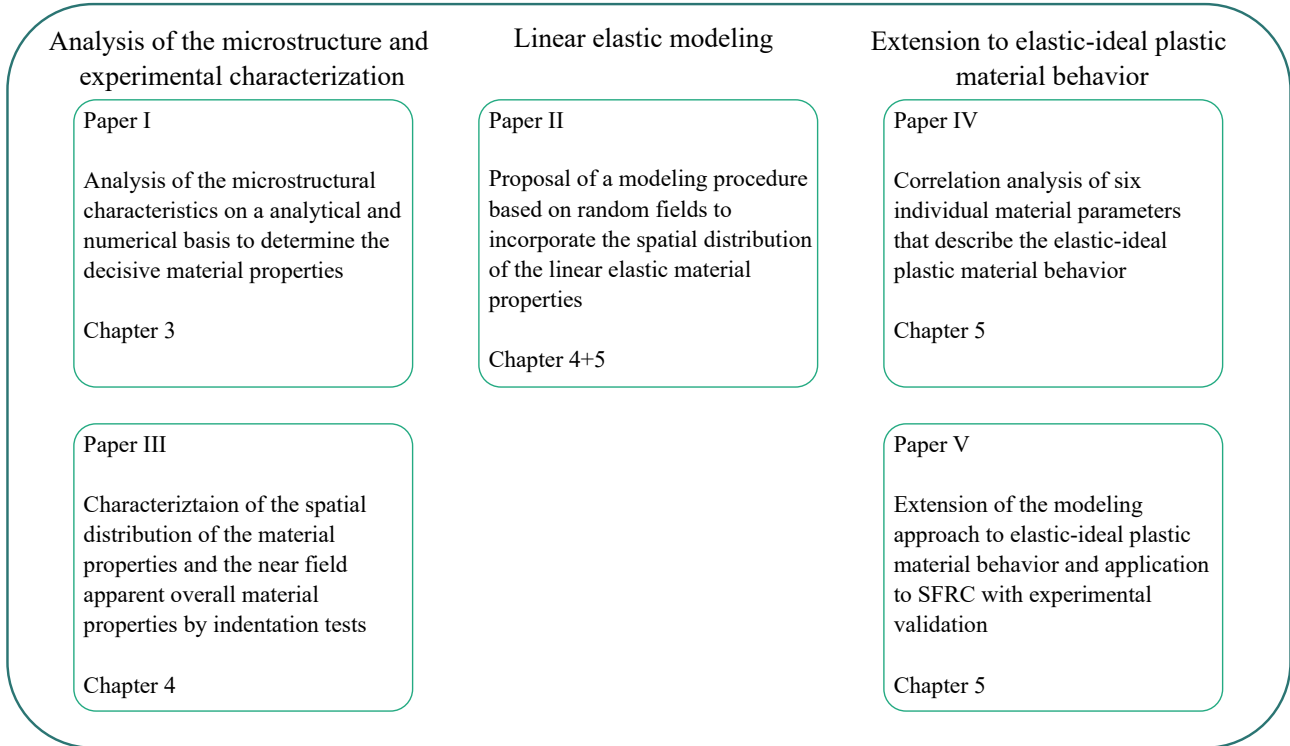


Figure 1.1: Contribution of the Papers to the overall objective of the cumulative Habilitation thesis.

is based on the moving window method and the determination of the spatial distribution of the apparent overall material properties. The correlation structure is obtained by a curve fit of the derived dimensionless correlation parameter with well-known correlation functions.

The next step contains the representation of the individual material parameters by random fields, which can now be synthesized. With these representations, numerical simulations of uniaxial tensile tests are conducted both on the mesoscale and the component level. To validate the results nanoindentation and component tensile tests are carried out. By comparing the results the correlation lengths of the random fields can be determined in the final step of the proposed procedure.

Since this is a cumulative Habilitation thesis the work consists of two parts (A and B). Part A gives a summary of the research that is presented in the papers collected in Part B. Subsequently, the research summary provided in Part A is structured as follows. Chapter 2 gives an introduction to the research fields of multi-scale modeling for heterogeneous materials and probabilistic material modeling approaches leading to the main objectives of this research. In Chapters 3 to 5 the main steps of the multi-scale modeling approach are summarized. First, the probabilistic characteristics of the microstructure are analyzed in Chapter 3. Next, the modeling approach on the mesoscale is presented in Chapter 4. In the last step, the gained knowledge is used to adapt the modeling approach from the mesoscale to the component level in Chapter 5. The research summary is concluded by Chapter 6. Part B comprises the publications of the cumulative thesis. Here, Figures 1.1 gives an overview of the contribution of each Paper to this cumulative Habilitation thesis and how the key findings are combined to the proposed modeling approach.

To preserve a consistent layout throughout the thesis the papers are reformatted. This includes a continuous numbering of the figures, tables, and equations as well as a uniform citation style and a combined bibliography at the end. Furthermore, each publication starts with an overview holding the main bibliographic information e.g. the title, authors, current status, journal, and abstract.

Chapter 2

Fundamentals of probabilistic multi-scale material modeling

This section gives only a brief overview of the stochastic concept and multi-scale modeling approach used in this work for the representation of spatially distributed material properties in the elastic and plastic domain of SFRC. Beside the literature provided in this Chapter, the reader is kindly referred to the publications of this cumulative Habilitation thesis [141–144, 146] for more details about the fundamental framework. Each paper contains the relevant background of the presented aspects.

2.1 Techniques of probabilistic modeling

2.1.1 Random variables

Quantities that are derived from random experiments and thus, are subject to the rules of probability theory are called random variables $Z(\omega)$. The result of an experiment gives a realization z of the random variable $Z(\omega)$. The main functions to characterize these random variables are first, the cumulative distribution function (CDF) holding information about the probability p of $Z(\omega) \leq z$ and second, its first derivative giving the PDF. One well-known example is the Gaussian bell curve, describing the normal distribution. Besides these two functions, the moments of the probability distribution are important quantities. In the context of continuum mechanics and material modeling second-order or L^2 theory is applied. This means that the first two moments of a random variable, which give the expected value and the mean square deviation, respectively, are finite [180].

2.1.2 Random fields

If random variables $Z(\omega)$ are a continuous function of the spatial coordinates one speaks of random fields $Z(\omega, \mathbf{x})$ [177]. Again the CDF and PDF as well as the moments of the probability distribution characterize this probabilistic quantity. Subsequently, random fields are fully described by the mean value $\mu(\mathbf{x})$, the variance $\sigma^2(\mathbf{x})$ and the correlation coefficient $\rho(\mathbf{x}, \mathbf{x}')$ [169, 176]. The correlation coefficient holds the point-to-point information [177], where the auto-correlation gives the information about two realizations of the same random field at different locations and the cross-correlation provides information about two realizations of different random fields.

Assuming homogeneous second-order random fields the mean value and the variance are independent of the spatial coordinates and hence, become constant [176]. Furthermore, the correlation is invariant to a translation and can, therefore, be described by relative coordinates. If the correlation is also independent of any orthogonal transformation the random field is isotropic [37, 176].

Utilizing homogeneous second-order Gaussian random fields in the context of continuum mechanics and especially material modeling it is important to note that this implies a normal distribution of the corresponding random variable. However, the assumption of a normal distribution allows negatively valued realizations [47, 169], which contradicts the parameter definition for most material properties since they are of positive nature. Following this, the application of Gaussian random fields to the multi-scale modeling of heterogeneous material like SFRC is controversial [163]. One solution is the use of non-Gaussian random fields, which guarantee a stochastic solution of second-order by avoiding negative realizations [27, 54, 55, 97, 110, 172]. However, mostly the PDF is unknown. In this case, the random fields are represented by a discrete number of realizations ω_i [132]. In addition, the stochastic modeling approach presented here is combined with FEM. In this context also only discretized random fields are used. In conclusion, the established modeling approach requires finite

sampling. Subsequently, the resulting Gaussian random fields differ not significantly from non-Gaussian random fields [141].

2.1.3 Synthesizing random fields

Following the main characteristics of random fields, a technique is required to generate a continuous representation of the correlation coefficient to synthesize random fields. One well-known approach is the KLE [106], which is in essence a generalization of the Fourier transform to probabilistic processes [108] that may be a function of time or the spatial coordinates. Thus, the KLE is a spectral decomposition of the known correlation functions. The corresponding eigenvalues and eigenfunctions are obtained by solving a Fredholm integral equation of the second kind. Following this approach, only auto-correlated random fields are synthesized. An extension to multiple cross-correlated random fields is provided in [25]. Utilizing the multiple correlated KLE (mcKL) first, different sets of uncorrelated random variables are generated for each variable. In a subsequent step, these sets are transformed into cross-correlated random variables. Hence, the procedure is suitable for the representation of material properties, which are multi-variate and strongly cross-correlated [142, 144].

Adapting the synthesis of random fields in the context of material modeling and numerical simulation a discrete representation is required. Due to the fact that there are closed solutions of the Fredholm integral equation only for a limited number of correlation functions and domain shapes usually, numerical integration methods are necessary. Examples are the midpoint method [32, 182], the spatial averaging [177], and the shape function method [88, 104, 105]. Besides these approaches, the main idea of the KLE was extended to spatial decomposition in [165]. One technique is the expansion optimal linear estimate (EOLE) introduced in [101], which is identical to the Nyström method [6] with a uniform integration point definition.

2.2 Multi-scale modeling

The approach of multi-scale modeling is based on the concept of the separation of scales [64]. This concept follows the existence of an RVE [70], where the size of an RVE must be small compared to the macroscopic dimension of the component. However, at the same time, it must be large enough to contain a statistically representative amount of information about the microstructure [190]. Subsequently, the size d of an RVE is much larger than the size l of e.g. an inclusion and much smaller than the dimension L on the macroscale [64], see Figure 2.1.

Following this, effective material properties can be computed for an RVE on the mesoscale that are independent of the boundary conditions [70]. However, as already indicated the homogenization of the material properties is only possible if the separation of scales is fulfilled. If the size of the selected volume element is too small, the effective material properties still depend on the boundary conditions, the microstructure and

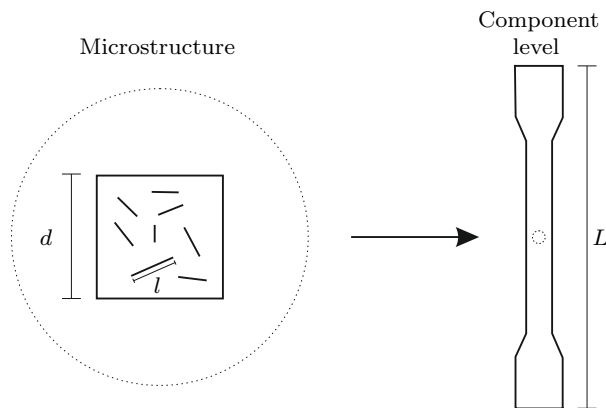


Figure 2.1: Scale definition based on a tensile test specimen made of SFRC, taken from Paper III [146].

the contrast of the involved material phases [67, 81]. The corresponding volume is called statistical volume element (SVE) [130]. Furthermore, instead of the effective material properties, one speaks of the apparent overall material properties [79, 80].

To determine the effective material properties the Hill Mandel condition must be satisfied [69], which states the energy conservation for scale transition [70]. Additionally, compatible boundary conditions must be selected. Among others, these are boundary conditions of Dirichlet type (pure displacement boundary conditions) and Neumann type (pure traction boundary conditions). In the case of an SVE, these boundary conditions lead to an upper and lower bound [150, 179], whereas the experimentally obtained properties lay in between these two bounds.

Chapter 3

Specimen definition and probabilistic characteristics of the microstructure

In this chapter first, the specification of the specimens used in this work is introduced. This is followed by the extraction methodology of the probabilistic microstructural characteristics induced by the manufacturing process of the specimens and a discussion of the results. For detailed information about the obtained results, the reader is kindly referred to Paper II of this cumulative Habilitation thesis provided in Part B [141]. Subsequently, the influence of these characteristics on the apparent overall material properties is analyzed. Details about this investigation can be found in Paper I of this cumulative Habilitation thesis [144].

3.1 Specimen definition

The numerical simulations and experimental investigations presented in this work are based on SFRC components. In an initial step plates made from Ultradur B 4300 G6 [21] with a size of 300 mm × 300 mm × 3 mm are manufactured by mold injection. Ultradur B 4300 G6 is a polybutylene terephthalate (PBT) matrix material filled with glass fibers and a fiber mass fraction of 30 %. With respect to the density of the two constituents, the fiber volume fraction is 18.22 %. The linear elastic material properties of the two phases are provided in Table 3.1.

From this plate, specimens are cut out that are later used for nanoindentation and tensile tests. The orientation and size of the different specimens that are used during these investigations are depicted in Figure 3.1. The tensile tests are limited to the melt flow direction, whereas the nanoindentation tests are conducted in the direction of the three major axes of the plate. These coincide with the melt flow direction as well as the thickness direction. The third axis is perpendicular to the melt flow and thickness direction.

3.2 Extraction methodology

The microstructure of the SFRC is significantly influenced by the melt flow properties and the induced shear forces during manufacturing [76]. Due to this not only the fiber distribution but also the fiber length and fiber diameter show probabilistic characteristics. Therefore, to be able to incorporate these probabilistic characteristics into a modeling approach microstructural information about the fiber length, orientation, and diameter are derived from a micrograph as proposed in [158]. The image processing toolbox of Matlab® is utilized to extract the geometrical information of each fiber represented by an ellipsoid. The procedure comprises three steps, which are depicted in Figure 3.2. First, the fibers are detected (see the second picture).

	Young's modulus GPa	Poisson's ratio -	Yield strength GPa	Density kg/m ³
Glass	72 ¹	0.22	4000	2500
PBT	2.6	0.41	3.5	1300

¹ For the influence and correlation analysis in Paper I a Young's modulus of 70 GPa is used. However, this does not affect the overall results, because the results are of qualitative nature.

Table 3.1: Linear elastic material properties of the fiber and matrix material.

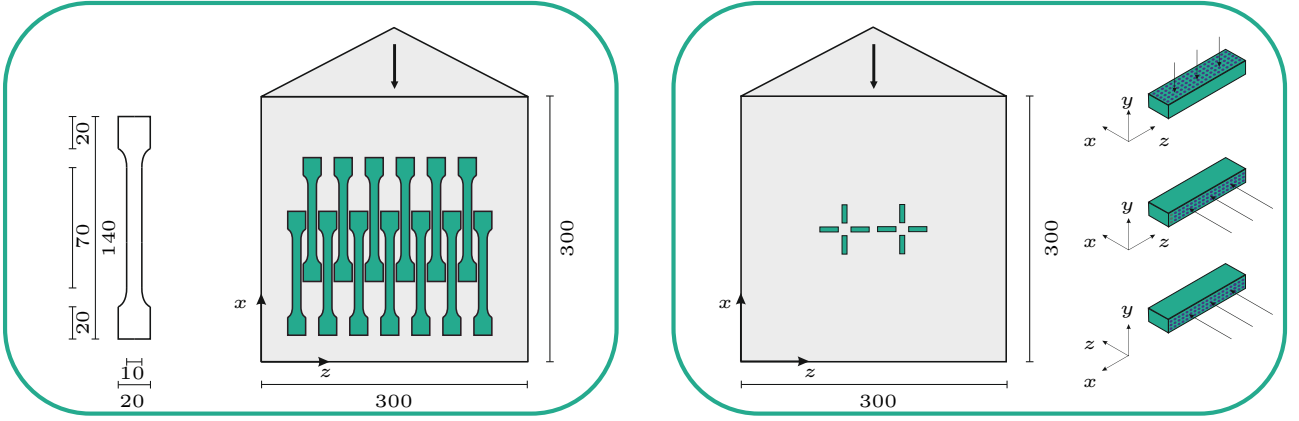


Figure 3.1: Specimen definition for the tensile and nanoindentation tests, cf. Paper II and Paper III [141, 146].

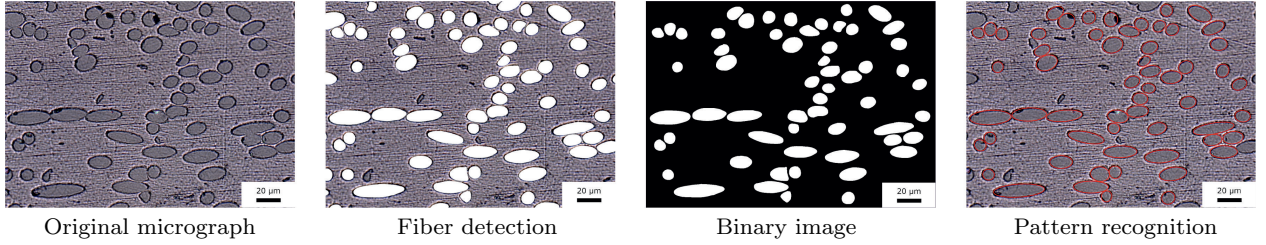


Figure 3.2: Different stages of image processing, taken from Paper II [141].

The image is then transformed into a binary picture, where black is assigned to the matrix material and white to the fibers (see the third picture). Finally, with the function *regionprops* of the image processing toolbox all relevant geometrical information of the fibers holding the orientation, coordinates of the centroid, and the major and minor axes are extracted. A reconstruction of the results is illustrated in the last picture of Figure 3.2, showing an excellent agreement between the results of the pattern recognition and the original micrograph.

From a theoretical prospective, the fiber orientation of a single fiber is described by the unity vector \mathbf{p} pointing in the direction of the fiber [100, 158]. Based on this vector \mathbf{p} in [2] the second-order fiber orientation tensor \mathbf{A} is introduced. This tensor holds information about the PDF of the fiber orientation distribution defined in [42]. Hence, with the information about the orientation of each fiber in the micrograph the tensor \mathbf{A} can be computed. Furthermore, the probability of fiber detection is directly linked to the fiber orientation. Therefore, in [158] a weighting factor is proposed. It is assumed that a fiber orientation perpendicular to the micrograph cross-section is very likely to be detected, whereas fibers parallel to the cross-section are only very rarely detectable.

For the extraction of the microstructural characteristics a micrograph of the size $3370 \mu\text{m} \times 3000 \mu\text{m}$ with a resolution of 558 px per $100 \mu\text{m}$ is used, assuming ergodicity for the extracted microstructure. In the stochastic framework, this means, that the extracted microstructure is representative of the whole specimen, which subsequently holds also for the probabilistic characteristics [11, 181].

3.3 Probabilistic characteristics of the microstructure

Analyzing the microstructural characteristics of SFRC includes two main aspects. One is the overall structure of the cross-section resulting from the melt flow and the shear stresses [76]. The second deals with the determination of the PDFs for the main microstructural characteristics like fiber length, diameter, and orientation. The results of both aspects are summarized below. Following the procedure proposed in [158] Figure 3.3 holds the main results about the fiber length and fiber orientation with respect to the specimen thickness coordinate.

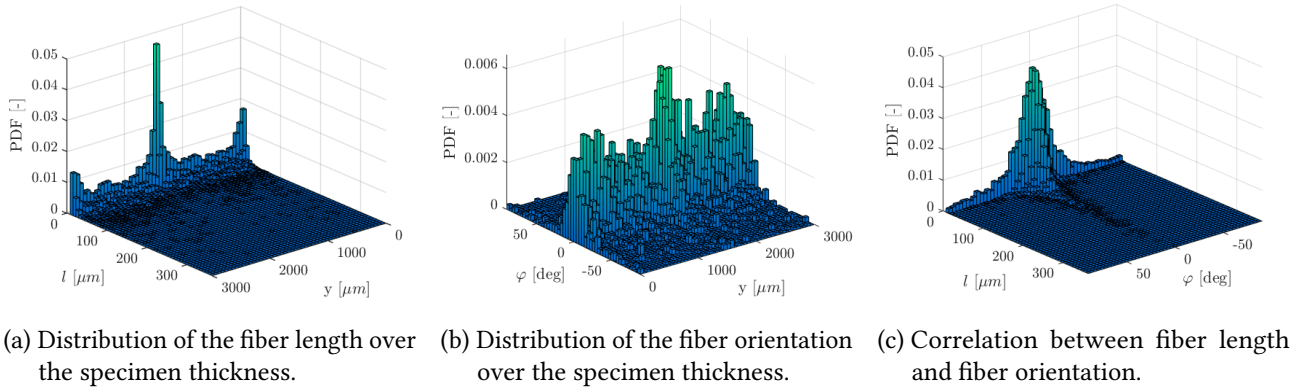


Figure 3.3: Results of the microstructural characteristics, cf. Paper II [141].

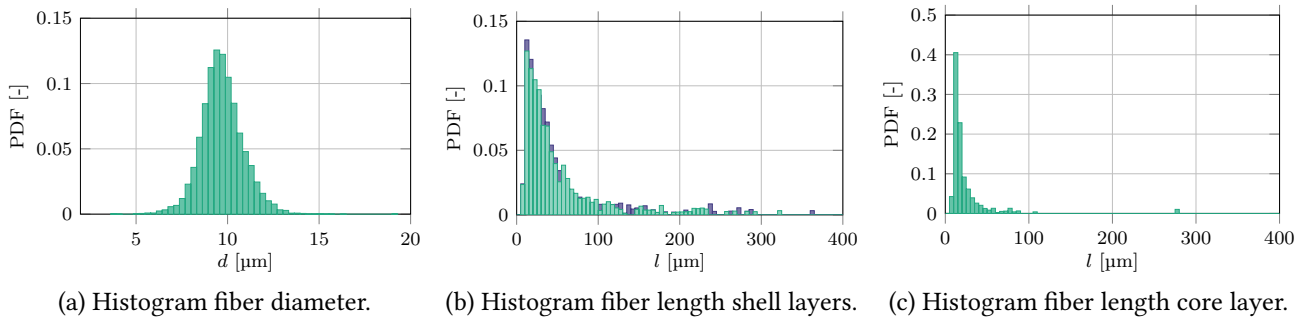


Figure 3.4: Histograms of the microstructural characteristics, cf. Paper II [141].

Furthermore, the correlation between fiber length and fiber orientation is given. Figure 3.4 illustrates the histograms of the fiber diameter and fiber length. The plotted histograms reveal the main characteristics of the microstructural cross-section properties, which can also be found in literature [19, 41, 43, 46, 58, 113, 154]. These can be summarized as follows:

- The results in Figures 3.3b and 3.3c indicate a preferred orientation of the fibers, which is induced by the mold injection process. Over the thickness of the specimen, the fibers are mostly oriented in the direction of the melt flow.
- Following the length distribution presented in Figure 3.3a and subsequently computing the orientation tensor components reveals that the cross-section of components made by mold injection can be divided into different layers. Here, in total five layers can be identified. Corresponding to the literature these are referred to as skin (at the upper and lower surface), core (in the center), and shell (between the skin and core) [19, 41, 43, 46, 113, 154] layers, which are characterized by their main fiber orientations. Within the shell layers, the fiber orientation mainly coincides with the melt flow direction. In contrast to this, the core layer shows a fiber orientation perpendicular to it. The fibers in the shell layers at the top and the bottom are randomly orientated [154]. More information and a plot of the orientation tensor components are provided in Paper II [141].
- The histogram of the fiber diameter in Figure 3.4a meets a normal distribution. The mean value is $9.6 \mu\text{m}$. This is a little bit below the expected value found in literature [58]. The reason for this are artifacts at the fiber-matrix interface on the micrograph. Furthermore, the fiber diameter distribution is independent of the layer scheme, because the fiber diameter is not affected by the mold injection. Instead, the fiber production process is responsible for the fiber diameter [58].
- Due to the mold injection process, which causes fiber breakage, the fiber length distribution is best described by a two-parameter Weibull distribution. However, even under the consideration of a weighting

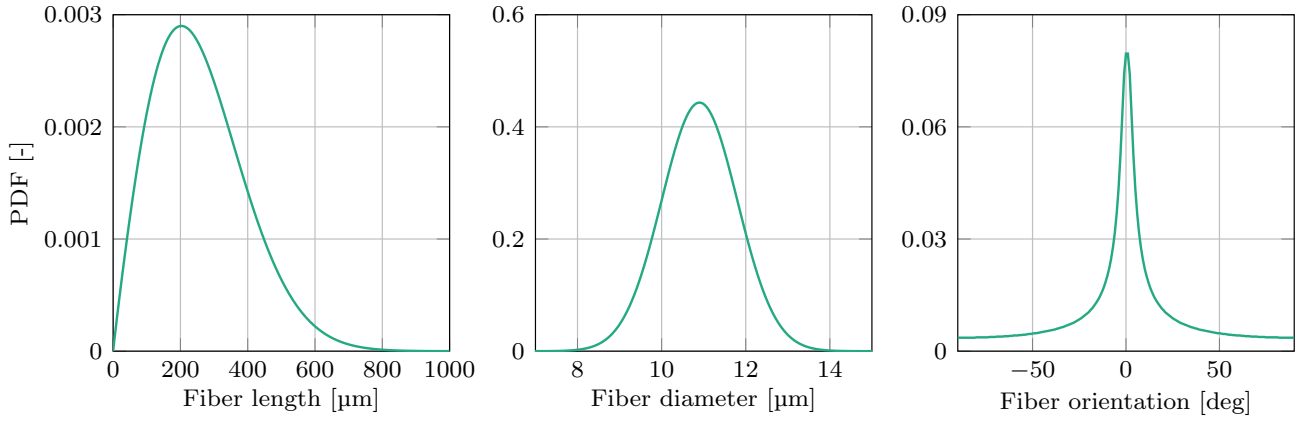


Figure 3.5: PDFs of the fiber length, fiber diameter, and orientation derived by μ CT, cf. Paper I [144]. Data taken from [58].

factor proposed in [158] an extensive amount of fibers is shorter than $20\text{ }\mu\text{m}$, leading to a mean value of $46.6\text{ }\mu\text{m}$. In comparison to the fiber length mean value of $260\text{ }\mu\text{m}$ obtained by μ CT [58], these values appear very low. The main reason lies in the difference between the two-dimensional and three-dimensional analysis of the microstructure.

- The fiber mass fraction varies between the different layers. For the shell layers, a fiber mass fraction of 0.28 is obtained, whereas the core layer has a fiber mass fraction of 0.33.

3.4 Influence of the probabilistic characteristics on the apparent overall material properties

The main objective of this work is the incorporation of spatially distributed material properties in a numerical modeling procedure of SFRC on the component level. Since the spatial distribution is caused by the probabilistic characteristics of the microstructure, the influence of the corresponding PDFs on the material properties is investigated. With this information at hand, all necessary data can later be added to the modeling procedure. As already presented in Section 3.3 the fiber length distribution is best described by a two-parameter Weibull distribution, whereas the fiber diameter shows a normal distribution. In addition to this the fiber orientation can be characterized by an elliptic probability function [58]. Given the final application on the component level, the probabilistic information used here is derived by μ CT and is taken from [58]. The corresponding PDFs are depicted in Figure 3.5.

At first, the influence of the geometrical fiber properties on the material properties is analyzed analytically by utilizing the well-known material model of Tandon and Weng [170]. This material model is based on the mean-field theory in combination with Eshelby's work [40] and fits the experimental data best [60, 174]. With the analytical framework, the engineering constants like Young's modulus and Poisson's ratio can be computed. Therefore, $1\text{e}6$ realizations of the fiber length and the fiber diameter are sampled following the corresponding PDFs. For each realization, a set of engineering constants is calculated by combining the stochastic quantity with the mean values of the remaining parameters. For example, the fiber length as a realization with respect to the two-parameter Weibull distribution is combined with the mean fiber diameter of $10.9\text{ }\mu\text{m}$, a fiber orientation of 0° , and a fiber mass fraction of 30 %. The resulting distribution of the Young's modulus in fiber direction is plotted in Figure 3.6 (upper left diagram).

The influence of the fiber orientation requires additional computation because the material model of Tandon and Weng gives only the engineering constants in a local ply coordinate system. Therefore, in an additional step, the elasticity tensor elements are computed considering a two-dimensional system under plane stress condition. Following the procedure introduced above the engineering constants are determined for a mean fiber length of $260\text{ }\mu\text{m}$ and a mean fiber diameter of $10.9\text{ }\mu\text{m}$. Subsequently, the fiber orientation is sampled

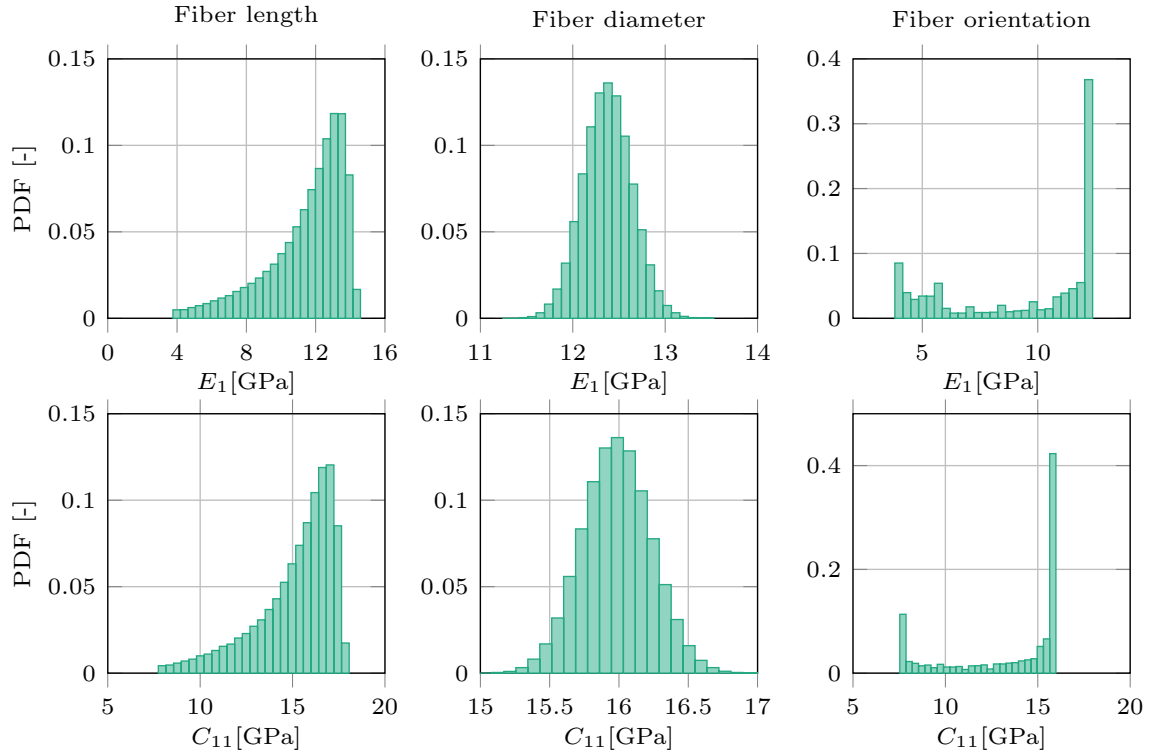


Figure 3.6: Results for the distribution of E_1 and C_{11} for a varying fiber length, diameter, and orientation based on the material model by Tandon and Weng, cf. Paper I [144].

with respect to the elliptic PDF, and the elasticity tensor elements are computed by a coordinate transformation. Finally, the effective engineering constants for the given fiber orientation are derived.

The results of the Young's modulus E_1 and the elasticity tensor element C_{11} for a variation of the fiber length (left), diameter (middle), and orientation (right) are provided in Figure 3.6. A detailed overview of all parameters and constants is given in Paper I of this cumulative Habilitation thesis [144]. The histograms reveal the resulting distribution of the material properties that are induced by the probabilistic characteristics of the microstructure. Similar results are obtained by assuming a plane strain state. This analysis gives only a preliminary insight into the influencing parameters because it is based on the assumption that all fibers have identical lengths and diameters. Therefore, in a second step, the influence of these parameters is analyzed on a numerical basis. The corresponding numerical models are derived from artificial microstructures with a size of $2500 \mu\text{m} \times 2500 \mu\text{m}$, which are generated by a Poisson process. According to this, at first, the coordinates of a new fiber centroid are sampled. The coordinates must be within the preset area of the microstructure. Afterward, the fiber length, diameter, and orientation are sampled following their PDFs. If the new fiber does not intersect with any already existing fiber and is within the preset area, the fiber is added to the artificial microstructure otherwise it is withdrawn. More information about the modeling procedure is provided in Paper I of this cumulative Habilitation thesis [144].

Starting from these artificial microstructures, small parts are extracted following the pattern depicted in Figure 3.7. The extracted windows have an edge length of $250 \mu\text{m}$, $500 \mu\text{m}$, and $750 \mu\text{m}$, respectively. Figure 3.7 gives all measures with respect to an edge length of $750 \mu\text{m}$. Additionally, a two-dimensional numerical model of the same size consisting of a structured mesh with rectangular elements is prepared. The information about the microstructure and the numerical model are combined by assigning the material properties of the fiber and the matrix to the corresponding integration points. By doing so explicit modeling of the microstructure is avoided. This approach is described in detail in Paper I of this cumulative Habilitation thesis [144]. To determine the apparent overall material properties pure displacement (KUBC) and pure traction boundary

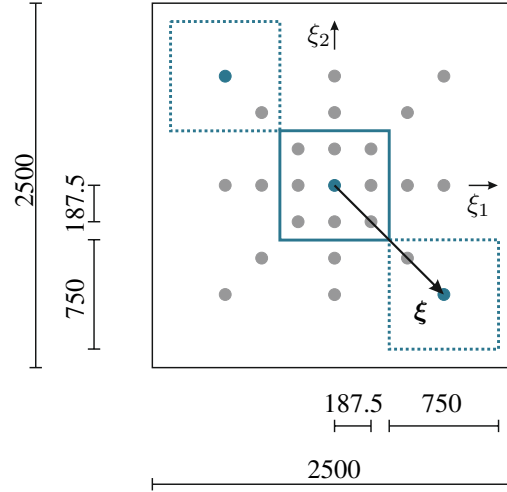


Figure 3.7: Moving window method applied to the artificial microstructure. All measures in μm . Taken from Paper IV [142], see also Papers I and II [141, 144].

	BC	$\overline{C_{11}}$ GPa	$\overline{C_{12}}$ GPa	$\overline{C_{22}}$ GPa	$\overline{C_{66}}$ GPa
Tandon-Weng		13.0	1.59	4.18	1.31
250 μm	KUBC	11.8	1.56	4.36	1.35
250 μm	SUBC	6.43	1.48	3.91	1.16
500 μm	KUBC	10.2	1.57	4.14	1.27
500 μm	SUBC	7.11	1.53	3.92	1.18
750 μm	KUBC	9.80	1.56	4.08	1.24
750 μm	SUBC	7.59	1.59	3.93	1.18

Table 3.2: Comparison of the mean values for the engineering constants based on the analytical and numerical analysis, cf. Paper I [144].

conditions (SUBC) consistent with the Hill Mandel condition are applied. Again, a plane stress state is assumed. For statistical reasons the procedure is repeated 500 times [157, 164]. The resulting mean values of the elasticity tensor elements are provided in Table 3.2. In addition Figure 3.8 illustrates the induced distribution of C_{11} . The main results can be briefly summarized as follows:

- The results summarized in Table 3.2 meet the theoretical framework of mesoscale modeling. For KUBC the mean value decreases with increasing window size. In contrast to this the mean value derived by SUBC increases with increasing window size. This effect is most obvious for C_{11} . Accordingly, the RVE size must be larger than 750 μm .
- The shift of the mean value with an increasing window size is also indicated in Figure 3.8.
- As expected the distribution width characterized by the standard deviation decreases with increasing window size.
- The window size significantly influences the parameter distribution. With an increasing window size, the Weibull distribution transforms into a normal distribution.

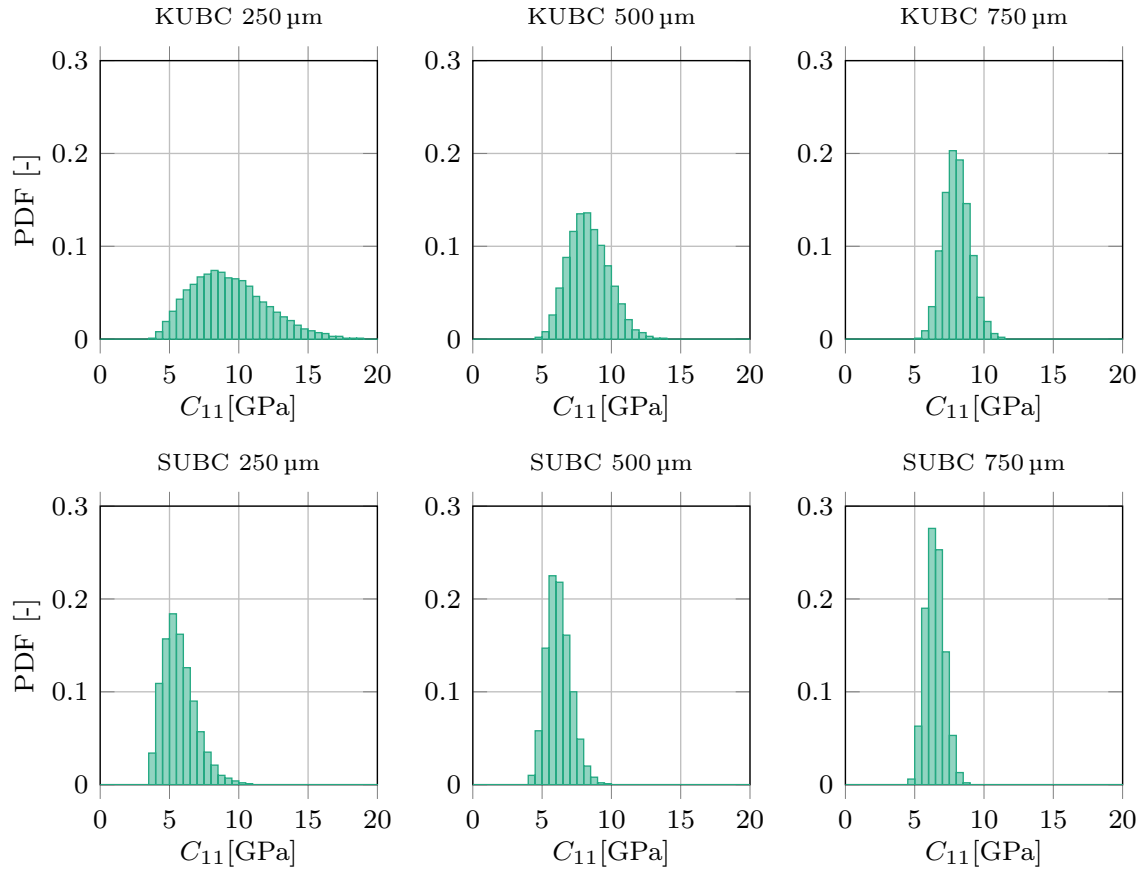


Figure 3.8: Distribution of the values for the elasticity tensor element C_{11} with respect to the boundary condition and the window size, cf. Paper I [144].

Chapter 4

Linear-elastic modeling on the mesoscale

The proposed modeling approach is validated by nanoindentation and tensile tests. Since the analysis of the probabilistic characteristics of the microstructure reveals the production-induced layered cross-section for components made from SFRC, it is important to know, whether this layered structure is significant for the numerical representation of the component under uniaxial tensile loading. Therefore, the influence of the cross-section layout on uniaxial tensile loading is investigated in this chapter. This is done by carrying out numerical simulations, which are subsequently validated by nanoindentation tests. The results are published in the Papers II and III of this cumulative Habilitation thesis [141, 146].

4.1 Numerical simulations

With the knowledge of the probabilistic characteristics of the microstructure obtained in Chapter 3.2 artificial microstructures are generated by a Poisson process as presented in Chapter 3.4. With respect to the micrograph of Chapter 3.2 the numerical model has an identical fiber mass fraction and is of the same size. To be able to analyze the influence of the microstructural layout on the structural response under uniaxial tensile loading different configurations are investigated:

- Configuration I:
Global PDFs are assumed for each characteristic. The layering of the structure is not taken into account.
- Configuration II:
Only the probabilistic information of the shell layers are used. Again, the layering of the structure is not taken into account.
- Configuration III:
Explicit modeling of the different layers with the corresponding PDFs and variation of the fiber mass fraction.

For each configuration 500 artificial microstructures are generated and tensile tests are simulated to derive the Young's modulus in horizontal and vertical direction. The generation of the numerical model is identical to the procedure introduced in Chapter 3.4. Furthermore, to include the restraint against transverse deformation induced by the core layer a plane strain state is assumed. Besides the artificial microstructures, a numerical simulation is conducted based on the original micrograph. The results for the Young's modulus obtained by the numerical simulation are summarized in Table 4.1, [141]. They lead to the conclusion that explicit modeling of the layered structure is not necessary to represent the overall structural response under uniaxial tensile loading, which meets the expectation from a mechanical point of view. Therefore, the subsequent numerical modeling presented in this work is based on the probabilistic information of the shell layers only.

4.2 Experimental verification

Since the numerical simulations in Chapter 4.1 are based on the probabilistic characteristics of the microstructure obtained by a micrograph, the results relate to the mesoscale and not the component level. Therefore, the experimental verification is limited to near-surface material properties, which can be determined by nanoindentation tests [52]. Nanoindentation tests cover a load cycle consisting of elastic and plastic loading and elastic unloading. Following this, the indentation modulus is obtained by the slope of the unloading curve

Value	Unit	Configuration I Homogeneous	Configuration II Shell layers	Configuration III Layered structure	Micrograph
\bar{E}_h	GPa	5.94	6.09	6.12	6.26
Std.	GPa	0.4	0.4	0.4	-
Dev. to micrograph	%	5.11	2.72	2.24	-
Dev. to Conf. II	%	2.46	-	0.49	2.79
\bar{E}_v	GPa	4.97	5.03	5.09	5.41
Std.	GPa	0.1	0.1	0.1	-
Dev. to micrograph	%	8.13	7.02	5.91	-
Dev. to Conf. II	%	1.19	-	1.19	7.55

Table 4.1: Results of the cross section analysis, cf. Paper II [141].

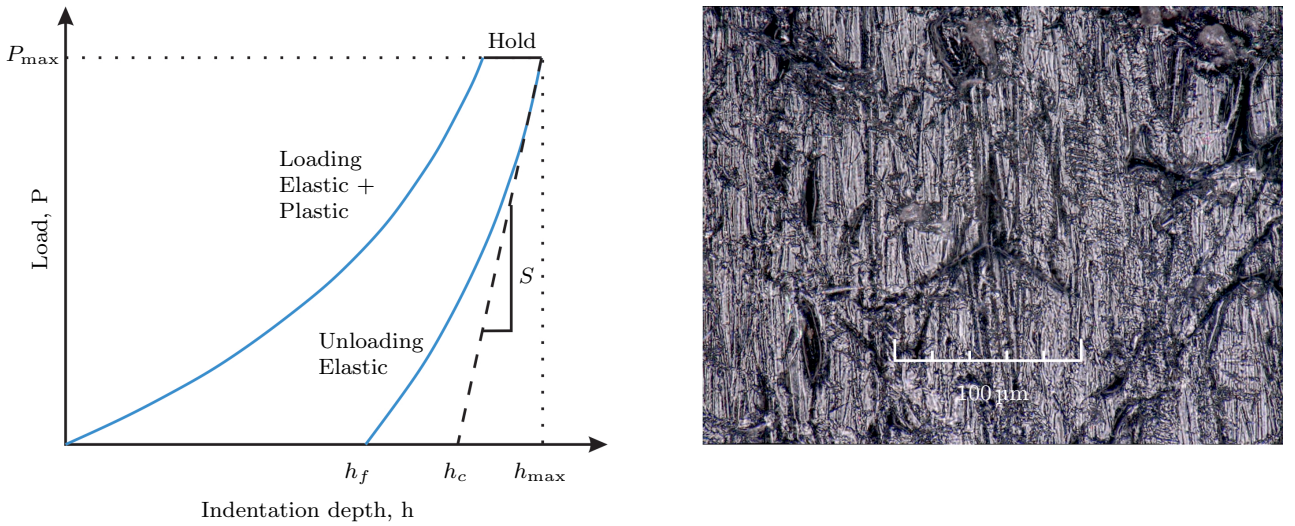


Figure 4.1: Scheme of a nanoindentation load cycle and a micrograph of the indentation area after unloading, taken from Paper II [141]. See also [103, 146, 171].

with respect to the indentation depth [125, 135]. In a subsequent step, the Young's modulus can be computed from the indentation modulus by considering the material properties of the indentation tip. A scheme of the load cycle and a micrograph of the indentation location after unloading are depicted in Figure 4.1.

For the experimental verification of the numerical modeling different test series are conducted regarding the maximal indentation force and the load orientation with respect to the melt flow direction. Following the specimen definition provided in Chapter 3.1 the indentation tests are conducted in all three axis-directions with a maximum indentation load of 500 mN and 1500 mN, respectively. For more details about the experimental setup and the theoretical framework the reader is kindly referred to the Papers II and III of this cumulative Habilitation thesis [141, 146]. The results are briefly summarized and discussed below.

In Figure 4.2 the results of the indentation tests at 500 mN and 1500 mN are plotted over the spatial coordinates for each load case. First of all the plots reveal the spatial distribution of the material properties. Furthermore, the measurements perpendicular to the melt flow confirms the results of the microstructural analysis presented in Chapter 3. The core layer can be clearly identified in the center of the cross-section. When taking into account the different fiber volume fractions of each layer, the measurement in melt flow direction also meets the expectation of the layered cross-section. Finally, the measurement in the thickness direction is characterized

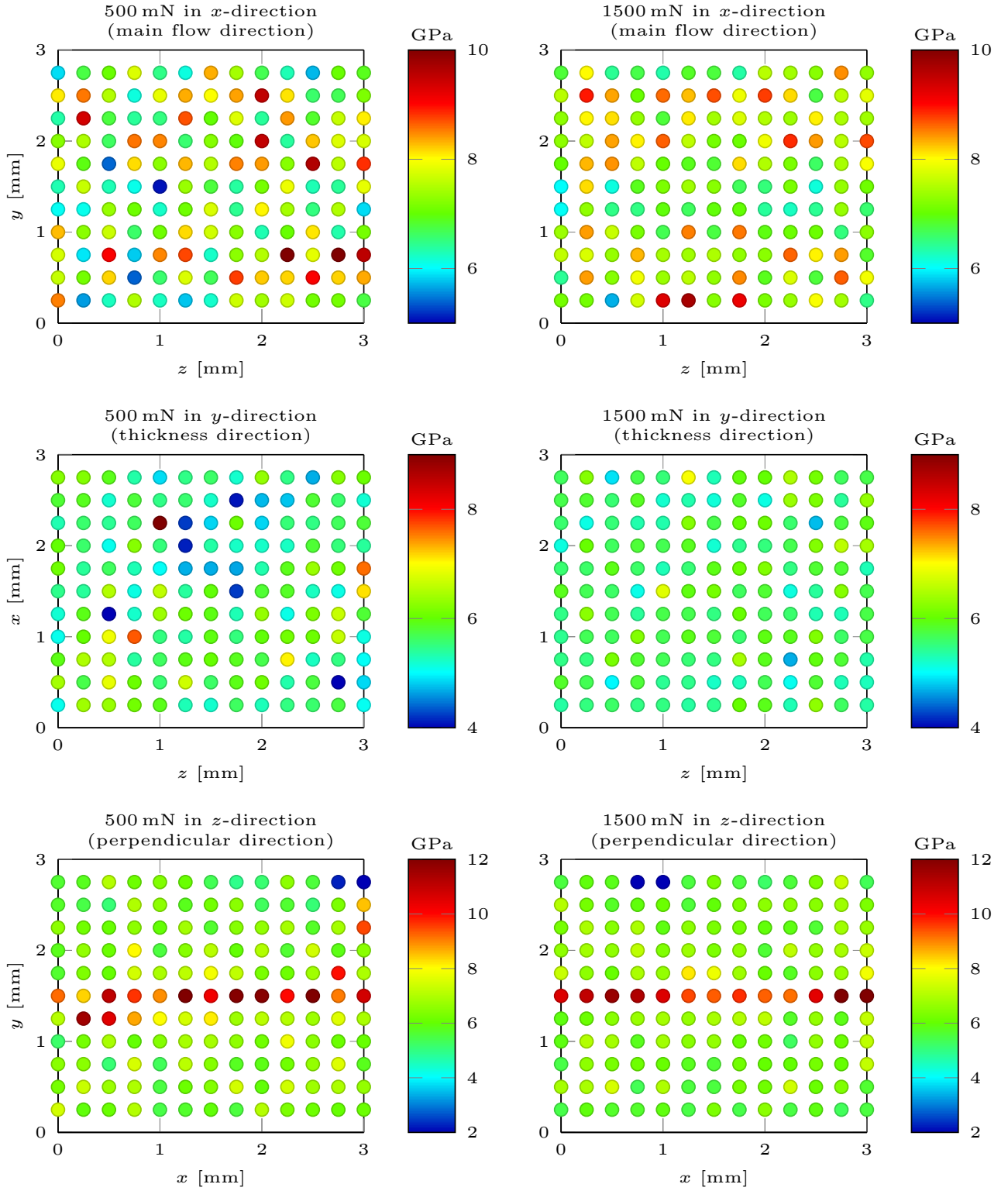


Figure 4.2: Spatial distribution of the indentation modulus for each load case and loading direction, taken from Paper III [146].

Study	Max. load mN	Direction	Mean GPa	Std. GPa	Min GPa	Max GPa	Range GPa
Paper II	500	x	6.78	1.07	-	-	-
Paper III	500	x	7.35	1.01	5.07	10.39	5.31
	500	y	5.64	0.72	3.10	9.03	5.94
	500	z	6.83	1.61	1.87	12.06	10.18
Paper II	1500	x	6.93	0.73	-	-	-
	1500	y	4.95	0.44	-	-	-
Paper III	1500	x	7.44	0.75	5.69	9.69	4.00
	1500	y	5.68	0.38	4.68	6.96	2.28
	1500	z	6.62	1.50	1.74	12.54	10.8

Table 4.2: Results of the experimentally obtained indentation modulus, cf. Papers II and III [141, 146].

		\bar{E}_h GPa	Std. GPa	\bar{E}_v^2 GPa	Std. GPa
Numerical simulation	Config. I	5.94	0.4	4.97	0.1
	Config. II	6.09	0.4	5.03	0.1
Indentation test at 500 mN	Paper II	5.84	1.07	-	-
	Paper III	6.33	0.88	5.64	0.72
Indentation test at 1500 mN	Paper II	5.97	0.73	4.95	0.44
	Paper III	6.41	0.65	5.68	0.38

² For the analysis in thickness direction the indentation modulus is given.

Table 4.3: Comparison of the experimentally and numerically obtained values, cf. Papers II and III [141, 146].

by an almost homogeneous material distribution caused by the random fiber orientation in the skin layers.

Following the measurement results, the obtained indentation modulus as well as the corresponding statistical quantities are summarized in Table 4.2. As already discussed the results indicate the fiber-reinforcement of the material and the induced direction-dependent material properties. To be able to compare the experimentally obtained results with the numerical modeling the Young's modulus is computed for the two directions that coincide with the tensile test directions defined in Chapter 3.1. Comparing the values provided in Table 4.3 shows a very good agreement between the numerical and the experimental investigations. Furthermore, the results are independent of the maximal load and therefore, also from the indentation depth and as already indicated by the numerical simulations, the layered structure of the cross section must not necessarily be incorporated into the probabilistic modeling approach of SFRC by random fields to capture the structural response under uniaxial tensile load sufficiently.

In the last step, the area is determined which is characterized by the nanoindentation test. Therefore, the measurement point pattern is projected on the micrograph microstructures. At each measurement point, a square is extracted with different edge lengths. The edge length starts at 50 μm and is stepwise increased by 50 μm up to an edge length of 500 μm . Following this procedure, uniaxial tensile tests are simulated and the stochastic quantities are computed. The results, depicted in Figure 4.3, reveal that nanoindentation tests

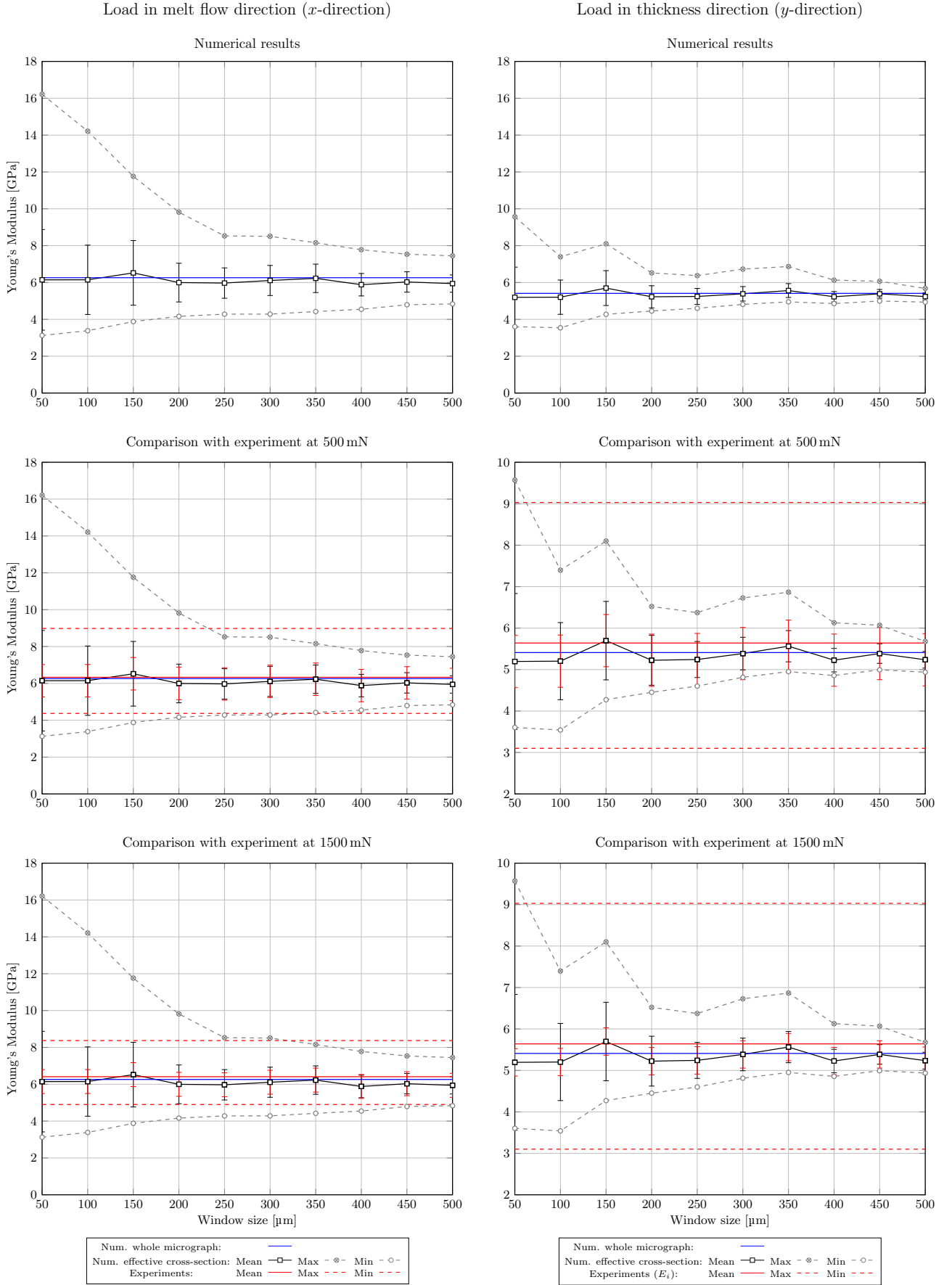


Figure 4.3: Results of the numerical simulation and comparison with the experimental results, taken from Paper III [146].

characterize an area, which is 25 times larger than the projected area of the indentation test. More details about this analysis are provided in Paper III of this cumulative Habilitation thesis [146].

Chapter 5

Adaption to the component level with elastic ideal plastic material behavior

In this chapter, the modeling approach is proposed that incorporates the spatially distributed material properties induced by the probabilistic characteristics of the microstructure on the component level. Since the thermoplastic matrix material exhibits profound plastic deformation even at low stress levels the approach comprises the elastic as well as the plastic domain. Numerical simulations are conducted and the results are validated by experimental investigations. Details about the elastic modeling with small deformation are provided in Paper II [141], the extension to finite deformation and hence, the combination of elastic and plastic deformation is introduced in the Papers IV and V of this cumulative Habilitation thesis [142, 143].

5.1 Experimental characterization by tensile tests

Before the modeling approach is presented tensile tests are conducted based on the specimens defined in Chapter 3.1. The geometry of the specimens that are cut out of the initially manufactured plate is defined in accordance with type 1B of DIN-ISO-527-1 [84]. Due to the plate dimensions, the total length of the specimen is set to 140 mm and the thickness is 3 mm.

The tensile tests are carried out following DIN-ISO-527-1 [84]. With a maximal available load of 50 kN the tensile test covers the elastic and plastic domain until the failure of the specimen. Since the specimen is tested until failure, the deformation is captured by an external contactless laser extensometer. For the elastic domain, the Young's modulus is computed from the measurement data by evaluating the slope of the stress-strain curve between a strain level of 0.1 % and 0.2 %. Besides this global observation, the measurement length is divided into segments of 5 mm each to analyze the local behavior. Based on this the spatial distribution of the material properties is qualitatively analyzed for three segments of 15 mm at one specimen.

For the analysis of the plastic deformation, the strain level at failure and the maximum stress level are derived from the measurement data. All results are summarized in Table 5.1. For each parameter, the mean value as well as the standard deviation is given. Furthermore, in addition to the measurement data information from the datasheet provided by the manufacturer is provided [21].

Comparing the experimental results with the data sheet reveals a significant deviation. This deviation is most likely caused by the manufacturing of the specimens since this significantly influences the fiber distribution, fiber length, and fiber orientation of the specimen as well as the quality of the fiber-matrix bonding. This deviation is also observable in the stress-strain curves plotted in Figure 5.1. The diagram on the left-hand side holds the measured stress-strain curves for each specimen (gray) and the datasheet information (black). Besides the discrepancies in the elastic as well as the plastic domain the plot reveals the prominent plastic deformation of the material. The diagram on the right-hand side gives the spatial distribution of the material

Number of specimens		\bar{E} GPa	Std GPa	$\bar{\sigma}_{\text{failure}}$ MPa	Std MPa	$\bar{\epsilon}_{\text{failure}}$ %	Std %
Data sheet	1	9.69	-	135	-	2.5	-
Experiments	8	7.95	0.87	96.1	6.22	1.97	0.14

Table 5.1: Experimental results obtained by tensile tests in the elastic and plastic domain, compare Paper IV [142].

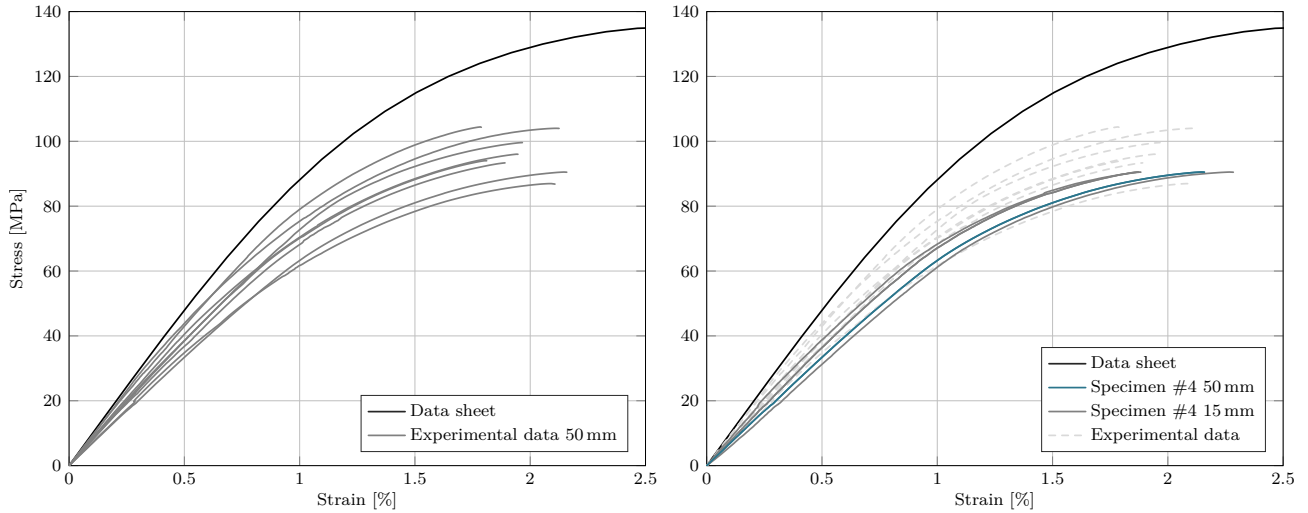


Figure 5.1: Experimental results and comparison with data sheet, Paper V [143].

properties for one specimen. Therefore, the corresponding global stress-strain curve is highlighted in green. In addition to this, the curves for three non-overlapping sections with a measurement length of 15 mm each are added to the diagram. The different curves confirm the spatial distribution of the material properties, which was also detected during the nanoindentation tests provided in Chapter 4.2.

5.2 Modeling approach

The main idea of the probabilistic modeling approach is the representation of the material properties by homogeneous second-order Gaussian random fields. To be able to synthesize these fields the correlation structure must be known in order to solve the Fredholm integral and hence, utilize the KLE or other numerical methods in case there is no closed solution. Therefore, the modeling approach proposed consists of six steps:

1. Probabilistic characteristics of the microstructure

The first step comprises the determination of the probabilistic characteristic of the microstructure. A procedure for near field and hence, two-dimensional information is provided in Chapter 3. Since the application on the component level requires three-dimensional information [141], PDFs derived from μ CT are taken from literature [58].

2. Artificial microstructures

Following the procedure presented in Chapter 3.4 artificial microstructures are generated by a Poisson process. Based on the PDFs of the geometrical fiber properties first, the coordinates of the centroid are sampled before the fiber length, diameter, and orientation are assigned. The overall size of the microstructures are 2500 mm \times 2500 mm.

3. Apparent overall material properties

Based on the pattern depicted in Figure 3.7 small windows are extracted from the artificial microstructure to determine the apparent overall material properties. The windows have an edge length of 250 mm, 500 mm, and 750 mm, respectively. Because the preliminary work, which focuses on the linear elastic material behavior indicates that pure displacement boundary conditions are suitable for the computation of the apparent overall material properties [141] pure traction boundary conditions are not considered at this stage.

4. Correlation analysis

Based on the apparent overall material properties for each extraction, the correlation function is determined by computing the correlation coefficient between the individual extractions and applying a curve fit. For the curve fit exponential, Gaussian, and triangle correlation functions are considered.

5. Synthesizing cross-correlated random fields

With the information about the apparent overall material properties and the correlation structure at hand cross-correlated random fields are synthesized by utilizing a combination of the EOLE and the mcKL to represent the spatial distribution of the material parameters.

6. Numerical simulation of tensile tests

The random fields are used in the final step to incorporate the spatial distribution of the material properties into the numerical modeling of a tensile test specimen under uniaxial tensile load in the elastic and plastic domain.

5.3 Apparent overall material properties and correlation analysis of elastic-ideal plastic material behavior

5.3.1 Apparent overall material properties

The numerical simulation of the elastic-ideal plastic material behavior of SFRC is based on finite deformation. Hence, a hyperelastic strain-energy density function in combination with a von Mises yield criterion is used to describe the structural behavior. For transversely-isotropic material behavior, the strain-energy density function is taken from [16], which makes use of five individual material parameters to represent the transversely-isotropic material behavior. Since the elasticity tensor is a function of the deformation, the elements are determined by a coefficient comparison at zero strain. Due to this linearization, it is possible to limit the determination of the apparent overall material properties representing the elastic response to linear-elastic simulations.

The yield strength, which is required to characterize the plastic deformation, is obtained by utilizing a homogenization procedure introduced in [83, 102, 138, 139]. Deriving the potential \tilde{U}_0 for a linear comparison composite from numerical simulations allows one to compute first, the yield function and subsequently, the yield strength [102]. Since the potential is taken from the linear comparison composite again linear-elastic simulations are sufficient to obtain the yield strength.

The results of the apparent overall material properties are collected in Table 5.2. It holds the mean values as well as the standard deviations of the hyperelastic strain-energy density function coefficients and the yield strength. In addition to this, the Young's modulus is given to allow a comparison with experimental data. The following conclusion can be derived:

- The mean values show a decreasing behavior for increasing window size. This meets the theoretical framework of the apparent overall material properties for an SVE under pure displacement boundary conditions. The same holds for the standard deviation.
- The experimentally obtained Young's modulus is based on 13 different specimens made from PBT GF 30. With a mean value of 9.75 GPa and a standard deviation of 0.27 GPa it meets the results at a window size of 750 μm best. However, all results are covered within the standard deviation.
- The results of the yield strength for a window size of 750 μm is also within the range of the data provided by the manufacturer [21].

5.3.2 Correlation analysis

The next step is the correlation analysis of the strain-energy density function coefficient and the yield strength. Since the correlation functions and the cross-correlation parameters might depend on the window size [144] Figures 5.2 and 5.3 hold the correlation lengths and the cross-correlation parameters for each parameter pair and window size within the 95% confidence interval. It is important to note, that the correlation length cannot surely be determined by numerical simulations, because it is directly linked to the window size by the correlation function. Therefore, the results presented in Figure 5.2 give the ratio of the correlation length to

		Λ	μ	α	β	γ	E_{11}	σ_y
		GPa	GPa	GPa	GPa	GPa	GPa	MPa
Mean	250 μm	5.62	1.34	-1.16	-0.20	1.35	11.9	151.7
	500 μm	5.43	1.24	-1.13	-0.14	1.19	10.5	130.0
	750 μm	5.38	1.20	-1.10	-0.13	1.13	10.0	125.7
	Experiment	-	-	-	-	-	9.75	
Std.	250 μm	0.492	0.192	0.239	0.081	0.475	3.85	57.1
	500 μm	0.224	0.097	0.131	0.033	0.244	1.96	24.2
	750 μm	0.140	0.064	0.090	0.020	0.148	1.26	14.7
	Experiment	-	-	-	-	-	0.27	

Table 5.2: Mean values and standard deviations of the strain energy density function coefficients as well as the yield strength, cf. Paper IV [142].

the window size for the best curve fit based on the exponential, Gaussian, and triangle correlation functions. The quality of the curve fit is measured by R^2 . The results are summarized below:

- The results of the curve fit for the auto-correlation indicate that the triangle correlation function is the best fit for the parameters Λ , β , γ , and σ_y , whereas the exponential correlation function fits the parameters μ and α best. This is also the reason for the different correlation lengths of these parameters.
- Consequently it is expected that the exponential correlation function is the best option for the cross-correlation of these two parameters. The remaining parameter pairs should be approximated best by the triangle cross-correlation function because the corresponding auto-correlation functions of these parameters are given by a triangle correlation function, which is confirmed by the R^2 values of the performed curve fits.
- The results show, that with increasing window size, the distance between b_1 and b_2 decreases. Furthermore, for an approximation with the triangle function the values converge to the edge length of the analyzed window. For the exponential function the value is $0.4l_w$.
- First, the dependence of the cross-correlation parameter a on the window size, as discussed before, is observable. Furthermore, the parameter pairs $\Lambda - \alpha$ and $\alpha - \beta$ are only very weakly cross-correlated, which is confirmed in Figure 5.3.

5.4 Application to tensile test specimens

In the last step, the modeling approach is applied to tensile tests under uniaxial loading covering the elastic and plastic domains. Following the proposed modeling procedure in Chapter 5.2 first, random fields must be synthesized before the structural response can be simulated. To incorporate the spatial distribution of the material properties in both the elastic and plastic domain in combination with a reduced complexity of the model only one parameter of the strain-energy density function and the yield strength are represented by a homogeneous second-order Gaussian random field. The remaining parameters are deterministic and hence, assumed to be homogeneous. Therefore, they are given by the mean value of the apparent overall material properties. All values correspond to a window size of 750 μm because the obtained mean values fit the experimental data best. The corresponding values of the different parameters are collected in Table 5.3. As indicated the parameter Λ of the strain-energy density function is represented by a random field. However, the given standard deviation does not meet the results of the apparent overall material properties provided in Table 5.2. Since the structural response under uniaxial stress is mostly characterized by the element C_{11} of the elasticity tensor and C_{11} is a function of all five strain-energy density function parameters the standard

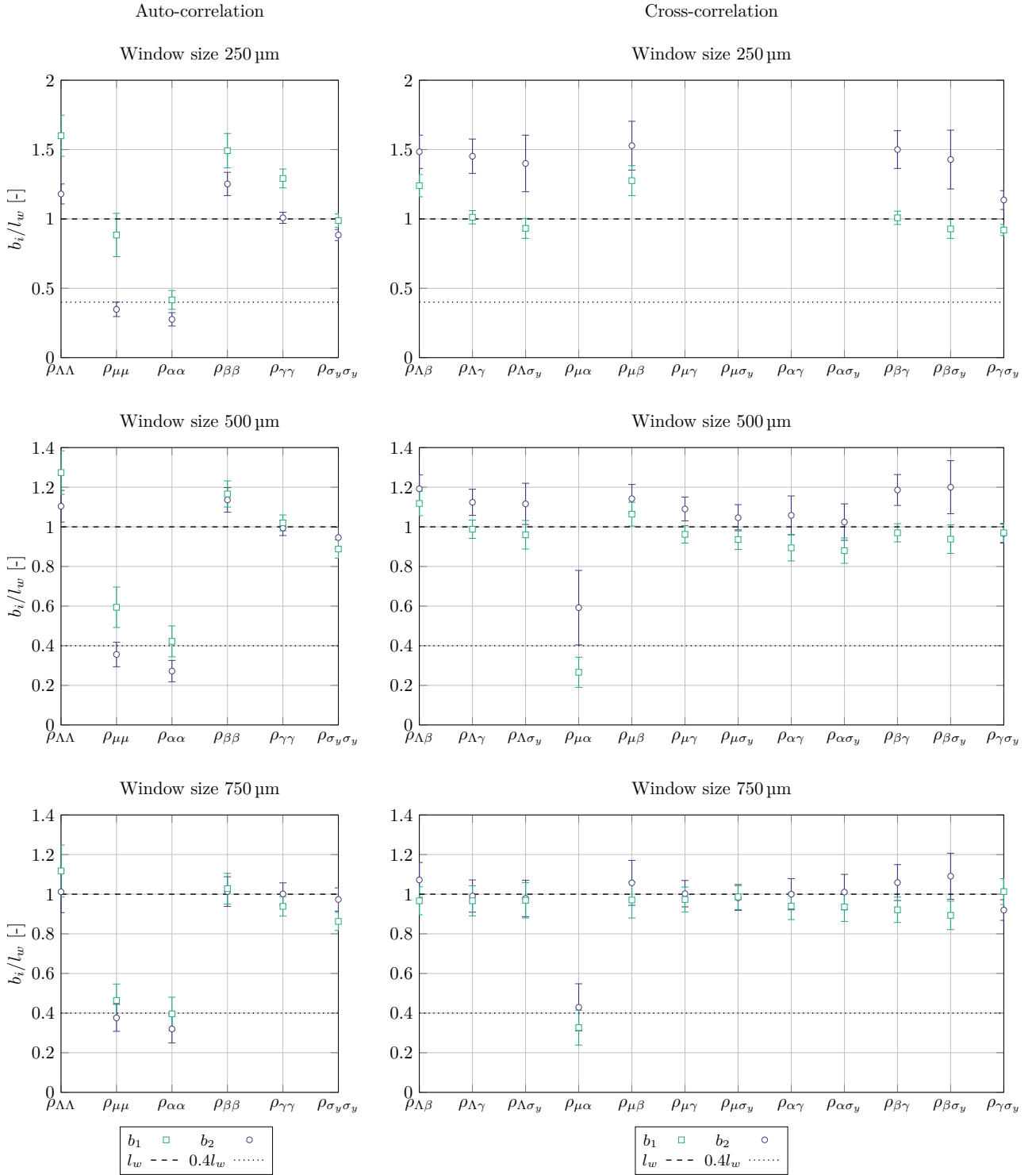
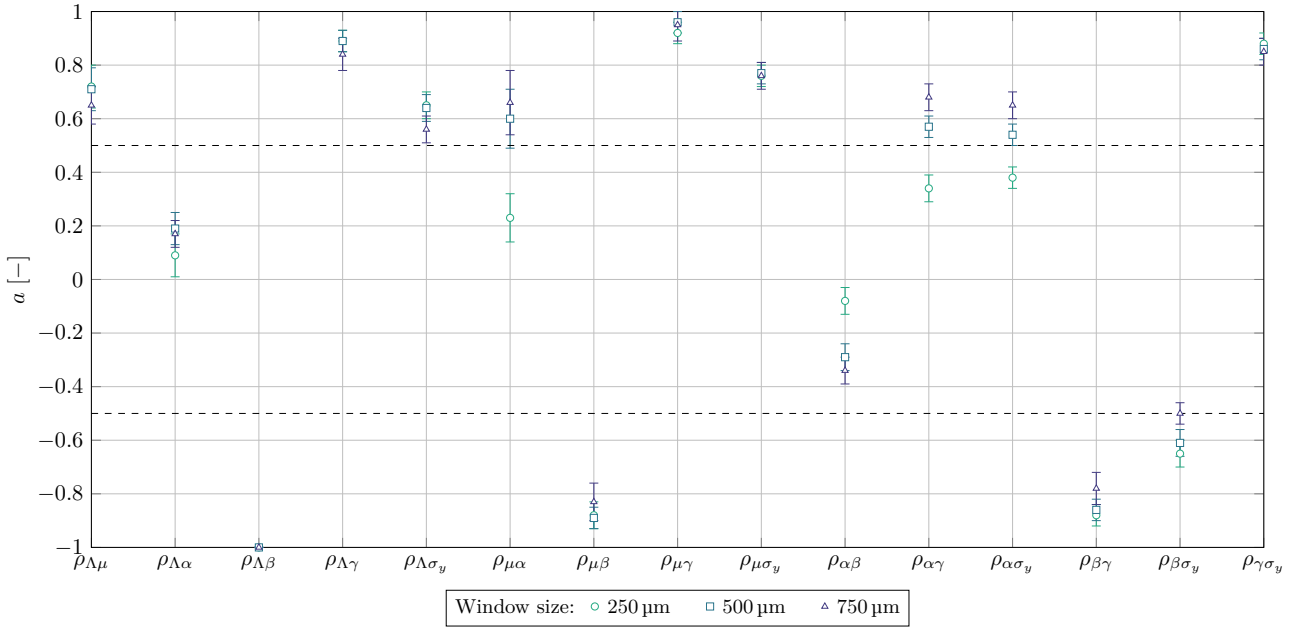


Figure 5.2: Analysis of the correlation length for each auto- and cross-correlation, taken from Paper IV [142].


 Figure 5.3: Cross-correlation coefficient a for all window sizes, taken from Paper IV [142].

	Mean GPa	Std GPa	b_1 mm	b_2 mm
Λ	5.38	1.2	5, 10, 15	0.3
μ	1.12	0	-	-
α	1.10	0	-	-
β	-0.13	0	-	-
γ	1.13	0	-	-
σ_y	0.13	0.02	5, 10, 15	0.3

Table 5.3: Material properties of numerical simulation.

deviation is significantly increased to capture the fluctuation of the other parameters as well. The same hold for the yield strength. As indicated by the strain-stress curve depicted in Figure 5.1 the used PBT-GF-30 shows plastic deformation even at low stress levels. Therefore, the standard deviation is selected in such a way as to allow early plastic deformation. As already discussed in Chapter 4.1 again a plane strain state is assumed.

Besides the mean value and the standard deviation, the numerical simulation and representation of the structural response are significantly influenced by the correlation length of the random field. As mentioned before, the correlation length cannot be derived from analytical or numerical treatment but from experimental results. The influence of the correlation length on the realization of the random fields is depicted in Figure 5.4, which gives realizations for Λ for a correlation length in horizontal direction of $l_x = 5$ mm, $l_x = 10$ mm, and $l_x = 20$ mm. In analogy to the description of oscillations, the correlation length can be interpreted as the wavelength of the dominant eigenfunction.

Since the material behavior is characterized by ideal plasticity the correlation length in the vertical direction is required to be smaller than the thickness of the specimen. Otherwise, no localized plastic deformation is achieved. Due to this, the vertical correlation length is set to 0.3 mm, which leads to a resemblance of the resulting stress-strain relation with experimental data for reinforced material. To allow comparability with experimental results the numerical simulations are carried out for eight different realizations per correlation

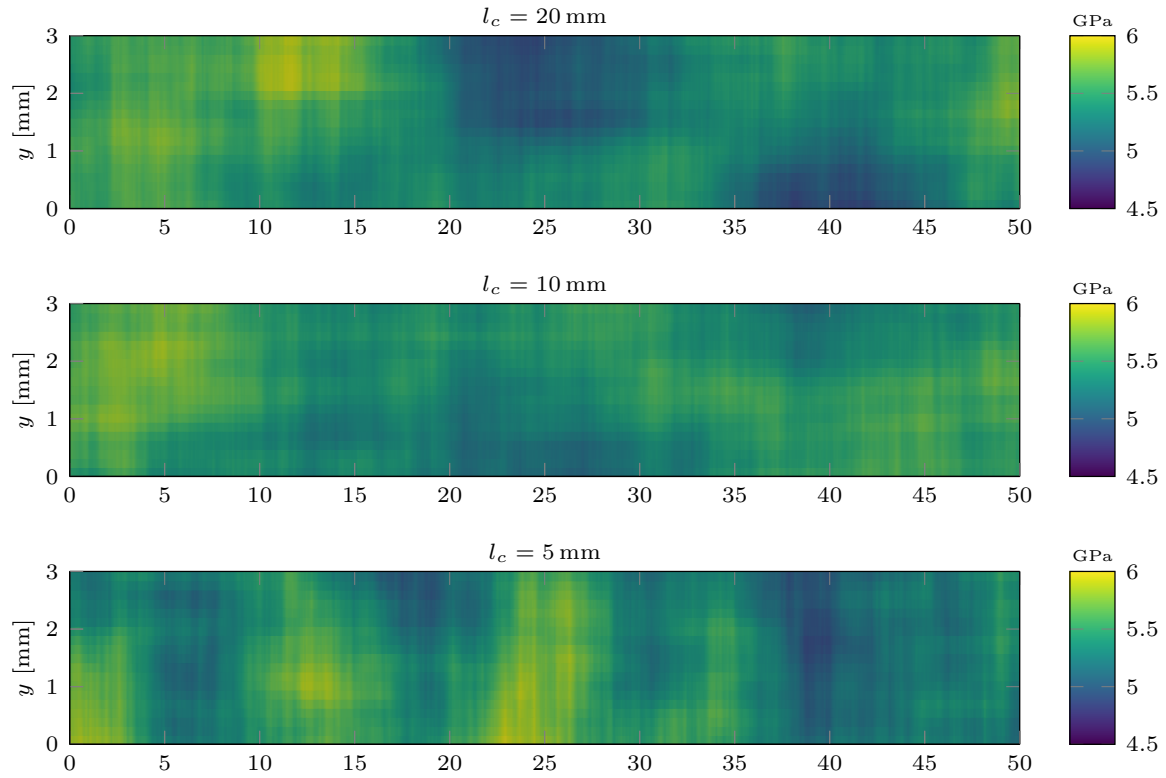


Figure 5.4: Discretizations of cross-correlated homogeneous second-order Gaussian random fields to represent the spatially distributed material parameter Λ for different values of l_x , taken from Paper V [143].

length. The results of in total 24 simulations are illustrated in Figure 5.5. Besides the overall behavior for a measurement length of 50 mm also the spatial distribution is provided by evaluating the simulation for three non-overlapping paths of 15 mm. In addition to this, the diagrams also hold the stress-strain curve taken from the data sheet (black) [21] and the experimental data (gray).

To give more insights on the influence of the correlation length on the numerically obtained data Table 5.4 holds the mean stress as well as the standard deviation for a strain level of 0.2 %, 0.5 %, 1.0 %, 1.5 %, and 2.0 %. This also includes the experimental data.

The main results are briefly discussed below.

- The diagrams provided in Figure 5.5 reveal that the numerical obtained stress-strain curves clearly show the expected elastic-plastic behavior. Despite the fact, that the nonlinear material behavior is modeled based on the assumption of ideal plasticity the resulting stress-strain curves show an overall good agreement with the experimental data. This is related to the spatially limited plastic deformation and the rearrangement of the applied loading.
- With a decreasing correlation length the numerical results show a better agreement with the experimental data. This is also indicated by the values provided in Table 5.4. For a decreasing correlation length, the mean stress state converges to the experimentally obtained values and for a correlation length of 5 mm the results show an overall good agreement.
- The modeling approach is endorsed by the results on the right-hand side of Figure 5.5 by two important aspects. First, the modeling approach leads to a plastic deformation covering the whole specimen and hence, is not limited to small areas. Second, when dividing the measurement length into small sections, each section shows slightly different behavior. Both phenomena are confirmed by the experimental investigation.

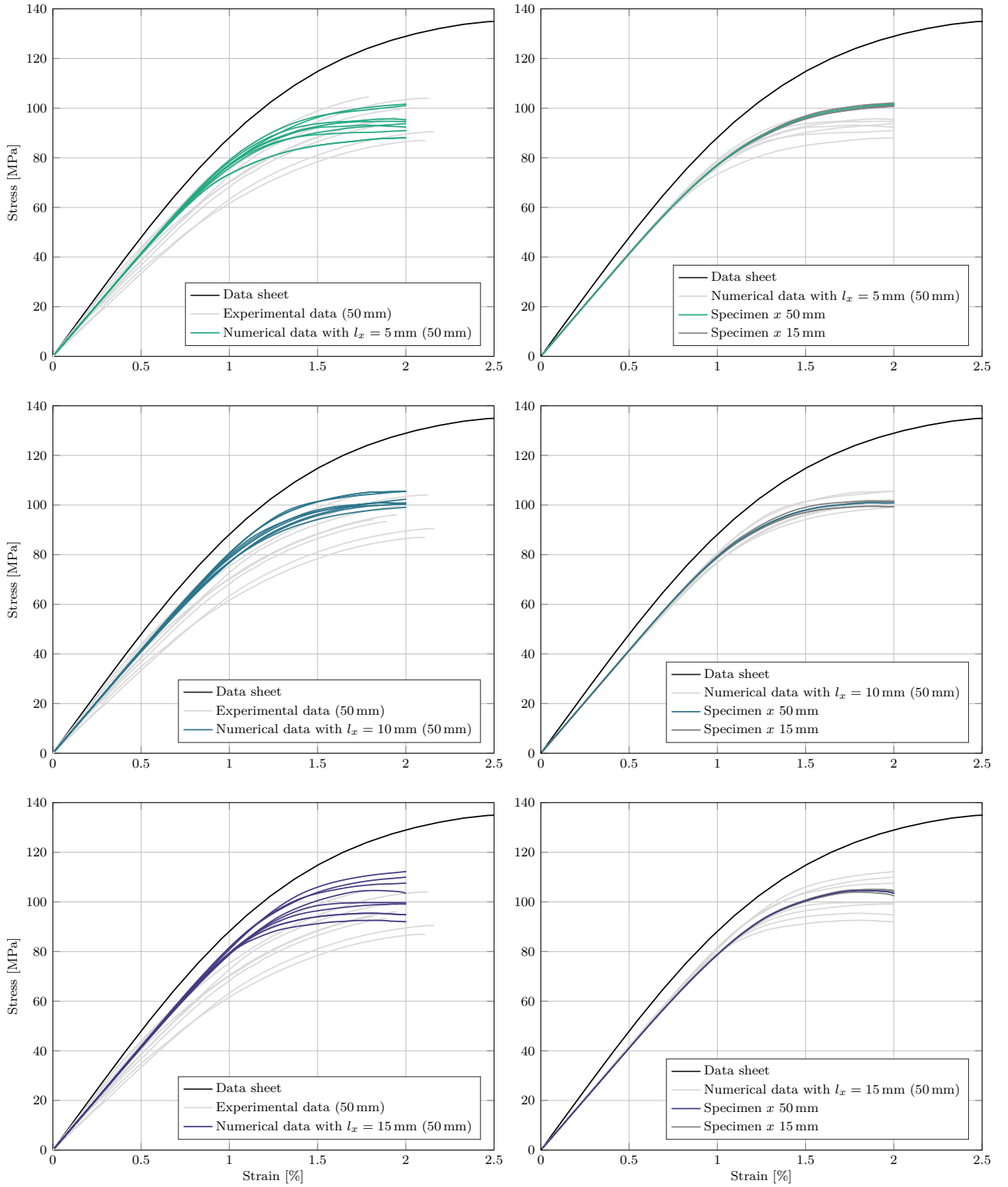


Figure 5.5: Results of the numerical simulation in comparison with the experimentally obtained results and a stress-strain curve provided by the manufacturer [21], taken from Paper V [143].

Strain level %	$l_x = 15 \text{ mm}$		$l_x = 10 \text{ mm}$		$l_x = 5 \text{ mm}$		Experimental data	
	mean	std	mean	std	mean	std	mean	std
	MPa	MPa	MPa	MPa	MPa	MPa	MPa	MPa
0.2	16.6	0.1	16.6	0.1	16.6	0.1	16.1	1.8
0.5	41.6	0.3	41.4	0.3	41.3	0.2	38.7	3.7
1.0	80.0	1.2	78.6	1.6	76.9	1.7	70.0	5.8
1.5	99.2	5.2	97.7	2.6	92.0	3.9	88.5	6.8
2.0	102.3	7.2	101.8	2.4	94.7	4.9	95.8	6.3

Table 5.4: Deviation of the single simulations at different strain levels and comparison with experimental data.

Chapter 6

Concluding remarks

In this cumulative Habilitation thesis, a new modeling approach is proposed, which incorporates the spatial distribution of the material properties in the elastic and plastic domain on the component level. The work comprises the findings of five Papers [141–144, 146] that have passed a peer-review process or are still under review.

Since the main objective of this work is the incorporation of the spatially distributed material properties due to the probabilistic characteristics of the microstructure by homogeneous second-order Gaussian random fields, these characteristics were analyzed on an analytical and numerical basis first. Therefore, the influence of the probabilistic distribution of the microstructural characteristics of the fiber length, fiber diameter, and fiber orientation on the engineering constants and the elasticity tensor elements is determined analytically by utilizing the material models of Tandon-Weng and Halpin-Tsai. This is followed by a numerical analysis. The analytical treatment reveals the impact of the probabilistic microstructure on the material properties. Most significant is the influence of the fiber length, fiber volume fraction, and fiber orientation on the Young's modulus E_{11} . Besides this, the remaining engineering constants are not affected by the geometrical fiber properties, only the fiber volume fraction and the fiber orientation contribute significantly. Following these findings, the elasticity tensor components are influenced by the same microstructural characteristics as the engineering constants. The resulting engineering constants and elasticity tensor component distributions are of the same kind as the microstructural characteristics. The subsequent numerical analysis includes not only the determination of the apparent overall material properties as a function of the influencing parameters, boundary conditions, and window size but also a correlation analysis. This is important because the correlation structure is essential for the synthesis of homogeneous second-order Gaussian random fields used later. In contrast to the analytical treatment now each fiber has its individual geometrical properties and all elements of the elasticity tensor can be computed individually. The results reveal the symmetry of the elasticity tensor as well as the transversely isotropy of the reinforced material and confirm the analytical results. Besides this, it is shown that with an increasing window size the distribution of the elasticity tensor components shifts from the microstructural induced to a normal distribution.

Following the gained knowledge the modeling approach for the spatially distributed material properties of SFRC based on second-order Gaussian random fields is introduced. The modeling approach comprises three steps. First, the microstructural characteristics of the material are derived from micrographs and μ CT images, respectively. Afterward, the apparent overall material properties and the correlation structure of the material properties are determined. Finally, the mCKL is used to synthesize cross-correlated random fields, which represent the spatial distribution of the material properties on the component level and are passed to the numerical simulation on the component level.

The analysis of the microstructure based on a two-dimensional micrograph reveals the layered structure of the material. Due to the shear forces in the melt flow, the fiber orientation varies over the thickness. They are randomly orientated at the surfaces and perpendicular to the melt flow in the center. Between these layers, the shell layers are located, which show a fiber orientation with the melt flow direction. This well-known structure can also be found in literature [41, 46]. Integrating the information about the layered structure in combination with the probabilistic characteristics of the fiber length, fiber diameter, fiber orientation, and fiber volume fraction into the modeling approach shows that it is sufficient to incorporate only the shell layer information when dealing with uniaxial tensile loading. To validate the results based on a two-dimensional micrograph experimentally, nanoindentation tests are conducted, because they provide near-field properties only. The tests are carried out in the direction of the three major axes (along the melt flow direction, perpendicular to

it, and in the thickness direction) and confirm the layered structure of the material as well as the results of the numerical simulations based on the two-dimensional probabilistic characteristics. In addition to these results, numerical simulations of different window sizes reveal that nanoindentation tests characterize an area 25 times larger than the indentation area. This is independent of the applied indentation load.

A comparison with experimental data on the component level by tensile tests, however, leads to significant deviations. Further investigations show that for the modeling approach on the component level the full three-dimensional microstructural characteristics derived by μ CT are required. Incorporating these characteristics the numerical results and the experimental data show an excellent agreement with a deviation of only 1.5 % for the linear elastic domain.

In a final step, the proposed approach is extended to the nonlinear domain by including ideal plasticity and finite deformation. Therefore, the material behavior is described in the linear domain by a transversely-isotropic strain-energy density function. This is combined with a classical J_2 -plasticity formulation utilizing a von Mises criterion with an associate flow rule, which requires the definition of a yield strength. Following this, the material behavior is represented by six individual material parameters. To be able to describe these properties by random fields, at first, the correlation structure must be determined. It is shown that by the linearization of the strain-energy density function at zero strain and the use of a homogenization procedure for the yield strength only linear elastic simulations are necessary to compute the apparent overall material properties and to derive the correlation structure by the moving window method. The apparent overall material properties are validated by experimental data, which shows a good agreement. Furthermore, the analysis reveals the link between the fiber mass fraction and the yield strength, which meets the expectation. Besides this, the obtained results reveal a complex auto- and cross-correlation structure that also includes a distinct cross-correlation between the yield strength and the parameters of the strain-energy density function. Furthermore, the correlation structure is affected by the window size, which is supported by the results for the cross-correlation parameter a . For the approximation of the correlation in most cases, the triangle correlation function shows the best fit. However, the auto-correlations of the parameters μ and α as well as the corresponding cross-correlation are best described by an exponential correlation function. Subsequently, the correlation lengths for these parameters differ. For an increasing window size l_w the correlation length converges to l_w for a triangle correlation function and to $0.4l_w$ for the exponential correlation function. Since the correlation length can be interpreted as an individual material parameter the final value must be derived from experimental data.

With this knowledge at hand, subsequently, cross-correlated second-order homogeneous Gaussian random fields are synthesized to represent the strain-energy density function coefficient Λ and the yield strength. With this procedure, it is ensured that in both the elastic and plastic domain the probabilistic information is included. Since, the yield strength and the elastic material behavior are spatially distributed, simulated tensile test specimens show localized plastic deformation even though elastic-ideal plastic material behavior is assumed. This leads to the expected strain-dependent reduction of the material stiffness.

Finally, the numerically obtained data and hence, the proposed probabilistic multi-scale modeling approach are validated by conducting uniaxial tensile tests in the elastic and plastic domain of specimens made from PBT-GF-30. This step is also essential to derive the final correlation length because it can be interpreted as an individual material parameter. Therefore, the numerically computed stress-strain curves are compared to the experimental results. The comparison reveals that with a decreasing correlation length the numerical data matches the experimental data quite well. However, the assumption of ideal plasticity leads to some deviations at large strains. Furthermore, the reduction of the complexity limits the fluctuation at low strains. Furthermore, the limitation to Gaussian random fields causes an underestimation of low values for the yield strength to avoid negative realizations.

Concluding the presented work, the spatially distributed material properties are experimentally detected by nanoindentation tests on the mesoscale and by tensile tests until failure on the component level. Following this, the presented comprehensive probabilistic multi-scale modeling approach is sufficient to incorporate spatially distributed material properties for the linear-elastic and elastic-ideal plastic material behavior. For the

required correlation analysis numerical simulations on the mesoscale are appropriate to derive the complex cross-correlation structure of the material properties covering the elastic and plastic domain. Even for nonlinear behavior, linear-elastic simulations are sufficient to derive the correlation structure. If the correlation analysis is related to a subsequent simulation on the component level, the probabilistic characteristics must be derived from μ CT. Otherwise, the probabilistic characteristics computed from a micrograph are sufficient for subsequent modeling on the mesoscale. The comparison with experimental data confirms the suitability of the proposed modeling approach for linear-elastic and elastic-plastic material behavior of SFRC including its spatial distribution on the component level without the need for explicit microstructural modeling.

In future work, the approach can be extended in different ways. At first, this comprises the representation of all material parameters for the elastic-ideal plastic modeling by random fields. Besides this, the use of non-Gaussian random fields is worthwhile to avoid negative realizations. Additionally, the implementation of hardening and visco-plasticity are to be discussed. Last but not least, for an extension within the probabilistic domain the approach can be integrated into a Markov chain Monte Carlo algorithm to derive the probability distribution of several material properties.

Part B

Publications of the Habilitation thesis

Paper I

Correlation structure in the elasticity tensor for short fiber-reinforced composites

Title: Correlation structure in the elasticity tensor for short fiber-reinforced composites

Authors: Natalie Rauter¹ and Rolf Lammering¹

Affiliation: ¹Helmut-Schmidt-University /
University of the Federal Armed Forces Hamburg
Holstenhofweg 85, 22043 Hamburg, Germany

Journal: Probabilistic Engineering Mechanics
62, pp. 103100, 2020

Status: Published

DOI: 10.1016/j.probengmech.2020.103100

Abstract: The present work provides a profound analytical treatment and numerical analysis of the material properties of SFRC on the mesoscale as well as the resulting correlation structure taking into account the probabilistic characteristics of the fiber geometry. This is done by calculating the engineering constants using the analytical framework given by Tandon and Weng as well as Halpin and Tsai. The input parameters like fiber length, diameter and orientation are chosen with respect to their probability density function. It is shown, that they are significantly influenced by the fiber length, the fiber orientation and the fiber volume fraction. The verification of the analytically obtained values is done on a numerical basis. Therefore, a two-dimensional microstructure is generated and transferred to a numerical model. The advantage of this procedure is, that there are several fibers with different geometrical properties placed in a preset area. The results of the numerical analysis meet the analytically obtained conclusions. Furthermore, the results of the numerical simulations are independent of the assumption of a plane strain and plane stress state, respectively. Finally, the correlation structure of the elasticity tensor is investigated. Not only the symmetry properties of the elasticity tensor characterize the correlation structure, but also the overall transversely-isotropic material behavior is confirmed. In contrast to the influencing parameters, the correlation functions vary for a plane strain and a plane stress state.

I.1 Introduction

Short fiber-reinforced composites (SFRC) are widely used in the automotive and aeronautical industry. One main advantage is the suitability of thermoplastic-based compounds for an automated serial production like mold injection, which allows high production rates with reasonable prices per piece. However, due to the finite fiber length and varying flow velocities and directions during the injection processes, the components show spatially distributed mechanical properties. Due to this the corresponding numerical simulation of the components is challenging and expensive. For an adequate material description, representative material properties need to be established.

From an analytic perspective in contrast to continuous fiber-reinforced composites, the local effects on stress and strain states due to microscopic inclusions must be taken into account. One approach for an analytic description of the resulting mechanical properties of SFRC is based on the mean-field theory in combination with Eshelby's work [40]. Mori and Tanaka [121] and later Tandon and Weng [170] expanded this. As a second approach self-consistent models are introduced. One very common representation of this group was developed by Halpin and Tsai [61, 62]. A detailed overview of the analytic modeling is given in [174]. It is concluded that the approach by Tandon and Weng shows the best results for the prediction of the elastic properties. This is also confirmed in [60]. However, as these material models are based on homogeneous material they are not capable of representing the spatial dependence of the material properties.

There are various analyses of the influencing parameters based on analytical material models. In [60] it is shown that for example the spatial fiber distribution must be taken into account. The effect of the fiber orientation on an analytical basis is given in [45]. Finally, in [78] a comprehensive analysis including not only the fiber orientation and fiber distribution but also the aspect ratio of the fiber is taken into account. However, these studies don't include the probability properties of the fiber characteristics.

Following the analytical treatment of the influencing parameters, the resulting fluctuation of the fiber volume fraction and fiber orientation should be added to numerical models of SFRC. To represent the spatial fiber distribution the fiber itself must be added to the model. However, as the fiber length is very small compared to component dimensions a multi-scale approach is required for numerical modeling. One possibility here is the use of second-order random fields, that represent spatial varying information on the mesoscale [57] and therefore, allow the modeling of inhomogeneous material properties [126]. For example in [189] this technique is used to simulate numerically the continuous mode conversion of Lamb waves in fiber reinforced composite structures, which is induced by the random distribution of the fibers on the microscale.

Other approaches for the numerical modeling of SFRC are based on the representative volume element (RVE). For example, in [68] the suitability of randomly generated characteristic volume elements using XFEM is analyzed to capture the local material response in concrete. XFEM is also used in [137] in combination with a cohesive zone model. In [183] micro-mechanical modeling of randomly oriented fiber polymer composites is presented. Furthermore, an overview of studies deriving a micromechanical model for randomly orientated fibers is given. The suitability of the orientation tensor is discussed in [9, 123].

The main goal of this research is to evaluate profoundly the microstructural properties of SFRC with respect to the probabilistic characteristic on both an analytical as well as on a numerical basis. These properties can later be used to generate second-order random fields for an adequate representation of the material properties on the component level. In a first step the analytic models of SFRC are used to analyze the influence of the main material characteristics like fiber length, fiber orientation, fiber diameter, and fiber volume fraction on the elasticity properties. Therefore, each characteristic is separately varied following its known probability density functions (PDF) and the elasticity parameters are calculated. Afterward, the results of all analytically obtained material properties are compared with each other to identify the characteristics influencing the material properties most. This analytic analysis is extended to two-dimensional numerical simulations, which is based on a predefined area containing randomly placed reinforcing fibers. The analytically obtained results are used to verify the numerical model by comparing the calculated engineering constants and elasticity coefficients.

For investigating the influence of the main characteristics again each characteristic is analyzed separately. Besides this, an additional simulation is carried out where all parameters are considered as varying. The simulations are performed under boundary conditions of Neumann and Dirichlet type, which allows to obtain an upper (Voigt) and a lower (Reuss) bound. From these analyses, the influence of the main material characteristics on the elasticity properties for SFRC are derived. Based on these results further numerical simulations are carried out. Now the main focus lies on the spatial dependence of the material properties. This behavior can be expressed by correlation functions. Therefore, the moving window method is used to obtain the correlation nature of the elasticity properties. A first analysis of the correlation analysis of the elasticity parameters is done in [157]. However, that analysis is limited to a checkerboard pattern and therefore, does not include effects based on the varying geometrical properties of the reinforcing fibers as well as their orientation. Therefore, in this study this approach is extended to randomly placed fibers in a predefined area.

The structure of the paper is as follows. Section 2 gives an overview of the theoretical background for multi-scale modeling of fiber-reinforced composites. This includes the determination of effective material properties as well as the framework of correlated second-order random fields. This is followed by a profound analysis of the microstructure in Section 3, which includes first an overview of probabilistic properties of the main geometrical characteristics of SFRC followed by the description of the microstructure generation and the corresponding numerical model. Furthermore, the influence of the geometrical characteristics and their probabilistic nature on the mechanical properties is presented. In Section 4 the verification of the analytical results by numerical simulations is presented. Moreover, the numerical simulation is used to investigate the correlation structure of the elasticity tensor. Finally, Section 5 gives a summary and conclusion of the presented work.

I.2 Theoretical Framework

In this section a brief overview of the main theoretical framework used in this study is given, which covers the multi-scale modeling based on the principle of separation of scales. Regarding this approach definitions of boundary conditions are presented, that are used to determine the effective material properties of SFRC on the mesoscale. Next is a short summary of the analytical modeling of SFRC and the resulting elasticity coefficients. Finally, this section is concluded by a short introduction of second-order random fields that can be used to represent the spatial fluctuation of fiber properties on the mesoscale.

I.2.1 Numerical multi-scale modeling

I.2.1.1 RVE

SFRC consists of two different components, namely the matrix material and randomly distributed embedded fibers. On this microscopic scale, reinforced materials are therefore heterogeneous. This contradicts the traditional continuum mechanics approach, which is based on homogeneous material properties independent of the volume size. Therefore, suitable techniques for the representation of microstructural inhomogeneities are necessary. One technique here is the homogenization, which takes heterogeneous properties from the microstructure into account. The goal is to define a RVE, for which the heterogeneous material properties can be replaced by homogeneous effective material properties. For the edge length d of a RVE

$$l \leq d \leq L \tag{I.1}$$

holds. Here, l is the size of an inclusion and therefore, is assigned to the microscale, whereas L represents the dimension of the macroscale [64]. This approach is also known as separation of scales. It states that on the macroscale the size d can be seen as a material point, however with respect to the size of the inclusion d must contain statistically representative information about the microstructure [190].

A well known definition of RVE can be found in [70]. Accordingly, the dimensions of a RVE must be selected in such a way that the resulting effective material properties are independent of the boundary conditions. If the

used scale is smaller than the corresponding RVE, the boundary conditions as well as the microstructure and the contrast of the different phases must be taken into account [67, 81]. In this case one speaks of a statistical volume element (SVE) [130]. The corresponding material properties are called apparent overall properties [79, 80].

I.2.1.2 Effective material properties

The homogeneous effective material properties of a RVE can be written as

$$\langle \boldsymbol{\sigma} \rangle = \mathbb{C}^{\text{eff}} : \langle \boldsymbol{\epsilon} \rangle \quad (\text{I.2})$$

and

$$\langle \boldsymbol{\epsilon} \rangle = \mathbb{S}^{\text{eff}} : \langle \boldsymbol{\sigma} \rangle \quad (\text{I.3})$$

respectively. Here, the strains $\boldsymbol{\epsilon}$ and stress $\boldsymbol{\sigma}$ provide information about the microscale, whereas $\langle \cdot \rangle$ indicates the volume average, which is defined as

$$\langle \cdot \rangle = \frac{1}{V} \int_V \cdot \, dV, \quad (\text{I.4})$$

and therefore, represent the whole RVE. This integral relation leads to the fact, that Equations (I.2) and (I.3) can not be inverted. Furthermore, \mathbb{C}^{eff} describes the effective elasticity tensor, whereas \mathbb{S}^{eff} is the effective compliance tensor.

For the determination of these effective material properties the Hill's condition is essential [69]. It states, that the conservation of energy for the scale transition can be written as

$$\langle \boldsymbol{\sigma} : \boldsymbol{\epsilon} \rangle = \langle \boldsymbol{\sigma} \rangle : \langle \boldsymbol{\epsilon} \rangle. \quad (\text{I.5})$$

The corresponding boundary conditions for the determination of the effective material properties must therefore, satisfy Equation (I.5). Beside others there are two boundary condition formulations that can be used for the determination of the effective material properties. Following the average strain theorem based on linear elastic material behavior as well as the average stress theorem [190] these boundary conditions can be written as

$$\mathbf{u} = \boldsymbol{\epsilon}_0 \cdot \mathbf{x} \quad (\text{I.6})$$

and

$$\mathbf{t} = \mathbf{t}_0 \cdot \mathbf{x}. \quad (\text{I.7})$$

Here Equation (I.6) gives the pure displacement boundary condition, where $\boldsymbol{\epsilon}_0$ is a constant macroscopic strain. In contrast to this, Equation (I.7) gives the pure traction boundary condition, with \mathbf{t}_0 being a constant macroscopic stress. As both boundary conditions are defined on the complete surface of the RVE, Equation (I.6) is a boundary condition of Dirichlet type and Equation (I.7) gives a boundary condition of Neumann type.

Considering a SVE on the mesoscale, the structure response depends on the boundary conditions as well as the contrast of the material components. The size of the SVE is usually described by the dimensionless parameter δ , that is given by

$$\delta = \frac{d}{l}. \quad (\text{I.8})$$

With respect to fiber-reinforced composites the contrast is given by

$$\alpha = \frac{E_f}{E_m}, \quad (\text{I.9})$$

where E_f represents the Young's modulus of the fiber and E_m of the matrix material, respectively. It can be shown that the application of the presented boundary conditions on the mesoscale does not lead to identical elasticity tensors. In accordance with upper and lower bounds of effective material properties by Voigt [179]

and Reuss [150] pure displacement boundary conditions lead to a stiffer response than the application of pure traction boundary conditions. As shown by [53] the experimentally obtained effective material properties lay between these two bounds. Therefore,

$$\langle \mathbb{S}_\delta^t \rangle^{-1} \leq \mathbb{C}_\delta^{\text{eff}} \leq \langle \mathbb{C}_\delta^u \rangle \quad (\text{I.10})$$

holds [69, 127, 190]. The index δ indicates the scale dependence, whereas u and t represent the displacement and traction boundary conditions, respectively.

I.2.2 Analytical modeling of SFRC

I.2.2.1 Mean field theory approach

The first analytic approach for the homogenization of a microstructure was presented by Voigt [179] and Reuss [150] who introduced an upper and lower bound for the effective material properties. Voigt formulated these material properties based on a constant strain field, whereas Reuss used a uniform stress field. These approaches belongs to the mean-field theory.

Many approaches that are recently used in this context are based on the work of Eshelby, who analyzed the influence of an elliptic inclusion [40]. This initial work was then used by Mori and Tanaka. They extended the original work adding influencing effects if more than one inclusion is added to the material [121]. Based on this framework, Tandon and Weng derived explicit formulations for the elastic constants. However, the formulation of the Poisson's ratios are coupled and therefore, needs to be determined by an iterative procedure. This was solved by Tucker and Liang [174], who found a decoupled formulation, which is also used in this study. The complete framework of the material parameter determination by Tandon and Weng is given in [170, 174].

I.2.2.2 Self-consistent method

A second approach for the formulation of the engineering constants for heterogeneous material is based on the self-consistent method by Hill [71]. One well-known material model in this context is given by Halpin and Tsai, who developed a semi-empiric material model for SFRC [61, 62]. Due to the simple implementation, this material model is widely in use [72]. In contrast to the material model by Tandon and Weng, only the Young's Modulus E_1 is formulated as a function of the fiber geometry. All other engineering constants remain constant for a variation of the fiber length and fiber diameter. Besides this, the fiber volume fraction influences all engineering constants. Detailed information about the determination of the engineering constants is provided in [61, 174].

I.2.2.3 Elasticity tensor for transversely-isotropic material behavior

There are many different possibilities to define a coordinate system in the context of fiber-reinforced materials. Commonly used is a so-called local or lamina coordinate system. Here, the first axis coincide with the fiber direction, whereas the second and third axes are perpendicular to the fiber direction. The first and second axes are in-plane with the lamina and the third axis points into the lamina thickness direction.

Based on this local coordinate system definition the elasticity tensor of transversely-isotropic material is given by

$$\mathbb{C} = \begin{bmatrix} C_{11} & C_{12} & C_{13} & 0 & 0 & 0 \\ C_{12} & C_{22} & C_{23} & 0 & 0 & 0 \\ C_{13} & C_{23} & C_{33} & 0 & 0 & 0 \\ 0 & 0 & 0 & \frac{1}{2}(C_{22} - C_{23}) & 0 & 0 \\ 0 & 0 & 0 & 0 & C_{66} & 0 \\ 0 & 0 & 0 & 0 & 0 & C_{66} \end{bmatrix}. \quad (\text{I.11})$$

It consists of five independent coefficients, that can be calculated by five independent engineering constants E_1 , E_2 , G_{12} , ν_{12} , and ν_{23} . Instead of ν_{23} the out-of-plane shear modulus G_{23} can be used as well. Using these engineering constants the reduced elasticity coefficients for a plane stress state can be obtained by [4]

$$C_{11} = \frac{E_1}{(1 - \nu_{21}\nu_{12})}, \quad (\text{I.12})$$

$$C_{12} = \frac{\nu_{21}E_1}{(1 - \nu_{21}\nu_{12})} = \frac{\nu_{12}E_2}{(1 - \nu_{21}\nu_{12})}, \quad (\text{I.13})$$

$$C_{22} = \frac{E_2}{(1 - \nu_{21}\nu_{12})}, \quad (\text{I.14})$$

$$C_{66} = G_{12}. \quad (\text{I.15})$$

For the plane strain state the framework is more complex as the material parameters characterizing the properties in thickness direction are involved, too. The elasticity coefficients are calculated by [187]

$$C_{11} = \frac{(1 - \nu_{23}^2)E_1}{(1 + \nu_{23})(1 - \nu_{23} - 2\nu_{12}\nu_{21})}, \quad (\text{I.16})$$

$$C_{12} = \frac{\nu_{21}E_1}{(1 - \nu_{23} - 2\nu_{12}\nu_{21})}, \quad (\text{I.17})$$

$$C_{22} = \frac{(1 - \nu_{12}\nu_{21})E_2}{(1 + \nu_{23})(1 - \nu_{23} - 2\nu_{12}\nu_{21})}, \quad (\text{I.18})$$

$$C_{66} = G_{12}. \quad (\text{I.19})$$

The influence of a varying fiber orientation is introduced by a transformation from the local to a global coordinate system. This can be written in matrix form as

$$\mathbf{C}' = \mathbf{T}\mathbf{C}\mathbf{T}^T \quad (\text{I.20})$$

with the transformation matrix for a elasticity matrix reduced to a two-dimensional case

$$\mathbf{T} = \begin{bmatrix} \cos^2 \theta & \sin^2 \theta & 2 \cos \theta \sin \theta \\ \sin^2 \theta & \cos^2 \theta & -2 \cos \theta \sin \theta \\ -\cos \theta \sin \theta & \cos \theta \sin \theta & \cos^2 \theta - \sin^2 \theta \end{bmatrix}, \quad (\text{I.21})$$

where the angle between the local and global coordinate system is given by θ . To analyze the influence of the fiber orientation on the engineering constants these parameters need to be extracted from the elasticity tensor defined in the global coordinate system. In case of a plane strain state this is not possible without a further assumption as there are only four independent equations containing five engineering constants. Due to the two dimensional modeling the material properties in thickness direction may be assumed constant and not affected by the fiber orientation.

I.2.3 Correlated second-order random fields

Random variables Z can be used to describe quantities whose values are determined by a random experiment, which is subject to the rules of probability theory. A realization of the random variable Z is given by z . If a random variable is furthermore, assigned to spatial coordinates, one speaks of a random field $Z(\mathbf{x})$. In the context of the continuum mechanics and for the synthesis of such random fields by using the Karhunen-Loève expansion, it is necessary that the variance of the random field as well as the random variable is finite. In this case the following definition for a realization ω holds

$$Z(\mathbf{x}) = Z(\omega, \mathbf{x}) \in L^2(\Omega; \mathbb{R}) \quad (\text{I.22})$$

and one speaks of second-order random fields and second-order random variables, respectively [13]. Their main properties are briefly presented below.

Random variables are characterized by two functions. First the probability of $Z \leq z$ is expressed by the cumulative distribution function

$$P(Z \leq z) = F_Z(z) = F(z). \quad (\text{I.23})$$

The second characteristic function is the first derivative of the cumulative distribution function called probability density function

$$f(z) = \frac{dF(z)}{dz}. \quad (\text{I.24})$$

A well-known function here is the Gaussian bell curve, which represents a normal distribution.

Like random variables, random fields are characterized by a cumulative probability distribution and probability density function as well. Furthermore, both random variables and random fields are characterized by moments of probability distribution [169, 176]. In general the n -th moment of a single random variable Z is defined as

$$E[Z^n] = \int_{-\infty}^{\infty} z^n f_Z(z) dz. \quad (\text{I.25})$$

Based on this definition the first moment, also called expected value, is given by

$$E[Z] = \mu_Z = \int_{-\infty}^{\infty} z f_Z(z) dz. \quad (\text{I.26})$$

The second moment of a random variable is known as the mean-square of Z . In addition to moments of the probability distribution so called central moments can be formulated considering the expected value. By using the second central moment the deviation of the values with respect to the expected values can be measured, which is also known as the variance. Reformulating Equation (I.25) leads first to the general definition of central moments

$$E[(Z - \mu_Z)^n] = \int_{-\infty}^{\infty} (z - \mu_Z)^n f_Z(z) dz \quad (\text{I.27})$$

and therefore,

$$E[(Z - \mu_Z)^2] = \int_{-\infty}^{\infty} z^2 f_Z(z) dz - \mu_Z^2 \quad (\text{I.28})$$

holds for the variance of the random variable Z . In addition, the standard deviation is often used, which can be derived from the variance by

$$\sigma_Z = \sqrt{\text{Var}(Z)}. \quad (\text{I.29})$$

The definitions provided in Equations (I.25) to (I.29) can be easily transferred to random fields by replacing Z with $Z(\mathbf{x})$. Therefore, in general the expected value as well as the variance are functions of the spatial coordinates \mathbf{x} . However, in case of a homogeneous random field both the expected value and the variance become constants [176].

The observation of a random field at different locations \mathbf{x}_i is described by the corresponding random variables $Z = Z_i$. In this case the relation between these random variables is expressed by the covariance, which is defined for two random variables Z_1 and Z_2 as

$$\text{Cov}(X_1, X_2) = E[(X_1 - \mu_1)(X_2 - \mu_2)] \quad (\text{I.30})$$

$$= E[X_1 X_2] - \mu_1 \mu_2. \quad (\text{I.31})$$

Usually this expression is reduced to a dimensionless parameter. Therefore, Equation (I.31) is divided by σ_1 and σ_2 , which leads to

$$\rho(X_1, X_2) = \frac{\text{Cov}(X_1, X_2)}{\sigma_1 \sigma_2}. \quad (\text{I.32})$$

	E GPa	ν -	ρ kg/m ³
Glass	70	0.22	2500
PBT	2.6	0.41	1300

Table I.1: Material properties of PBT and Glass fibers.

Here $\rho(X_1, X_2)$ is the dimensionless correlation parameter. If the two random variables Z_1 and Z_2 are part of the same random field $Z(\mathbf{x})$, Equations (I.31) and (I.32) give the auto-covariance and auto-correlation, respectively. In case they belong to two different random fields $Y(\mathbf{x})$ and $Z(\mathbf{x})$ the results of Equations (I.31) and (I.32) are the cross-covariance and cross-correlation, respectively.

Usually the probability density function is unknown and hence, the random field is represented by a discrete number realizations ω_i [132]. In this case the mean of the discrete values

$$\overline{Z(\mathbf{x})} = \frac{1}{N} \sum_{i=1}^N Z(\omega_i, \mathbf{x}) \quad (\text{I.33})$$

can be used as expected value of the random field. In addition the variance is rewritten as

$$s^2(\mathbf{x}) = \overline{Z(\mathbf{x})^2} - \overline{Z(\mathbf{x})}^2. \quad (\text{I.34})$$

Finally the dimensionless correlation coefficient for two random variables Z_1 and Z_2 is given by

$$\rho(X_1, X_2) = \frac{\overline{[Z_1 - \overline{Z_1}][Z_2 - \overline{Z_2}]}}{s_1 s_2}. \quad (\text{I.35})$$

I.3 Analytical treatment

In this section, the influence of geometrical fiber properties, as well as fiber volume fraction and fiber orientation on the engineering constants and the elasticity coefficients of the material, is analyzed analytically using the material models by Tandon and Weng as well as Halpin and Tsai. The goal is to identify those parameters that influence the material properties significantly and therefore, must be taken into account when analyzing the microstructural effect on the overall mechanical behavior of SFRC on a numerical basis. First, the material properties and their probabilistic characteristics are presented. This is followed by a detailed description of the analytical treatment procedure. At the end of this section, those parameters are identified that influence the mechanical properties of SFRC significantly.

I.3.1 Material properties and their probabilistic characteristics

All presented analyses are based on a polybutylene terephthalate (PBT) matrix reinforced with glass fibers. The engineering constants and densities for these two components are given in Table I.1. For SFRC the amount of reinforcing fibers is usually expressed by the fiber mass fraction φ_m . However, within the analytical framework of material properties the fiber volume fraction φ is used. Between these two parameters the following relation holds

$$\varphi_m = \frac{\rho_f \varphi}{\rho_f \varphi + \rho_m (1 - \varphi)}. \quad (\text{I.36})$$

In this study an overall fiber mass fraction of $\varphi_m = 30\%$ is assumed, which equals a fiber volume fraction of $\varphi = 18.22\%$.

For the investigation of the influence of SFRC characteristics like fiber length, fiber orientation, fiber diameter, and fiber volume fraction their probabilistic properties must be known. For the analytical as well as the consecutive numerical analysis in Section I.4 the probability distributions of these characteristics are taken from [58]. Like the material used in this study, the probability density functions are based on a SFRC consisting of a thermoplastic material reinforced with glass fibers and a fiber mass fraction of $\varphi_m = 30\%$. The characteristics are determined for tensile test specimens made by mold injection.

The probability density function of the fiber length l is usually approximated by a two-parameter Weibull distribution, that can be written as [24, 44]

$$f(l|a, b) = \frac{b}{a} \left(\frac{l}{a} \right)^{b-1} \exp \left(- \left(\frac{l}{a} \right)^b \right). \quad (\text{I.37})$$

For the chosen material the Weibull parameter a and b are set to

$$a = 292 \quad b = 1.96. \quad (\text{I.38})$$

The corresponding mean of the fiber length is $\bar{l} = 260 \mu\text{m}$. In contrast to the fiber length, the fiber diameter d shows a normal distribution. The corresponding probability density function reads

$$f(d) = \frac{1}{\sigma \sqrt{2\pi}} \exp \left[- \frac{1}{2} \left(\frac{d - \mu}{\sigma} \right)^2 \right] \quad (\text{I.39})$$

with a mean value $\mu = 10.9 \mu\text{m}$ and a standard deviation $\sigma = 0.9 \mu\text{m}$. The main reason why these two parameters show different probabilistic characteristics lays in the production process. While the fiber diameter is mostly influenced by the production process of the fiber itself the fiber length is not only affected by the fiber production but also by the mold injection process [58].

The fiber orientation is described by an elliptic probability density function [58]. Therefore,

$$f(\theta) = \frac{h_2}{\sqrt{1 - \frac{h_1^2 - h_2^2}{h_1^2} \cos^2(\theta)}} \quad (\text{I.40})$$

holds. Here, h_1 and h_2 are the semi-minor and semi-major axis, respectively. The semi axes ratio for this probability density function measured by μCT is 22.1.

Based on these probability density functions the distribution of the three main characteristics, fiber length, fiber diameter, and fiber orientation are obtained. Figure I.1 gives an overview of the presented probability density functions.

The spatial distribution of the fiber volume fraction depends strongly on the window size and is therefore, not described by a probability density function [156].

I.3.2 Procedure

For the analytic analysis, the influence of the geometrical fiber properties on the engineering constants and elasticity coefficients is investigated based on the material model by Tandon and Weng, which fits experimentally obtained values best [60, 174]. As a second approach the material model by Halpin and Tsai is used. This material model is commonly used due to the simple implementation process [72]. Both material models provide equations for the engineering constants of SFRC as a function of the fiber length, fiber diameter and the fiber volume fraction.

The influence of the different geometrical fiber properties on the elasticity coefficients is analyzed separately on an analytical basis. Therefore, the engineering constants are calculated based on the mean values given for the fiber length and fiber diameter. The chosen fiber volume fraction equals a fiber mass fraction of 30%. In

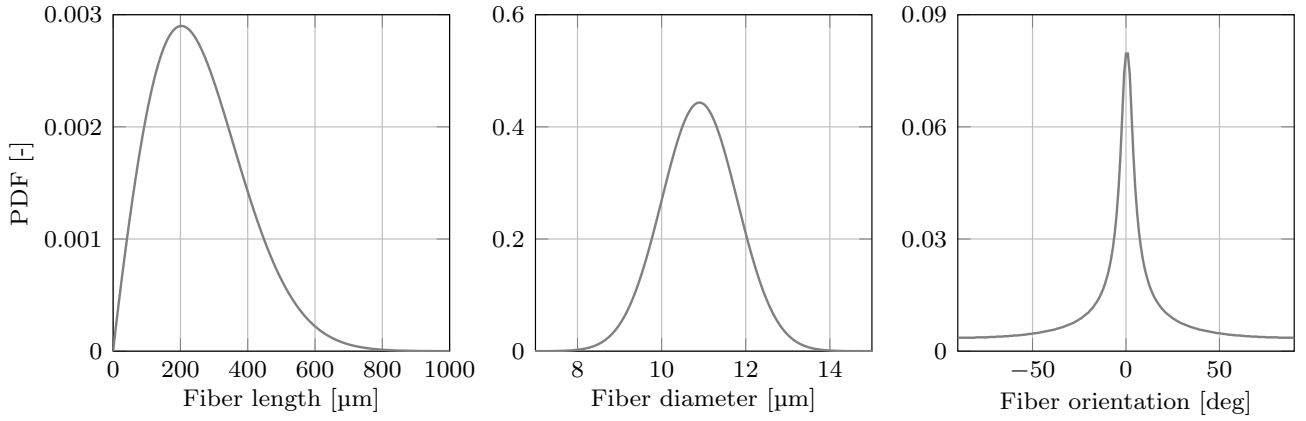


Figure I.1: Probability density functions.

	E_1 GPa	E_2 GPa	G_{12} GPa	G_{23} GPa	ν_{12} -
Tandon-Weng	12.4	3.99	1.31	1.26	0.379
Halpin-Tsai	11.2	4.12	1.30	1.25	0.375
Deviation	1.2	0.13	0.01	0.01	0.004

Table I.2: Results of the engineering constants for Tandon-Weng and Halpin-Tsai.

addition one of these parameters is varied. This is done by generating 1e6 values of the varying parameter following the probability density function. For each value first the engineering constants using the material model of Tandon and Weng are calculated. Based on the material model by Halpin and Tsai only the varying Young's Modulus E_1 is considered. The remaining engineering constants are independent of the fiber geometry. Based on these engineering constants the elasticity coefficients are calculated assuming a plane stress state and hence, using Equations (I.12) to (I.15).

A determination of the fiber orientation influence can only be made indirectly by first determining the elasticity tensor based on the engineering constants for the local coordinate system. This elasticity tensor can then be related to a fiber orientation by a coordinate transformation using Equation (I.20). By calculating the effective material properties based on the resulting elasticity tensor referring to a global coordinate system, it is finally possible to determine the engineering constants concerning a varying fiber orientation. All presented analyses consider a two-dimensional representation under plane stress assumption. However, an analytical treatment based on a plane strain state show similar results.

As there is no probability density function describing the fiber volume fraction, the resulting values are plotted for the range of 10% to 30%. This fits the results of an analysis for a spatial fiber volume fraction fluctuation based on the moving window method presented in [156].

I.3.3 Results

First of all Table I.2 gives the engineering constants calculated for both material models using the mean values for the fiber length of 260 μm and for the fiber diameter of 10.9 μm. The fiber mass fraction is set to 30% and the fibers are assumed to be all aligned in the 0° direction. The values of the shear moduli and Poisson ratios are almost identically, whereas the Young's moduli show a deviation of up to 8%. This meets the results presented in [174].

As an example, Figure I.2 shows the results of the engineering constants based on the material model by

Tandon and Weng with a varying fiber length. It can be seen that the fiber length influences the Young's modulus E_1 significantly, whereas the shear moduli are almost independent. The Young's modulus E_2 as well as the Poisson ratio ν_{12} react only slightly to a variation of the fiber length. Following this only the coefficient C_{11} is significantly influenced by the fiber length. A minor influence can be recognized for the coefficient C_{12} as this coefficient depends also on E_1 . The remaining coefficients C_{22} and C_{66} are nearly independent (see Figure I.3). Furthermore, the distribution of the engineering constants as well as the elasticity coefficients can be approximated by a Weibull distribution, which also describes the distribution of the fiber length itself.

The analysis based on the material model by Halpin and Tsai leads to identical conclusions. As only E_1 is formulated as a function of the fiber length, the remaining constants are independent and only C_{11} is significantly influenced by the fiber length. Again, the distribution of E_1 as well as the resulting elasticity coefficients can be approximated by a Weibull distribution.

Based on these results the following analyses of the fiber diameter influence, as well as the fiber orientation, are concentrated on E_1 and C_{11} . The full results of the analytic analysis for both material models regarding the fiber diameter and fiber orientation can be found in I.A. In Figures I.4 and I.5 the results of E_1 and C_{11} are given based on the material model by Tandon and Weng and Halpin and Tsai, respectively. Starting from left to right they show the results for the fiber length, fiber diameter, and fiber orientation, respectively. It can be observed, that both material models lead to similar results. The engineering constants as well as the elasticity coefficients are significantly influenced by the fiber length and fiber orientation. However, the fiber diameter has just little impact on the material properties. Furthermore, the fiber orientation shows very high values for angles close to zero. As the fiber angle increases the values are dropping rapidly. This is indicated by a second local maximum at the lower spectrum of the values, which corresponds to fiber orientation of 60° up to 90° .

Finally Figure I.6 gives the results of main material properties as a function of the fiber volume fraction for both material models. As shown in [156] the fiber volume fraction influences significantly the parameters E_1 and C_{11} . Furthermore, the influence on E_2 and G_{12} and the corresponding elements of the elasticity tensor is still significant for both material models in the range of 10% to 30% fiber volume fraction.

Based on the results of this analytical treatment it can be concluded that the fiber length as well as the fiber orientation and fiber volume fraction influence the material properties of SFRC significantly, whereas the fiber diameter shows only a minimal influence. This corresponds to the results presented in [134]. Furthermore, it can be observed that the distribution of the engineering constants, as well as the elasticity coefficients, can be approximated with the same type of probability density function as the varied parameter itself. This also holds when assuming a plane strain state.

I.4 Numerical analysis

The numerical analysis covers the influence of the microstructure properties of SFRC on the mechanical behavior as well as the correlation structure of the resulting elasticity tensor. First, the numerical procedure is presented. This is followed by the determination of a sufficient element size for the numerical model. Finally, the influence of the microstructure on the mechanical properties is analyzed and the correlation structure of the elasticity tensor is presented.

I.4.1 Generation of the microstructure

For all numerical analyses first, a microstructural model is generated representing randomly placed fibers in a preset area. Later this microstructure is transferred to a numerical model. The generation of the microstructure is based on an adapted Poisson process. First, a set of two integers within the preset area is randomly chosen. These integers represent the midpoint of the new fiber. Next, the fiber length, fiber diameter and the fiber orientation of this fiber are determined following their probability density functions. With all the necessary information about the fiber, it is checked if there are any overlaps with other fibers. Only if there are no overlaps the fiber is finally added to the area, which is represented by a two-dimensional array with a step size of $1\text{ }\mu\text{m}$ along both axes. In comparison with an average fiber diameter of $10\text{ }\mu\text{m}$ and an average fiber

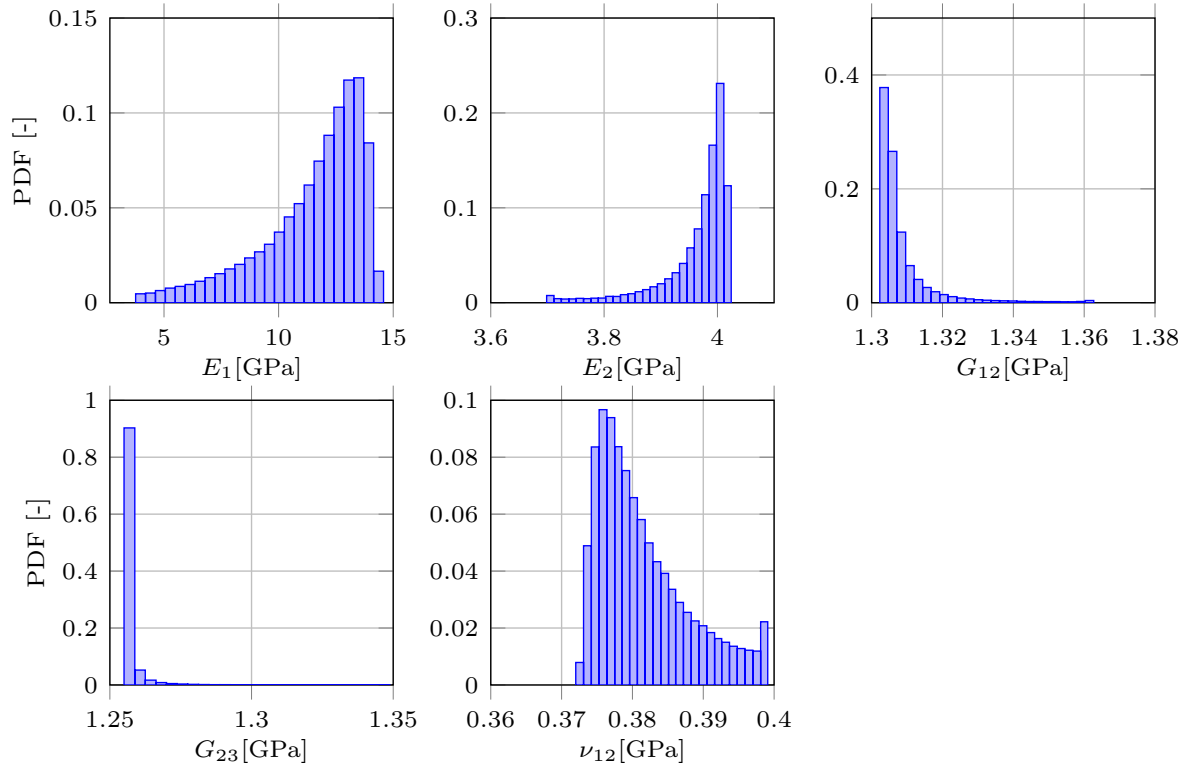


Figure I.2: Engineering constants due to a varying fiber length for the material model by Tandon and Weng.

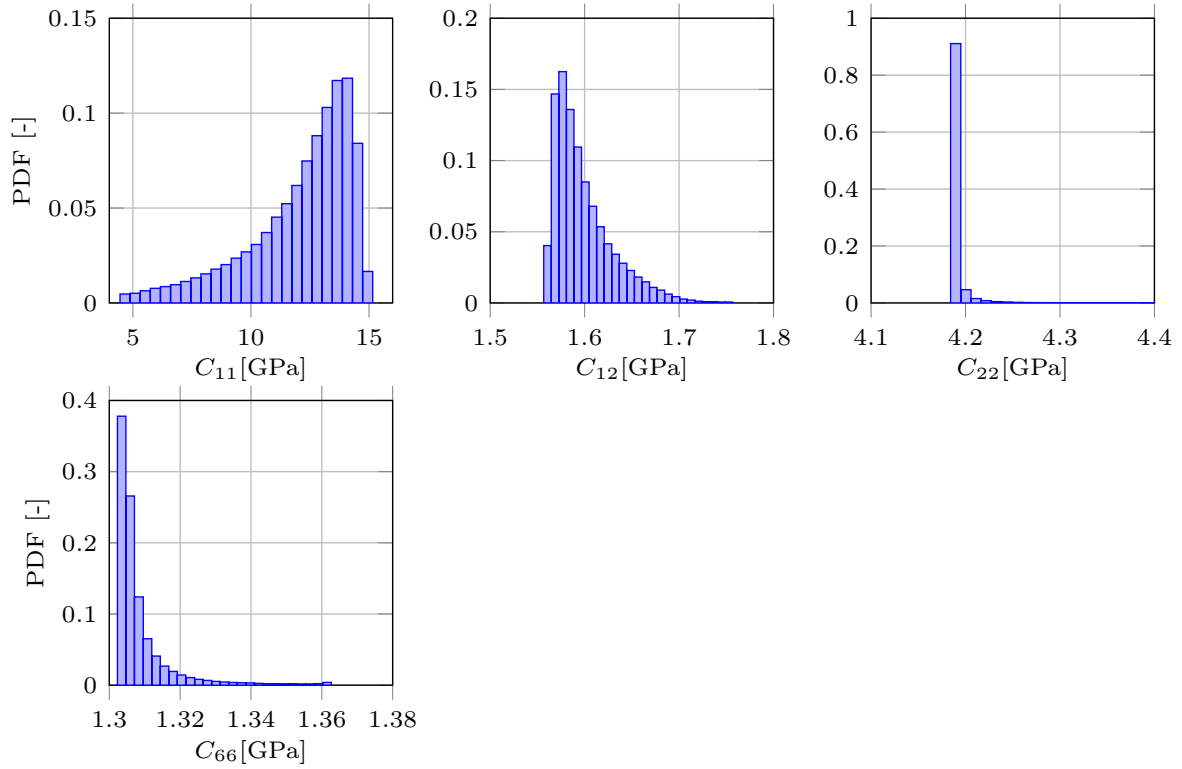


Figure I.3: Elasticity coefficients due to a varying fiber length for the material model by Tandon and Weng.

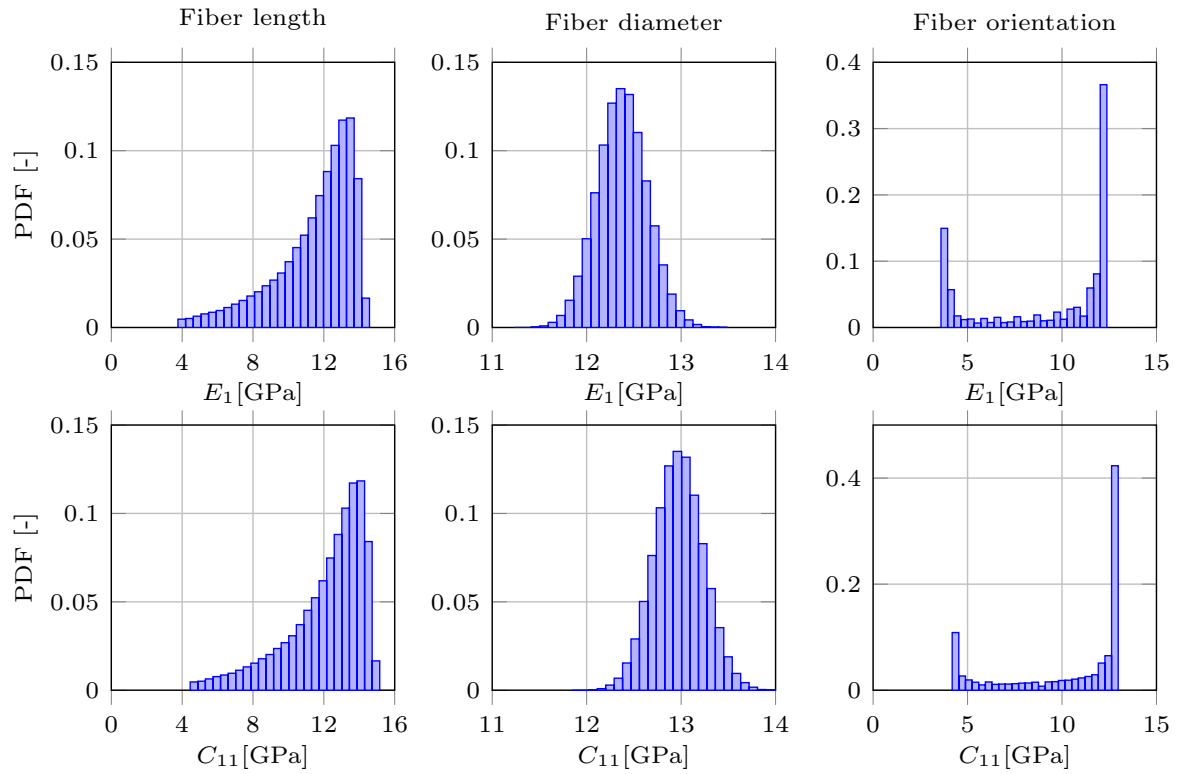


Figure I.4: Results for the distribution of E_1 and C_{11} with respect to a varying fiber length, diameter, and orientation based on the material model by Tandon and Weng.

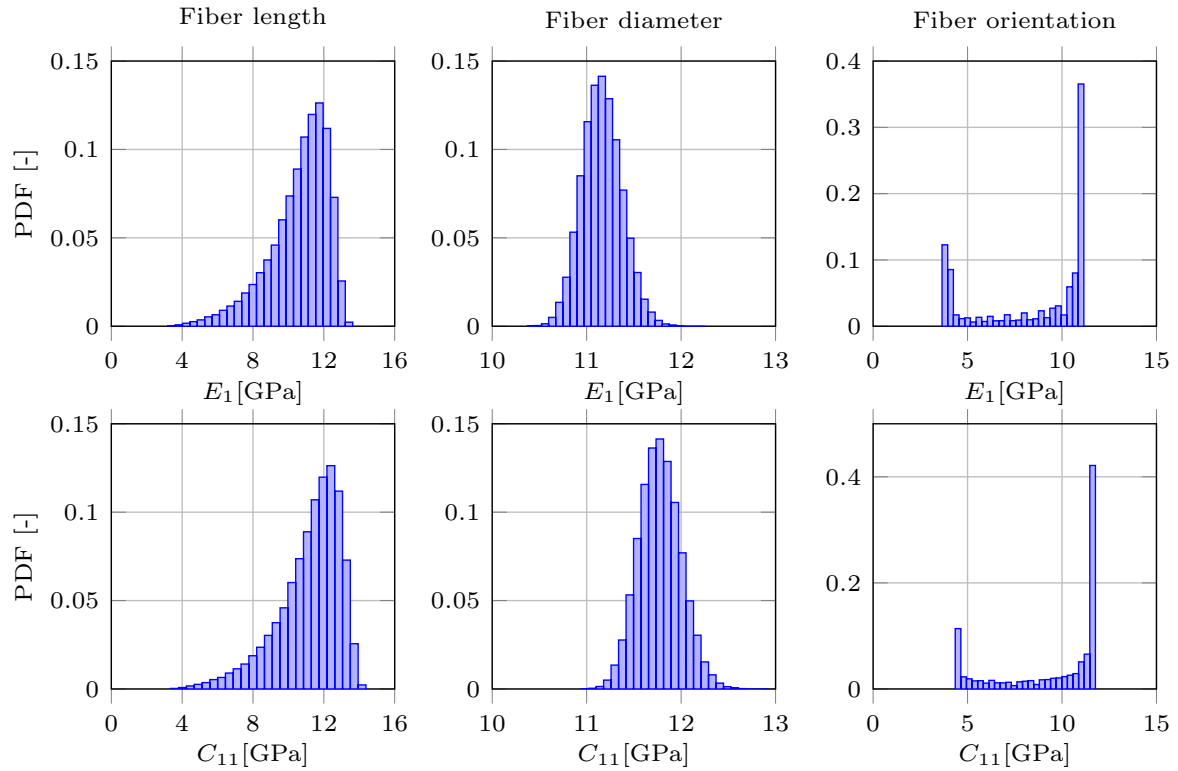


Figure I.5: Results for the distribution of E_1 and C_{11} with respect to a varying fiber length, diameter, and orientation based on the material model by Halpin and Tsai.

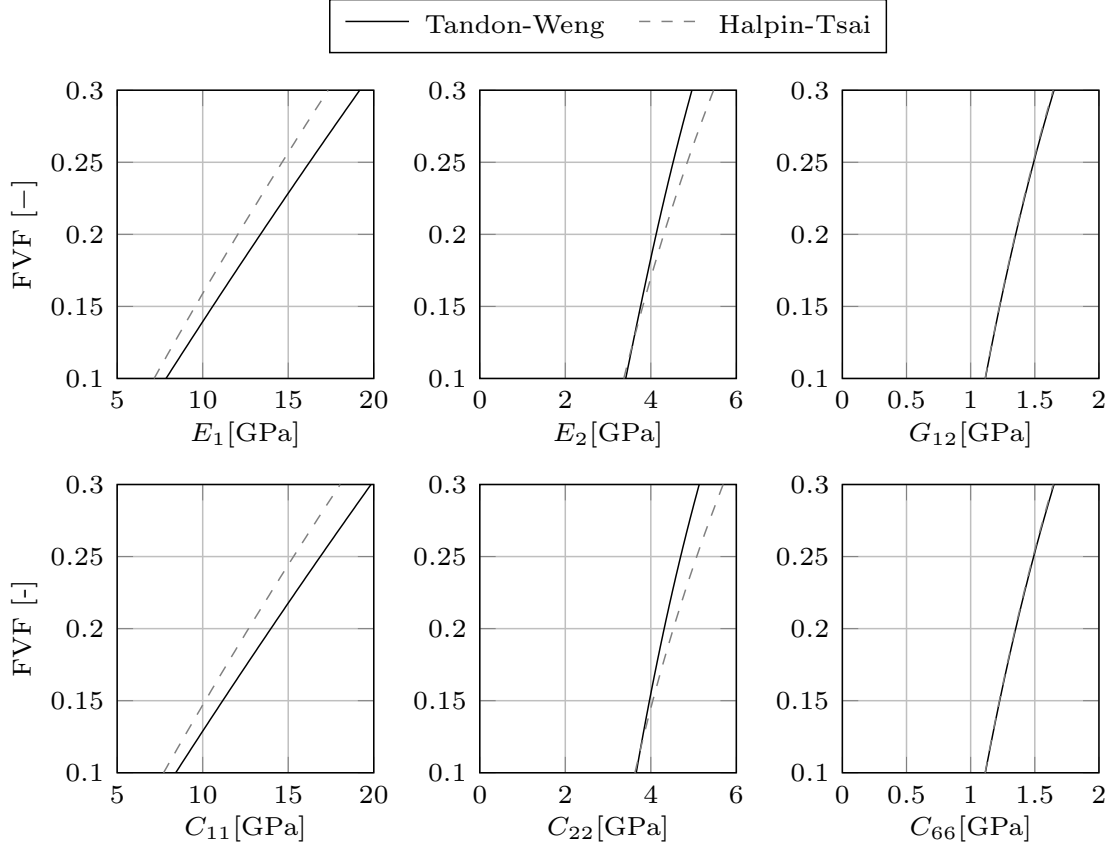


Figure I.6: Influence of the fiber volume fraction on the material properties of SFRC.

length of $260\ \mu\text{m}$ the grid size of $1\ \mu\text{m}$ is sufficient. The procedure is repeated until a predefined fiber volume fraction is reached. Figure I.7 shows an exemplarily generated microstructure with a size of $2500\ \mu\text{m} \times 2500\ \mu\text{m}$. Here, a significant difference between the analytical prediction and the numerical modeling is getting obvious. In contrast to the analytical description, the numerical model can consist of several fibers with different geometrical properties. Furthermore, the fiber orientation, as well as the fiber volume fraction, can show spatial fluctuations. Regarding the analytical modeling all fibers are assumed to have identical geometrical properties as well as orientations.

Below microstructures with different varying characteristics are analyzed numerically. In comparison to the analytical modeling first besides one parameter, all remaining are set to the mean value. By doing so the influence of a varying fiber length, fiber diameter, and fiber orientation can be investigated separately. In a further step, a microstructure is generated, that is much larger than the analyzed window size. Extracting a smaller window from a larger microstructure enables one, to analyze a varying fiber volume content, as depicted in Figure I.7. In a final step, a microstructure is generating where all characteristics are set with respect to their probabilistic characteristic.

I.4.2 Finite Element Model

After implementing the microstructure a numerical model is generated using Comsol. The numerical model consists of a square in plane stress state discretized by a structured mesh consisting of squared Lagrange elements with quadratic shape functions. In the last step, the material properties (see Table I.1) are passed to the numerical model. This is done by first saving the material properties in arrays that have the same structure as the array representing the microstructure itself. As both components show isotropic material behavior, these arrays provide the distribution of the Young's Modulus as well as the Poisson's ratio of the two materials over

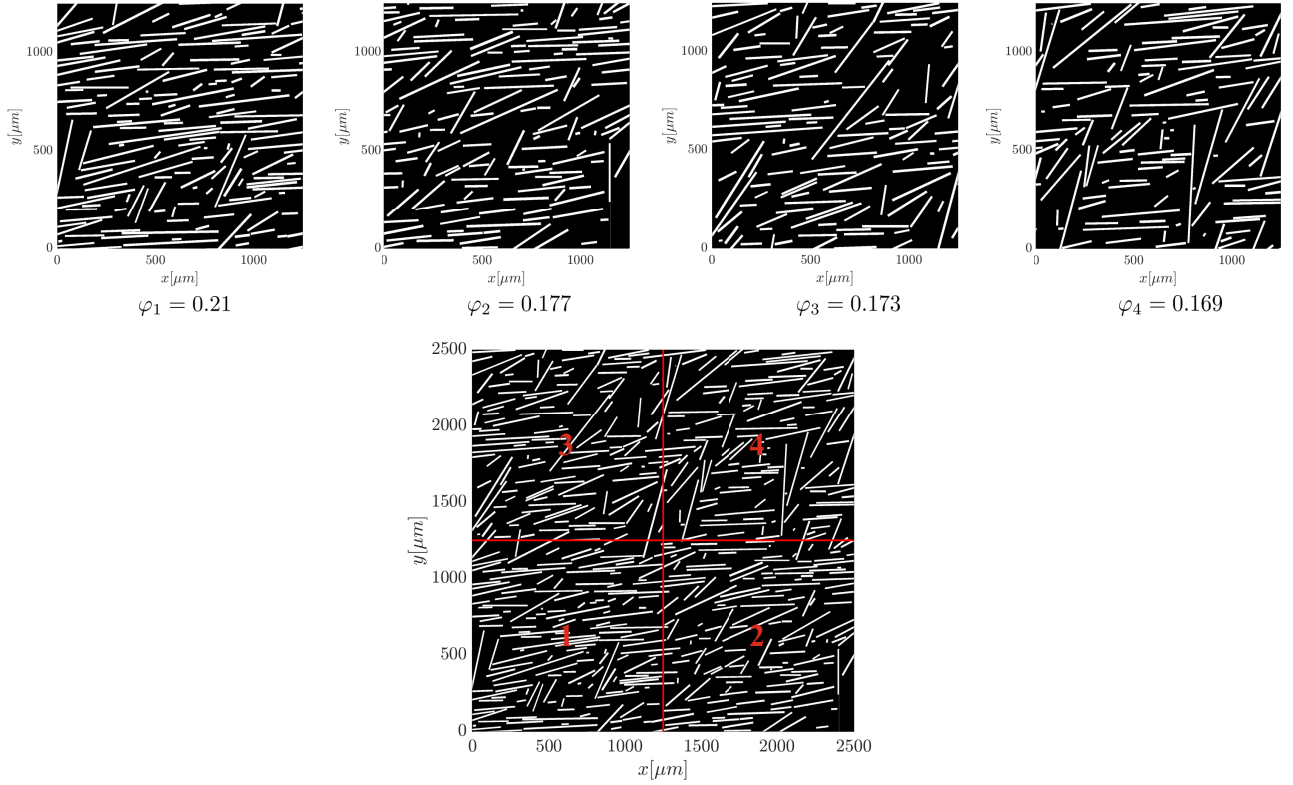


Figure I.7: SFRC microstructure of $2500 \mu\text{m} \times 2500 \mu\text{m}$ with a over all fiber volume fraction of 18.2%.

the microstructure. Finally, to each integration point the corresponding material properties are passed. This procedure is depicted in Figure I.8. However, assigning the material properties to the integration points leads to a mesh dependent representation of the microstructure. Therefore, to ensure a sufficient representation of the resulting material properties, the influence of the element size is analyzed in detail in Section I.4.3.

To determine the elasticity coefficients the boundary conditions are defined in accordance with Equations (I.6) and (I.7). Usually, individual simulations for each elasticity tensor component are performed [127, 190]. However, in [188] it is shown that it is also possible to use just three independent load cases to be able to calculate all nine elasticity coefficients of a two-dimensional model individually. This is done by formulating three independent boundary conditions, where always just one strain component is not equal zero. Table I.3 gives an overview of all load cases used to determine the elasticity coefficients for pure kinematic as well as pure traction boundary conditions in accordance with the Hill condition given by Equation [I.5].

I.4.3 Analysis of the element size

One crucial aspect of this approach is the element size. Hence, before the influence of the microstructure is analyzed by numerical simulations, a sufficient element size must be determined. This is done by performing numerical simulations based on a microstructure of $250 \mu\text{m} \times 250 \mu\text{m}$ with different element sizes. For each configuration, the pure displacement and pure traction boundary conditions are applied and the elasticity coefficients are determined based on the framework given in I.B.1. For statistical reasons, the simulation is carried out for 500 different microstructures [157, 164]. Table I.4 provides the mean values of the elasticity coefficients first for pure displacement and afterward for pure traction boundary conditions.

First of all the values indicate, that the symmetry of the elasticity tensor is still valid. However, there is a small deviation between the elasticity coefficients C_{12} and C_{21} . Furthermore, the dependence on the boundary conditions of the results and hence the scale dependence of C_{11} , C_{22} and C_{66} is clearly observable. As presented in Section I.2.1 the displacement boundary conditions lead to an upper bound whereas the traction boundary

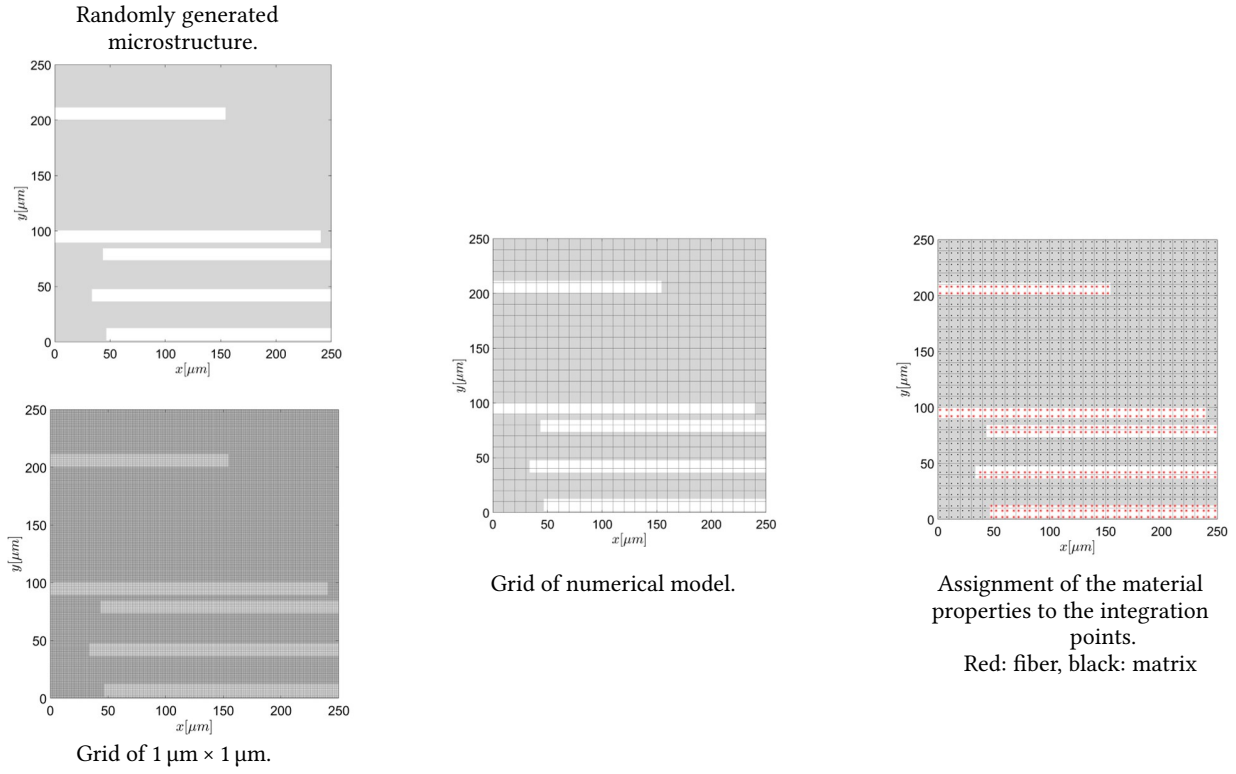


Figure I.8: Procedure to generate a numerical model representing a SFRC microstructure.

BC	Load case	Left edge $x = 0$	Right edge $x = d$	Upper edge $y = 0$	Lower edge $y = d$
Pure displ.	1	$u_1 = 0$	$u_1 = u_0$	$u_1 = u_0 x$	$u_1 = u_0 x$
		$u_2 = 0$	$u_2 = 0$	$u_2 = 0$	$u_2 = 0$
	2	$u_1 = 0$	$u_1 = 0$	$u_1 = 0$	$u_1 = 0$
		$u_2 = u_0 y$	$u_2 = u_0 y$	$u_2 = u_0$	$u_2 = 0$
	3	$u_1 = 0$	$u_1 = 0$	$u_1 = 0$	$u_1 = 0$
		$u_2 = 0$	$u_2 = u_0$	$u_2 = u_0 x$	$u_2 = u_0 x$
Pure trac.	1	$t_1 = \frac{t_0}{2}$	$t_1 = -\frac{t_0}{2}$	$t_1 = 0$	$t_1 = 0$
		$t_2 = 0$	$t_2 = 0$	$t_2 = 0$	$t_2 = 0$
	2	$t_1 = 0$	$t_1 = 0$	$t_1 = 0$	$t_1 = 0$
		$t_2 = 0$	$t_2 = 0$	$t_2 = \frac{t_0}{2}$	$t_2 = -\frac{t_0}{2}$
	3	$t_1 = 0$	$t_1 = 0$	$t_1 = \frac{t_0}{2}$	$t_1 = -\frac{t_0}{2}$
		$t_2 = -\frac{t_0}{2}$	$t_2 = \frac{t_0}{2}$	$t_2 = 0$	$t_2 = 0$

Table I.3: Load cases for the determination of the elasticity coefficients in accordance with the Hill condition [188].

	Element size μm	C_{11} GPa	C_{12} GPa	C_{21} GPa	C_{22} GPa	C_{66} GPa	φ_m -
KUBC	16.7	12.0	1.62	1.51	4.67	1.47	0.302
	10	11.7	1.56	1.49	4.36	1.35	0.303
	5	11.6	1.53	1.48	4.21	1.30	0.302
	2.5	11.6	1.51	1.48	4.06	1.26	0.302
SUBC	16.7	6.34	1.49	1.60	4.01	1.20	0.302
	10	6.42	1.49	1.58	3.91	1.16	0.303
	5	6.46	1.51	1.56	3.89	1.15	0.302
	2.5	6.51	1.52	1.54	3.83	1.14	0.302

Table I.4: Results of the elasticity coefficients with respect to the element size.

conditions lead to a lower bound. Therefore, these results confirm Equation (I.10).

Comparing the values for the different element sizes with each other show only minor variations for an element size of 10 μm or less. In this case the obtained results for the elasticity coefficients of a window with a size of 250 $\mu\text{m} \times 250 \mu\text{m}$ does not depend on the element size. Therefore, for all following simulations the element size is set to 10 $\mu\text{m} \times 10 \mu\text{m}$.

I.4.4 Influence of the microstructure

I.4.4.1 Overall properties of the elasticity tensor

Before analyzing the influencing geometrical properties in detail the overall characteristics of the elasticity tensor with respect to the window size and the boundary condition is presented. This is done based on a microstructure where all main properties are assumed to show probabilistic behavior. This ensures an overall realistic representation of the microstructure.

Figure I.9 gives the minimal and maximal value of each elasticity coefficient for both types of boundary conditions and a window size of 250 μm , 500 μm , and 750 μm . First of all the scale dependence of the elasticity coefficients can be found as the range of the coefficients decreases with increasing window size. In addition, the symmetry properties of the elasticity tensor are observable. Not only C_{12} and C_{21} show an almost identical behavior, but also C_{16} and C_{61} as well as C_{26} and C_{62} coincide very well. However, in contrast to C_{12} the mean values of C_{16} and C_{26} are approximately zero. As their fluctuation starts to vanish with an increasing window size the overall assumption of transversely-isotropic material behavior holds. This is also independent of the boundary condition. The overall transversely-isotropic material behavior is also indicated by the elements C_{11} and C_{22} . Due to the aligned characteristic of the fibers predicted by the corresponding PDF, see Figure I.1, the value of C_{11} is greater than the value of C_{22} .

Finally, the results of the elasticity coefficients show that the values for pure kinematic boundary conditions are higher compared to pure traction boundary conditions, which meets the theoretical framework of the multiscale modeling.

For taking a closer look at the distribution of the individual coefficients Figure I.10 shows the histogram of each elasticity coefficient for a window size of 250 μm and pure displacement boundary conditions based on 16.500 data sets. Again the symmetry properties of the elasticity tensor, as well as the anisotropic effect due to the limited window size, can be observed. However, not all coefficients can be approximated best with the same probability distribution type. Whereas C_{11} , C_{12} , C_{22} , and C_{66} seem to meet a Weibull distribution best, the remaining parameters are most likely normal distributed. Observing this over an increasing window size reveals that the distribution of the elasticity coefficients depends on the window size of the analyzed

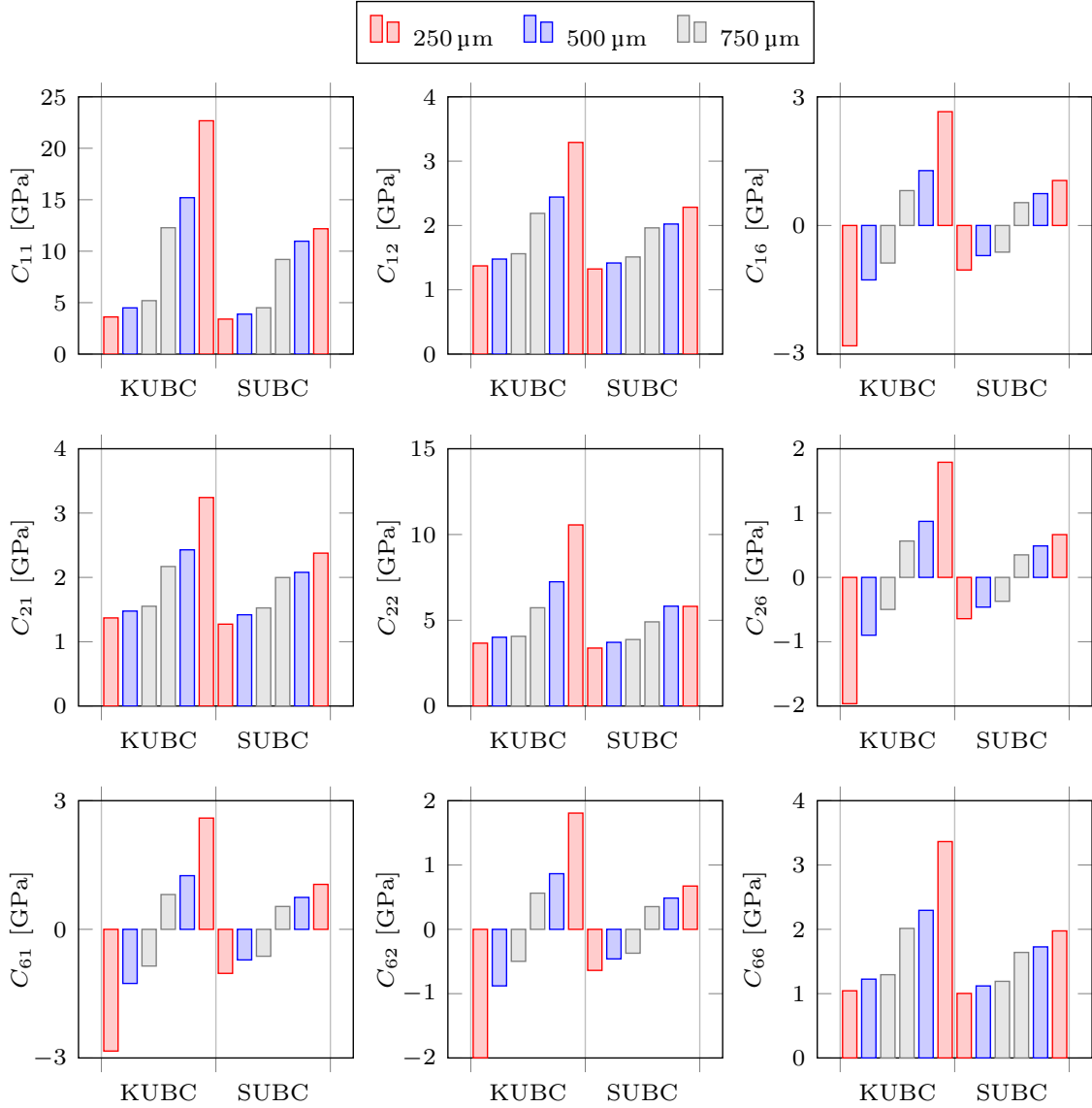


Figure I.9: Symmetry analysis of the elasticity tensor.

microstructure as depicted in Figure I.11. In this figure the histogram of C_{11} is given for both boundary condition types as well as all window sizes. The histogram indicates, that the distribution of C_{11} equals a Weibull distribution for small window sizes whereas for an increasing window size the distribution starts to meet a normal distribution. This observation is independent of the boundary condition. Therefore, it can be concluded that the distribution of the elasticity coefficients is significantly influenced by the microstructural properties on the mesoscale. However, when the SVE gets close to the RVE the microstructure does not affect the distribution any longer.

I.4.4.2 Parameter identification

For the analysis of the geometrical parameters influencing the material properties of SFRC on the mesoscale, first, the different parameters are observed individually. Finally, all parameters are combined. For the analysis of the fiber length, orientation, and diameter influence, the microstructure is generated with respect to the varying parameter and the window size. The remaining parameters are set to the mean value according to their probabilistic characteristics. Considering a locally distributed fiber volume fraction a microstructure is

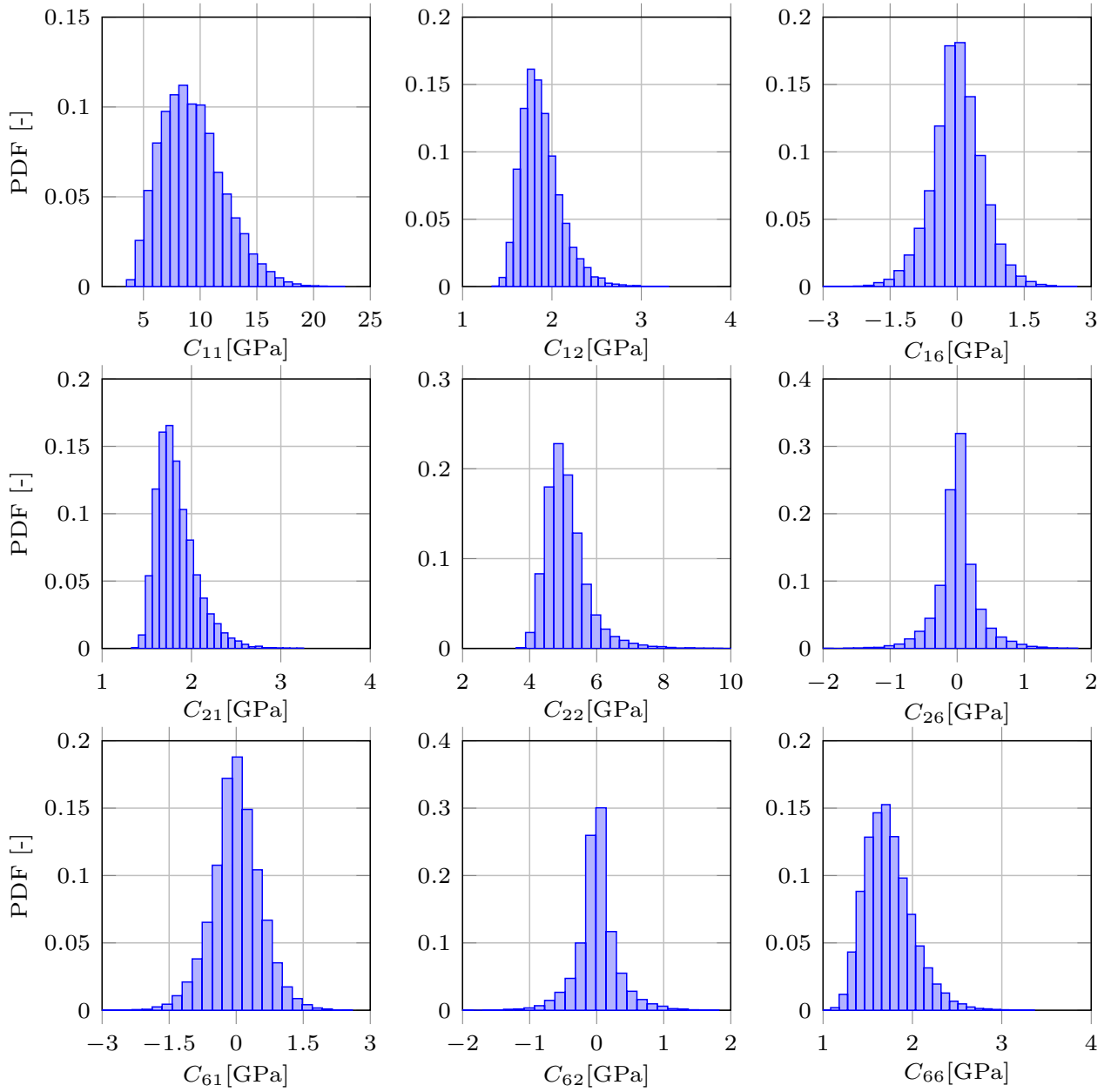


Figure I.10: Distribution of the elasticity coefficients under pure displacement boundary conditions with respect to a 250 μm window size.

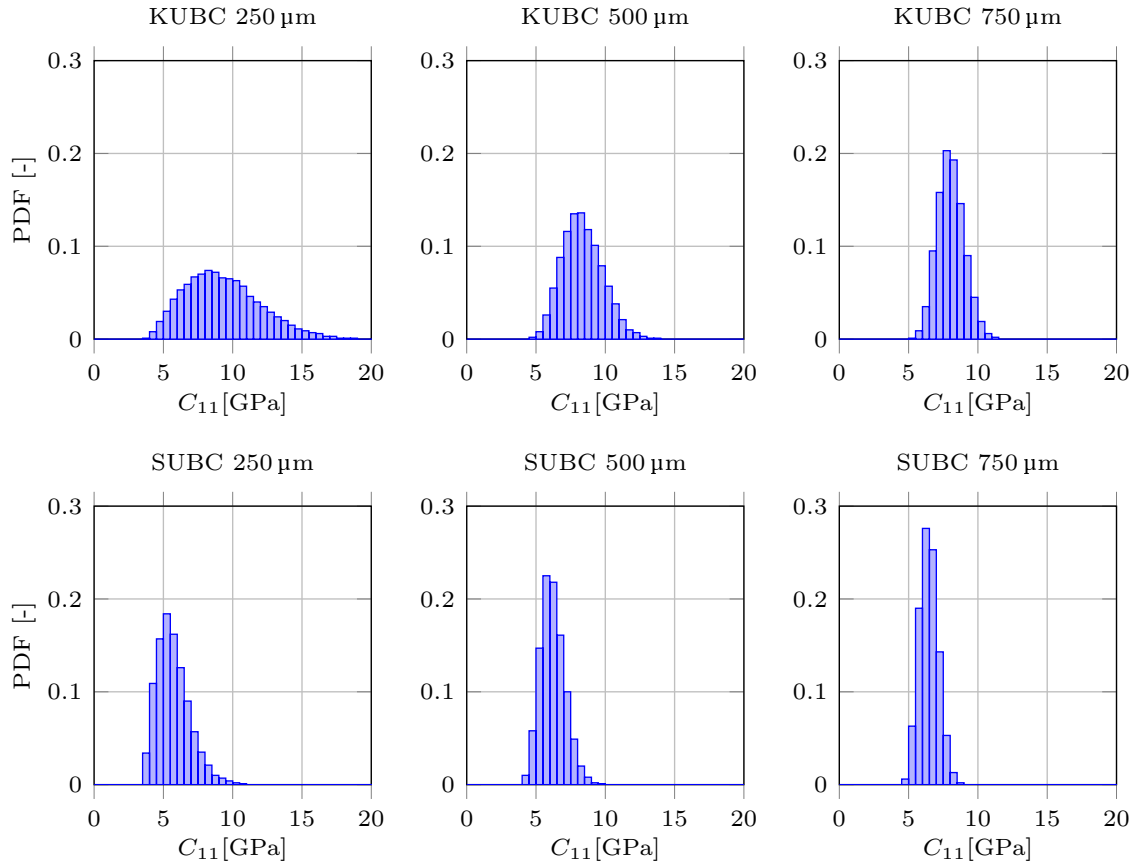


Figure I.11: Distribution of the values for the elasticity tensor element C_{11} with respect to the boundary conditions and the window size.

generated that is larger than the actual window size. By extraction a window from a greater microstructure, the corresponding fiber volume fraction is not constant, see Figure I.7.

Again for statistical reasons, the simulations for each analysis are carried out for 500 different microstructures [157, 164]. Furthermore, as the material properties on the mesoscale depend on the window size the procedure is done for a window size of 250 μm , 500 μm , and 750 μm .

Figure I.12 and I.13 show the mean value and the standard deviation of each elasticity coefficient with respect to the boundary conditions as well as the window size for each analyzed configuration. The coefficients can be divided into two groups, those who have a mean value of zero (C_{16} , C_{26} , C_{61} , C_{62}) and the remaining coefficients. The coefficients with a mean value of zero show a significant scattering mainly induced by a varying fiber orientation. This is not only indicated by the standard deviation but also by the mean values of these elasticity coefficients. This fits the analytic description of composite materials. As long as the fibers are all aligned with the symmetry axis

$$C_{16} = C_{26} = C_{61} = C_{62} = 0 \quad (\text{I.41})$$

holds. However, when rotating the fiber orientation by a coordinate transform these elements are no longer equal to zero.

The sensitivity to the orientation of the fiber can also be found for the remaining elasticity coefficients. Here again, not only the mean values are significantly influenced, but also the standard deviation increases significantly. Furthermore, the standard deviation of these coefficients is also sensitive to the fiber volume fraction. Finally, there is only a slight influence of the fiber length as well as the fiber diameter.

I.4.5 Comparison of the analytical and numerical results

First of all the numerical results of the reference elasticity tensor are compared to the analytical results of the elasticity tensor based on the engineering constants given in Table I.2. For both analyses, the fiber geometry equals the mean value of the fiber length and fiber diameter. The fiber mass fraction is set to 30% and the fiber orientation is 0°. The results of the numerical analysis are provided in Table I.5. As the coefficients C_{12} and C_{21} can be calculated individually in this case, the given value of C_{12} represents the mean of C_{12} and C_{21} . The comparison of the numerical and analytical results agrees very well for the coefficients C_{12} , C_{22} , and C_{66} . This is independent of the boundary condition as well as the window size. In contrast to this, the coefficient C_{11} is approximated higher by using the analytical models of Tandon and Weng as well as Halpin and Tsai than the numerical simulations indicate. Finally, the mean values of C_{16} , C_{26} , C_{61} , and C_{62} based on the numerical simulations are close to zero. This fits the analytical results for fibers aligned with the symmetry axis. Therefore, the analytical and numerical results show an overall good agreement.

I.4.6 Correlation analysis

I.4.6.1 Moving window

The moving window method is used to characterize the random local properties of composites [8, 51, 157]. In this context, a window of a microstructure is moved to different locations and marks a rectangular part of the microstructure. The procedure is depicted in Figure I.14b for a microstructure with a size of 2500 $\mu\text{m} \times 2500 \mu\text{m}$ and window sizes of 500 $\mu\text{m} \times 500 \mu\text{m}$. With respect to the correlation analysis, this technique can be used to analyze the local dependence of the material properties by evaluating overlapping windows. If the windows do not overlap the correlation should be zero, as their microstructures are independent of each other.

In this study the basis of the correlation analysis is a microstructure of 2500 $\mu\text{m} \times 2500 \mu\text{m}$. To analyze the scale dependence of the correlation structure the window size is varied. Here, the maximum possible window size regarding a microstructure edge length of 2500 μm is 833 μm . In this case, it is possible to place three windows next to each other without any overlap. With a maximum window size of 833 μm and in accordance with the analysis presented so far the correlation analysis is done using again window sizes of 250 μm , 500 μm , and 750 μm . With respect to an average fiber length of 260 μm this domain can be assigned to the mesoscale.

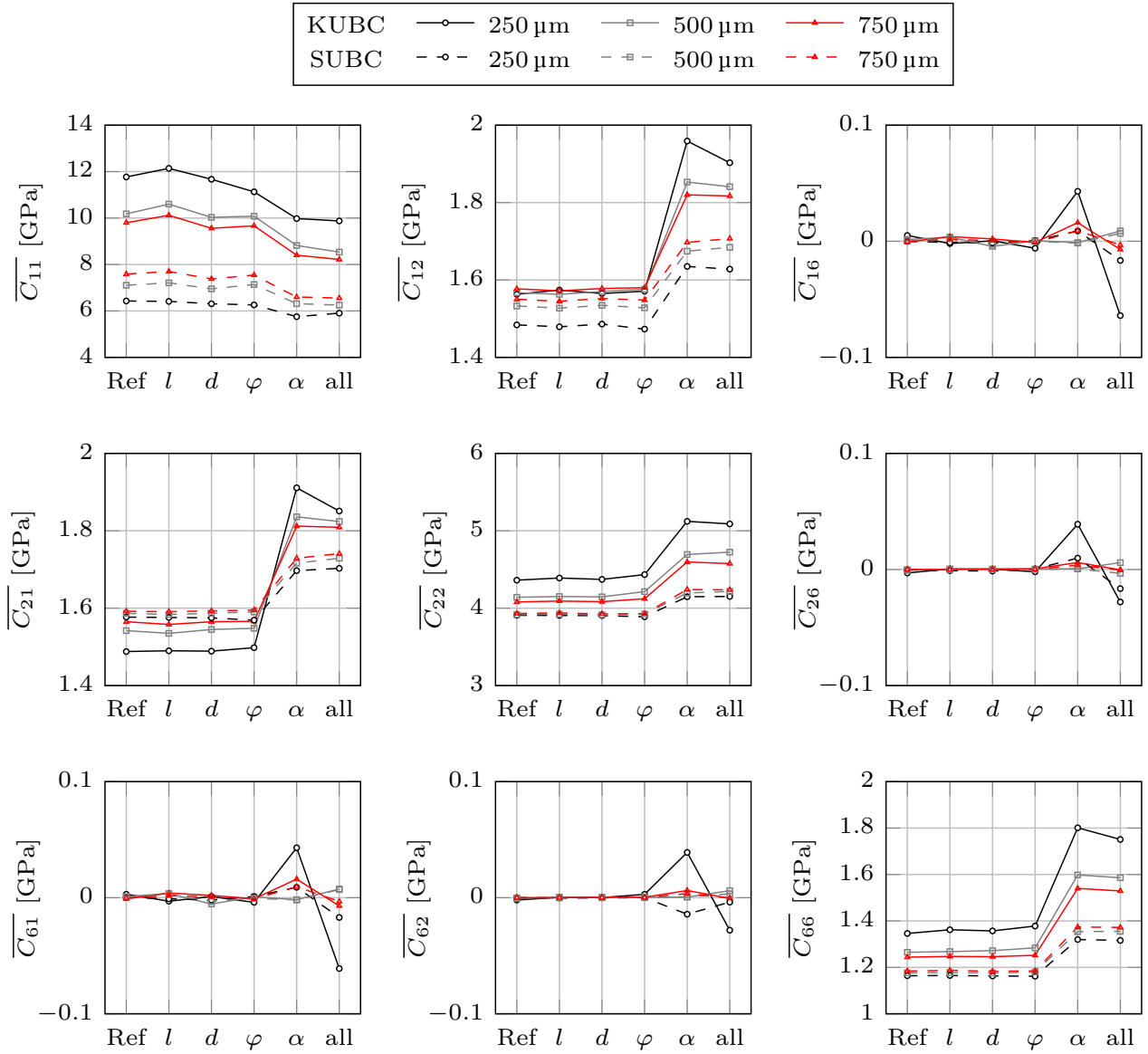


Figure I.12: Mean values of the elasticity coefficients in dependence of the geometrical fiber properties as well as the fiber volume fraction and fiber orientation on the elasticity coefficients.

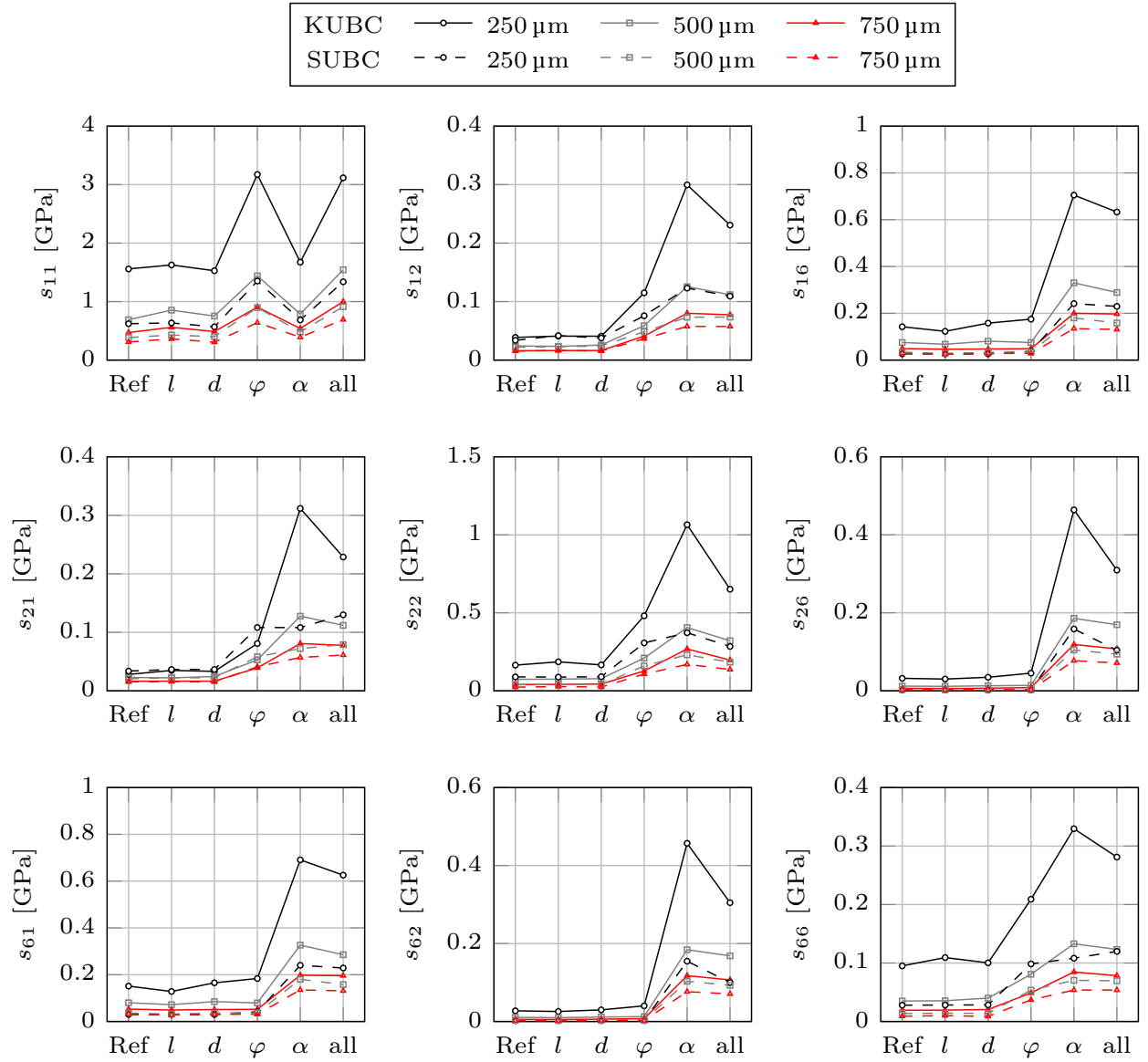


Figure I.13: Standard deviation of the elasticity coefficients in dependence of the geometrical fiber properties as well as the fiber volume fraction and fiber orientation on the elasticity coefficients.

BC		$\overline{C_{11}}$ GPa	$\overline{C_{12}}$ GPa	$\overline{C_{22}}$ GPa	$\overline{C_{66}}$ GPa
Tandon-Weng		13.0	1.59	4.18	1.31
Halpin-Tsai		12.0	1.63	4.34	1.30
250 μm	KUBC	11.8	1.56	4.36	1.35
250 μm	SUBC	6.43	1.48	3.91	1.16
500 μm	KUBC	10.2	1.57	4.14	1.27
500 μm	SUBC	7.11	1.53	3.92	1.18
750 μm	KUBC	9.80	1.56	4.08	1.24
750 μm	SUBC	7.59	1.59	3.93	1.18

Table I.5: Comparison of the mean values for the engineering constants based on the analytical and numerical analysis.

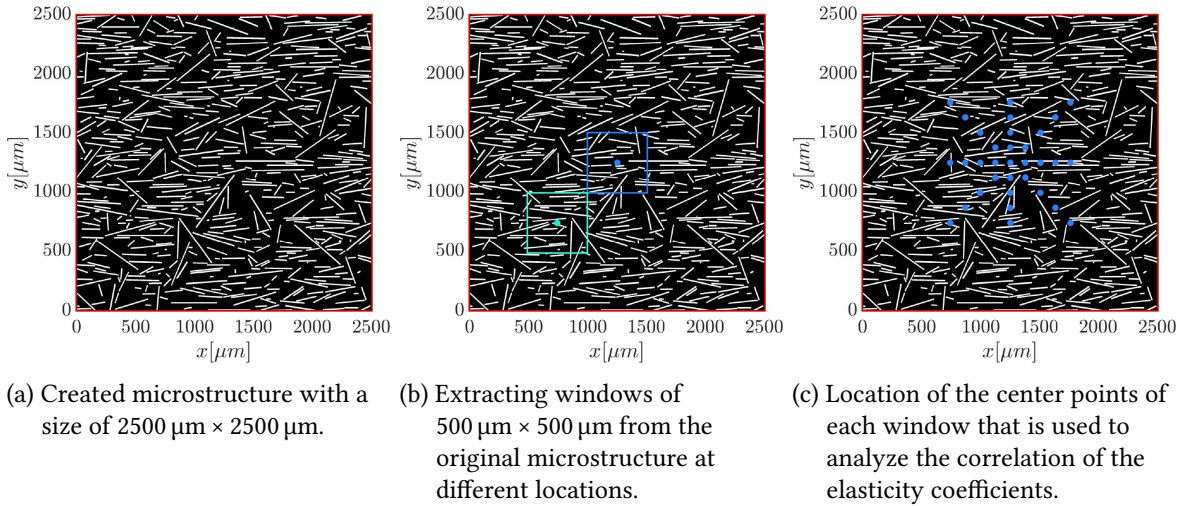


Figure I.14: Moving window procedure

This is also indicated by the results of the elasticity tensor properties presented in Section I.4.4.1 which clearly show a scale dependence of the elasticity coefficients for window sizes up to 750 μm .

To determine the correlation structure the dimensionless correlation parameter is calculated by evaluating Equation (I.35) based on 33 extracted windows at different locations from the same microstructure, see Figure I.14c. Starting from the center point of the microstructure the window is moved to the left and right as well as to the top and bottom four times. The distance between the equidistantly arranged center points of the extracted windows in the same direction is a quarter of the current window size. Therefore, the outer windows and the window in the center of the microstructure do not overlap. In the same way, windows are placed along the diagonals of the microstructure. Here, the distance between two center points is $\sqrt{2}l_{\text{window}}$. This procedure is repeated for a total of 500 microstructures to ensure convergence of the dimensionless correlation parameters [157, 164].

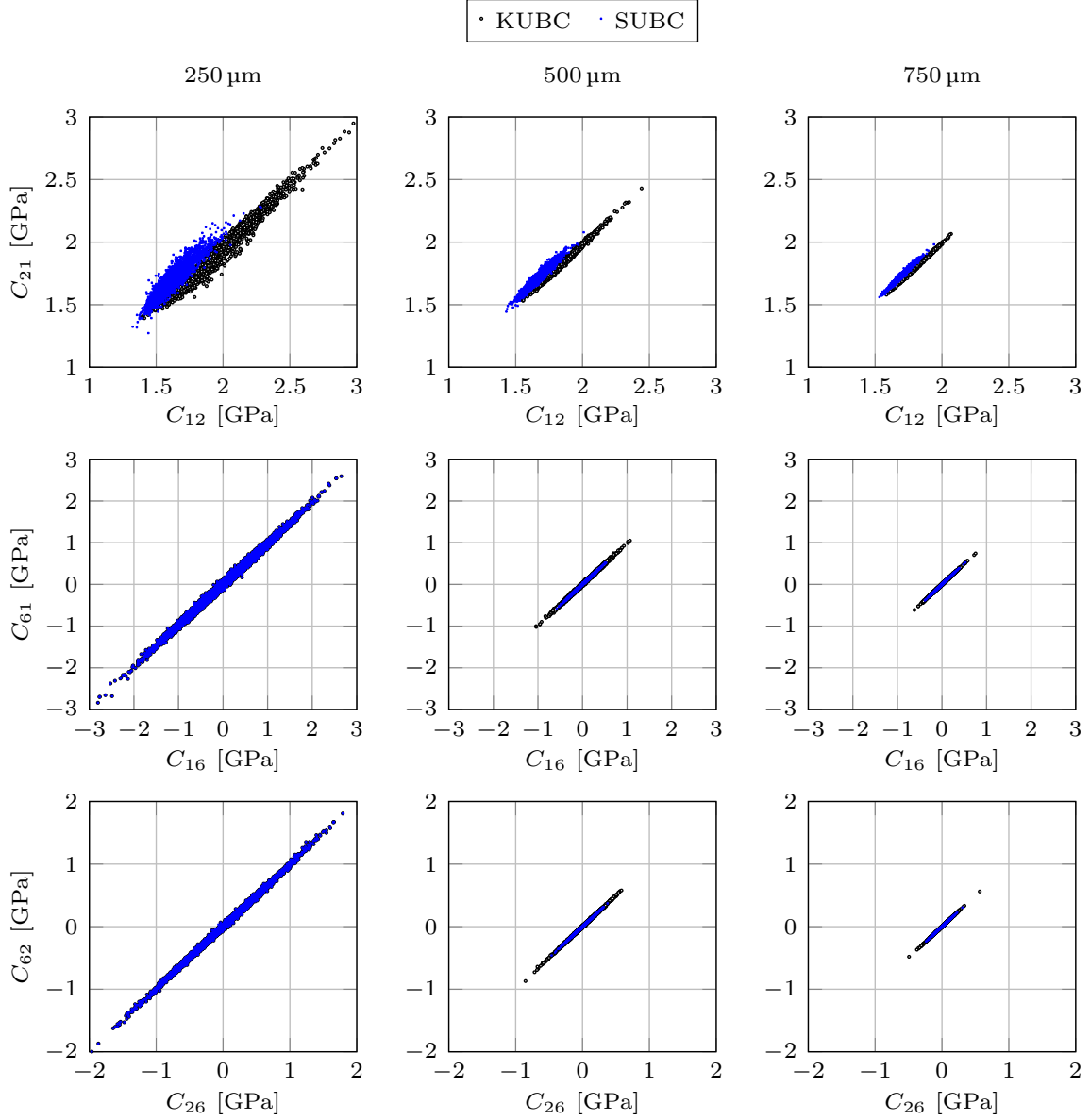
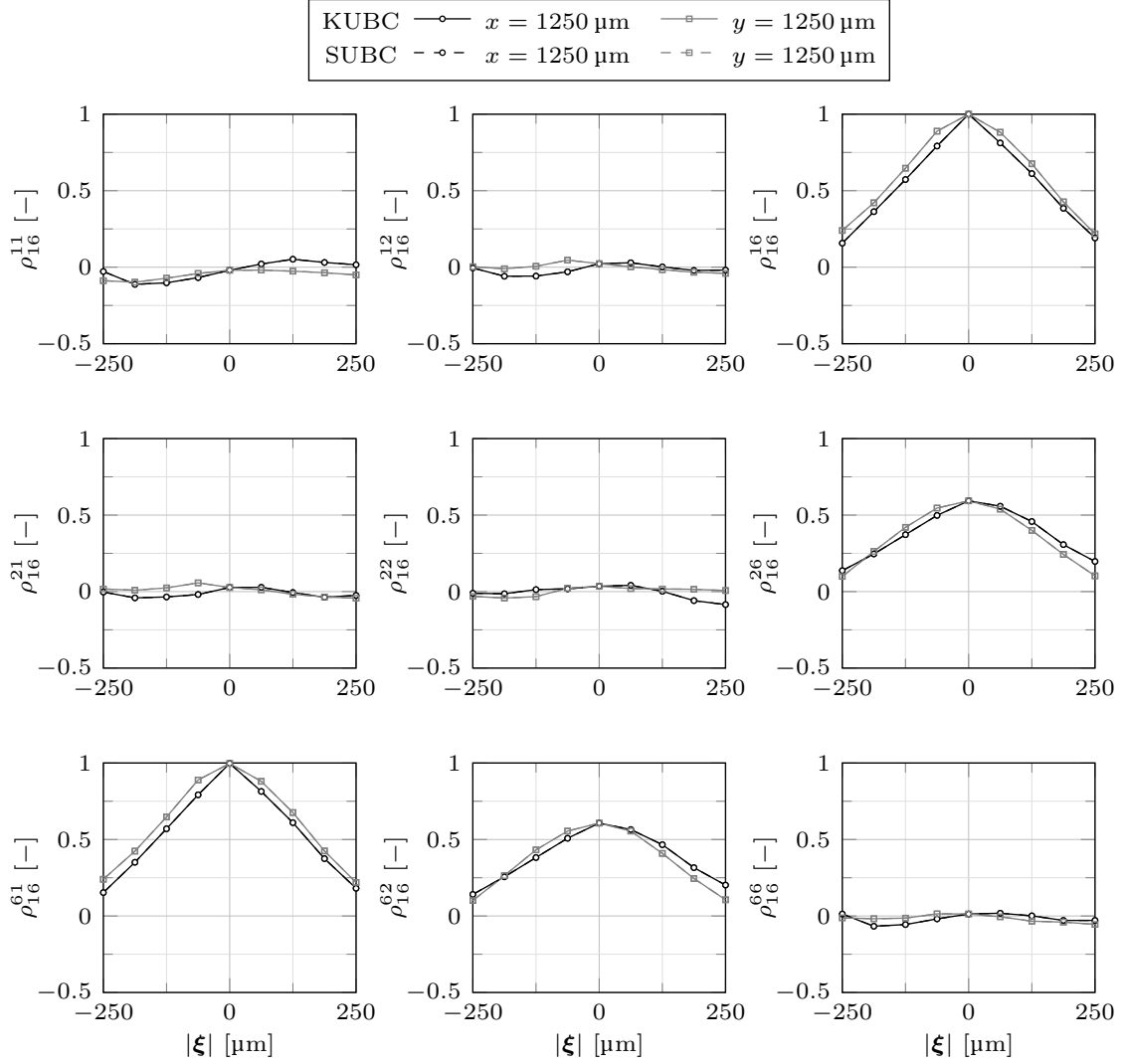


Figure I.15: Symmetry analysis of the elasticity tensor.

I.4.6.2 Cross-correlation

In this section, the correlation structure of the elasticity tensor is analyzed in detail. The main focus lays on the cross-correlation of the elasticity coefficients with respect to the boundary condition and the window size. First, the symmetry of the elasticity tensor is analyzed. Of particular interest are the elements C_{12} and C_{21} . Furthermore, as the varying fiber orientation leads to the anisotropy of the material the elements C_{16} and C_{61} as well as C_{26} and C_{62} are taken into account as well. Therefore, Figure I.15 shows the results of each simulation, where C_{12} is plotted against C_{21} , C_{16} is plotted against C_{61} , and C_{26} is plotted against C_{62} , respectively. The correlation between these elasticity coefficients is clearly indicated by a strong alignment of the points. Furthermore, the values of C_{16} , C_{26} , C_{61} , and C_{62} fluctuate around zeros, which leads to the conclusion that the mean value of these elements is close to zero. This behavior is independent of the boundary condition. However, the anisotropic effect (C_{16} , C_{26} , C_{61} , $C_{62} \neq 0$) starts to vanish with an increasing window size. This meets the assumption of overall transversely-isotropic material properties.

For analyzing the correlation structure of the anisotropic effect more in detail, Figure I.16 depicts the


 Figure I.16: Correlation analysis of the elasticity tensor based on the element C_{16} for a window size of $250 \mu\text{m}$.

correlation structure of C_{16} with respect to a window size of $250 \mu\text{m}$. Here, the lower index gives the reference for the dimensionless correlation parameter and the upper index refers to the elasticity coefficient that is calculated based on the moving window. Therefore, for ρ_{16}^{11} C_{16} is calculated for the window extracted of the microstructure center and C_{11} is determined for the extract of the moving window. Furthermore, $|\xi|$ gives the distance between the moving window and the center point of the microstructure.

The following essential characteristics can be derived. First, the correlation structure with respect to C_{16} is independent of the boundary condition. Second, the symmetry properties of the elasticity tensor can also be found within the correlation structure as ρ_{16}^{16} is almost identical to ρ_{16}^{61} . The same holds for ρ_{16}^{26} and ρ_{16}^{62} . Finally, there are only cross-correlations between the elements C_{16} and C_{61} due to the symmetry as well as between C_{16} and C_{26} and C_{16} and C_{62} , respectively. All other elements are uncorrelated to C_{16} . As indicated by Figure I.17, that shows the dimensionless correlation parameter between C_{16} and C_{26} for all three window sizes as well as both boundary conditions, these conclusions are also independent of the window size. Furthermore, the dimensionless correlation parameter is calculated in two different ways. First, the reference is C_{16} and C_{26} is calculated for the moving window. Subsequently, the values are exchanged, which means that the reference is C_{26} and C_{16} is calculated for the moving window. Based on the identical correlations for both variants,

$$\rho_{16}^{26} = \rho_{26}^{16} \quad (\text{I.42})$$

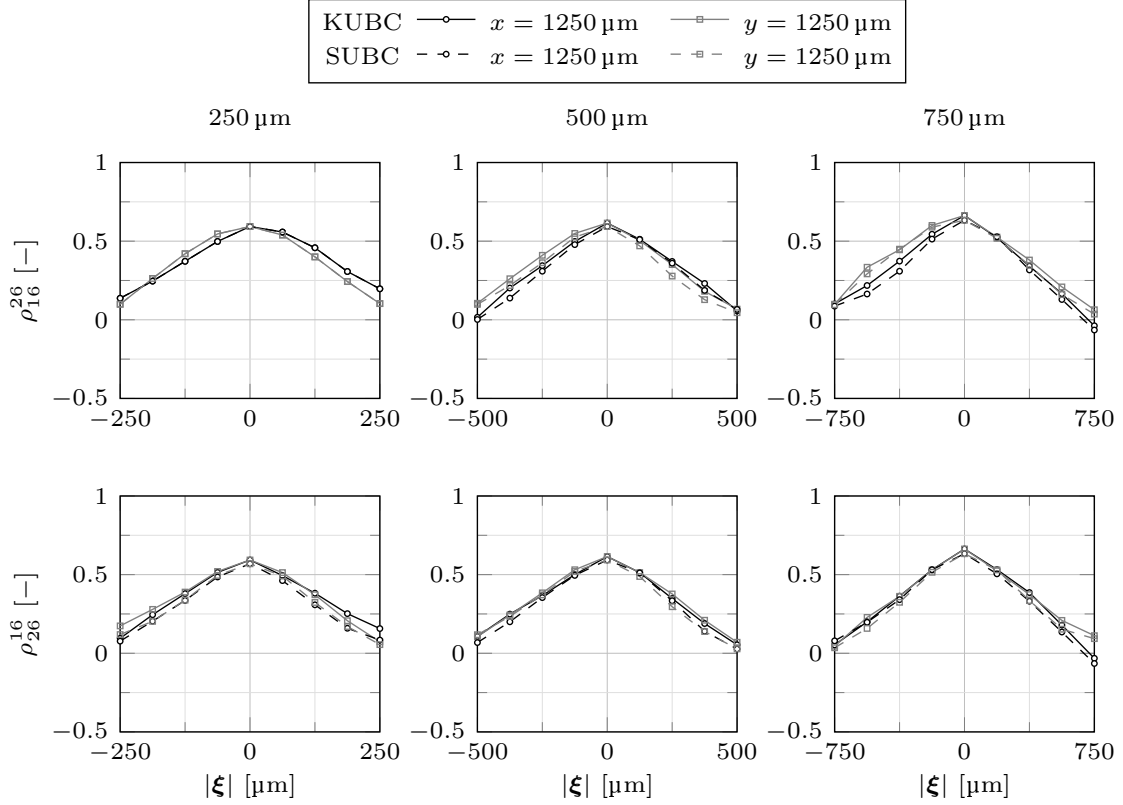


Figure I.17: Comparison of ρ_{16}^{26} and ρ_{26}^{16} .

holds under the condition, that a sufficient number of realizations is taken as a basis. This leads to the conclusion that the correlation structure shows the same symmetry properties as the elasticity tensor and therefore,

$$\rho_a^b = \rho_b^a \quad (\text{I.43})$$

can be assumed. Hence, the remaining number of independent correlation parameters can be reduced to

$$\rho_{11}^{12}, \rho_{11}^{22}, \rho_{11}^{66}, \rho_{12}^{22}, \rho_{12}^{66}, \rho_{22}^{66}. \quad (\text{I.44})$$

These conclusions are also valid for the correlation structure based on a plane strain state as shown in Figures I.26 and I.27.

The results of the cross-correlation for the remaining elasticity coefficients are presented in Figures I.18 and I.19. Here, the dimensionless correlation parameter is again divided into two groups. For one the correlation is independent of the window size (Figure I.18). The other group shows a decreasing correlation for an increasing window size, which is indicated by a decreasing value for $|\xi| = 0$. The overall shape of the correlation is not necessarily affected. One example is ρ_{11}^{66} . If the correlation depends on the window size, it is only relevant as long as the structure is represented by a SVE. In the case of a RVE the correlation vanishes.

These results also meet the theoretical framework as there is a clear connection between C_{11} and C_{12} via the Poisson ratio ν_{12} . However, the two elasticity coefficient C_{11} and C_{66} are independent on the macroscale.

The same correlation structure can be also derived on the basis of a plane strain assumption, see Figures I.28 and I.29. However, the correlation functions can not be approximated by the same function. Therefore, when using second-order random fields for numerical simulations of components the correlation functions must be determined with respect to the overall load assumption.

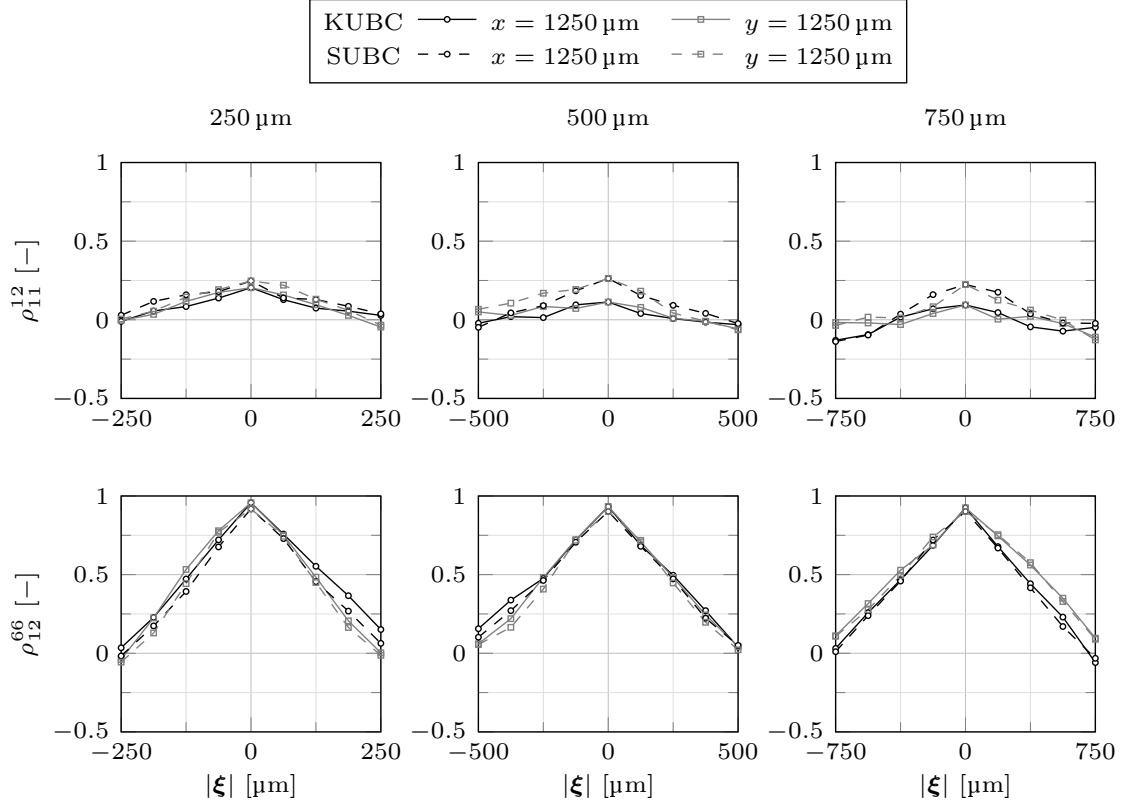


Figure I.18: Dimensionless correlation parameters that are independent of the window size.

I.5 Conclusion

In the presented work first, an analytical treatment is performed. Based on the material models by Tandon and Weng as well as Halpin and Tsai the influence of the different geometrical properties like fiber length, fiber diameter, fiber orientation, and fiber volume fraction on the material properties is investigated. The results show that the Young's Modulus E_1 is the most affected material property by the geometrical properties. This is supported by the material model of Halpin and Tsai, where only E_1 is modeled as a function of the fiber length and fiber diameter. The main influencing parameters of E_1 are the fiber length, fiber orientation, and fiber volume fraction. The remaining engineering constants are only slightly affected by the geometrical fiber properties. However, the fiber orientation, as well as the fiber volume fraction, also have a significant effect on these constants. This can also be found when analyzing the elasticity coefficients. Furthermore, the distribution of the resulting elasticity tensor, as well as the elasticity coefficients, can be approximated by the same function as the probability density function of the influencing parameter itself.

In the next step, this analysis is repeated on a numerical basis. However, there is one important difference between the numerical analysis and analytical treatment. The numerical model consists of several fibers of different length, diameter, and orientation. In contrast to that the analytical treatment is based on the assumption that all fibers have the same length, diameter, and orientation. Furthermore, by evaluating the numerical model each element of the elasticity tensor can be calculated individually. Therefore, the symmetry of this tensor is not presupposed, but the numerical results clearly confirm the symmetry of the resulting elasticity tensor. Furthermore, the overall transversely-isotropic material properties are affirmed by the numerical simulations as the mean of the elasticity coefficients C_{16} and C_{26} equals zero and the standard deviation decreases with increasing window size.

Summarizing the numerical simulations show a good agreement with the results of the analytical investigation. The material properties of the microstructure is influenced significantly by the fiber orientation and

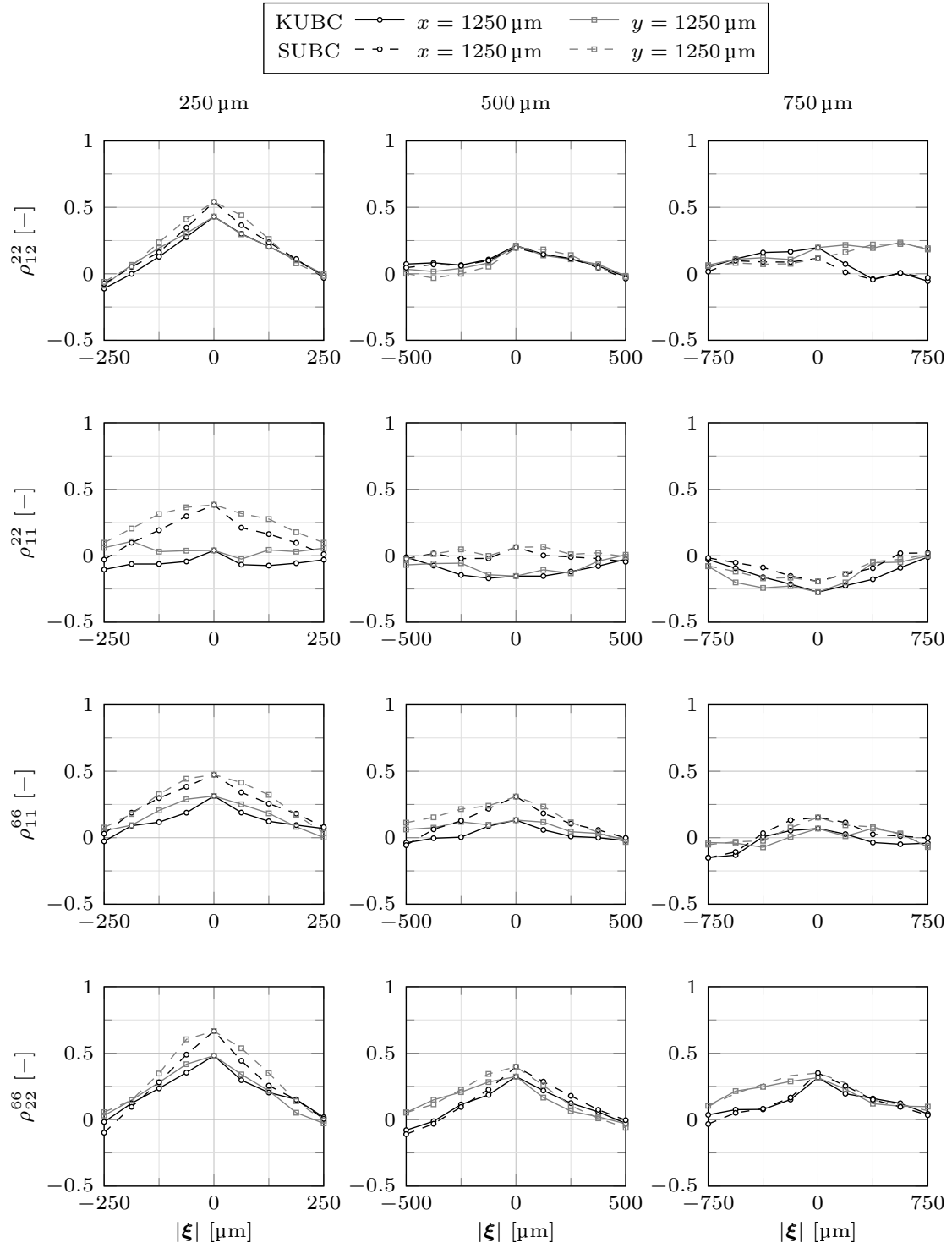


Figure I.19: Dimensionless correlation parameters that depend on the window size.

the fiber volume fraction. Furthermore, on the mesoscale, the distribution of the elasticity coefficients can be approximated with the same probability distribution as the influencing parameter itself. However, with increasing window size, the distribution starts to shift to a normal distribution.

Regarding the numerical correlation analysis, the symmetry of elasticity tensor can also be found within the correlation structure of the elasticity coefficients. In addition, the dimensionless correlation parameters can be divided into two independent groups. The first group gives the correlation between the non zero elasticity coefficients of transversely-isotropic material behavior. The second group comprises only a correlation of C_{16} and C_{26} .

It can be concluded, that the correlation structure of the elasticity tensor for SFRC can be approximated by numerical simulations on the mesoscale and the results are independent of the chosen boundary conditions. However, the results depend not only on the window size but also on the overall assumption of a plane stress and a plane strain state in case of a two-dimensional model, respectively.

I.A Analytical results

Below the remaining results of the analytical treatment are shown. This includes the influence of the fiber diameter and fiber orientation on the engineering constants as well as the elasticity coefficients based on the material model by Tandon and Weng. Furthermore, the results based on the material model by Halpin and Tsai are given. This covers the Young's Modulus E_1 as well as the elasticity coefficients, both in dependence of the fiber length, diameter and fiber orientation.

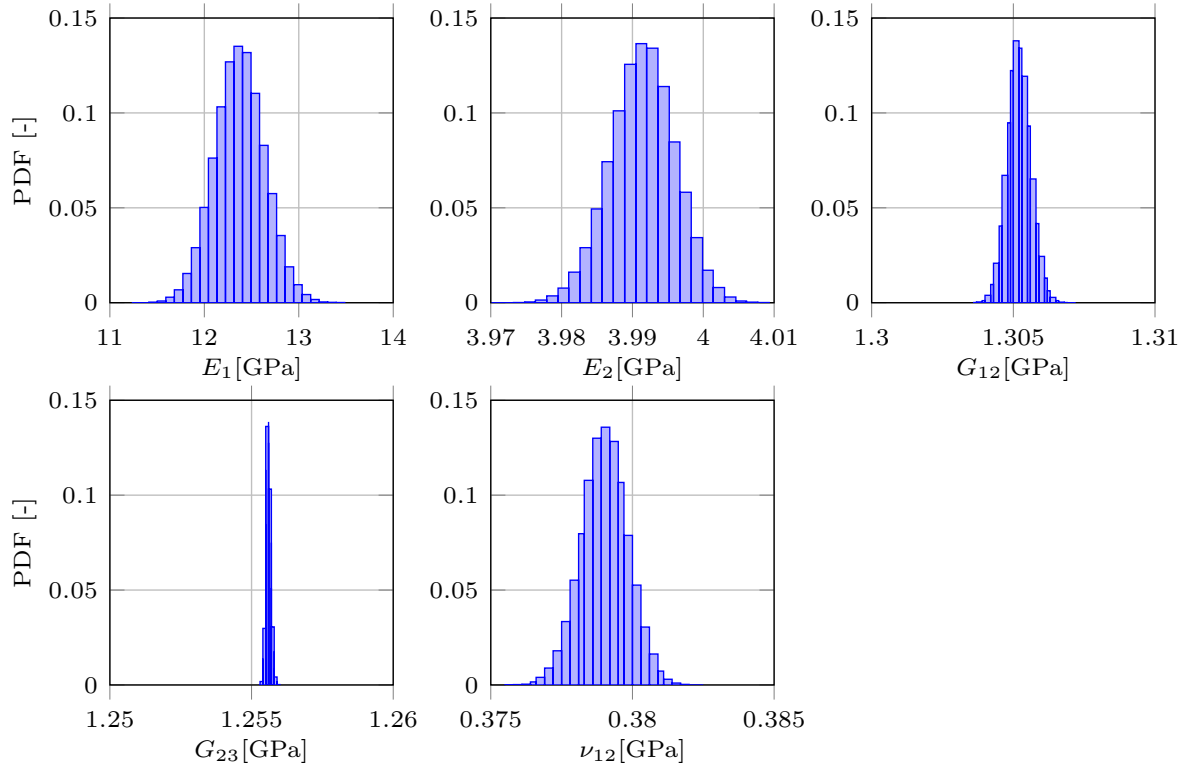


Figure I.20: Engineering constants due to a varying fiber diameter calculated with the Tandon-Weng material model.

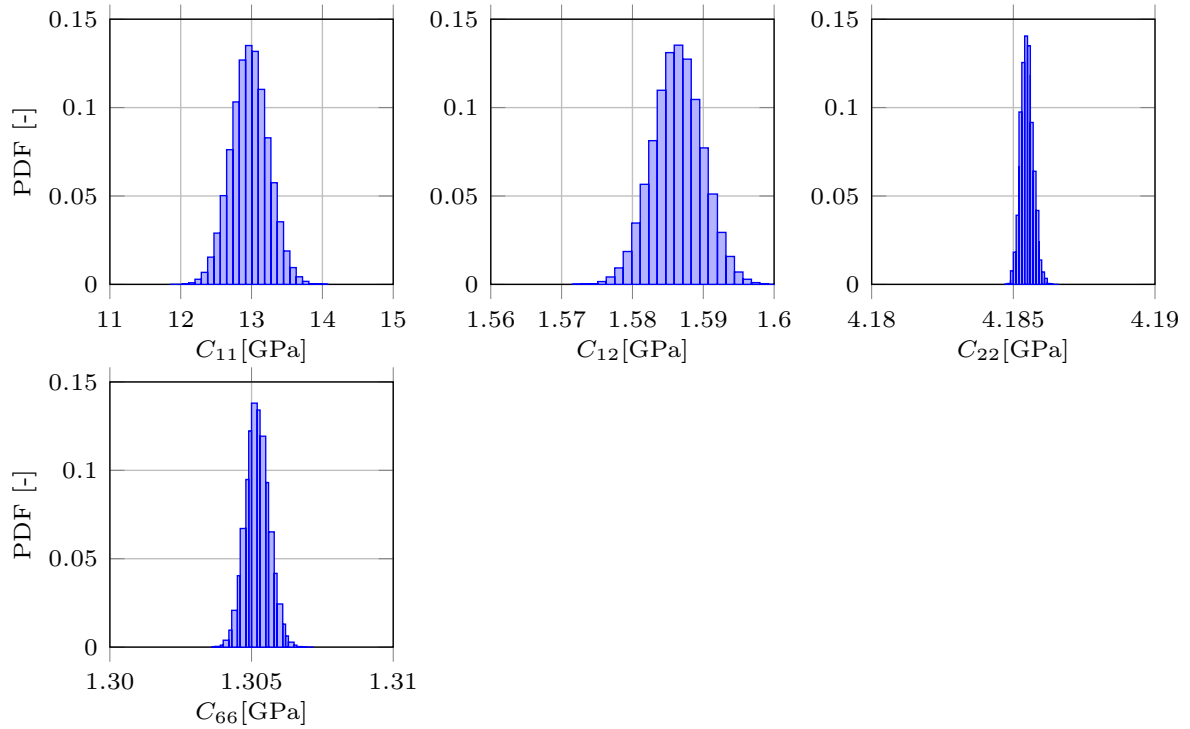


Figure I.21: Elasticity coefficients due to a varying fiber diameter calculated with the Tandon-Weng material model.

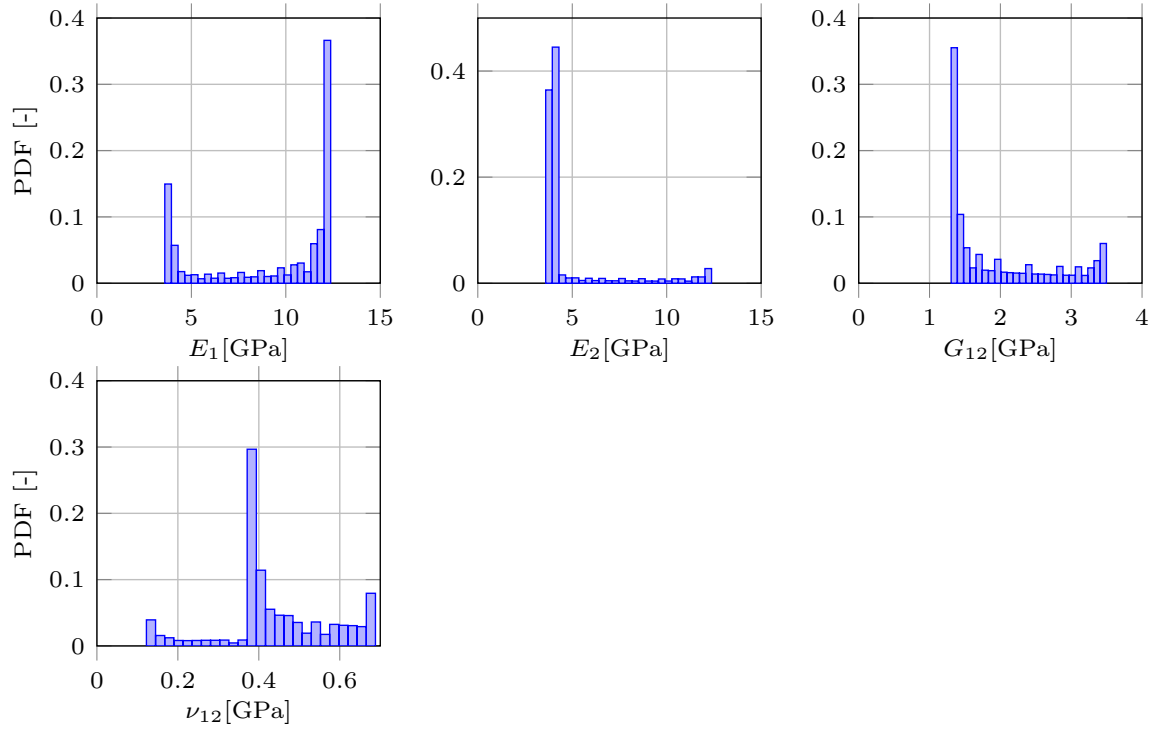


Figure I.22: Engineering constants due to a varying fiber orientation calculated with the Tandon-Weng material model.

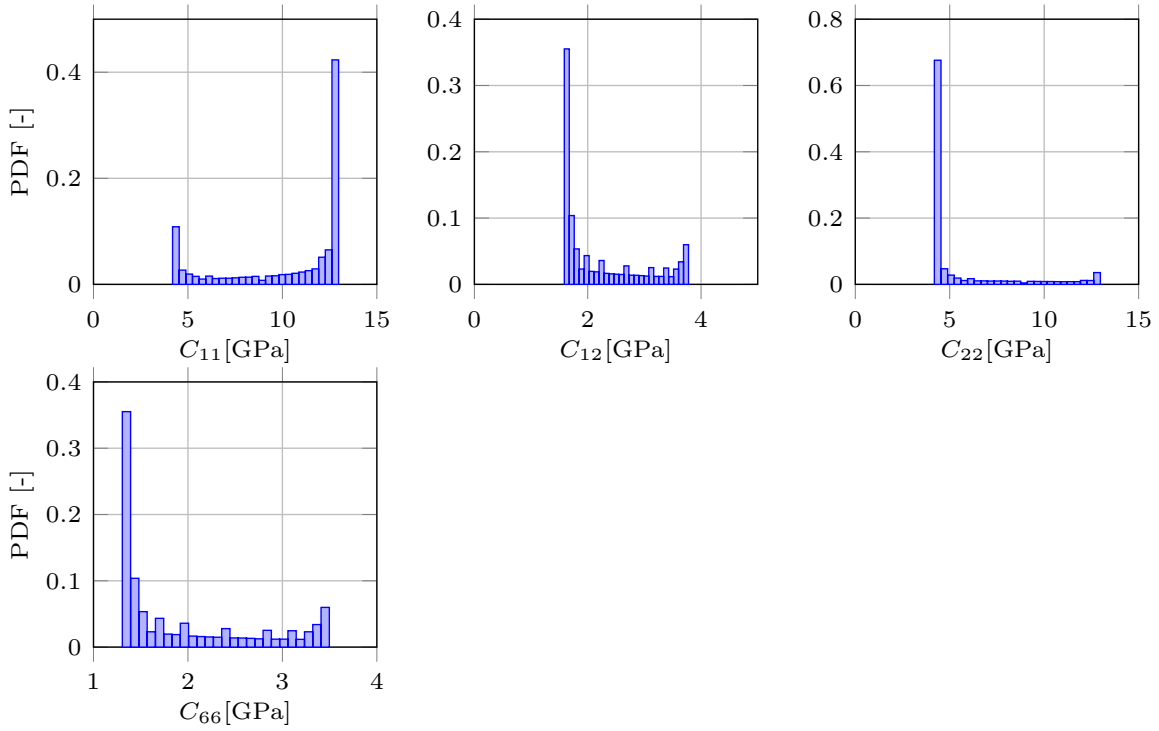


Figure I.23: Elasticity coefficients due to a varying fiber orientation calculated with the Tandon-Weng material model.

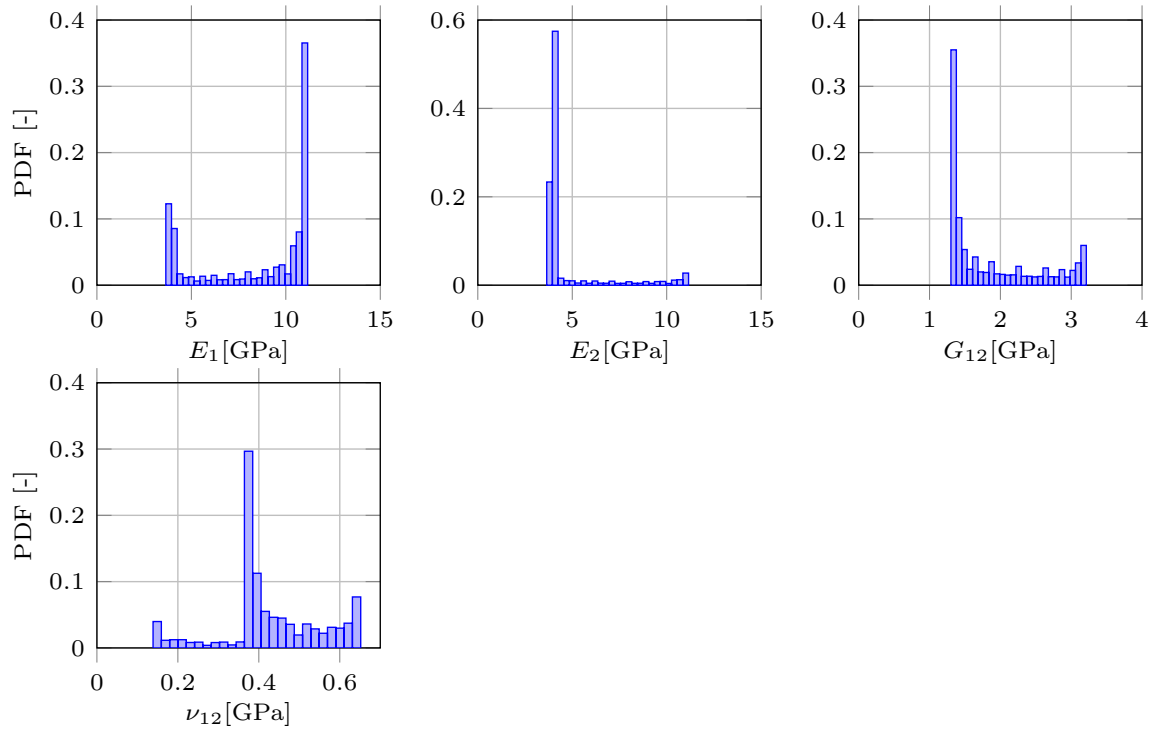


Figure I.24: Engineering constants due to a varying fiber orientation calculated with the Halpin-Tsai material model.

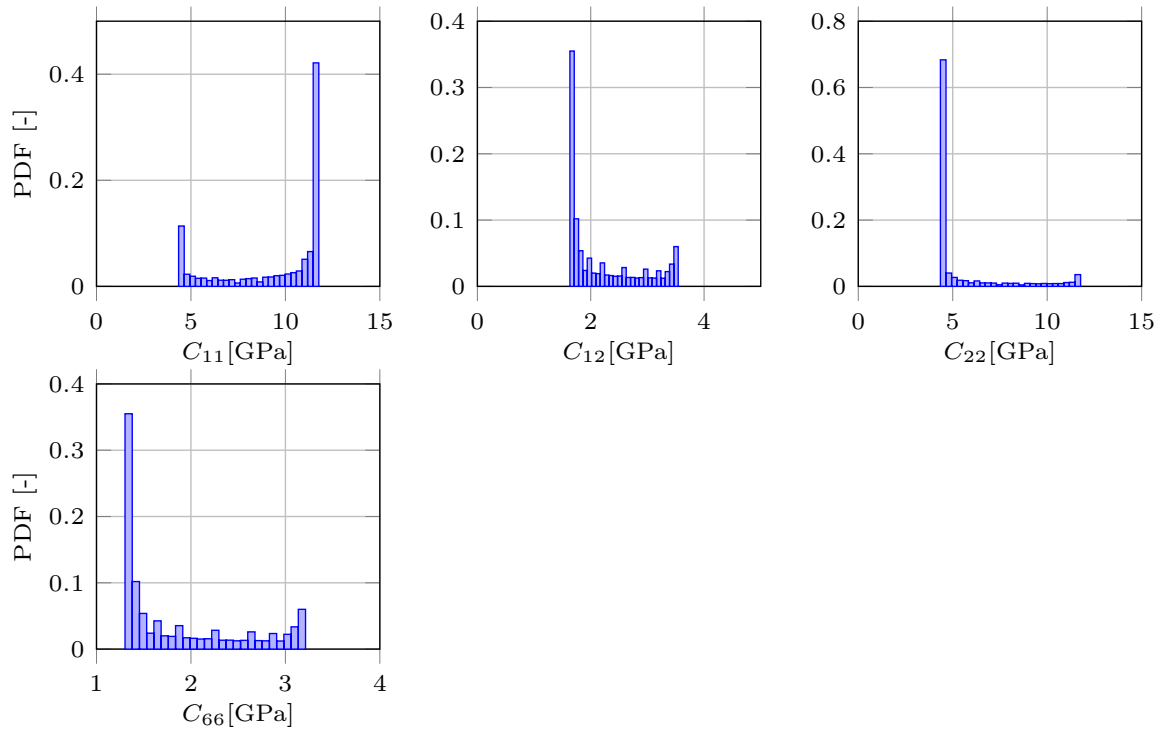


Figure I.25: Elasticity coefficients due to a varying fiber orientation calculated with the Halpin-Tsai material model.

I.B Numerical analysis

I.B.1 Determination of the elasticity tensor elements

To calculate the elasticity coefficients a system of equations can be formulated based on the three independent load cases. Hooke's law for a finite volume element reads

$$\langle \sigma \rangle = C^{\text{eff}} : \langle \epsilon \rangle. \quad (\text{I.2})$$

Reducing this formulation to the 2D case and using Voigt notation leads to

$$\begin{bmatrix} \langle \sigma_1 \rangle \\ \langle \sigma_2 \rangle \\ \langle \sigma_6 \rangle \end{bmatrix} = \begin{bmatrix} C_{11}^{\text{eff}} & C_{12}^{\text{eff}} & C_{16}^{\text{eff}} \\ C_{21}^{\text{eff}} & C_{22}^{\text{eff}} & C_{26}^{\text{eff}} \\ C_{61}^{\text{eff}} & C_{62}^{\text{eff}} & C_{66}^{\text{eff}} \end{bmatrix} \begin{bmatrix} \langle \epsilon_1 \rangle \\ \langle \epsilon_2 \rangle \\ 2\langle \epsilon_6 \rangle \end{bmatrix}. \quad (\text{I.45})$$

Each stress component can be written in an individual equation

$$\langle \sigma_1 \rangle = \begin{bmatrix} C_{11}^{\text{eff}} & C_{12}^{\text{eff}} & C_{16}^{\text{eff}} \end{bmatrix} \begin{bmatrix} \langle \epsilon_1 \rangle \\ \langle \epsilon_2 \rangle \\ 2\langle \epsilon_6 \rangle \end{bmatrix} \quad (\text{I.46})$$

which can be rearranged to

$$\langle \sigma_1 \rangle = \begin{bmatrix} \langle \epsilon_1 \rangle & \langle \epsilon_2 \rangle & 2\langle \epsilon_6 \rangle \end{bmatrix} \begin{bmatrix} C_{11}^{\text{eff}} \\ C_{12}^{\text{eff}} \\ C_{16}^{\text{eff}} \end{bmatrix}. \quad (\text{I.47})$$

Now the individual load cases can be summarized in this system of equations

$$\begin{bmatrix} \langle \sigma_1^{\text{LC1}} \rangle \\ \langle \sigma_1^{\text{LC2}} \rangle \\ \langle \sigma_1^{\text{LC3}} \rangle \end{bmatrix} = \begin{bmatrix} \langle \epsilon_1^{\text{LC1}} \rangle & \langle \epsilon_2^{\text{LC1}} \rangle & 2\langle \epsilon_6^{\text{LC1}} \rangle \\ \langle \epsilon_1^{\text{LC2}} \rangle & \langle \epsilon_2^{\text{LC2}} \rangle & 2\langle \epsilon_6^{\text{LC2}} \rangle \\ \langle \epsilon_1^{\text{LC3}} \rangle & \langle \epsilon_2^{\text{LC3}} \rangle & 2\langle \epsilon_6^{\text{LC3}} \rangle \end{bmatrix} \begin{bmatrix} C_{11}^{\text{eff}} \\ C_{12}^{\text{eff}} \\ C_{16}^{\text{eff}} \end{bmatrix} \quad (\text{I.48})$$

which can be solved by

$$\begin{bmatrix} C_{11}^{\text{eff}} \\ C_{12}^{\text{eff}} \\ C_{16}^{\text{eff}} \end{bmatrix} = \begin{bmatrix} \langle \epsilon_1^{\text{LC1}} \rangle & \langle \epsilon_2^{\text{LC1}} \rangle & 2\langle \epsilon_6^{\text{LC1}} \rangle \\ \langle \epsilon_1^{\text{LC2}} \rangle & \langle \epsilon_2^{\text{LC2}} \rangle & 2\langle \epsilon_6^{\text{LC2}} \rangle \\ \langle \epsilon_1^{\text{LC3}} \rangle & \langle \epsilon_2^{\text{LC3}} \rangle & 2\langle \epsilon_6^{\text{LC3}} \rangle \end{bmatrix}^{-1} \begin{bmatrix} \langle \sigma_1^{\text{LC1}} \rangle \\ \langle \sigma_1^{\text{LC2}} \rangle \\ \langle \sigma_1^{\text{LC3}} \rangle \end{bmatrix}. \quad (\text{I.49})$$

Expanding this procedure to the remaining stress components $\langle \sigma_2 \rangle$ and $\langle \sigma_6 \rangle$ the elasticity coefficients can be derived from

$$\begin{bmatrix} C_{n1}^{\text{eff}} \\ C_{n2}^{\text{eff}} \\ C_{n6}^{\text{eff}} \end{bmatrix} = \begin{bmatrix} \langle \epsilon_1^{\text{LC1}} \rangle & \langle \epsilon_2^{\text{LC1}} \rangle & 2\langle \epsilon_6^{\text{LC1}} \rangle \\ \langle \epsilon_1^{\text{LC2}} \rangle & \langle \epsilon_2^{\text{LC2}} \rangle & 2\langle \epsilon_6^{\text{LC2}} \rangle \\ \langle \epsilon_1^{\text{LC3}} \rangle & \langle \epsilon_2^{\text{LC3}} \rangle & 2\langle \epsilon_6^{\text{LC3}} \rangle \end{bmatrix}^{-1} \begin{bmatrix} \langle \sigma_n^{\text{LC1}} \rangle \\ \langle \sigma_n^{\text{LC2}} \rangle \\ \langle \sigma_n^{\text{LC3}} \rangle \end{bmatrix} \quad (\text{I.50})$$

with $n = 1, 2, 6$.

I.B.2 Results based on a plane strain assumption

The following figures show the results for the correlation analysis assuming a plane strain state.

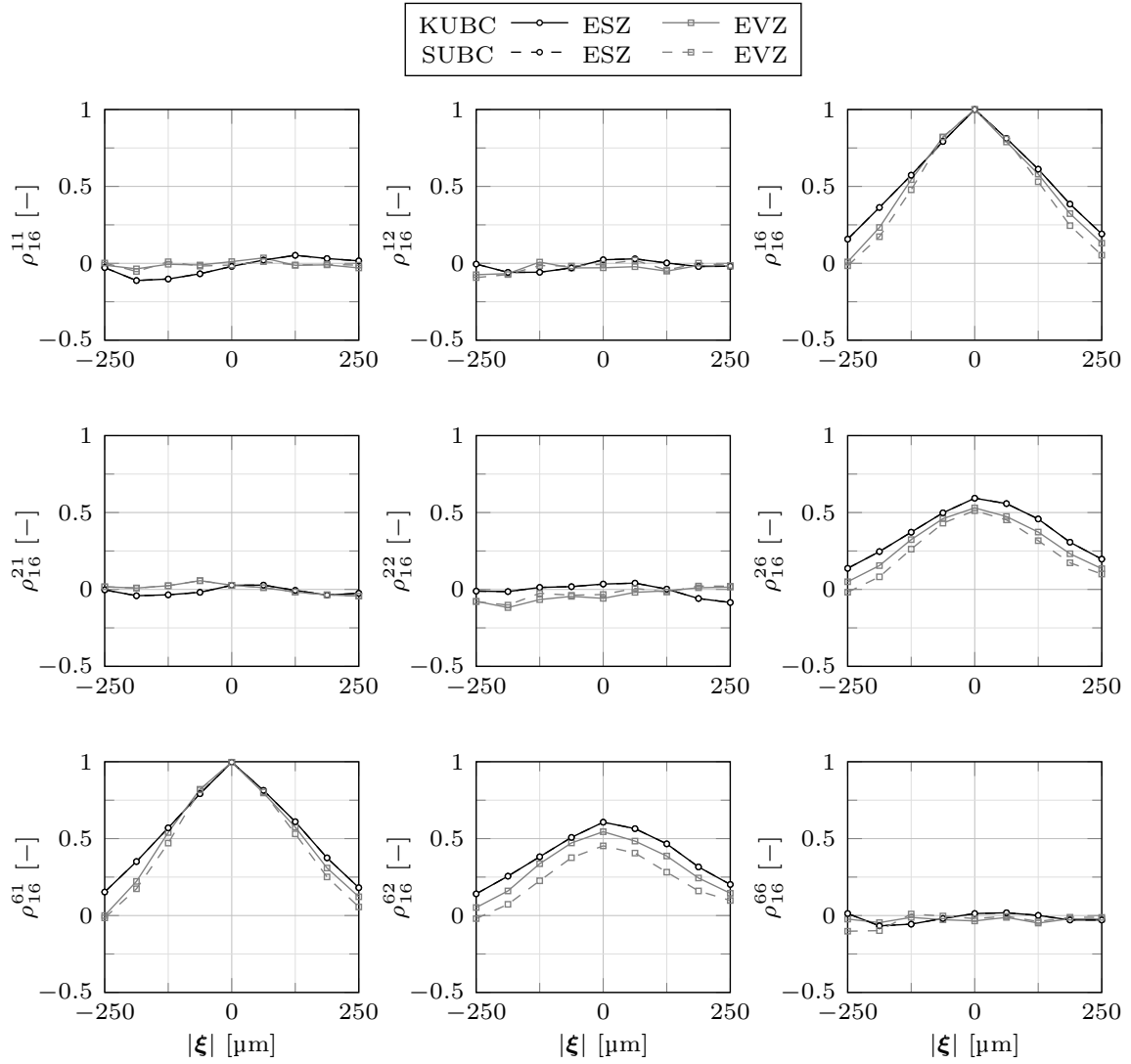


Figure I.26: Comparison of the dimensionless correlation parameters based on C_{16} assuming plane strain and plane stress states for a window size of $250 \mu\text{m}$ at $x = 1250 \mu\text{m}$.

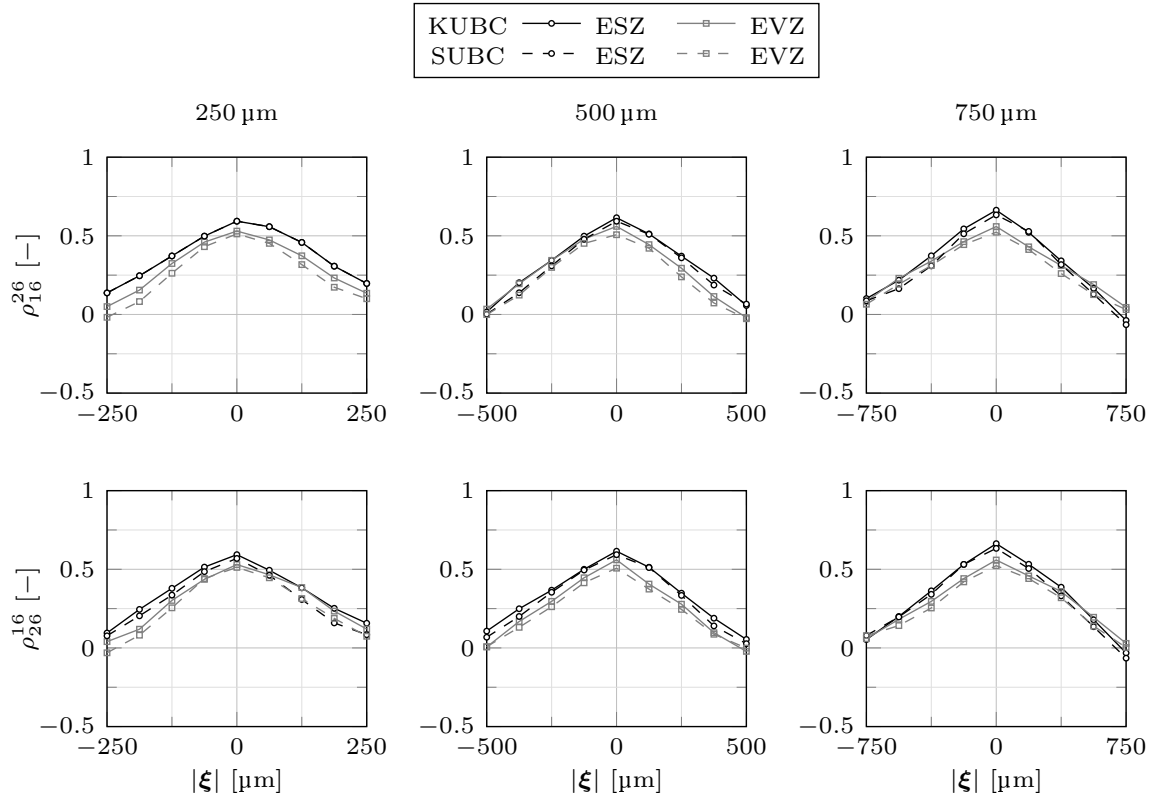


Figure I.27: Comparison of ρ_{16}^{26} and ρ_{26}^{16} assuming plane strain and plane stress states at $x = 1250 \mu\text{m}$.

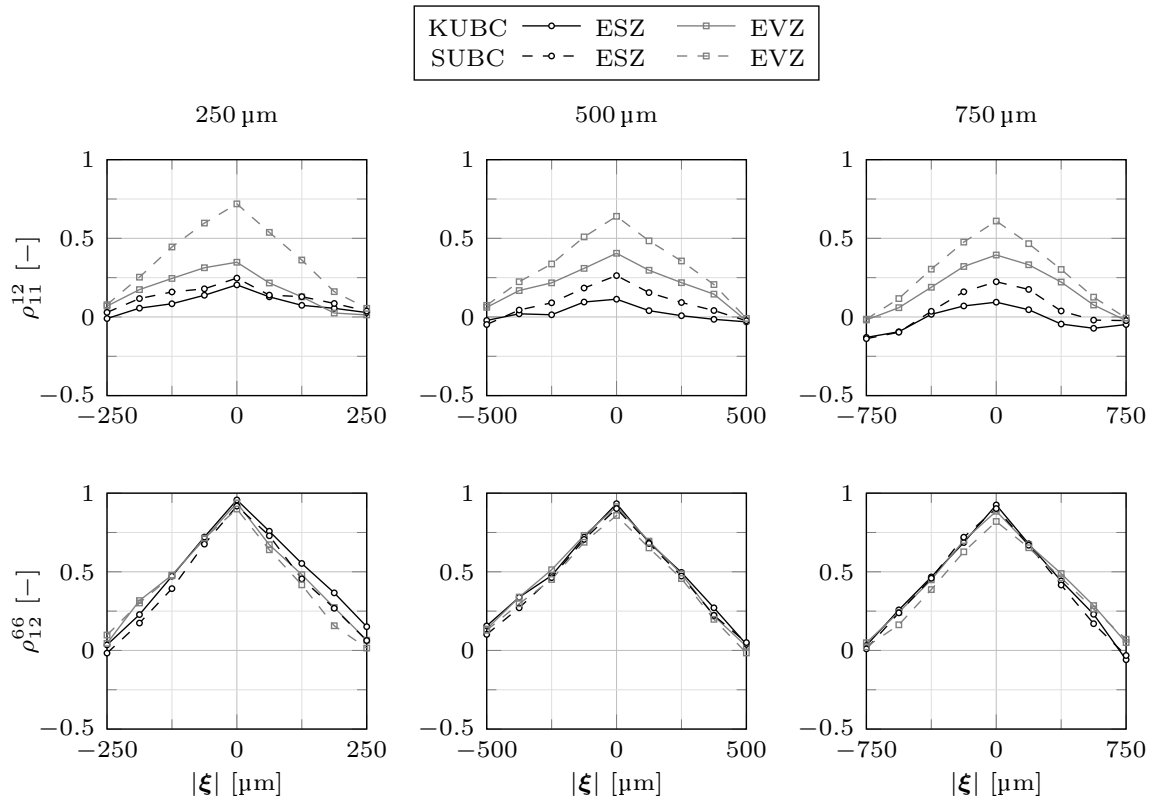


Figure I.28: Comparison of the dimensionless correlation parameters that are independent of the window size assuming plane strain and plane stress states at $x = 1250 \mu\text{m}$.

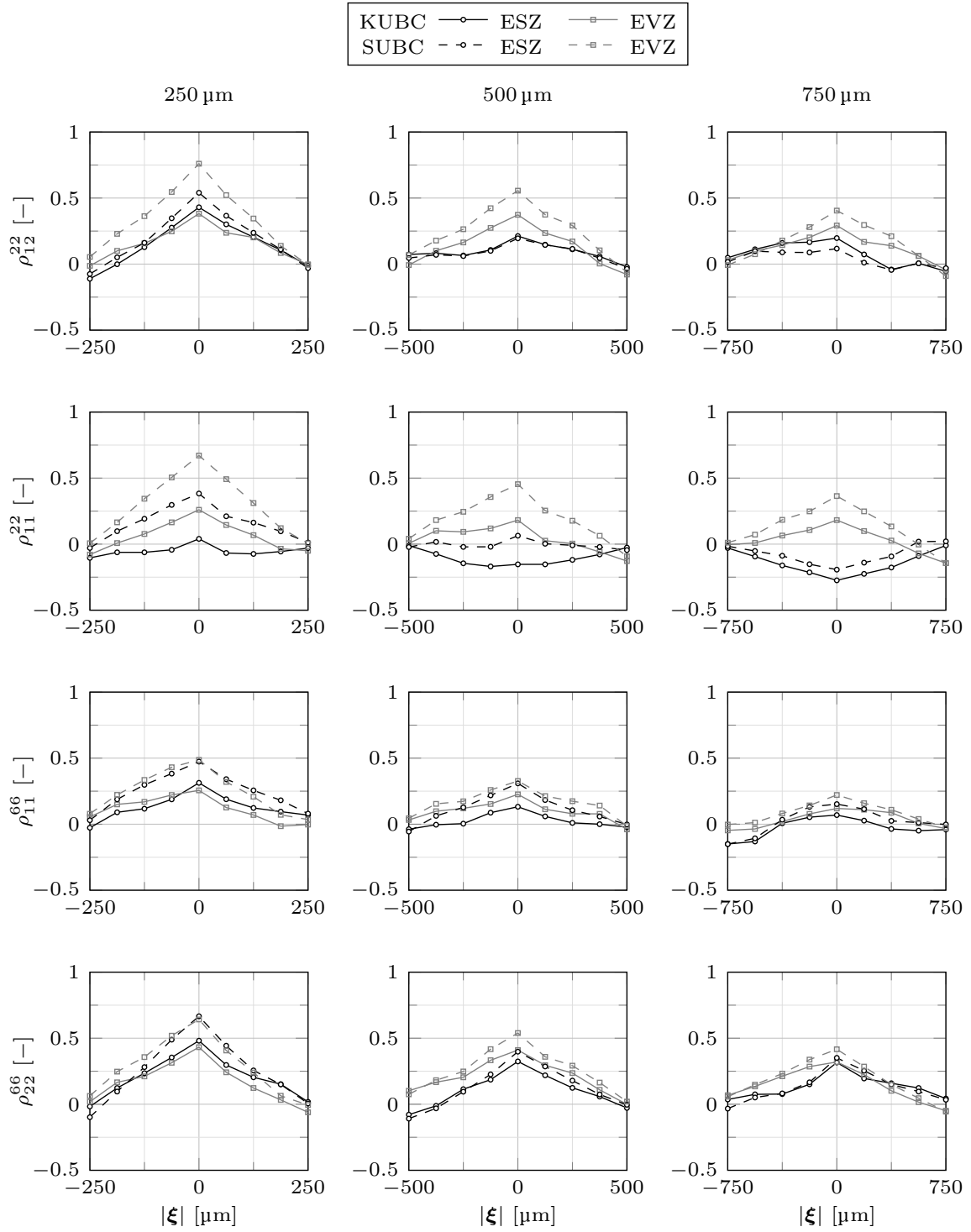


Figure I.29: Comparison of the dimensionless correlation parameters that depend on the window size assuming plane strain and plane stress states at $x = 1250 \mu\text{m}$.

Paper II

A computational modeling approach based on random fields for short fiber-reinforced composites with experimental verification by nanoindentation and tensile tests

Title: A computational modeling approach based on random fields for short fiber-reinforced composites with experimental verification by nanoindentation and tensile tests

Author: Natalie Rauter¹

Affiliation: ¹Helmut-Schmidt-University /
University of the Federal Armed Forces Hamburg
Holstenhofweg 85, 22043 Hamburg, Germany

Journal: Computational Mechanics
67, pp. 699 - 722, 2021

Status: Published

DOI: 10.1007/s00466-020-01958-3

Abstract: In this study a modeling approach for short fiber-reinforced composites is presented which allows one to consider information from the microstructure of the compound while modeling on the component level. The proposed technique is based on the determination of correlation functions by the moving window method. Using these correlation functions random fields are generated by the Karhunen-Loève expansion. Linear elastic numerical simulations are conducted on the mesoscale and component level based on the probabilistic characteristics of the microstructure derived from a two-dimensional micrograph. The experimental validation by nanoindentation on the mesoscale shows good conformity with the numerical simulations. For the numerical modeling on the component level the comparison of experimentally obtained Young's modulus by tensile tests with numerical simulations indicate that the presented approach requires three-dimensional information of the probabilistic characteristics of the microstructure. Using this information not only the overall material properties are approximated sufficiently, but also the local distribution of the material properties shows the same trend as the results of conducted tensile tests.

II.1 Introduction

The compatibility of thermoplastic material for automated serial production like mold injection allows high production rates with a reasonable price per piece. Adding short fibers or nanoparticles to the base material of pure plastics leads to a significant increase of the stiffness and strength of the material without losing the ability to process the material by automated serial production. Hence, this combination results into a high interest in short fiber-reinforced composite (SFRC) not only in the automotive industry.

The main disadvantage due to the reinforcing elements is the spatial fluctuation of the material properties. The representation of the non-equally distributed material properties is hence, challenging and connected with high computational costs due to the use of probabilistic methods. This consequently is worthwhile to represent the probabilistic characteristics of the microstructure on the component level by appropriate stochastic methods without extensive computational costs.

The spatial distribution of the material properties is mainly assigned to the finite fiber length as well as a production process induced variation of the fiber orientation due to different melt flow velocities and shear forces over the cross-section [95]. Since the fiber length is usually much smaller in comparison to the component the microstructural information must be transferred from the micro- and mesoscale to the component level. Therefore, a multi-scale approach appears advantageous for a sufficient modeling procedure for SFRC.

In the literature many different approaches are presented for the modeling of the probabilistic characteristics of reinforced materials. One approach is based on the orientation tensor introduced in [2]. In [9] the orientation tensor is implemented directly in the material description. An extended approach is used in [33], where the orientation tensor is combined with a material model based on a coupled micro-mechanical and phenomenological approach. The suitability is also discussed in [123]. A second approach is based on the extended finite element method (XFEM), which was developed for the numerical simulation of crack growth and interfaces [122]. In [68] the method is applied to reinforced concrete. It is also used in [137], where it is combined with a cohesive zone model. All these approaches have in common the lack of a scale transition. A first attempt for a scale transition is presented in [156] where XFEM is combined with a Monte Carlo simulation to estimate the size of a representative volume element (RVE) for random composites.

One technique for the representation of spatial varying parameters with a scale transition is the use of random fields [176] and hence, allow the modeling of inhomogeneous material properties [126]. For the discretization of random fields for the use in a numerical simulation the Karhunen-Loève expansion is a suitable tool. This allows a separation of the deterministic numerical modeling and the probabilistic representation of the material properties. In context of structural mechanics this approach is also referred to as the stochastic finite element method (SFEM) [112, 131]. In [86] SFEM is combined with cohesive zone models for the analysis of crack growth in fiber reinforced cementitious composites. The fluctuation of the volume fraction is represented by random fields in [57]. The influence of the fiber mass fraction, the window size, and the contrast between the phases on the correlation structure is discussed in [157]. Finally, a combination of the SFEM with the concept of RVE is presented in [56, 164].

The main objective of this research is to establish a robust computational modeling approach for components made of SFRC using homogeneous second-order random fields discretized by the Karhunen-Loève expansion. In this study a tensile test specimen is used exemplary. First the microstructural properties of the material are extracted from a two-dimensional micrograph as shown in [158]. Using the probabilistic characteristics of the fiber length, fiber orientation, fiber diameter, and the information about the layered structure of the tensile test specimen, cross-sections with different micromechanical representations of the specimen are analyzed and compared with each other. This is done by linear elastic numerical simulations that are validated by experimental investigations. For the numerical simulation artificial microstructures are generated on the basis of the derived microstructural characteristics. Using these artificial microstructures, a numerical model is established and the Young's modulus is determined by simulating tensile tests. In addition, the Young's modulus is also experimentally obtained by nanoindentation. This allows one to reduce the three-dimensional

effects on the results and hence, to determine the near surface material properties [52]. Based on the results of the numerical and experimental investigations on the mesoscale the best approach is derived by taking also into account the aspect of computational costs. The selected approach is then used to expand the procedure to a representation of the material on the component level by taking into account the spatial distribution of the material properties induced by the microstructural characteristics. This is achieved by representing the components of the elasticity tensor by homogeneous second-order random fields. Therefore, the material properties are still modeled probabilistically and not deterministically. This also indicates that there is no scale transition to the macroscale. For the discretization of these fields the Karhunen-Loève expansion is used, which requires the determination of correlation functions first.

Finally, the influence of the probabilistic microstructure characteristics on material properties obtained on the component level is analyzed. This is done by simulating tensile tests on a numerical basis. Again the numerically obtained values for the Young's modulus are compared with experimental results. Consequently, this study gives a comprehensive analysis of a computational modeling approach for components made of SFRC by numerical simulation, that is validated by experimental investigations.

The structure of the presented work is as follows. Section II.2 gives a brief overview of the most important theoretical background including homogeneous second-order random fields, the Karhunen-Loève expansion for the discretization of random fields as well as the main aspects of the multi-scale modeling with respect to Hill's condition. In Section II.3 the different specimens used in this study are presented. This is followed by the extraction of the probabilistic characteristics from a micrograph in Section II.4. The numerical simulations and experimental investigations on the mesoscale and the impact of the resulting microstructural characteristics on the component level are shown in Section II.5 and Section II.6, respectively. Finally, Section II.7 gives a summary and a conclusion of the presented work.

II.2 Karhunen-Loève expansion

II.2.1 Second-order random fields

Among others probabilistic quantities are described by random variables $Z(\omega)$. A realized value, e.g. of a material parameter, is denoted by z . In context of random fields $Z(\omega, \mathbf{x})$ the random variables are also assigned to spatial coordinates \mathbf{x} . For the synthesis of random fields by using the Karhunen-Loève expansion, it is necessary that the variance of the random field as well as the random variable are finite. In this case the following definition for random fields holds

$$Z(\mathbf{x}) = Z(\omega, \mathbf{x}) \in L^2(\Omega; \mathbb{R}) \quad (\text{II.1})$$

and one speaks of second-order random fields [13]. Their main properties are briefly presented below.

Random fields are characterized by moments of their probability distribution [169, 176]. In general, the n -th moment of a single random variable Z is defined as

$$\mathbb{E}[Z^n] = \int_{-\infty}^{\infty} z^n f_Z(z) \, dz, \quad (\text{II.2})$$

where $f_Z(z)$ is the probability density function. Based on this definition the first moment of a random field, also called expected value, is given by

$$\mathbb{E}[Z(\mathbf{x})] = \mu_Z(\mathbf{x}) = \int_{-\infty}^{\infty} z(\mathbf{x}) f_Z(z, \mathbf{x}) \, dz. \quad (\text{II.3})$$

The mean square of $Z(\mathbf{x})$ is given by the second moment. Besides these two moments central moments with respect to the expected value are introduced. The deviation of a value to the expected value is given by the second central moment, also known as the variance. Reformulating Equation (II.2) provides the definition for

the variance of a random field $Z(\mathbf{x})$

$$\text{Var}[Z(\mathbf{x})] = \int_{-\infty}^{\infty} z(\mathbf{x})^2 f_Z(z, \mathbf{x}) dz - \mu_z(\mathbf{x})^2. \quad (\text{II.4})$$

In addition, the standard deviation is often used, which is derived from the variance by

$$\sigma_Z(\mathbf{x}) = \sqrt{\text{Var}[Z(\mathbf{x})]}. \quad (\text{II.5})$$

Hence, the expected value as well as the variance are functions of the spatial coordinates \mathbf{x} . However, in case of a homogeneous random field both the expected value and the variance become constants [176].

The observation of a random field at different locations \mathbf{x}_i is described by corresponding random variables $Z = Z_i$. Besides the relation between an observation and the expected value of the random field the relation between observations at different points of a random field is of great interest. This relation is expressed by the covariance and reads for two random variables Z_1 and Z_2

$$\text{Cov}[Z_1, Z_2] = E[Z_1 Z_2] - \mu_1 \mu_2. \quad (\text{II.6})$$

Usually this expression is reduced to a dimensionless correlation parameter ρ_{12} by dividing Equation (II.6) by σ_1 and σ_2

$$\rho_{12} = \rho_{Z_1, Z_2} = \frac{\text{Cov}[Z_1, Z_2]}{\sigma_1 \sigma_2}. \quad (\text{II.7})$$

Equations (II.6) and (II.7) are referred to as the auto-covariance and auto-correlation, respectively, if Z_1 and Z_2 are part of the same random field $Z(\mathbf{x})$. Otherwise, Equations (II.6) and (II.7) are the cross-covariance and cross-correlation, respectively.

Since the probability density function is unknown for most times the random field is represented by a discrete number of realizations ω_i [132]. In this case the mean of the discrete values

$$\overline{Z(\mathbf{x})} = \frac{1}{N} \sum_{i=1}^N Z(\omega_i, \mathbf{x}) \quad (\text{II.8})$$

is used as expected value of the random field. In addition, the variance is rewritten as

$$s^2(\mathbf{x}) = \overline{Z(\mathbf{x})^2} - \overline{Z(\mathbf{x})}^2. \quad (\text{II.9})$$

Finally, the dimensionless correlation coefficient for two random variables Z_1 and Z_2 is given by

$$\rho_{Z_1, Z_2} = \frac{[\overline{Z_1 - \overline{Z_1}}][\overline{Z_2 - \overline{Z_2}}]}{s_1 s_2}. \quad (\text{II.10})$$

II.2.2 Auto-correlated random fields

The Karhunen-Loève expansion is a generalization of the Fourier transform to probabilistic processes. A commonly used formulation for the expansion of a stochastic process $X(\omega, \mathbf{x})$ is given by [25]

$$X(\omega, \mathbf{x}) = \sum_{n=0}^{\infty} \sqrt{\lambda_n} \phi_n(\mathbf{x}) Z_n(\omega), \quad (\text{II.11})$$

where Z_n are a set of uncorrelated random variables and λ_n and $\phi_n(\mathbf{x})$ are an eigenpair of a Fredholm integral equation of the second kind. The derivation of the integral equation is briefly summarized below by using the analogy to the Fourier transform as done in [108]. Hence, stochastic processes $X(\mathbf{x})$ are represented by a series

expansion of orthonormal functions $\phi_n(\mathbf{x})$ as

$$X(\omega, \mathbf{x}) = \sum_{n=1}^{\infty} Z_n \phi_n(\mathbf{x}). \quad (\text{II.12})$$

With this series expansion the position-dependent part is separated from the probabilistic component of the stochastic process, where the functions $\phi_n(\mathbf{x})$ are orthonormal. Furthermore, it is beneficial to split the random field additively into a deterministic and a stochastic field. This separation can be written as

$$\begin{aligned} Z(\omega, \mathbf{x}) &= \mu(\mathbf{x}) + \alpha(\omega, \mathbf{x}), \\ &= \mu + X(\omega, \mathbf{x}) \end{aligned} \quad (\text{II.13})$$

where the mean of the random field $\mu(\mathbf{x})$ represents the deterministic part and $\alpha(\omega, \mathbf{x})$ gives a random field with an expected value of zero. Due to this separation the expected value of the series expansion $\mathbb{E}[X(\mathbf{x})]$ and the expected value of the random variables Z_n equal zero. In addition to the expected value the variance of the random variable is given by

$$\sigma_{Z_n}^2 = \mathbb{E}[Z_n^2] = \lambda_n > 0 \quad (\text{II.14})$$

In context of random variables orthogonality is equivalent to independent and uncorrelated random variables, respectively. In this case the covariance reads for values of the same homogeneous random field $X(\mathbf{x})$ at the two locations \mathbf{x} and \mathbf{x}'

$$\text{Cov}[X(\mathbf{x}), X(\mathbf{x}')] = \mathbb{E}[X(\mathbf{x})X(\mathbf{x}')] - \mu\mu' \quad (\text{II.15})$$

Introducing $\mu = 0$ and the independence of the random variables leads to

$$\mathbb{E}[X_m(\mathbf{x})X_n(\mathbf{x}')] = \lambda_n \delta_{mn}. \quad (\text{II.16})$$

In addition, combining the series expansion in Eq. (II.12) with the orthogonality provides

$$Z_n = \int_0^x X(\mathbf{x}) \phi_n(\mathbf{x}) d\mathbf{x} \quad (\text{II.17})$$

for the random variables, where $\phi_n(\mathbf{x})$ are the eigenfunctions of the auto-correlation. The corresponding eigenvalues are given by λ_n . Therefore, before generating random fields by using the Karhunen-Loève expansion the auto-correlation must be determined. Expressing $X(\mathbf{x})$ and $X(\mathbf{x}')$ by using Eq. (II.12) and taking into account the independence of the random variables the auto-correlation is written as

$$\mathbb{E}[X(\mathbf{x})X(\mathbf{x}')] = \sum_{m=1}^{\infty} \phi_m(\mathbf{x}) \phi_m(\mathbf{x}') \lambda_m \quad (\text{II.18})$$

which leads finally to the following eigenvalue problem

$$\int_0^X \text{Cov}[Z_1, Z_2] \phi_n(\mathbf{x}) d\mathbf{x} = \sum_{n=1}^{\infty} \lambda_n \phi_n(\mathbf{x}'). \quad (\text{II.19})$$

For a known correlation function the eigenvalues λ_n and eigenfunctions $\phi_n(\mathbf{x})$ can be calculated by solving the Fredholm integral equation of the second kind in Eq. (II.19). A closed solution is only possible for a few correlation functions. One example here is the exponential correlation function, which is given for homogeneous random fields by [47, 128, 169]

$$\text{Cov}[X(\mathbf{x}), X(\mathbf{x}')] = \sigma(\mathbf{x})\sigma(\mathbf{x}') \exp\left(-\frac{|\mathbf{x}_i - \mathbf{x}'_i|}{b_i}\right), \quad (\text{II.20})$$

with the correlation length b_i . An important property is the multiplicative decomposition of the different directions, which is used for the generation of two-dimensional random fields, as shown in Section II.2.3.

Introducing the correlation function the eigenvalue problem in Eq. (II.19) is rewritten for a one-dimensional field $[-l, l]$ as

$$\int_{-l}^l \exp\left(-\frac{x-x'}{b}\right) \phi_n(x') dx' = \sum_{n=1}^{\infty} \lambda_n \phi_n(x). \quad (\text{II.21})$$

The solution of this eigenvalue problem is given by [169]

$$\lambda_i = \frac{2b}{1 + \omega_i^2 b^2} \quad (\text{II.22})$$

$$\phi_i = \alpha_i \cos \omega_i x \quad (\text{II.23})$$

with

$$\alpha_i = \frac{1}{\sqrt{l + \frac{\sin 2\omega_i l}{2\omega_i}}} \quad (\text{II.24})$$

for odd i and

$$\lambda_i = \frac{2b}{1 + \omega_i^2 b^2} \quad (\text{II.25})$$

$$\phi_i = \alpha_i \sin \omega_i x \quad (\text{II.26})$$

with

$$\alpha_i = \frac{1}{\sqrt{l - \frac{\sin 2\omega_i l}{2\omega_i}}} \quad (\text{II.27})$$

for even i . The values of ω_i are obtained by solving

$$\frac{1}{l} - \omega_i \tan \omega_i l = 0 \text{ in } \left[(i-1)\frac{\pi}{l}, (i-\frac{1}{2})\frac{\pi}{l} \right] \quad (\text{II.28})$$

and

$$\frac{1}{l} \tan \omega_i l + \omega_i = 0 \text{ in } \left[(i-\frac{1}{2})\frac{\pi}{l}, i\frac{\pi}{l} \right] \quad (\text{II.29})$$

for odd and even values of i , respectively.

The computational solution of Eqs. (II.28) and (II.29) is not trivial since the range boundaries are poles with a transition from a positive to a negative sign. Usually, algorithms for the determination of zeroing are based on a sign transition. However, precision limitations may lead to an inaccurate evaluation of the boundary values. Therefore, these algorithms require a manually defined offset to ensure a correct calculation of the zeroing, see Figure II.1. In [25] a different approximation for ω_i is given with

$$(\omega_i - c_i^2) \tan(\omega_i l) - 2c_i \omega_i = 0. \quad (\text{II.30})$$

This approach does not require a case differentiation between odd and even values of i . However, the problem regarding the sign transition at poles is still not solved, resulting in a missing sign transition. Therefore, in this work a further approach for a robust determination of zeroing is achieved by multiplying Eqs. (II.28) and (II.29). In this case there is no sign transition at the poles but within the interval for the determination of ω . Hence, a

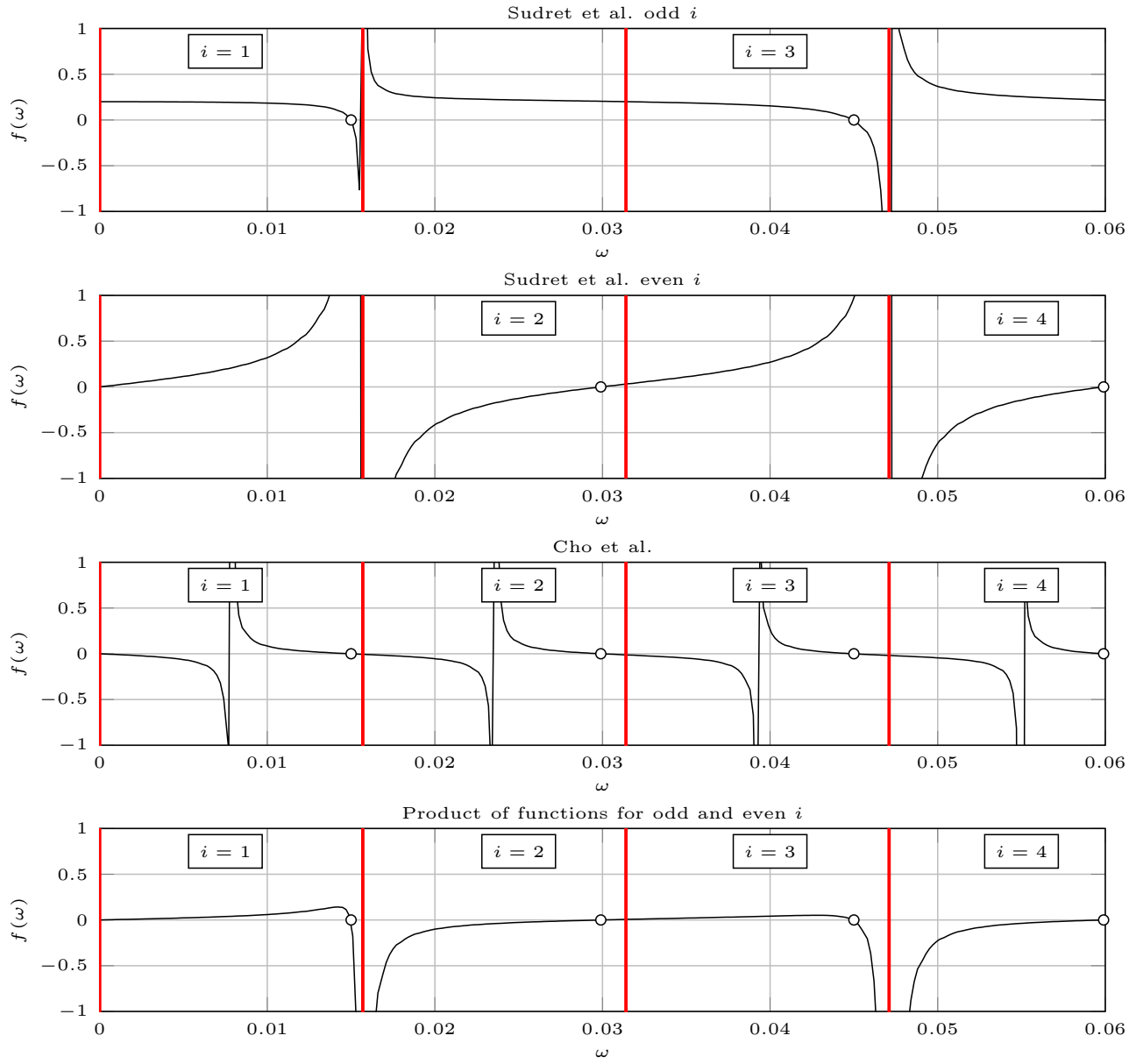


Figure II.1: Evaluation of the transcendental equation for ω_i .

manually defined offset is no longer necessary. Figure II.1 shows a comparison of the different approaches, for a correlation length of $b = 5$ mm and a field length of $l = 200$ mm.

II.2.3 Two-dimensional random fields

Applying random fields to problems in the field of mechanical engineering mostly requires the representation of two-dimensional or even three-dimensional components. The Karhunen-Loève expansion is adapted to two-dimensional components by separating the correlation structure of the different directions following the multiplicative decomposition of the correlation functions. Hence, the two-dimensional eigenfunctions and eigenvalues are expressed by the product of the eigenfunctions and eigenvalues of each direction

$$\phi_n(x_1, x_2) = \phi_i^1(x_1)\phi_j^2(x_2) \quad (\text{II.31})$$

and

$$\lambda_n = \lambda_i^1 \lambda_j^2. \quad (\text{II.32})$$

For a rectangular component of the dimension $l_1 \times l_2$ and an exponential correlation function this leads to [48]

$$\lambda_i^1 \lambda_j^2 \phi_i^1(x_1)\phi_j^2(x_2) = \int_{-\frac{l_1}{2}}^{\frac{l_1}{2}} \exp\left(-\frac{|x_1 - x'_1|}{b_1}\right) \phi_i^1(x'_1) dx'_1 \int_{-\frac{l_2}{2}}^{\frac{l_2}{2}} \exp\left(-\frac{|x_2 - x'_2|}{b_2}\right) \phi_j^2(x'_2) dx'_2 \quad (\text{II.33})$$

with the individual solution of each direction

$$\lambda_i^1 \phi_i^1(x_1) = \int_{-\frac{l_1}{2}}^{\frac{l_1}{2}} \exp\left(-\frac{|x_1 - x'_1|}{b_1}\right) \phi_i^1(x'_1) dx'_1 \quad (\text{II.34})$$

and

$$\lambda_j^2 \phi_j^2(x_2) = \int_{-\frac{l_2}{2}}^{\frac{l_2}{2}} \exp\left(-\frac{|x_2 - x'_2|}{b_2}\right) \phi_j^2(x'_2) dx'_2, \quad (\text{II.35})$$

respectively. The eigenvalues and eigenfunctions of these two individual equations are identical to the those presented in Section II.2.2.

II.2.4 Apparent material properties

One technique to extract the relation between information of different locations \mathbf{x}_i is the moving window method [8, 51]. Within this method a window of predefined size is used to extract segments of a larger microstructure. For these extractions the material properties are determined by numerical simulation. With the material properties available at different locations the correlation functions are obtained by a curve fit.

The numerical simulations for the determination of the material properties are conducted in accordance with Hill's condition [69]

$$\langle \boldsymbol{\sigma} : \boldsymbol{\epsilon} \rangle = \langle \boldsymbol{\sigma} \rangle : \langle \boldsymbol{\epsilon} \rangle. \quad (\text{II.36})$$

This procedure ensures the correct calculation of the effective material properties.

For a RVE [70] the homogeneous material properties are written as

$$\langle \boldsymbol{\sigma} \rangle = \mathbb{C}^{\text{eff}} : \langle \boldsymbol{\epsilon} \rangle \quad (\text{II.37})$$

and

$$\langle \boldsymbol{\epsilon} \rangle = \mathbb{S}^{\text{eff}} : \langle \boldsymbol{\sigma} \rangle \quad (\text{II.38})$$

respectively. Here, \mathbb{C}^{eff} and \mathbb{S}^{eff} are the effective stiffness and compliance tensor. The strains $\boldsymbol{\epsilon}$ and stresses $\boldsymbol{\sigma}$

hold information about the microstructure. In contrast to this $\langle \cdot \rangle$ gives the volume average, defined by

$$\langle \cdot \rangle = \frac{1}{V} \int_V \cdot dV. \quad (\text{II.39})$$

For the determination of the effective material properties among others the following two kinds of boundary conditions can be derived from Hill's condition. Based on the average strain theorem with linear elastic material properties as well as the average stress theorem [190] these boundary conditions read

$$\mathbf{u} = \boldsymbol{\epsilon}_0 \cdot \mathbf{x} \quad (\text{II.40})$$

and

$$\mathbf{t} = \mathbf{t}_0 \cdot \mathbf{x}, \quad (\text{II.41})$$

respectively. Here Eq. (II.40) holds a boundary condition of Dirichlet type, because only pure displacement boundary conditions with the constant macroscopic strain $\boldsymbol{\epsilon}_0$ are defined on the complete surface. In contrast to this Eq. (II.41) holds a boundary condition of Neumann type, since only pure traction boundary conditions, with a constant macroscopic stress \mathbf{t}_0 are defined on the complete surface. In case of a RVE the material properties obtained for these two boundary conditions are equal and hence, the material is assumed to be homogeneous. If the used volume is smaller than the RVE one speaks of apparent overall properties [66, 67, 81]. To determine these properties, the same procedure is used as for the effective material properties. However, in this case the results depend on the size of the extracted volume as well as the boundary conditions. Such kind of extraction on the mesoscale is referred to as a statistically volume element (SVE) [130].

II.3 Specimen specification

Figure II.2 gives an overview of all specimens and their orientations used in this research. The raw material of the conducted analyses is a polybutylenterephthalat (PBT) filled with glass fibers. The fiber mass fraction is specified with 30% (PBT GF 30). The initial component is a plate with the dimensions of 300 mm x 300 mm x 3 mm fabricated by an injection mold process (1). With this plate a coordinate system is introduced that is used throughout the whole investigation. The main objective of this research is the implementation of a linear elastic numerical modeling procedure for the numerical simulation of components made of SFRC that provides not only the global material behavior but also information about the spatial distribution of the material properties on the mesoscale. This is done exemplary for a tensile test specimen. Therefore, in a first step tensile test specimens are cut out of the plate, while the orientation of the tensile test specimen coincides with the main flow direction of the melt front (2). The tensile test specimens are used to obtain the global Young's modulus on the component level in Section II.6.2 of the material for a validation of the presented procedure. As the numerical model should also conclude information about the material microstructure a cross-section is defined (3), for which the microstructural properties are determined based on a micrograph (4). The selected cross-section of 3.37 mm x 3 mm is parallel to the main flow direction and hence, coincide with the load direction of the tensile test in Section II.6.2 (2). By doing so, the cross-section is used to analyze the Young's modulus of the specimen's microstructure on a numerical basis in Section II.5.1 (5). Afterwards, the results are validated experimentally by nanoindentation in Section II.5.2. Here, the specimens are small cuboids, where one side of the cuboid is perpendicular to the micrograph cross-section (6). The surface of the plate is the second side. This allows one to conduct indentation tests in the main flow direction as well as in thickness direction of the plate and specimens, respectively. The cuboids have an edge length of 20 mm x 5 mm x 3 mm.

The numerical simulation on the component level assuming linear elastic material behavior refers to the same cross-section as the microstructural analysis. Here, the dimensions coincide with the standard measurement length of a tensile test specimen defined in [84]. Therefore, the edge length is 50 mm x 3 mm.

The material properties of the two components used for the numerical simulations are provided in Table II.1

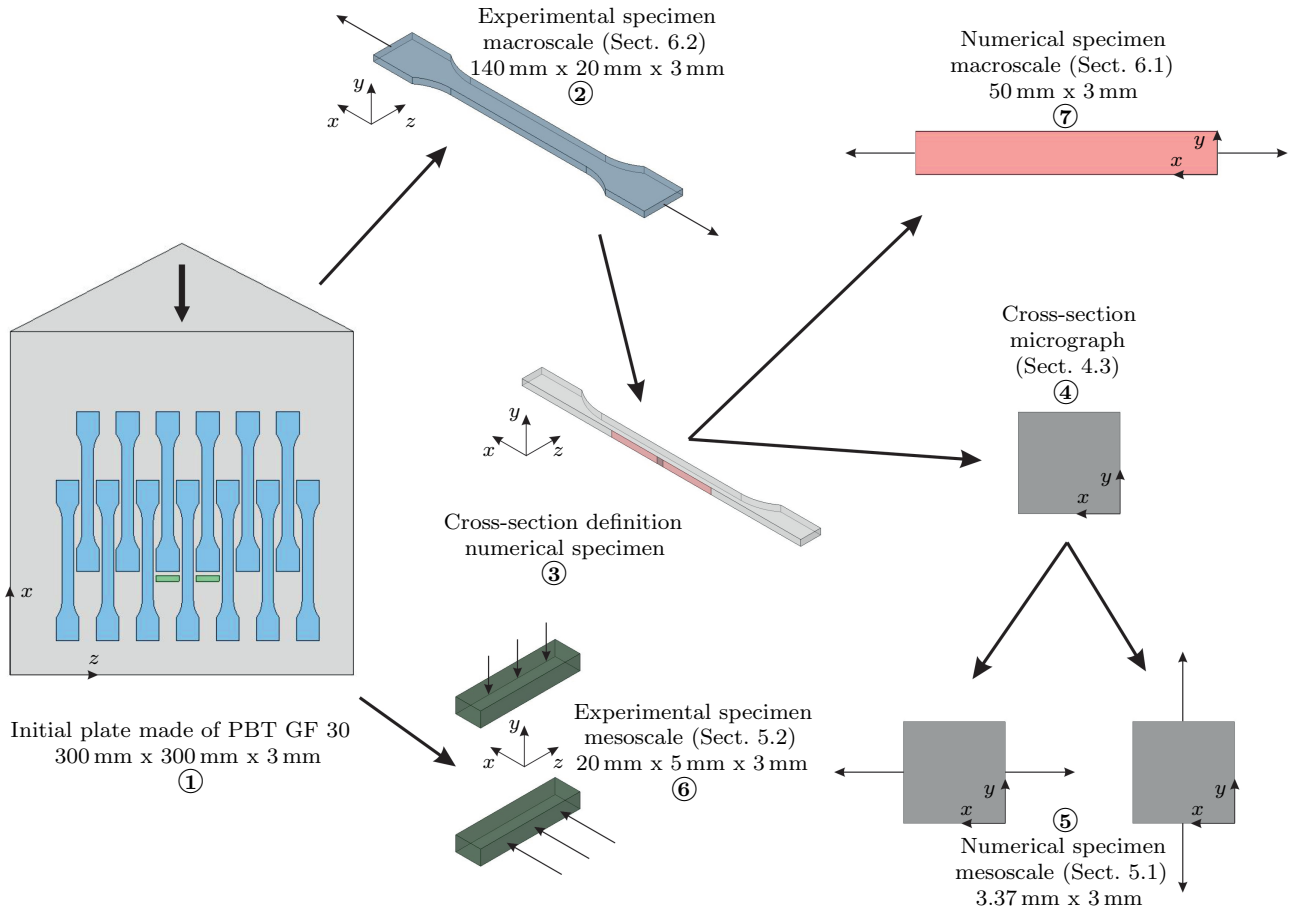


Figure II.2: Specification of the experimental and numerical specimens.

II.4 Extraction of the probabilistic characteristics

II.4.1 Theoretical description of the fiber orientation

The orientation of a single fiber is expressed by the unity vector \mathbf{p} , that points in the direction of the fiber axis as shown in Figure II.3. The components of this vector are expressed by the angles introduced in Figure II.3 as [100, 158]

$$\mathbf{p} = \begin{bmatrix} \sin \theta \cos \varphi \\ \sin \theta \sin \varphi \\ \cos \theta \end{bmatrix} \quad (\text{II.42})$$

	Young's modulus GPa	Poisson's ratio -	Density kg/m ³
Glass	72	0.22	2500
PBT	2.6	0.41	1300

Table II.1: Material properties of the fiber and matrix material.

To derive the orientation from the micrograph the components of the orientation vector are formulated in terms of the geometrical properties of the fiber cross-section. In this case the minor and major axis of the ellipse as well as its horizontal and vertical dimensions with respect to the coordinate system are used, which leads to the following expressions for the trigonometrical functions of φ

$$\sin \varphi = \frac{\Delta_h}{l_{ma}} \quad \cos \varphi = \frac{\Delta_v}{l_{ma}} \quad (\text{II.43})$$

and θ

$$\sin \theta = \sqrt{1 - \frac{l_{min}^2}{l_{ma}^2}} \quad \cos \theta = \frac{l_{min}}{l_{ma}}. \quad (\text{II.44})$$

Here Δ_h and Δ_v are the projection of the elliptic cross-section on the x - and y -axis, respectively. The parameters l_{min} and l_{ma} are introduced in Figure II.3.

For a group of fibers, the orientation is given by the second order orientation tensor \mathbf{A} introduced in [2] as

$$\mathbf{A} = \oint_S \Psi(\mathbf{p}) \mathbf{p} \mathbf{p}^T dS = \begin{bmatrix} A_{11} & A_{12} & A_{13} \\ A_{21} & A_{22} & A_{23} \\ A_{31} & A_{32} & A_{33} \end{bmatrix}. \quad (\text{II.45})$$

Here, $\Psi(\mathbf{p})$ is the probability density distribution function for the fiber orientation defined in [42] and S the surface of the unit square. In context of a component made by mold injection and with respect to the introduced coordinate system the elements on the diagonal represent a fiber orientation in the melt flow direction (A_{11}), perpendicular to the melt front (A_{33}), and in thickness direction (A_{22}). The sum of these three elements equals one [186]. With the fiber orientation vector defined in Eq. (II.42) the elements of the orientation tensor is written as

$$\begin{aligned} A_{ij} &= \langle p_i p_j \rangle \\ &= \begin{bmatrix} \langle \sin^2 \theta \cos^2 \varphi \rangle & \langle \sin^2 \theta \sin \varphi \cos \varphi \rangle & \langle \sin \theta \cos \theta \cos \varphi \rangle \\ \langle \sin^2 \theta \sin \varphi \cos \varphi \rangle & \langle \sin^2 \theta \sin^2 \varphi \rangle & \langle \sin \theta \cos \theta \sin \varphi \rangle \\ \langle \sin \theta \cos \theta \cos \varphi \rangle & \langle \sin \theta \cos \theta \sin \varphi \rangle & \langle \cos^2 \theta \rangle \end{bmatrix}. \end{aligned} \quad (\text{II.46})$$

In terms of the geometrical properties of the elliptic cross-section this leads to [158]

$$\begin{aligned} A_{ij} &= \langle p_i p_j \rangle \\ &= \begin{bmatrix} \langle \Delta_v^2 \left(\frac{1}{l_{ma}^2} - \frac{l_{min}^2}{l_{ma}^4} \right) \rangle & \langle \Delta_v \Delta_h \left(\frac{1}{l_{ma}^2} - \frac{l_{min}^2}{l_{ma}^4} \right) \rangle & \langle \Delta_v^2 \sqrt{\frac{1}{l_{ma}^2} - \frac{l_{min}^2}{l_{ma}^4}} \rangle \\ \langle \Delta_v \Delta_h \left(\frac{1}{l_{ma}^2} - \frac{l_{min}^2}{l_{ma}^4} \right) \rangle & \langle \Delta_h^2 \left(\frac{1}{l_{ma}^2} - \frac{l_{min}^2}{l_{ma}^4} \right) \rangle & \langle \Delta_h^2 \sqrt{\frac{1}{l_{ma}^2} - \frac{l_{min}^2}{l_{ma}^4}} \rangle \\ \langle \Delta_v^2 \sqrt{\frac{1}{l_{ma}^2} - \frac{l_{min}^2}{l_{ma}^4}} \rangle & \langle \Delta_h^2 \sqrt{\frac{1}{l_{ma}^2} - \frac{l_{min}^2}{l_{ma}^4}} \rangle & \langle \frac{l_{min}^2}{l_{ma}^2} \rangle \end{bmatrix}. \end{aligned} \quad (\text{II.47})$$

II.4.2 Methodology

For the numerical simulation of SFRC the probabilistic characteristics of the microstructure are required. In [158] a procedure is presented, that allows one to derive the second-order orientation tensor of the fibers from a micrograph. This procedure is adapted to obtain the probabilistic characteristics and their spatial distribution of the fiber length, diameter, and orientation as well as the second-order orientation tensor from a micrograph in this study. All presented results are based on a micrograph with a size of $3370 \mu\text{m} \times 3000 \mu\text{m}$ captured with a

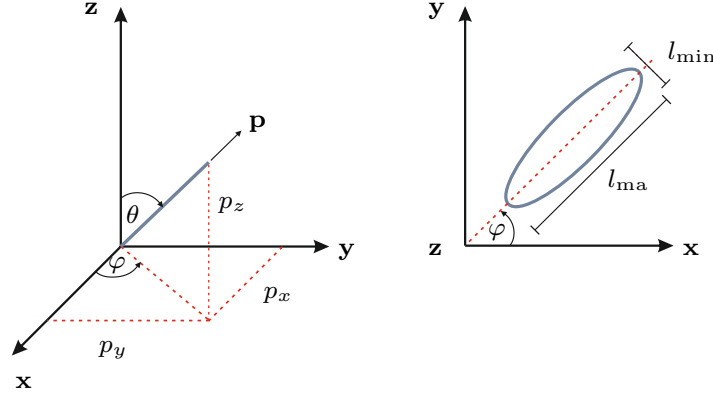


Figure II.3: Angle and cross-section definition for the description of the fiber orientation and fiber length, see also [59, 100, 158].

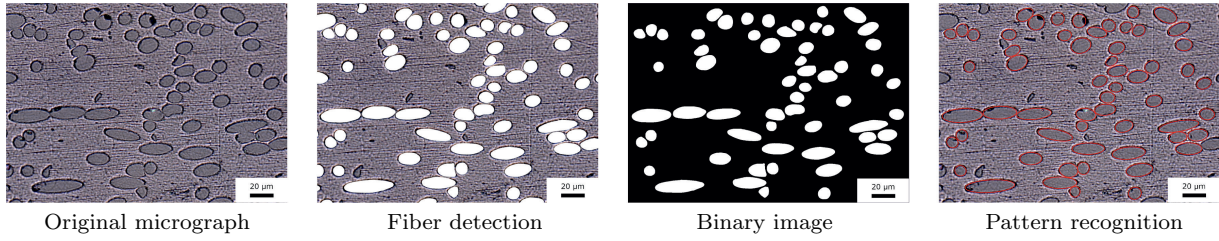


Figure II.4: Different stages of the image processing routine.

digital microscope KEYENCE VHX-5000. The panorama image is generated by stitching 323 individual images with a magnification of 1500. This leads to a resolution of 558 px per 100 μm . Hence, the procedure implies ergodicity for the extracted microstructural properties with respect to the manufactured plate with an edge length of 300 μm .

The main steps for the extraction of the probabilistic characteristics are depicted in Figure II.4. Based on the original micrograph first the fibers are detected before the image is transformed to a binary image. This binary image is then further processed with the image processing toolbox of Matlab[®]. Using the function *regionprops* the orientation, centroid as well as major and minor axes of each ellipse are determined. With these values the elements of the orientation tensor A_{ij} given in Eq. (II.47) are calculated.

II.4.3 Probabilistic characteristics

II.4.3.1 General results

For the determination of the probabilistic characteristics only fibers are taken into account that are within the boundaries of the micrograph. Fibers reaching over the micrograph edges are neglected since a correct determination of the major axis is not possible. In total 9721 fibers are detected within the micrograph cross-section. Below the results of the main fiber characteristics like fiber length (major axis), fiber diameter (minor axis), fiber orientation, and fiber volume fraction as well as their spatial distribution are discussed. Figure II.5 a) shows the spatial distribution of the obtained fiber length. As the probability of detection for a single fiber depends strongly on the orientation of the fiber, in [158] a procedure is proposed that weights the fiber length with respect to its probability of detection. It is assumed, that fibers parallel to the micrograph cross-section are less likely to be detected in a micrograph than fibers perpendicular to it. In context of the presented framework this component of the fiber orientation is given by the angle θ as defined in Figure II.3

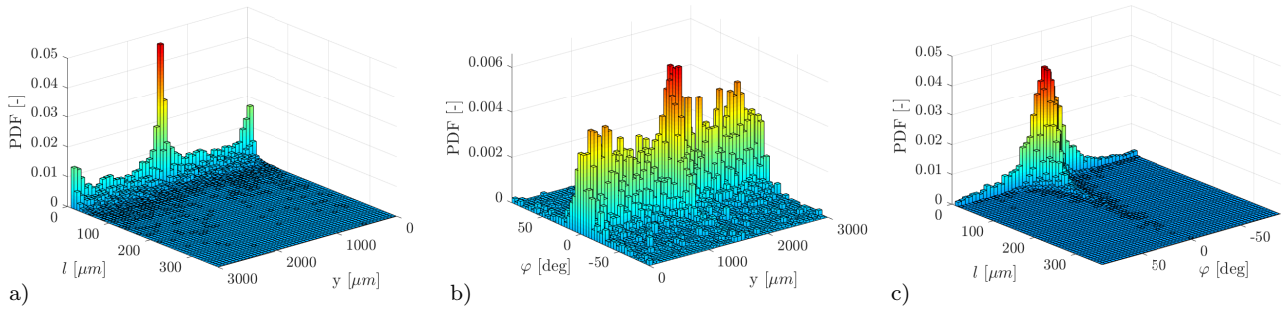


Figure II.5: Results of the fiber length, fiber orientation, as well as correlation between fiber length and fiber orientation based on the micrograph.

and Eq. (II.44). Using this angle the weighting factor is given by [158]

$$w_i = \frac{1}{\cos \theta} = \frac{l_{\text{ma}}}{l_{\text{min}}}. \quad (\text{II.48})$$

The results given in Figure II.5 a) already include the weighting. Even then a profuse amount of short fibers with a length of less than 20 μm is indicated. This is also supported by a mean fiber length of 46.6 μm. Besides this, the results lead to the conclusion of a layered structure due to the mold injection process as shown in [19, 41, 43, 46, 113, 154]. This is discussed more in detail in Section II.4.3.2.

Next is the fiber orientation φ , that describes the angle between the major axis of the ellipse and the horizontal axis as shown in Figure II.3. The results are depicted in Figure II.5 b). Again the distribution is plotted against the specimen thickness coordinate. The distribution clearly shows a preferred orientation of the fibers along the specimen and therefore, with the melt flow direction. In contrast to the fiber length, the orientation is independent of the location of the fiber. The preferred orientation of the fibers and therefore, an orientation dependence of the material properties of the compound with respect to the overall specimen orientation is further confirmed by the correlation analysis of the fiber length and the fiber orientation. With an increasing fiber length, the fiber orientation shows a decreasing spreading around an orientation angle of 0°, see Figure II.5 c).

The overall results of the fiber diameter are given in Figure II.6. The probability density function of the fiber diameter meets the expectation of a normal distribution with a mean of 9.6 μm. Compared to the results of other studies this value appears a little bit low. Usually, the diameter of glass fibers is approximated with 10 μm [58]. The fiber diameter corresponds with the minor axis of the pattern recognition results. If the fibers are cut perpendicular to the fiber length these two magnitudes coincide very well. Only if the fiber is almost parallel to the micrograph cross-section there might be a significant deviation. However, since the probability of detection of these fibers is small and there is no weighting considered for the fiber diameter the influence is neglectable. Another influence is more significant. As shown in Figure II.4 (left) there is a dark shadow between the fiber and the matrix material that cannot be clearly assigned to one of the two components. The difference between the inner and outer circle of the shadow is approximately 3 – 5 px. This leads to a deviation of up to 1 μm by a resolution of 0.18 μm per px in vertical and horizontal direction. Hence, the deviation of the obtained fiber diameter and the values taken from the literature can be assigned to this phenomenon.

Finally, the overall fiber volume fraction is 16.7%, which equals a fiber mass fraction of 28% based on the material properties provided in Table II.1. For the raw material a fiber mass fraction of 30% was specified. Therefore, the overall fiber mass fraction appears a little bit below the specification. The fiber mass and fiber volume fraction are connected by the density of the matrix and fiber material, respectively. The precise density of the two components is unknown and the data provided in Table II.1 are taken from literature, which usually gives only approximated values since the specific values vary between different charges. Taking these variations into account a fiber volume fraction of 16.7% leads to a fiber mass fraction in a range of 27% up to

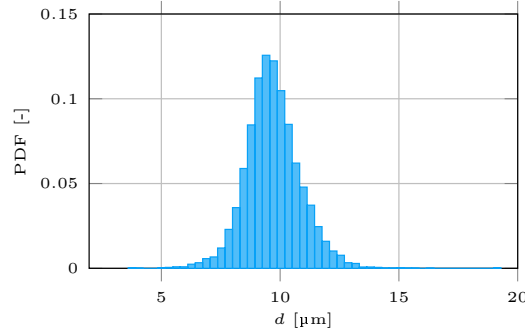


Figure II.6: PDF fiber diameter.

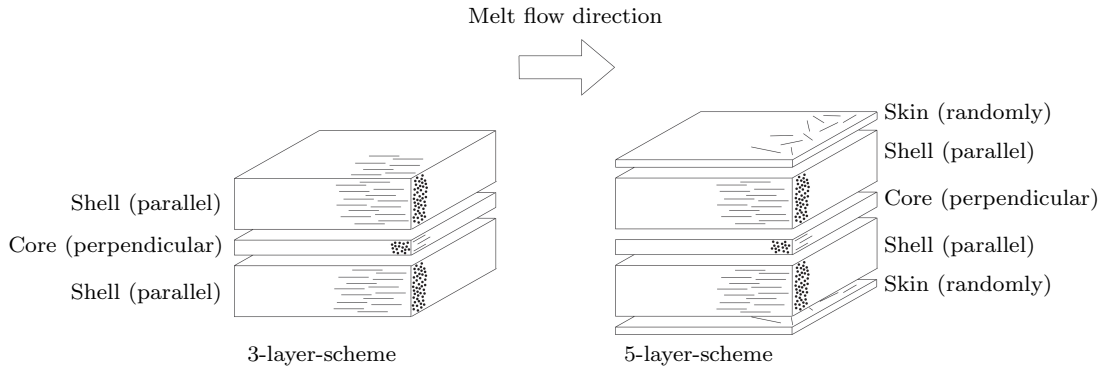


Figure II.7: Fiber orientation schemes due to mold injection process, compare [154].

30%, which meets the specifications.

II.4.3.2 Analysis of the layered structure

During the injection mold process, the fiber orientation varies over the specimen thickness due to different flow velocities and shear forces [95]. With respect to the fiber orientation the cross-section of the component made by mold injection is divided into different layers. Figure II.7 gives an overview of the two commonly used orientation schemes [19, 41, 43, 46, 113, 154].

The results of the fiber length distribution over the thickness indicates that the used specimen shows this kind of layered structure as well. To analyze the layered structure more in detail the components A_{11} and A_{33} of the orientation tensor introduced in Eq. (II.47) are calculated and plotted over the cross-section thickness. As discussed in Section II.4.1 the probability of detection of a fiber orientation parallel to the melt flow direction is given by A_{11} ($\varphi = 0^\circ$, $\theta = 90^\circ$). Perpendicular to the melt flow direction the probability is expressed by A_{33} ($\varphi = \theta = 0^\circ$). The results depicted in Figure II.8 confirm the assumption based on the fiber length distribution. Five individual layers are recognizable. Furthermore, the values of A_{11} and A_{33} indicate also that the orientation component in thickness direction A_{22} is small compared to the other two components. This supports the overall assumption of mainly horizontally aligned fibers, since high values of A_{22} would indicate vertically orientated fibers.

In the following sections a numerical modeling procedure for SFRC is presented. Since the main objective is the representation of the microstructural effects on the component level the layered structure must also be taken into account. Therefore, the layer thicknesses are determined based on the obtained orientation tensor as well as the distribution of the fiber length. The fiber length is an indirect measurement of the fiber orientation as short fibers with an almost circular cross-section are orientated perpendicular to the micrograph cross-section ($\theta = 0^\circ \rightarrow A_{33}$), whereas long fibers are parallel to the micrograph cross-section ($\theta = 90^\circ \rightarrow A_{11}$). Based on the results shown in Figure II.8 for the orientation tensor elements A_{11} and A_{33} as

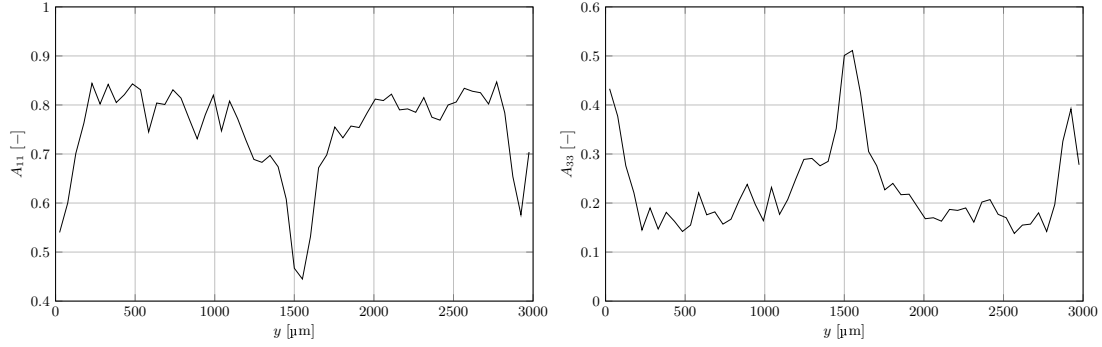


Figure II.8: Results for the elements A_{11} and A_{33} of the orientation tensor based on the micrograph.

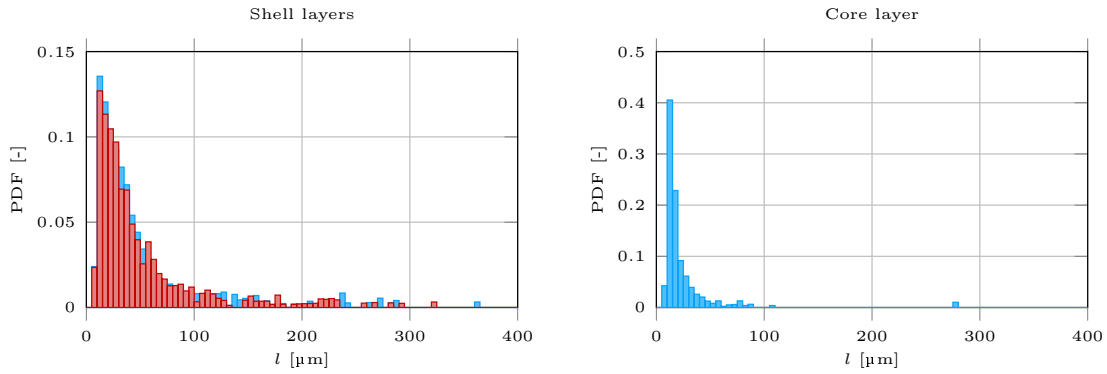


Figure II.9: Histogram of the fiber length for the shell and core layers.

well as the results for the fiber length distribution Figure II.5 a) the cross-section consists of five layers. The thickness of the skin layers at the top and bottom of the cross-section is approximated with $100\text{ }\mu\text{m}$, the core layer in the middle of the cross-section is $300\text{ }\mu\text{m}$ thick. Therefore, the shell layers between the skin and core layers have a thickness of $1250\text{ }\mu\text{m}$ each.

To determine the probabilistic characteristics of the numerical simulation in Section II.5 the layers are analyzed individually and the results are compared with each other. However, due to the limited number of fibers within the skin layers these are not taken into account. In Figure II.9 the histogram of the fiber length is shown for the two shell layers (left) and the core layers (right). The results of the two shell layers (colored in red and blue) coincide very well. Therefore, these two layers can be modeled using the same probabilistic characteristics for the fiber length.

The fiber diameter distribution is independent of the layer scheme as the fiber diameter is only minimally affected by the mold injection process. The main influence is the initial fiber production [58]. Therefore, no further analysis is conducted regarding the fiber diameter.

For the fiber orientation both aspects the information about the layer as well as the correlation with the fiber length as depicted in Figure II.5 b) and II.5 c) are taken into account. As already derived from Figure II.5 b) the fiber orientation distribution described by φ does not vary significantly between the different layers. However, as indicated in Figure II.5 c) the correlation between φ and the fiber length must be considered for the modeling of artificial SFRC microstructures.

The presented results seem to contradict the assumption of ergodicity of the micrograph at first, because the probabilistic characteristics of the fiber length depends on the spatial coordinates due to the layered structure of the cross-section. This means that the microstructural properties are no longer homogeneous or stationary, which implies that they cannot be ergodic. But as shown in Figure II.9 and discussed before the fiber length characteristics for the two analyzed shell layers show almost identical characteristics. The same holds for the orientation of the fibers as depicted in II.8. Based on this and the fact that the fiber diameter characteristics are

independent of the layered structure, each layer is assumed to be homogeneous and hence, layer-wise ergodic estimators appear appropriate.

II.5 Modeling on the mesoscale

In this section a procedure is introduced for the numerical modeling of SFRC on the mesoscale. The first approach is based on the micrograph used in Section II.4 to extract the probabilistic characteristics of the microstructure. This is followed by the use of artificial microstructures. Here, the numerical model still represents the microstructure and hence, shows the same probabilistic properties on the microscale as the micrograph.

II.5.1 Numerical simulations

II.5.1.1 Model description

The numerical model on the mesoscale represents the micrograph used in Section II.4 to extract the probabilistic properties of the microstructure. It has a rectangular shape with an edge length of $3370 \mu\text{m} \times 3000 \mu\text{m}$. The material definition and mesh generation follow the results presented in [145]. Therefore, the model is discretized by a mapped mesh consisting of second order Lagrange elements with an edge length of $10 \mu\text{m} \times 10 \mu\text{m}$ and the material properties are passed to the integration points by arrays that represent the underlying microstructure. In contrast to the results presented in [145] a plain strain state is assumed as the micrograph is a cross-section of a larger tensile test specimen. An overview of the specimen's geometry as well as the material properties of the two components are provided in Section II.3, Figure II.2 (3) and Table II.1.

For the numerical simulation of the tensile test, the horizontal displacement is fixed at the left edge and the vertical displacement is fixed at the lower edge of the numerical model. Two load cases are analyzed with this model. First a load of 100 MPa is applied at the right edge, second is a load of 100 MPa at the upper edge. Using these two load cases the Young's modulus in horizontal and vertical direction are obtained by extracting the horizontal (x) and vertical (y) displacement components at the right and upper edges, respectively. The Young's modulus is then calculated by

$$E_h = \frac{\sigma_r}{\langle u_h \rangle} l_h \quad \text{and} \quad E_v = \frac{\sigma_u}{\langle u_v \rangle} l_v, \quad (\text{II.49})$$

where the indices h and v represent the horizontal and vertical component and the indices r and u the right and upper edge, respectively. All numerical simulations are based on linear theory. Finite deformations are not taken into account.

II.5.1.2 Numerical simulation based on the micrograph

In a first step the material properties of the micrograph cross-section itself are analyzed. This is done by generating three different arrays, one for each material parameter. The arrays represent the micrograph cross-section with a resolution of $1 \mu\text{m} \times 1 \mu\text{m}$. This is in accordance with the findings in [145]. With these arrays the material properties are passed to the integration points.

Table II.2 contains the results of the mean strain as well as Young's modulus in horizontal and vertical direction.

II.5.1.3 Numerical simulation based on the artificial microstructure

Below the analyzed configurations, the generation process of the microstructure as well as the numerical results are presented

Direction	Mean strain %	Young's modulus GPa
Horizontal	1.597	6.26
Vertical	1.847	5.41

Table II.2: Results of the numerical simulation based on the micrograph.

Layer	Conf. I Homogeneous	Conf. II Shell layers	Conf. III Layered structure
1	0.28	0.28	0.28
2	-	-	0.33
3	-	-	0.28

Table II.3: Fiber mass fraction for each layer of the artificial microstructure.

Analyzed configurations

The analysis of the microstructure emanates from a layered structure of the cross-section. As presented in Section II.4.3.2 the cross-section can be divided into five layers. Based on this finding three different configurations are investigated here. With this approach the influence of the layered structure on the material properties is analyzed. This is important for the representation of the microstructure by random fields in Section II.6. The following, three different configurations are under investigation. (I) For the first configuration the probabilistic characteristics of the microstructural properties of the whole cross-section are used. This leads to some kind of homogenized material properties. (II) Next is the generation of an artificial microstructure based on the probabilistic characteristics of the microstructural properties of the shell layers only. Therefore, the influence of the skin layers as well as the core layer are neglected. (III) In a last step the core layer is taken into account as well. Therefore, in this case the numerical model consists of three different layers. As discussed in Section II.4.1 the probabilistic properties of the skin layers are not sufficient to derive the probabilistic characteristics of these layers. Due to this an artificial five-layer microstructure is not investigated. Furthermore, the representation of all layers contradicts a compact and cost saving approach of modeling SFRC.

Generation of the microstructure

The microstructure of the SFRC is generated in accordance with the procedure presented in [145]. In addition, the correlation between the fiber length and fiber orientation is taken into account. Hence, the generation of the microstructure comprises the following steps. First the fiber centroid is generated by a Monte Carlo sampling. If necessary, the coordinates are then assigned to one of the layers and the fiber length is sampled based on the corresponding layer characteristics. The layer identification is only required for configuration III, though. The overall characteristics are used to set a fiber diameter due to the missing correlation as shown in Section II.4.3. For the assignment of the fiber orientation however, the correlation with the fiber length is essential. Finally, the fiber is added to the preset area if there is no overlap with an already existing fiber. The procedure is repeated until a predefined fiber volume fraction is reached. Since the fiber volume fraction of the different layers are not equal, the threshold varies for each configuration and the different layers. Table II.3 gives an overview of the fiber mass fraction for each configuration and layer. In Figure II.10 the shell layers of the microstructure and an artificial microstructure are mapped one above the other. There are no major differences between the images recognizable.

The generated microstructures are analyzed in the same way as the numerical model of the micrograph.

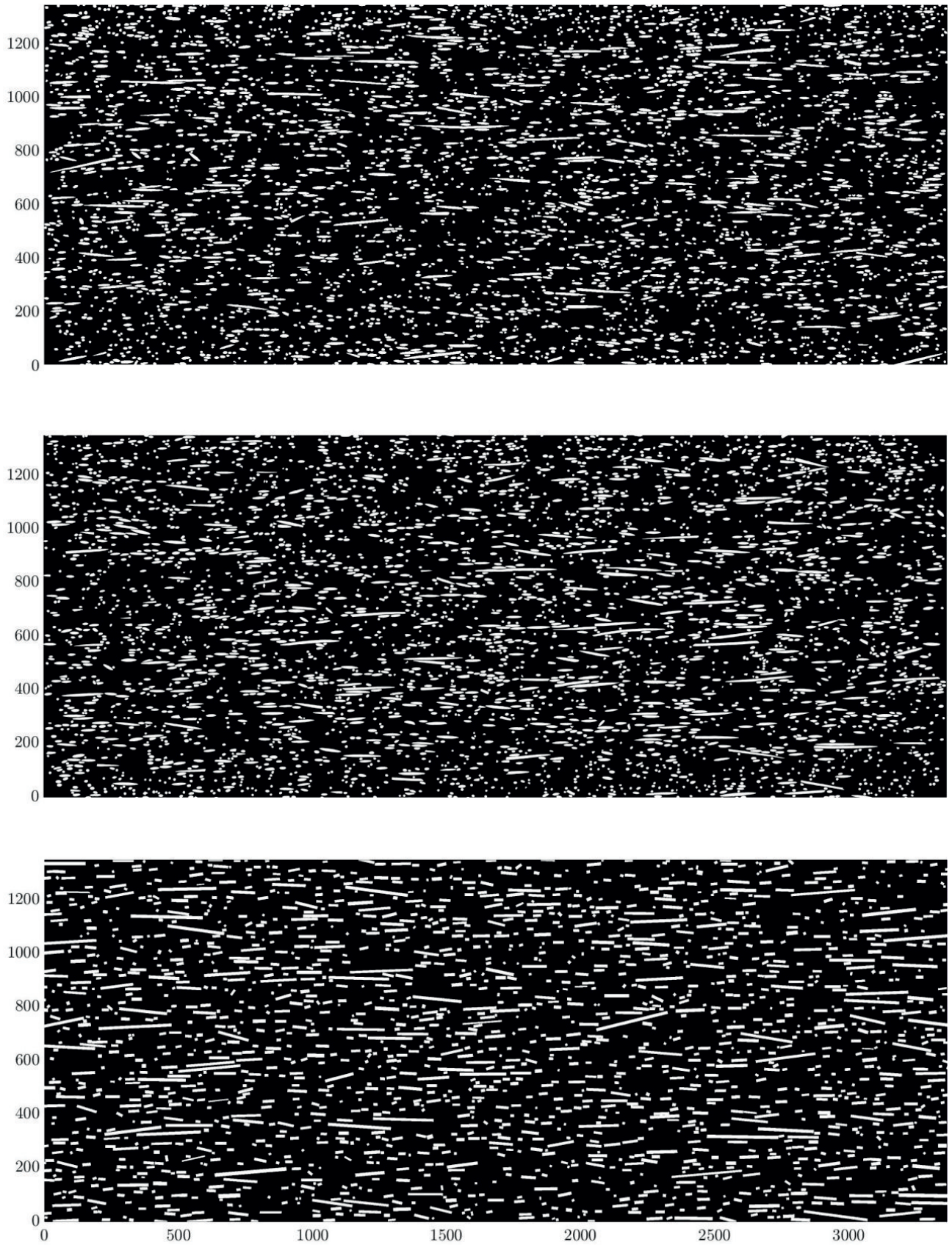


Figure II.10: Comparison of shell layers of the micrograph (upper two images) and an artificial microstructure (lower image). All measures in μm .

Value	Unit	Conf. I Homogeneous	Conf. II Shell layers	Conf. III Layered structure	Micrograph
E_h	GPa	5.94 ± 0.04	6.09 ± 0.04	6.12 ± 0.04	6.26
Dev. to micrograph	%	5.11	2.72	2.24	-
Dev. to Conf. II	%	2.46	-	0.49	2.79
E_v	GPa	4.97 ± 0.01	5.03 ± 0.01	5.09 ± 0.01	5.41
Dev. to micrograph	%	8.13	7.02	5.91	-
Dev. to Conf. II	%	1.19	-	1.19	7.55

Table II.4: Results of the numerical simulation based on the artificial microstructures.

Instead of the micrograph cross-section the arrays represent now the artificial microstructure. For statistical reasons the simulation is done for 500 different microstructures of each configuration.

Results of the numerical simulation

Table II.4 gives an overview of the numerical results for the artificial microstructures. In addition to the mean value and standard deviation of the Young's modulus for the horizontal and vertical direction the deviation to the results of the micrograph are calculated. The results of the artificial microstructures meet the results based on the micrograph within a maximal deviation of 5% for the horizontal and 8% for the vertical direction. In both directions the highest deviations are observed for configuration I, where the different layers and their probabilistic characteristics are not distinguished. The deviation to the micrograph decreases for configuration II and III. The impact of modeling three different layers instead of only one is marginal compared to the computational costs. Hence, it appears to be convenient to reduce the modeling of the microstructure to the shell layers for the determination of the correlation structure, that is required for the numerical simulation on the component level in Section II.6. This assumption is verified experimentally first. Furthermore, the numerical results indicate only a minor anisotropy of the material. This can be assigned to the derived aspect ratio of 4.9 based on the mean values of the fiber length and fiber diameter.

II.5.2 Experimental validation

The results of the numerical simulation presented in Section II.5.1 are verified by an experimental investigation of the Young's modulus based on the material, that was characterized in Section II.4. As the presented results and the probabilistic characteristics of the material are based on a two-dimensional analysis of the cross-section the Young's modulus is experimentally determined by nanoindentation. Compared to standard tensile tests this procedure allows one to measure the near surface material properties [52] and hence, in combination with a projected indentation area of approximately $7000 \mu\text{m}^2$ characterize the material on the mesoscale.

II.5.2.1 Framework nanoindentation

For the experimental determination of the material properties by nanoindentation the slope of the force-displacement curve of the unloading process is calculated, see Figure II.11 (left). The indentation or reduced modulus is obtained by [125, 135]

$$E_r = \frac{dP}{dh} = \frac{1}{\beta} \frac{\sqrt{\pi}}{2} \frac{S}{\sqrt{A_p(h_c)}}, \quad (\text{II.50})$$

where S is the stiffness of the contact, A_p the projected area of the indentation tip for a contact depth h_c , and β an empirical correction factor of the indenter uniaxial symmetry when using pyramidal indenter [65, 173]. As

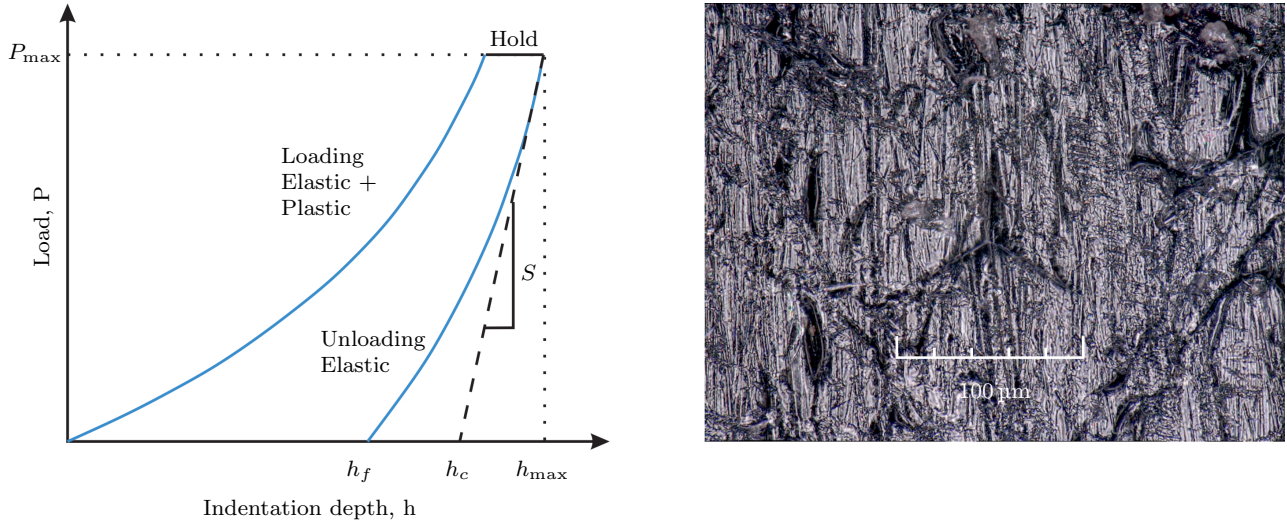


Figure II.11: Scheme load cycle nanoindentation [103, 171] (left), micrograph of the indentation location after unloading (right).

done in [93] β is set to one in this analysis. This is possible as the value of β usually varies between 1.02 and 1.08, which leads to a deviation of the indentation modulus of up to 3 % [125, 135]. The projected area of a perfectly sharp Berkovich tip, which is used in this study, is usually approximated by [35]

$$A_p = \pi h_c^2 \tan^2 \varphi = 24.5 h_c^2, \quad (\text{II.51})$$

with an effective semi-angle of $\varphi = 70.32^\circ$ [23]. Due to imperfections, a calibration of the projected surface is mostly used. For this calibration the projected surface is approximated with the function [125]

$$A_p(h_c) = 24.56 h_c^2 + C_1 h_c^1 + C_2 h_c^{1/2} + C_3 h_c^{1/4} + \dots + C_8 h_c^{1/128} \quad (\text{II.52})$$

In Figure II.11 (right) the indentation mark of a Berkovich tip is depicted. Finally, between the indentation modulus and the Young's modulus of the specimen material the following relation holds

$$E_r = \frac{1 - \nu^2}{E} + \frac{1 - \nu_i^2}{E_i}. \quad (\text{II.53})$$

Here, E_i and ν_i are the Young's modulus and Poisson's ratio of the indentation material, respectively. In this study the indentation tip is made of diamond with a Young's modulus of 1143 GPa and a Poisson's ratio of 0.0691 [91].

II.5.2.2 Setup and Results

For the experimental verification of the numerical simulation on the mesoscale the indentation modulus is measured at the surfaces of the cuboid. First is the measurement in x -direction. The measurement points are arranged in a grid of 37×9 points, that cover an area of $9000 \mu\text{m} \times 1600 \mu\text{m}$. Consequently, the distance between the measurement points is $200 \mu\text{m}$ in z - and $250 \mu\text{m}$ in y -direction, respectively. For this configuration the indentation modulus is measured with a maximum indentation force of 500 mN and 1500 mN. The results are given in Table II.5. The indentation modulus for both load cases match within the standard deviation. Hence, the indentation modulus is independent of the maximum indentation force in a range of 500 mN to 1500 mN. As in the numerical simulations, the indentation modulus is also determined experimentally in a second direction. Therefore, the indentation test is repeated in y -direction. Here only one load case is

Direction	Max. load mN	Indentation modulus GPa	Standard deviation GPa	Young's modulus GPa
Horizontal	500	6.78	1.07	5.84
(x - axis)	1500	6.93	0.73	5.97
Vertical	1500	4.95	0.44	-
(y - axis)				

Table II.5: Results of the indentation tests.

Direction	Analysis	Young's modulus GPa	Std. GPa	Dev. Mic. %	Dev. Exp. 1500 mN %
Horizontal (x - axis)	Micrograph	6.26	-	-	4.86
	Art. homogeneous (I)	5.94	0.04	5.11	0.50
	Art. shell layers (II)	6.09	0.04	2.72	2.01
	Art. layered structure (III)	6.12	0.04	2.24	2.51
	Nanoindentation 500 mN	5.84	1.07	6.60	2.18
	Nanoindentation 1500 mN	5.97	0.73	4.62	-
Vertical (y - axis)	Micrograph	5.41	-	-	9.29
	Art. homogeneous (I)	4.97	0.01	8.13	0.40
	Art. shell layers (II)	5.03	0.01	7.02	1.62
	Art. layered structure (III)	5.09	0.01	5.91	2.83
	Nanoindentation 1500 mN	4.95 ¹	0.44	8.50	-

Table II.6: Comparison of the experimental and numerical obtained results.

conducted with a maximum load of 1500 mN. The result is also provided in Table II.5.

In Table II.5 not only the results of the indentation tests are summarized, but also the calculated values of the Young's modulus are given. This is done by evaluating Eq. (II.53). For this the Poisson's ratio of the analyzed cross-section is obtained by using the analytical material model introduced by Halpin and Tsai [61, 62, 174] and the probabilistic characteristics provided in Section II.4.1. Besides a Poisson's ratio of 0.379 a Young's modulus of 6.21 GPa is calculated. As this value meets the numerical results of the micrograph with a deviation of less than 1 % for the Young's modulus, this Poisson's ratio is used to derive the material Young's modulus from the reduced modulus obtained by indentation in x -direction. However, the obtained Poisson's ratio for the correction in x -direction cannot be used for a correction in y -direction, because the assumption of transversally isotropic material behavior is not applicable for the analyzed cross-section. The main reason is the varying orientation of the fibers. This holds not only when considering the layered structure of the cross-section, but also when reducing the representation of the cross-section to the shell layers only. This conclusion is supported by the mismatch of the Young's modulus in x - and y -direction, as shown in Table II.4.

II.5.2.3 Comparison with numerical results

Table II.6 gives an overview of the experimentally and numerically obtained values of the Young's modulus on the mesoscale. For both directions the results of the numerical simulations meet the results of the experimental

investigation within the standard deviation. Consequently, the presented modeling approach on the mesoscale is verified by the conducted experiments. Furthermore, the reduction of the cross-section representation to the shell layers, as suggested in Section II.5.1.3, appears to be valid.

II.6 Modeling on the component level

So far the modeling process is based on the microstructural properties of the analyzed cross-section (see Section II.4) given by the mean and standard deviation of the fiber length, fiber diameter, and fiber orientation. The aim of this section is to provide a numerical modeling approach on the component level including the microstructural properties of short fiber-reinforced material.

This is done by representing the material properties by homogeneous random fields. Since random fields also involve information about local correlation between the realization at each point the correlation structure and correlation function are determined first. In this context the artificial microstructures, introduced in Section II.5 are used to derive the correlation functions of the elasticity tensor coefficients.

The procedure for the generation of the artificial microstructures for SFRC introduced in Section II.5.1 leads to almost identical mechanical properties as the microstructure of the micrograph of Section II.4.1. This is not only found on a numerical basis, but also verified experimentally by nanoindentation in Section II.5.2. Hence, in this section the procedure is used to expand the modeling approach to the component level.

A crucial issue for the representation of material properties is their positive nature. Since Gaussian random fields assume normal distributed underlying random variables, negative realizations are possible [47, 169]. Therefore, due to the elliptic property of the elasticity partial differentiation operator the use of Gaussian random fields for the representation of material properties is not suitable in context of multi-scale modeling of heterogeneous material [163]. Hence, the use of non-Gaussian random fields is required to ensure a stochastic solution of second-order and the positive nature of the elasticity coefficients, which is also state of the art [27, 54, 55, 97, 110, 172].

A non-Gaussian random field $M(\omega, \mathbf{x})$ is given by

$$M(\omega, \mathbf{x}) = \mathcal{G}\{X(\omega, \mathbf{x})\}, \quad (\text{II.54})$$

where \mathcal{G} is a non-linear mapping operator and $X(\omega, \mathbf{x})$ a centered, homogeneous Gaussian random field as introduced in Section II.2 [55]. In this study discretized random fields are used. Although the stochastic solution obtained here (using a Gaussian field) is not of second-order, computational (sample-wise) results may not be strongly impacted given the choice of model parameters and are thus presented below.

II.6.1 Numerical simulation

II.6.1.1 Correlation structure

As shown in Section II.2.1 to Section II.2.3 random fields describe the spatial distribution of random variables. The main characteristic is the correlation function which gives an information about the dependence of values at different locations. Hence, the correlation functions of the elasticity tensor elements must be determined first.

The correlation analysis is done in accordance with the procedure presented in [145] and hence, is based on the assumption of a SVE. As homogeneous second-order random fields are used to represent the material properties of a tensile test specimen, the correlation analysis as well as all remaining numerical simulations are based on the plain strain assumption. Using pure displacement and pure traction boundary condition as introduced in [188] the auto- and cross-correlation lengths of the elasticity tensor coefficients are calculated, respectively. Taking into account that the elasticity tensor coefficients for a plain strain state depend not only on the in-plane material properties but also on ν_{23} it is not possible to derive the engineering constants

¹Indentation modulus

Correlation function	Value	Unit	C_{11}	C_{12}	C_{22}	C_{66}
Exponential	b_1	μm	183.9	145.9	151.9	135
	b_2	μm	145.1	142.3	132.3	121.6
	RMSE	μm	0.08	0.11	0.06	0.06
Gaussian	b_1	μm	276.3	241.4	241.5	244.4
	b_2	μm	253.6	242.1	234.3	232.4
	RMSE	μm	0.07	0.05	0.08	0.10
Triangle	b_1	μm	165.6	137.5	138.1	129
	b_2	μm	128.2	132	122.6	106.5
	RMSE	μm	0.10	0.70	0.12	0.13

Table II.7: Results of the auto-correlation lengths of the elasticity tensor coefficients using different correlation functions and a window size of 250 μm .

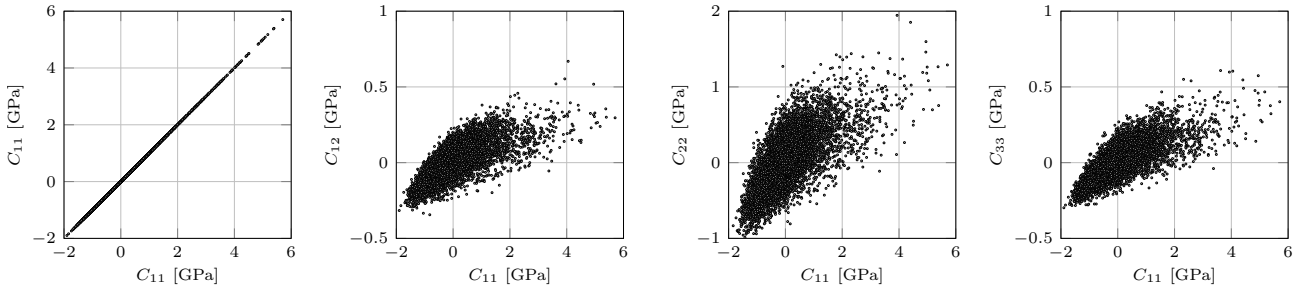


Figure II.12: Auto- and cross-correlation of the elasticity tensor elements.

from the elasticity tensor coefficients without any further assumption. Due to this the correlation structure is obtained for the elasticity tensor coefficients instead of the engineering constants. In a next step these parameters are used to describe the material properties of the composite on the component level.

Using the moving window method, the auto- and cross-correlation is analyzed for a window size of 250 μm , 500 μm , and 750 μm . As there are closed solutions for the Fredholm integral equation given in Equation (II.19) for an exponential, Gaussian and triangle correlation function the use of one of these kernels is preferable.

Table II.7 gives the results of the correlation lengths for these three correlation functions and the corresponding root mean square error (RMSE). The results indicate, that all correlation functions approximate the numerically obtained correlation behavior of the elasticity tensor coefficients within a RMSE of less than 1 μm . Due to the common use of the exponential correlation function in the literature [47, 128, 169, 181], this correlation function is selected for the following generation of random fields using the Karhunen-Loève expansion.

II.6.1.2 Generation of random fields

Independent of the correlation function the Karhunen-Loève expansion always assume a linear correlation between the parameters. For the numerical model of the elasticity tensor coefficients of SFRC this assumption is satisfied not only for the auto-correlation but also the cross-correlation, as shown in Figure II.12.

One main parameter for the accuracy and convergence of the expansion of random fields is the amount of considered eigenvalues and hence, the number of terms used in the Karhunen-Loève expansion. Moreover,

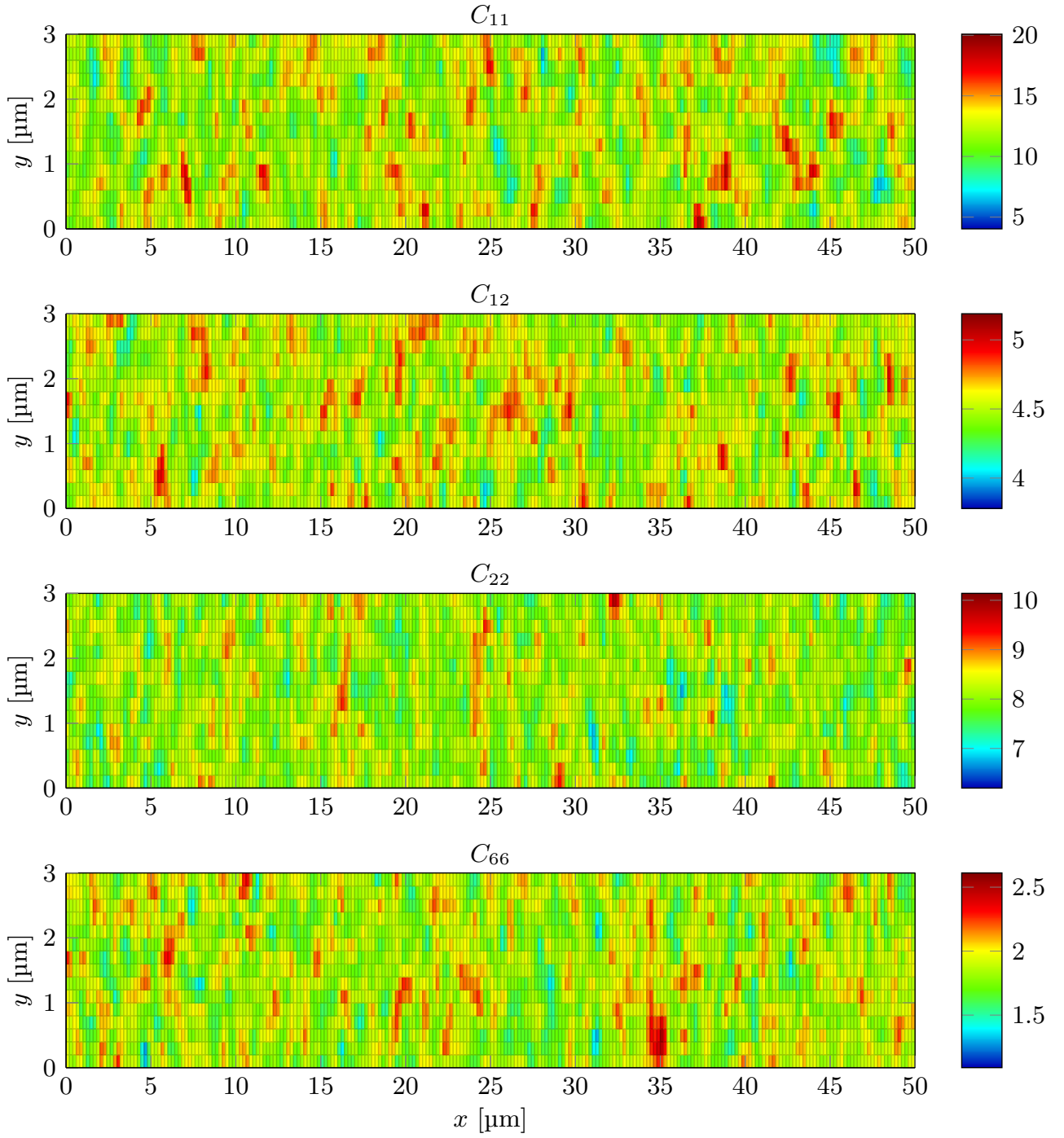


Figure II.13: A realization for the four independent elasticity coefficients for the modeling of the material properties of SFRC based on the correlation length derived from a window size of 250 μm and an exponential correlation functions. All values in GPa.

Elasticity coefficient	Mean value GPa	Standard deviation GPa	Minimal value GPa	Maximal value GPa
C_{11}	12.17	2.20	4.02	20.1
C_{12}	4.52	0.20	3.78	5.19
C_{22}	8.09	0.53	6.20	10.1
C_{66}	1.86	0.21	1.09	2.61

Table II.8: Results of the analysis of the exemplary random fields with respect to possible negative realizations due to the underlying Gaussian distribution.

the required amount of terms is strongly affected by the ratio of the correlation length and the dimension of the random field [78]. Low ratios coincide with highly correlated random fields, which allows one to reduce the terms of the Karhunen-Loève expansion to represent the random field. However, for large domains or small correlation lengths and hence, an increasing ratio, more terms should be considered. Since the ratio of the correlation length and observed area is considerably large in this study 3000 terms are used during the series expansion. This meets the magnitude of terms used in [189] for the numerical simulation of the wave propagation in thin-walled structures, which is also characterized by a weak correlated random field and hence, a large ratio of domain expansion to correlation length.

Figure II.13 shows examples of random fields for the elasticity tensor elements, that are not equal to zero, based on a window size of 250 μm and exponential correlation functions, when assuming a two-dimensional model and fiber reinforced material. As shown in [145] the symmetry property still holds.

As mentioned before, for the representation of the elasticity coefficients Gaussian random fields are used. This may lead to negative realization. To show, that in this case the use of Gaussian random fields is appropriate the generated fields are analyzed in detail. For this Table II.8 provides the mean values, the standard deviation, as well as the minimal and maximal values. For the generation of these exemplary random field the underlying distribution is not modified to avoid negative realizations. Due to the moderate standard deviation only positive results are calculated, even if a Gaussian distribution is used for the elasticity coefficients. Furthermore, the results of this analysis may be checked for plausibility. The minimal and maximal values can be explained by areas where almost no fiber is found and by areas with a relatively high fiber volume fraction, respectively. Cases where C_{11} is smaller than C_{22} the fiber can be assigned to a variation of the fiber orientation.

II.6.1.3 Numerical model

The numerical model for the analysis of the material properties of SFRC is based on a tensile test specimen. Since the standard observation length defined in [84] is 50 mm the specimen is represented by a rectangle with an edge length of 50 mm x 3 mm. Vertical and horizontal displacements are fixed on the left and lower edge of the rectangle, respectively. As done in Section II.5.1 100 MPa are applied on the right edge. Again all simulations are carried out assuming a plain strain state as well as linear theory.

For the determination of an adequate element size a convergence study is performed. This is done by increasing the number of elements in the vertical and horizontal direction until the variation of the resulting Young's modulus is less than 0.5%. The aspect ratio of the element is not affected by the convergence analysis and therefore, is fixed with a value of 1. Table ?? gives the results for the convergence analysis based on the Young's modulus. The element size is varied between an edge length of 200 μm up to 1 mm. Therefore, the smallest element size and hence, the distance between the integration points is comparable to the smallest correlation length. Based on the obtained mean value the results indicate that an element size of 1 mm x 1 mm is sufficient for the numerical simulation on the component level.

Compared to the obtained correlation length in Table II.7 the material information at the integration points

Elements x	Elements y	Edge length mm	Displacement u mm	Young's modulus GPa	Total dev. %	Step dev. %
50	3	1.00	0.785	6.373	0	-
100	6	0.50	0.785	6.352	0.33	0.33
150	9	0.33	0.785	6.347	0.41	0.08
200	12	0.25	0.785	6.345	0.44	0.03
250	15	0.20	0.785	6.343	0.46	0.03

Table II.9: Results of the convergence study for the element size of the numerical model on the component level.

Analysis	Result GPa	Standard Deviation GPa	Deviation experiment %
Experiment	9.75	0.27	-
250 KUBC	6.40	0.01	34.4
500 KUBC	5.87	0.01	39.8
750 KUBC	5.68	0.01	41.7
250 SUBC	4.04	0.01	58.6
500 SUBC	4.16	0.01	57.3
750 SUBC	4.20	0.01	56.9

Table II.10: Results of the experimentally obtained Young's modulus and deviation to the previous observations.

are independent of each other. This means that a Karhunen-Loève expansion is not stringently necessary to derive the random fields representing the material properties. The information can also be generated by a Monte Carlo sampling at each integration point. This circumstance allows one to neglect the cross-correlation between the elasticity tensor elements, that is provided in [145]. However, the auto-correlation and hence, the random fields used in this section to represent the material properties of the SFRC are still derived by Karhunen-Loève expansion. The simulations are carried out for all window sizes and boundary condition types used in Section II.6.1.1 to analyze the correlation structure.

II.6.1.4 Results

The results of the numerical analysis based on the microstructural characteristics derived from a two-dimensional micrograph are summarized in Table II.10. As expected the values based on an analysis with pure displacement boundary conditions (KUBC) decrease with an increasing window size whereas values based on pure traction boundary conditions (SUBC) increase with an increasing window size. This meets the multi-scale modeling approach with the Voigt and Reuss bounds [70] for a SVE. The very small standard deviation can be assigned to the element size, which has the same magnitude as the obtained correlation length.

II.6.2 Experimental validation

II.6.2.1 Experimental Setup

The numerical results are validated experimentally by a standard tensile test. The tensile test specimens have the dimensions of 140 mm x 20 mm x 3 mm as shown in Figure II.2 (2). As depicted in Figure II.2 the specimens are taken from a plate made by mold injection. The main orientation of the specimens coincides with the melt flow direction. In total 13 specimens are analyzed. To compare the results of the numerical simulation with the experimentally obtained values, the Young's modulus is determined for the linear elastic range. Therefore, the Young's modulus is calculated for a strain range of 0.05 % to 0.25 %. Based on the specimen geometry this equals a load range of 150 N to 750 N and is characterized by purely linear-elastic material behavior. The measurement length for the overall Young's modulus of a specimen is 45 mm.

II.6.2.2 Results and comparison

The results for the experimentally obtained Young's modulus is given in Table II.10. For a comparison with the numerical analyses the results of the modeling on the component level and their deviation to the experimental results are included as well. The results of the numerical simulation based on the probabilistic characteristics of the microstructure determined in Section II.4.1 show a significant deviation from the experimental results of 34.3 % up to 58.4 %. However, the numerical data matches the results of the simulation on the mesoscale very good. The Young's modulus in fiber direction is approximated on the mesoscale with 6 GPa in Section II.5. This meets the numerical simulation conducted here with a minimal deviation of 2.2 % for the correlation structure derived from a window size of 500 μm and pure displacement boundary condition. Therefore, the main reason for the significant deviation to the numerical simulation on the component level is assumed in the use of probabilistic characteristics of the microstructure obtained by a two-dimensional micrograph. This data is sufficient for numerical simulation of the material response on the mesoscale. However, for the representation of the material properties on the component level, which is done by the generation of homogeneous second-order random fields with the Karhunen-Loève expansion, requires a different set of input variables.

II.6.3 Modeling based on three-dimensional microstructure characteristics

II.6.3.1 Application of the procedure on values taken from literature

As discussed in Section II.6.2.2 the results obtained by numerical simulation in Section II.6.1.3 and the results of tensile tests presented in Section II.6.2 do not match. It is assumed that the main reason is the lack of information about the three-dimensional micromechanical properties. To confirm this conclusion, the presented procedure is applied to three-dimensional microstructural data provided in [58]. In contrast to the analyses presented so far, tensile test specimens made of PA 6 are used in [58]. However, in both cases the fiber mass fraction is specified with 30%.

In a first step the correlation functions as well as the three-dimensional microstructure information of the elasticity tensor components are identified by taking into account the slightly different material parameters of PA 6 compared to PBT. The material properties provided in Table II.11 are assumed dry as molded.

To generate the microstructure for the correlation function analysis the probabilistic characteristics of the fiber length, fiber diameter, and fiber orientation are taken from [58]. The characteristics of the fiber length and fiber orientation are given for tensile test specimens directly produced by mold injection. The probability density function of the fiber length meets a two-parameter Weibull distribution [24, 44] given by

$$f(l|a, b) = \frac{b}{a} \left(\frac{l}{a} \right)^{b-1} \exp \left(-\frac{l}{a} \right)^b. \quad (\text{II.55})$$

Material	Young's modulus GPa	Poisson's ratio -
Glass	72	0.22
PA 6	2.9	0.39

Table II.11: Material properties of the matrix and fiber material of PA 6 GF 30 dry as molded.

Correlation function	Value	Unit	C_{11}	C_{12}	C_{22}	C_{66}
Exponential	b_1	μm	242.9	177.7	166.5	187.7
	b_2	μm	179.4	181.7	178.9	181.7
	RMSE	μm	0.10	0.11	0.07	0.08
	Mean	GPa	12.10	4.514	8.088	1.851
	Stand. dev.	GPa	2.478	0.262	0.714	0.281

Table II.12: Results of the auto-correlation lengths of the elasticity tensor coefficients using an exponential correlation functions and a window size of 250 μm based on the microstructure characteristics provided in [58] and the material properties of PA 6 GF 30.

Analysis	Result GPa	Standard Deviation GPa	Deviation experiment %
Experiment	9.2	0.1	-
250 KUBC	9.34	0.01	1.54
500 KUBC	8.53	0.01	7.28
750 KUBC	8.24	0.01	10.43
250 SUBC	6.00	0.01	34.8
500 SUBC	6.48	0.01	29.6
750 SUBC	6.74	0.01	26.7

Table II.13: Results of the numerically obtained Young's modulus based on the microstructural characteristics of PA 6 given in [58] and deviation to the experimentally obtained Young's modulus.

Correlation function	Value	Unit	C_{11}	C_{12}	C_{22}	C_{66}
Exponential	b_1	μm	233.4	163.3	157.0	169.8
	b_2	μm	191.8	171.1	178.1	165.6
	RMSE	μm	0.10	0.12	0.10	0.10
	Mean	GPa	13.05	5.144	8.698	1.799
	Stand. dev.	GPa	2.953	0.267	0.749	0.285

Table II.14: Results of the auto-correlation lengths of the elasticity tensor coefficients using an exponential correlation functions and a window size of 250 μm based on the microstructure characteristics provided in [58] and the material properties of PBT GF 30.

The Weibull parameters a and b are determined as

$$a = 292 \quad b = 1.96. \quad (\text{II.56})$$

The corresponding mean of the fiber length is $\bar{l} = 260 \mu\text{m}$. The fiber orientation is described by an elliptic probability density function [58]. Therefore,

$$f(\theta) = \frac{h_2}{\sqrt{1 - \frac{h_1^2 - h_2^2}{h_1^2} \cos^2(\theta)}} \quad (\text{II.57})$$

holds. Here, h_1 and h_2 are the semi-minor and semi-major axis, respectively. The semi axes ratio for this probability density function measured by μCT is 22.1. The fiber diameter d is analyzed for tensile test specimens cut out of a pre-produced plate. Since the fiber diameter is not influenced significantly by the mold injection process these values can be combined. As expected the fiber diameter shows a normal distribution. The corresponding probability density function is written as

$$f(d) = \frac{1}{\sigma \sqrt{2\pi}} \exp \left[-\frac{1}{2} \left(\frac{d - \mu}{\sigma} \right)^2 \right] \quad (\text{II.58})$$

with a mean value $\mu = 10.9 \mu\text{m}$ and a standard deviation $\sigma = 0.9 \mu\text{m}$. The derived information of the correlation structure is summarized in Table II.12.

The results of the numerical simulation of a tensile test using the presented data for the representation of the microstructure are provided in Table II.13. In addition, the numerically obtained Young's modulus of the material is characterized experimentally in [58] as well. Therefore, Table II.13 also holds the results of the conducted experiments and the deviation between the numerical simulations and experiments.

The results presented in Table II.13 indicate that the introduced procedure for the numerical simulation of SFRC on the component level including information of the three-dimensional microstructure leads to plausible results. The numerical simulations based on random fields characterized by correlation functions obtained for a window size of 250 μm and the mean values for pure displacement boundary conditions show a minimal deviation of 1.54 %. The deviation starts to increase with an increasing window size. This indicates that the use of larger window sizes leads to a loss of information about the microstructure, that is necessary to obtain the correct material response on the component level. Due to the larger aspect ratio of 23.9 the results also reveal a more distinct anisotropy in contrast to the simulation based on the microstructure.

A further validation step is the comparison of an experimentally obtained local Young's modulus distribution with the spatial fluctuation of the Young's modulus based on the modeling with random fields. Unfortunately, a local distribution of the Young's modulus is not provided in [58]. Therefore, in a last step the presented

Analysis	Result GPa	Standard deviation GPa	Deviation experiment %	Min GPa	Max GPa
Experiment	9.75	0.27	-	9.28	10.2
250 KUBC	9.74	0.01	0.10	9.42	10.1

Table II.15: Results of the numerically obtained Young's modulus based on the microstructural characteristics of PA 6 given in [58] in combination with the material properties of PBT GF 30 and deviation to the experimentally obtained Young's modulus.

	Mean	Std.	1	2	3	4	5	6	7	8	9	10
Experiment	9.48	1.26	10.4	6.9	9.95	10.9	11.2	9.34	9.48	8.15	9.94	-
Simulation	9.46	0.42	9.39	10.1	9.46	8.99	9.10	9.23	9.35	10.0	9.99	8.96

Table II.16: Local distribution of the material properties based on numerical simulations and experiments. All values in GPa

characteristics are combined with the material properties of PBT GF 30.

II.6.3.2 Transfer of the microstructural characteristics to PBT GF 30

First a correlation analysis based on the new combination of microstructural and material properties is conducted, Table II.14. As the previous analysis indicates that the representation of the microstructure with random fields for a correlation structure based on a window size of 250 μm shows the best fit, the final analysis is limited to this configuration. The results of the numerical and experimental analysis, given in Table II.15, confirm the presented procedure. The deviation between the numerically and experimentally obtained values is less than 1%. Furthermore, the obtained minimal and maximal values show the same trend for the numerical simulation as well as the experiments. These values indicate the Young's modulus range for the analyzed specimens.

However, a further important property is the local distribution of the material property within one specimen. Therefore, the Young's modulus distribution over the observation length is measured by dividing the original measurement length into sections with a length of 5 mm. For each section the Young's modulus is obtained individually on a numerical and experimental basis. The results are given in Table II.16. The mean values of the chosen data sets fit very well. In contrast to this, the standard deviation of the experimentally obtained data set is higher than the one obtained for the numerical results. This is also indicated by the range of the values. The corresponding minimal and maximal values are marked in Table II.16. The reason for this is determination of the correlation length on the mesoscale in combination with the used element size for the numerical simulation.

II.7 Summary and Conclusion

The presented work consists of three steps that build together the proposed modeling approach for a tensile test specimen made of SFRC. These are the analysis of the microstructure, the determination of the correlation structure of the elasticity tensor elements and the generation of random fields for the representation of the material properties by the Karhunen-Loève expansion on the component level.

The analysis of the microstructure is based on a two-dimensional micrograph which reveals a layered structure of the cross-section. Based on the data the cross-section can be divided into five layers, namely a core layer, that is surrounded by a shell and a skin layer at the top and bottom. This meets the well-known

orientation scheme due to mold injection process. Numerical simulation based on the derived probabilistic characteristics of the fiber length, fiber diameter, fiber orientation as well as fiber volume fraction show that the information about the layered structure influences the Young's modulus of the analyzed cross-section. A validation with experimentally obtained Young's modulus by nanoindentation indicates, that a homogenization based on the overall probabilistic characteristics underestimates the material properties of the cross-section. In contrast to this the modeling based on a layered structure consisting of the core and shell layers shows only a marginal deviation to an approach limited to the shell layers. Therefore, the representation of the microstructure by the shell layers only appears sufficient and is used for the determination of the correlation structure for the numerical simulation on the component level.

For the numerical simulation on the component level first the probabilistic characteristics based on a two-dimensional micrograph of the shell layers is used to derive the correlation structure. However, a comparison with conducted tensile tests show large deviations between the numerically and experimentally obtained results for the Young's modulus. In fact, the numerical results meet the Young's modulus obtained by nanoindentation instead. This leads to the conclusion that the numerical modeling on the component level requires a full three-dimensional analysis of the microstructure as a tensile test is no longer reduced to near surface measurements. This conclusion is proven by applying the presented approach to probabilistic characteristics of a microstructure of SFRC obtained by μ CT. The resulting minimal deviation of the numerical simulation and the conducted experiment is about 1.5 %. Finally, the local distribution of the material properties is investigated both numerically and experimentally. The results show the same trend. However, the spatial fluctuation seems to be more prominent experimentally than for the numerical simulations. One reason might be the used correlation lengths, that are smaller than the element size. This issue could be solved by deriving the correlation length of each elasticity tensor component not by the moving window method in the mesoscale. Instead the correlation lengths give additional independent parameters like the engineering constants. The correlation lengths are then determined in the same way as the material properties by fitting the parameters to experimental data. This approach is already successfully used in [188, 189], where the correlation length of the Young's modulus is determined in such a way that the phenomenon of the continuous wave mode conversion, detected by the experimental observation of guided ultrasonic waves in carbon fiber reinforced plastics, can be observed in numerical simulations as well. This approach will be combined with the use of non-Gaussian random fields.

It is concluded, that the presented procedure is suitable for the numerical simulation of components made of SFRC. For an adequate representation on the mesoscale the probabilistic characteristics of a two-dimensional cross-section is sufficient. The numerical simulation on the component level, however, require a knowledge of the three-dimensional probabilistic properties of the microstructure.

Paper III

Experimental characterization of short fiber-reinforced composite on the mesoscale by indentation tests

Title: Experimental characterization of short fiber-reinforced composite on the mesoscale by indentation tests

Author: Natalie Rauter¹ and Rolf Lammering¹

Affiliation: ¹Helmut-Schmidt-University /
University of the Federal Armed Forces Hamburg
Holstenhofweg 85, 22043 Hamburg, Germany

Journal: Applied Composite Materials
pp. 1747 - 1765, 2021

Status: Published

DOI: 10.1007/s10443-021-09937-4

Abstract: Indentation tests are widely used to characterize the material properties of heterogeneous material. So far there is no explicit analysis of the spatially distributed material properties for short fiber-reinforced composites on the mesoscale as well as a determination of the effective cross-section that is characterized by the obtained measurement results. Hence, the primary objective of this study is the characterization of short fiber-reinforced composites on the mesoscale. Furthermore, it is of interest to determine the corresponding area for which the obtained material parameters are valid. For the experimental investigation of local material properties of short fiber-reinforced composites, the Young's modulus is obtained by indentation tests. The measured values of the Young's modulus are compared to results gained by numerical simulation. The numerical model represents an actual microstructure derived from a micrograph of the used material. The analysis of the short fiber-reinforced material by indentation tests reveals the layered structure of the specimen induced by the injection molding process and the oriented material properties of the reinforced material are observed. In addition, the experimentally obtained values for Young's modulus meet the results of a corresponding numerical analysis. Finally, it is shown, that the area characterized by the indentation test is 25 times larger than the actual projected area of the indentation tip. This leads to the conclusion that indentation tests are an appropriate tool to characterize short fiber-reinforced material on the mesoscale.

III.1 Introduction

Reinforced materials have become of high interest over the last decades due to the improved weight-specific material properties. Those heterogeneous materials usually consist of two components, the matrix material and reinforcing particles or fibers, respectively. One example here are short fiber-reinforced composites (SFRC), where thermoplastic matrix materials are combined with fibers of 100 to 300 length. Due to the finite length of the reinforcing elements, these materials are capable of serial production processes like injection molding. However, the manufacturing with injection molding results in a probabilistic microstructure of the component and hence leads to a spatial fluctuation of the material properties.

Since these fluctuations on the mesoscale influence, the structural response on the component level the representation of the varying material properties for numerical simulations of the component is of particular interest. For an adequate verification of proposed modeling approaches on the mesoscale experimental investigations are essential. One testing technique, that is frequently used for small-scale testing is nanoindentation [89]. By nanoindentation, the material properties are analyzed in the nm to μm domain using indentation loads in the range of μN to mN. This allows one to not only characterize the material on the mesoscale but also to derive a spatial distribution of the near-surface material properties [52]. With quasi-static indentation tests test elastic as well as plastic material properties can be derived. The elastic material response is obtained by measuring the Young's modulus, whereas the plastic behavior is characterized by the hardness. Due to this multivariate use, indentation tests are used in a wide range of applications for the analysis of heterogeneous material properties. This includes the characterization of MEMS-devices [34, 36], biomedical material like brain tissue [20, 175], dental restorative composites [133, 155], as well as nanocomposites [5, 89, 92]. For fiber-reinforced polymers so far only the interphase between the two constituents are analyzed experimentally by nanoindentation for example in [73, 90, 119]. A comprehensive review of nanoindentation applications for polymer composites is provided in [49].

The results presented in the literature provide promising results on the analysis of the microstructural properties of reinforced heterogeneous materials. But so far, in contrast to the macroscopic analysis as shown in [29, 30], there is only little investigation on the combination of this experimental approach with the characterization of SFRC on the mesoscale and corresponding numerical simulations. Therefore, in this work first, the spatial distribution of the linear-elastic quasi-static material properties for a thermoplastic matrix filled with glass fibers on the mesoscale is experimentally obtained by indentation tests. In contrast to the work presented in [73, 90, 119] not the interface properties and the characteristics of the constituents are measured individually, but a region comparable to a statistic volume element is considered. The size of this area defined by the projected area of the indentation tip at maximum load varies between $2500\ \mu\text{m}^2$ and $7000\ \mu\text{m}^2$ and hence, includes not only a single phase of the heterogeneous material but the constituents as well as the interphase. Due to this, the experimentally obtained results are not only affected by the projected area but also by the surrounding material. This study aims to determine the size of the effective cross-section, analyzed by indentation tests on the mesoscale.

The structure of the presented work is as follows. First, the fundamentals of the multiscale approach are introduced in Section III.2. Next, Section III.3 gives a brief overview of the theoretical framework for the material characterization by indentation tests as well as the experimental setup and procedure of this study. This is followed by the presentation of the experimental results in Section III.4. These results are discussed in detail in Section III.5. This includes the numerical simulations as well as the determination of the effective cross-section size. Finally, Section III.6 gives a summary and a conclusion of the presented work.

III.2 Multiscale approach

Usually, materials are assumed to be homogeneous when observed at the component level. However, the microstructure of materials is mostly heterogeneous. This leads to the conclusion, that the material properties of a volume element, taken from a component, depend on the volume's edge length d . In case that the material properties of the volume element are independent of its origin, one speaks of a representative volume element

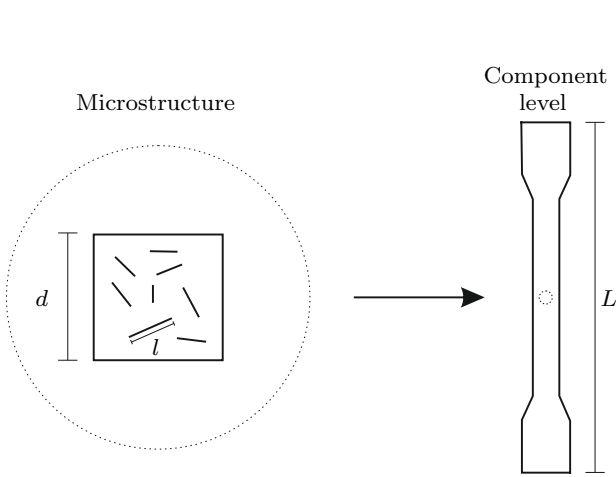


Figure III.1: Multiscale approach, [127].

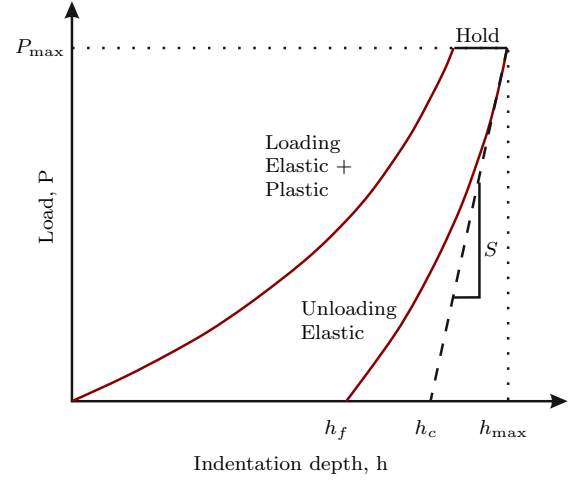


Figure III.2: Scheme load cycle indentation test, [103, 171].

(RVE). A well-known definition of the RVE size is given in [70]. For an RVE the effective material properties are independent of the used load case. This is equivalent to the fact, that an RVE consists of a statistically sufficient number of inhomogeneities to be representative of the microstructure. Therefore, the material properties of this volume can be replaced by a homogeneous representation. It is obvious that the scale d must be much larger than the size l of an inhomogeneity and much smaller than the component scale L . This approach is known as the separation of scales, which is also formulated as [28, 129, 190]

$$l \ll d \ll L. \quad (\text{III.1})$$

The dimension l is assigned to the microscale, L to the macroscale, and the edge length d of the RVE to the mesoscale. The concept is also shown in Figure III.1.

III.3 Indentation tests

III.3.1 Theory

For the experimental determination of the linear-elastic quasi-static material properties by indentation tests the slope of the force-displacement curve of the unloading process is evaluated in order to derive the indentation modulus, see Fig. III.2. Hence, the indentation modulus, which is also referred to as the reduced modulus, is expressed by [125, 135]

$$E_r = \frac{dP}{dh} = \frac{1}{\beta} \frac{\sqrt{\pi}}{2} \frac{S}{\sqrt{A_p(h_c)}}, \quad (\text{III.2})$$

where S is the stiffness of the contact, A_p the projected area of the indentation tip for a contact depth h_c , and β an empirical correction factor of the indenter uniaxial symmetry when using pyramidal indenter [65, 173].

The indentation or reduced modulus is not equal to the Young's modulus of the specimen's material, because the measurement is affected by the material of the indentation tip. Therefore, a correction of the obtained indentation modulus is necessary. Regarding the Poisson's ration ν_i and the Young's modulus E_i of the indentation tip the Young's modulus of the specimen E_s is obtained by evaluating

$$E_s = \frac{1 - \nu_s^2}{\frac{1}{E_r} - \frac{1 - \nu_i^2}{E_i}} \quad (\text{III.3})$$

	Young's modulus GPa	Poisson ratio -	Density kg/m ³
Glass	72	0.22	2500
PBT	2.6	0.41	1300

Table III.1: Material properties of the fiber and matrix material.

It is obvious that for the determination of the Young's modulus the Poisson's ratio ν_s of the analyzed material must be known or needs to be approximated first. The tip material is usually diamond or sapphire. The presented framework was developed for homogeneous material. However, in context of determining the apparent material properties of a heterogeneous material, it seems appropriate to use these formulas since the apparent material properties are a homogeneous representation of a heterogeneous material on the mesoscale.

The definition of the indentation modulus in Eq. (III.2) shows that the result of an indentation test is influenced significantly by the geometry of the indentation tip. There is a variety of shapes available for material characterization by indentation tests. This includes pyramids, flat punch, and conospherical indentation tips. Most common is a three-sided triangular based pyramid, the Berkovich tip [12], which is also used in this study. The pyramidal shape is characterized by a nominal angle of 65.3° between the face and the normal to the base at apex as well as an angle of 76.9° between edge and normal. The radius of the tip is less than $0.1 \mu\text{m}$ [15]. Corresponding to the geometry the projected area of a perfectly sharp Berkovich tip is given by [35]

$$A_p = \pi h_c^2 \tan^2 \varphi = 24.5 h_c^2, \quad (\text{III.4})$$

where φ is the effective semi-angle of 70.32° [23].

Since imperfections influence the true projected area of a Berkovich tip significantly, instead of using Eq. (III.4) a calibration function is mostly used to approximate the projected area. This function is expressed as [125]

$$A_p(h_c) = 24.56 h_c^2 + C_1 h_c^1 + C_2 h_c^{1/2} + C_3 h_c^{1/4} + \dots + C_8 h_c^{1/128}. \quad (\text{III.5})$$

Finally, the empirical correlation factor β needs to be determined. It is shown in [125, 135], that the value of β usually varies between 1.02 and 1.08. This results in a deviation of up to 3 % regarding the indentation modulus. Due to this the value for β is set to one in this study as done in [93].

The used Berkovich tip is made of diamond with a Young's modulus of 1143 GPa and a Poisson ratio of 0.0691 [91].

III.3.2 Experimental procedure

For the characterization of the material properties of SFRC on the mesoscale cuboids with an edge length of 20 mm x 5 mm x 3 mm are used. The specimens are cut out of a quadratic plate of 300 mm x 300 mm x 3 mm produced by injection molding. The used material is a polybutylenterephthalat (PBT) filled with glass fibers. The fiber mass fraction is specified with 30% (PBT GF 30) and the material properties of the two components are given in Tab. III.1. Due to the manufacturing process, the reinforcement of the matrix by the fibers is directional for the component, so that the material properties are non-isotropic and, hence, depending on the direction. Because of that, different orientations of the specimens with respect to the main melt flow direction of the initial plate are analyzed. They are cut out perpendicular to and in the direction of the main melt flow direction. This allows one to derive the linear-elastic quasi-isotropic material properties in the three main directions namely with the main flow direction, perpendicular to it, and in the thickness direction. Figure III.4 gives an overview of the used specimens. There is also a coordinate system introduced, that is used throughout this study.

For the characterization of the material properties for PBT GF 30 the indentation or reduced modulus is

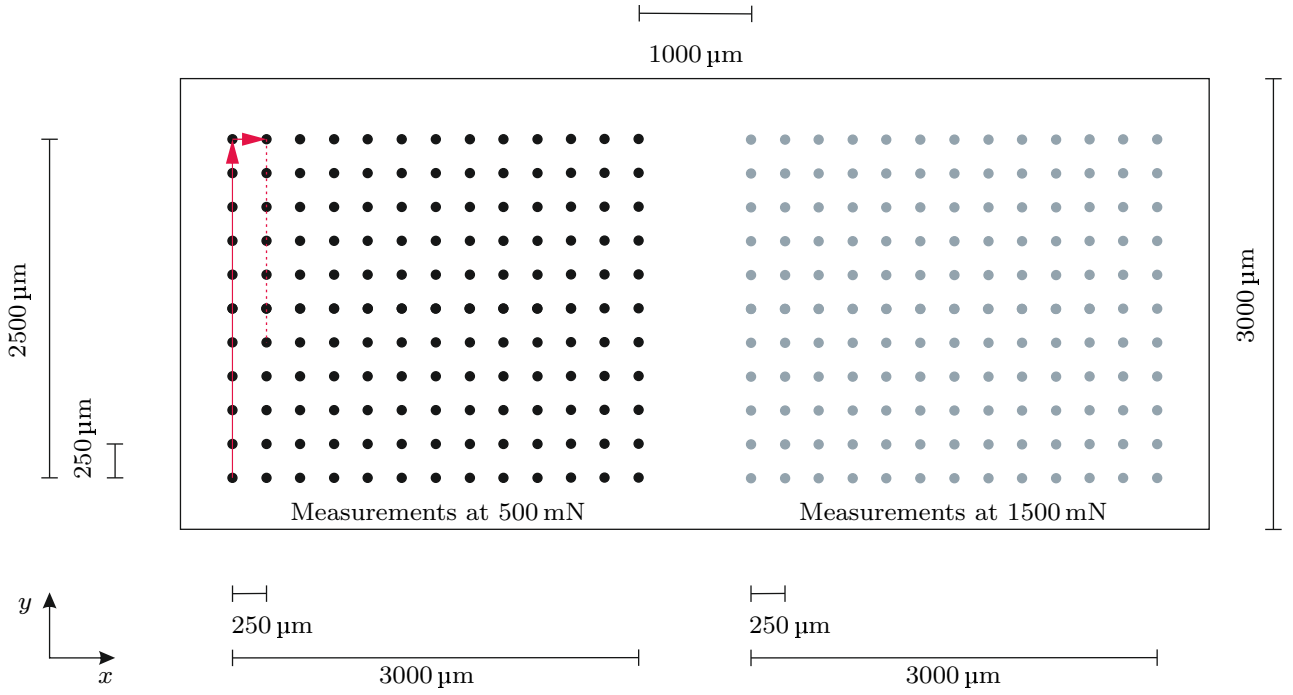


Figure III.3: Spatial distribution of the numerically obtained indentation modulus for each load case and direction.

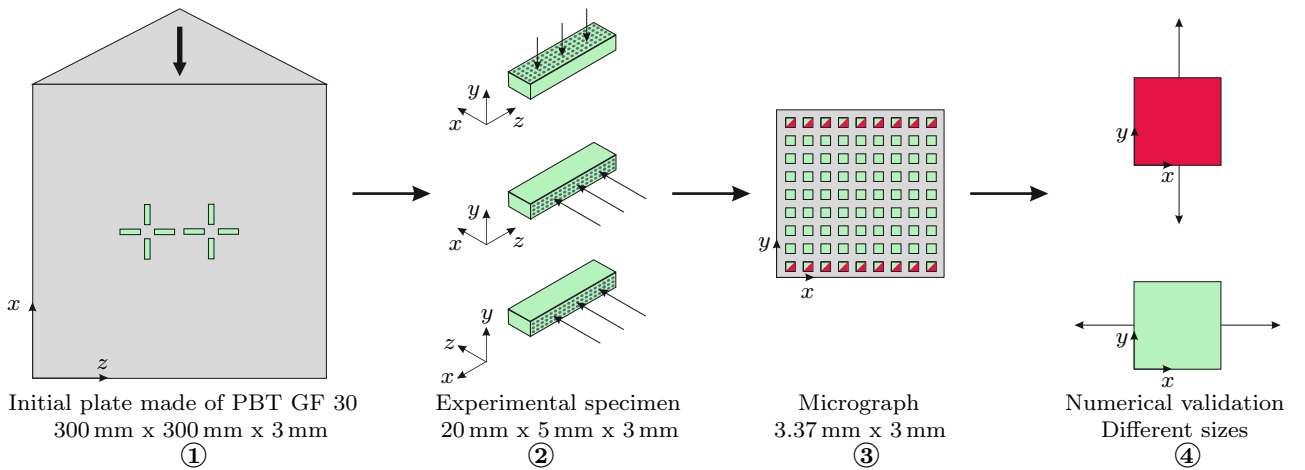


Figure III.4: Specimens for experimental investigation and numerical validation.

Max. load mN	Direction	Mean GPa	Standard deviation GPa	Min GPa	Max GPa	Range GPa
500	x	7.35	1.01	5.07	10.39	5.31
500	y	5.64	0.72	3.10	9.03	5.94
500	z	6.83	1.61	1.87	12.06	10.18
1500	x	7.44	0.75	5.69	9.69	4.00
1500	y	5.68	0.38	4.68	6.96	2.28
1500	z	6.62	1.50	1.74	12.54	10.8

Table III.2: Results of the experimentally obtained indentation modulus.

measured at several points to obtain the spatial distribution as well as the statistical characteristics. The measurement points are arranged in a grid with a vertical and horizontal distance of 250 μm between each point, see Figure III.3. Since the experimental procedure is validated by numerical simulations based on a two-dimensional micrograph with a size of 3.37 mm x 3 mm the number of measurement points is selected in such a way that an identical area is covered. To minimize boundary effects a distance of 250 μm to each specimen boundary is kept. In accordance with the distance of the measurement points to the edges and between each other the measurement points are arranged in a grid of 13 x 11 points, see Figure III.3. Hence, in total 143 measurements per grid are performed.

At each of these points first, the indentation modulus is determined for a maximum load of 500 mN and 1500 mN, respectively. The used range for the approximation of the indentation modulus is set to 98 % and 40 % of the maximum load. As discussed in Section III.3.1, the indentation area function $A_p(h_c)$ of the used Berkovich tip is calibrated before obtaining the indentation modulus with respect to Eq. (III.2).

III.4 Results

Based on the experimentally obtained indentation modulus mean values and the corresponding standard deviations for the analysis of the material properties in each direction are derived. The results are summarized in Table III.2. In addition, the minimal and maximal value of each measurement series is provided. Figure III.5 gives an overview of the spatial distribution of the indentation modulus for each analysis.

III.5 Discussion

Below first the experimentally obtained results are discussed in detail in Section III.5.1. This is followed by a numerical analysis based on the microstructure of the specimen in Section III.5.2. The discussion is concluded by a comparison of the results obtained by experimental investigation and numerical analysis in Section III.5.3.

III.5.1 Experimental results

The main aspects can be derived from the results provided in Tab. III.2 in combination with the microstructural properties of the cross-section given in Table III.3. First, the measured values indicate that, compared to a tensile test specimen on the component level, there is only a small degree of anisotropy due to the reinforcing fibers on the mesoscale. The main reason here is the considerably small aspect ratio of the detected fibers. Based on a mean fiber length of 46.6 μm and a mean diameter of 9.6 μm the aspect ratio is 4.85, whereas a three-dimensional characterization on the component level results in an aspect ratio of up to 25 [58]. Furthermore, the obtained mean value of the Young's modulus for each direction appears to be independent of the maximal indentation force used. This meets the results presented in [15]. Finally, the standard deviation and the range

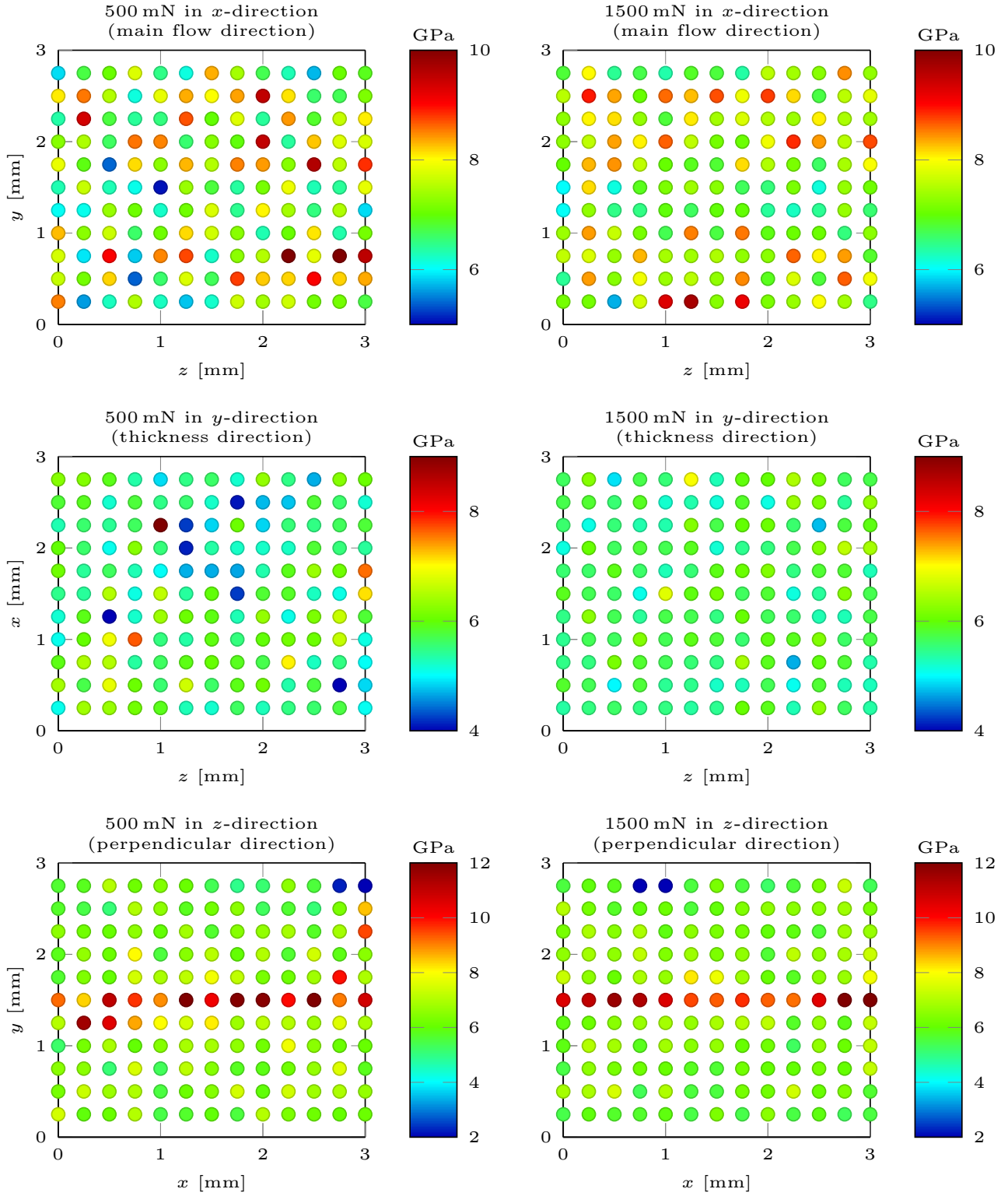


Figure III.5: Spatial distribution of the indentation modulus for each load case and direction.

	Parameter	Value
\bar{l}	Mean fiber length	46.6 μm
\bar{d}	Mean fiber diameter	9.6 μm
φ^s	Fiber mass fraction shell	0.28
φ^c	Fiber mass fraction core	0.33

Table III.3: Microstructural characteristics of the specimen taken from [145].

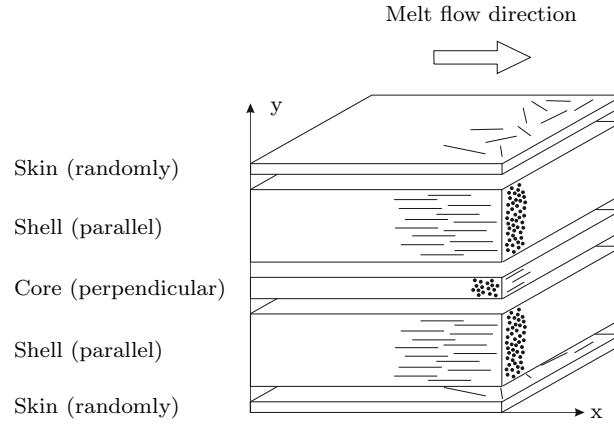


Figure III.6: Fiber orientation schemes consisting of five different layers due to injection molding process, compare [154].

of the obtained indentation modulus decrease with an increasing indentation force. Since the indentation force correlates with the indentation depth and hence, the projected area, the characterized cross-section is larger for a higher indentation force. In combination with the decreasing standard deviation and range, this allows one to assign the conducted experiments to the mesoscale in context of the multi-scale approach [28, 190].

Components manufactured by an injection molding process show a layered structure in thickness direction due to different melt flow velocities and shear forces [76]. As shown in Figure III.6, usually the cross-section is characterized by three or five individual layers, namely skin, shell, and core layers [19, 41, 43, 113, 154]. Each of these layers shows a different main fiber orientation. For the core layer, located in the middle of the cross-section, the fiber is orientated mainly perpendicular to the main melt flow direction, whereas the adjacent shell layers show a fiber orientation, that coincides with the main melt flow direction. The skin layers at the upper and lower surface are only used within the five-layer characterization. In these thin layers, the fibers are usually randomly orientated. Since the material properties are highly influenced by the fiber orientation as shown in [141] the layers have different material properties.

This variation of the material properties and hence, the layered structure of the cross-section can be clearly observed in the experimental results of the indentation test in the z -direction. In the center of the cross-section, the obtained Young's modulus is significantly higher in comparison to the remaining cross-section. This also meets the results of the microstructural analysis of the cross-section presented in [145]. However, this characteristic of the cross-section is not detected by the results shown in Figure III.5 for the indentation test in the x -direction. At first, this contradicts the results of the measurement in the z -direction as well as the findings regarding the cross-section layout due to an injection molding process as described in [19, 41, 43, 113, 154] and the results of the cross-section analysis in [145]. This is resolved by analyzing the obtained values more in detail. Therefore, the mean value is calculated for each layer. The information about the corresponding coordinates is derived from the results of the indentation tests in the z -direction. The values measured at $y \leq 1.25 \text{ mm}$ and $1.75 \text{ mm} \leq y \leq 2.75 \text{ mm}$ are assigned to the shell layers, whereas the experimentally obtained

Direction	Layer	E at 500 mN GPa	E at 1500 mN GPa	φ
x	Core	6.72	6.90	0.33
x	Shell	7.41	7.49	0.28
z	Core	10.4	10.5	0.33
z	Shell	6.48	6.23	0.28

Table III.4: Mean values of the indentation modulus.

values at $y = 1.25$ mm are assigned to the core layer. The results are provided in Table III.4. Furthermore, the corresponding fiber mass fraction φ taken from the microstructural analysis in [145] is given.

First of all, again the mean values of the measurement results at 500 mN and 1500 mN match very well for each layer, which meets the results presented in [15]. The results also indicate a layered structure of the cross-section not only based on the experiments conducted perpendicular to the main melt flow (z -direction) but also in the main flow direction (x -direction). However, the difference between the shell and core layers is less prominent in the melt flow direction (x -direction) and hence, cannot be observed in Figure III.5. There are two main reasons for the more pronounced difference of the mean indentation modulus between the shell and core layers perpendicular to the main flow direction (z -direction). First, the fiber mass fraction is not identical for the shell and core layers as shown in Table III.3 and Table III.4. Due to the higher fiber mass fraction of the core layer in combination with a 0° fiber orientation the difference to the shell layer with a lower fiber mass fraction and a fiber orientation of 90° is more significant in contrast to an interchanged combination. Second is the orientation within the core and shell layers. The shell layers show an overall orientation characteristic in melt flow direction whereas the fibers in the core layer are mostly orientated perpendicular to the melt front. However, the orientation characteristics are not identical when transforming one by 90° [145]. Because of the different fiber mass fraction and slightly different fiber orientation in these layers, the mean value for the shell layer in a fiber direction of 0° and the corresponding value of the core layer differ significantly.

III.5.2 Numerical simulation

It is expected that the experimentally obtained values for the indentation modulus are not only affected by the projected area A_p but also its surroundings. Therefore, the effective cross-section of the indentation test is analyzed by numerical simulations. The term effective cross-section is interpreted as the area that is characterized by the indentation test. In other words, the surface of the material around the indentation center, which influences the results of the indentation test, defines the effective area. The numerical simulations are based on a two-dimensional micrograph of the used material. Since the micrograph represents the x - y -plane the numerical validation is exemplarily done for these two directions.

The validation process consists of two steps. First, the overall properties on the mesoscale are derived by obtaining the Young's modulus for the complete micrograph with a size of 3.37 mm x 3 mm in both, the x - and y -directions by numerical simulations of tensile tests. For the determination of the Young's modulus, the following boundary conditions are applied. For the analysis in the x -direction a horizontal load of 100 MPa is applied to the right edge, whereas for the analysis in y -direction a vertical load of 100 MPa is applied to the upper edge of the numerical model, which represents the micrograph. In both cases, the horizontal displacement is fixed at the left edge and the vertical displacement is fixed at the lower edge, see Figure III.7. The generation of the numerical model is described in detail in [145] and will, therefore, only be discussed briefly here. To be able to analyze the overall material properties of the micrograph by numerical simulation the obtained image is transferred to an array that holds a zero or one for each pixel of the image, indicating whether the pixel represents matrix or fiber material. Based on these additional arrays are constructed holding

Max. load mN	Direction	mean h_c μm	A_c μm^2	l_e μm
500	x	10.1	2499	50.0
500	y	9.97	2435	49.3
1500	x	16.6	6751	82.2
1500	y	16.6	6751	82.2

Table III.5: Summary indentation characteristics.

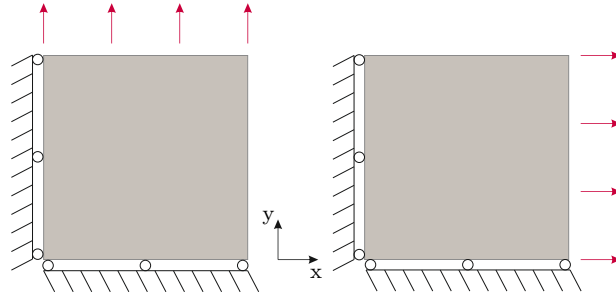


Figure III.7: Numerical models used for the determination of the Young's Modulus by tensile tests.

the material properties of linear-elastic material, the Young's modulus, Poisson's ratio, and the density for each coordinate. The numerical model itself is a rectangle of the same size as the micrograph discretized by a mapped mesh. To model the microstructure of the SFRC the arrays are used to pass the material properties directly to the integration points.

Second is the analysis of the effective cross-section. This is done by extracting squares with different edge lengths at different locations from the original micrograph. These squares are referred to as windows and the window size gives the edge length of the corresponding square. In this case, the same grid of measurement points is applied to the micrograph as used for the experimental analysis in Section III.3. This leads to a grid of 12×11 measurement points. Each measurement point is interpreted as the center of indentation by the Berkovich tip and with respect to the numerical analysis as the center of an extracted window. Based on the experimentally obtained contact depth, which depends on the maximum load, the corresponding projected area A_p is approximated by evaluating Eq. (III.4). A square with an edge length of $l_e = \sqrt{A_p}$ gives the smallest value of the effective cross-section and therefore, is used as an initial window size for the numerical analysis. The results, provided in Table III.5, indicate that the projected area is only influenced by the maximum load and not by the direction of the indentation test, which allows one to use the same window sizes for the analysis in both directions. Based on this the smallest window size analyzed by numerical simulation has an edge length of 50 μm . With an overall size of 3.37 mm x 3 mm and a minimum distance of 250 μm to the micrograph boundaries the maximum window size, that can be extracted, has an edge length of 500 μm . With these boundaries window sizes with an edge length of 50 μm to 500 μm in 50 μm steps are investigated. At each point of the grid and for each window size a square with the corresponding edge length is extracted. The microstructure and hence, the corresponding material properties are again represented by arrays, as done in [145]. The information of the material properties, stored in these arrays, are passed to the integration points of the numerical model of a square with identical edge length. For the analysis of the effective cross-section, the Young's modulus in x - and y -direction are determined by applying the same two load cases as done before. Furthermore, it is considered that the indentation modulus in the y -direction is only measured at the surface of the specimen. Therefore, with respect to the micrograph, the Young's modulus in the y -direction is only derived at the measurement points located at the upper and lower row of the grid. For more details, see Figure III.4. In contrast to this, the

Max. load mN	Direction	Mean GPa	Standard deviation GPa	Min GPa	Max GPa	Range GPa
500	x	6.33	0.88	4.37	8.98	4.61
1500	x	6.41	0.65	4.90	8.37	3.47

Table III.6: Results of the experimentally obtained Young's modulus in x -direction.

Young's modulus in the x -direction is obtained for all extracted cross-sections.

The results of the numerical simulations are depicted in the first row of Figure III.8. The diagrams show the results of both performed investigations. This includes the Young's modulus of the complete cross-section as well as the mean value for each window size and the corresponding minimum and maximum. Furthermore, the standard deviation is indicated by error bars. On the left-hand side, the results for the analysis in the melt flow direction (x -direction) are shown. The diagrams in the right column give the results for the analysis in the thickness direction (y -direction). For the numerical simulation in the x -direction the range, as well as the standard deviation of the obtained Young's modulus decrease continuously with an increasing window size and the maximum and minimum, converge to the mean value. Furthermore, the mean values are constant within the standard deviation over all window sizes and meet the Young's modulus of the whole micrograph. Based on this observation the numerical simulation can also be clearly assigned to the mesoscale with respect to the multi-scale modeling approach. The results for the analysis in thickness direction indicate a similar trend. However, the minimum and maximum don't show a monotonously increasing and decreasing behavior, respectively. The main reason is the low number of analyzed cross-sections in comparison to the analysis in the melt flow direction. Instead of 132 only 24 cross-sections are used due to the extraction limited to the near-surface area.

A detailed summary of the results is provided in Appendix III.A.

III.5.3 Comparison

For the comparison of the numerically obtained values and the measurement results, the Young's modulus needs to be derived from the indentation modulus. As discussed in Section III.3.1 for this the Poisson's ratio of the specimen material needs to be approximated first. Based on the microstructural properties of the material provided in Table III.3 and the material model by Halpin-Tsai [61, 62] the Young's modulus and the Poisson's ratio are predicted. The framework of the material model by Halpin-Tsai is given in Appendix III.B. For the Young's modulus, a value of 6.21 GPa is obtained. The Poisson's ratio is approximated at 0.379 which is used to derive the Young's modulus of the specimen from the indentation modulus in the x -direction. Due to the oriented material properties, this Poisson's ratio cannot be used for the remaining two testing directions, which is also indicated by the mismatch of the mean indentation modulus in each direction. The results are provided in Table III.6. Comparing the calculated Young's modulus in Table III.6 with the analytical value shows a good agreement. Therefore, the use of the predicted Poisson's ratio of 0.379 appears to be suitable for the determination of the specimen's Young's modulus. Furthermore, the local variation of the Poisson's ratio due to the changing fiber volume fraction has only a small impact on the resulting Young's modulus. For a fiber volume fraction range of 0 % up to 44 %, which is equal to a maximum fiber mass fraction of 60 %, the Poisson's ratio lays between 0.326 and 0.42. Calculating the Young's modulus using these values leads to an upper and lower bound of 6.61 GPa and 6.15 GPa. With respect to the resulting value of 6.33 GPa given in Table III.6, this equals an error of 4 % which is covered by the standard deviation.

The comparison between the experimentally obtained values and the results of the numerical analysis are done individually for each load case and each load direction. First, in the second row of Figure III.8 is the comparison of the indentation test at 500 mN in the main flow direction (x -direction) on the left-hand side and in the thickness direction (y -direction) on the right-hand side. In addition to the diagrams in the first

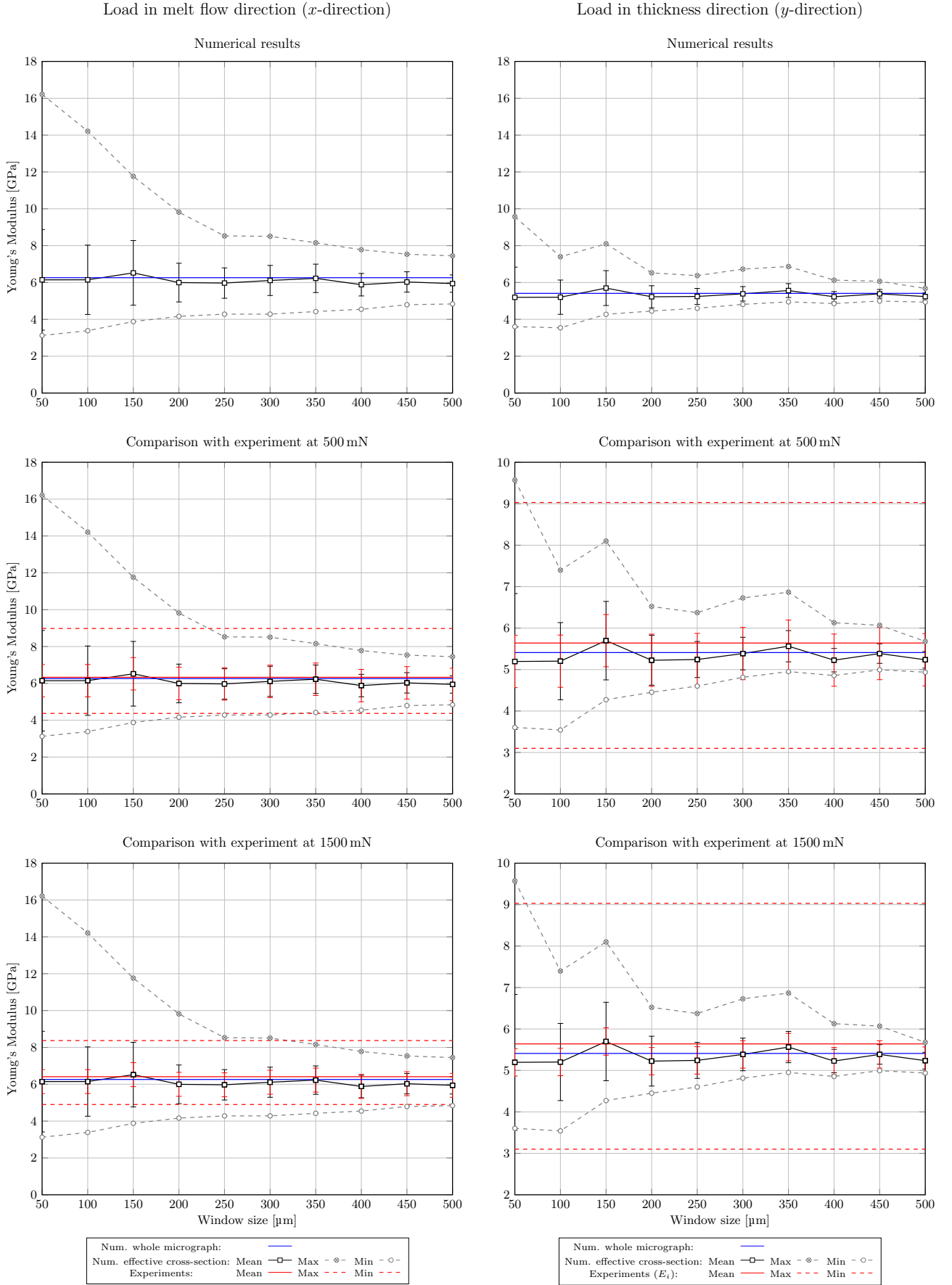


Figure III.8: Results of the numerical simulation in x - and y -direction and comparison with experimental results.

row, the experimentally obtained mean values, as well as the minimal and maximal measured value for the Young's modulus, are added (for the analysis in y -direction the indentation modulus is used). Furthermore, the standard deviation is indicated. To be able to compare the standard deviation of the experimental results with the standard deviation of the numerical analysis the error bars of the experimental results are added to the numerically obtained mean values. Therefore, at each window size, two error bars are depicted at the numerical mean value. One represents the standard deviation resulting from the numerical analysis (black) and a second corresponding to the experimental investigation (red). The Young's modulus derived from experimentally obtained indentation modulus, the Young's modulus characterizing the complete microstructure represented by a two-dimensional micrograph, and the mean value regarding the effective cross-section size analysis show only small deviations for the investigation in the x -direction. This holds for both indentation forces. In contrast to this in the y -direction the experimental results are higher than the values obtained by numerical simulation. The main reason here is the use of the indentation modulus instead of the Young's modulus. In addition to this, the center point of the extracted window has a distance of 250 μm to the surface of the micrograph. Hence, the ratio of the shell and skin layers in the extracted window may differ from the effective cross-section of the indentation test and may also lead to a slight deviation between the results.

In the next step, the size of the effective cross-section is determined by the window size where the standard deviations show the best match. For the experimental investigation in melt flow direction at 500 mN this is the case for a window size of 250 μm . In contrast to this at a load of 1500 mN the corresponding window size is 400 μm , as depicted in the third row of Figure III.8. This meets the expectation because with an increasing maximum load the indentation depth increases and hence, the effective area should do so as well. Comparing these values with the edge length l_e of the projected area given in Table III.5 leads in both cases to a factor of 5 between the window size and the edge length, which corresponds to a factor of 25 between the projected area and the effective cross-section. The same correlation is found for the results in the thickness direction.

Another approach for the determination of the effective cross-section is the comparison of the maximal and minimal obtained values of both investigations. In this case, the window size, where the numerical obtained values coincide with the experimental measuring results, gives the effective cross-section. However, the test results of the investigation in x -direction reveal that this procedure indicates not a specific value but a range for the effective cross-section. Furthermore, the values obtained based on the minimum and maximum do not necessarily coincide. For the test at 500 mN, for example, the maximal value of the numerical analysis and the experimental investigation indicates an effective cross-section of approximately 200 μm to 250 μm , which meets the conclusion based on the standard deviation. This is also indicated by the minimal value. In contrast to this, the test with a maximal indentation force of 1500 mN reveals a discrepancy between the effective cross-section based on the minimal and maximal value. For the maximal value, an effective cross-section edge length of 300 μm to 350 μm is derived whereas the minimal value indicates an edge length of 500 μm . One reason for this is the sensitivity of the minimum and maximum on the number of samples, as discussed before. This can also be observed for the analysis in the thickness direction. Due to the limited number of extracted windows, the comparison of the minimal and maximal values is not suitable to derive the effective cross-section size.

In summary, the effective cross-section is determined sufficiently based on the comparison of the standard deviation obtained by numerical simulation and experimental investigation. A prediction of the effective cross-section based on the minimal and maximal obtained values appears to be not suitable.

III.6 Conclusion

The presented work consists of two parts. First is the experimental characterization of a SFRC made of PBT filled with glass fibers and a fiber mass fraction of 30 % with special regard to the determination of the Young's modulus. The experimentally obtained results are validated by analytical treatment and numerical simulations in a second step to determine the effective cross-section size.

The material characterization of SFRC by indentation tests along the three major axis that is along and

perpendicular to the main flow direction of the injection molding process as well as in thickness direction reveals the layered structure of the cross-section due to different melt flow velocities during manufacturing. Furthermore, the deviation of the obtained means for the Young's modulus for the two different indentation loads stays within the standard deviation. This meets the observations described in [15]. In contrast to this, the results for the different analyzed orientations differ, which is assigned to the oriented material properties of reinforced material. However, the anisotropy is not very profound due to the small aspect ratio of the reinforcing fibers.

The numerical simulations for the determination of the Young's modulus are based on the microstructural characteristics of the used material. They confirm the results of the indentation tests. Furthermore, the numerically obtained results for different window sizes clearly indicate that the presented approach is assigned to the mesoscale because the minimal and maximal value derived by the numerical simulation converges to the mean value for increasing window size and the standard deviation also shows a decreasing development with increasing window size.

Comparing the experimentally obtained standard deviation with the standard deviation of the numerical simulations for different window sizes reveals, that the ratio between the indentation area and the effective cross-section of the indentation test is independent of the maximum indentation load. In this study, experiments are conducted with a maximum load of 500 mN and 1500 mN. In both cases, the standard deviation of the numerical simulation meets the experimentally obtained value for window sizes 25 times larger than the indentation area.

It is concluded that indentation tests are a suitable procedure to determine the material properties of SFRC on the mesoscale. This does not only involve the overall material properties but also the spatial distribution. The obtained values characterize the material for an effective cross-section that is 25 times larger than the projected area of the used Berkovich tip for a given indentation depth. Furthermore, the procedure is adaptable to other fiber volume fractions. In this case, the ratio between the effective cross-section and the projected area might be different due to the differing reinforcement level and the change in the microstructural properties.

III.7 Declarations

The authors have no conflicts of interest to declare that are relevant to the content of this article.

III.8 Data availability

The datasets generated and analysed during the current study are available from the corresponding author on reasonable request.

III.A Numerical results

In Table III.7 the mean value, standard deviation, as well as minimal and maximal values of the Young's modulus are provided for each window size and both load cases.

III.B Theoretical framework Halpin-Tsai

The following definition of the engineering constants by Halpin and Tsai is taken from [61, 174]. The longitudinal and transverse Young's modulus are obtained by

$$E_{11/22} = \frac{1 + \xi \eta \varphi}{1 - \eta \varphi} E_m, \quad (\text{III.6})$$

Window size μm	Direction	Mean GPa	Standard deviation GPa	Min GPa	Max GPa	Range GPa
50	x	6.14	2.73	3.13	16.2	13.1
100	x	6.15	1.88	3.38	14.2	10.8
150	x	6.52	1.74	3.88	11.8	7.88
200	x	6.00	1.05	4.16	9.82	5.65
250	x	5.97	0.82	4.28	8.53	4.25
300	x	6.11	0.82	4.28	8.51	4.22
350	x	6.23	0.77	4.42	8.16	3.74
400	x	5.88	0.61	4.55	7.78	3.23
450	x	6.03	0.55	4.79	7.54	2.74
500	x	5.94	0.47	4.84	7.45	2.61
Whole	x	6.26	-	-	-	-
50	y	5.20	1.64	3.60	9.57	5.97
100	y	5.20	0.93	3.54	7.40	3.86
150	y	5.70	0.95	4.27	8.10	3.83
200	y	5.22	0.60	4.45	6.52	2.07
250	y	5.24	0.43	4.60	6.37	1.77
300	y	5.39	0.39	4.81	6.73	1.91
350	y	5.56	0.38	4.95	6.87	1.92
400	y	5.23	0.28	4.86	6.13	1.27
450	y	5.39	0.24	4.99	6.07	1.07
500	y	5.24	0.20	4.94	5.68	0.74
Whole	y	5.41	-	-	-	-

Table III.7: Results of the numerically obtained Young's modulus.

where

$$\eta = \frac{\frac{E_f}{E_m} - 1}{\frac{E_f}{E_m} + \xi_{E_{11/22}}} \quad (\text{III.7})$$

and

$$\xi_{E_{11}} = \frac{2L}{D} \quad \xi_{E_{22}} = 2. \quad (\text{III.8})$$

Here, the index f represents the material properties of the fiber, whereas the index m indicates the matrix material. The shear modulus is given by

$$G_{12/23} = \frac{1 + \xi \eta \varphi}{1 - \eta \varphi} G_m \quad (\text{III.9})$$

with

$$\eta = \frac{\frac{G_f}{G_m} - 1}{\frac{G_f}{G_m} + \xi_{G_{12/23}}} \quad (\text{III.10})$$

and

$$\xi_{G_{12}} = 1 \quad \xi_{G_{23}} = \frac{\frac{K_m}{G_m}}{\frac{K_m}{G_m} + 2}. \quad (\text{III.11})$$

The compression modulus K_m reads

$$K_m = \frac{E_m}{3 - 6\nu_m}. \quad (\text{III.12})$$

The remaining Poisson's ration ν_{12} is calculated by the elementary mixture rules for fiber reinforced composites with the fiber volume fraction φ , which can be found in [4].

$$\nu_{12} = \varphi \nu_{12f} + (1 - \varphi) \nu_{12m}. \quad (\text{III.13})$$

Paper IV

Correlation analysis of the elastic-ideal plastic material behavior of short fiber-reinforced composites

Title: Correlation analysis of the elastic-ideal plastic material behavior of short fiber-reinforced composites

Author: Natalie Rauter¹

Affiliation: ¹Helmut-Schmidt-University /
University of the Federal Armed Forces Hamburg
Holstenhofweg 85, 22043 Hamburg, Germany

Journal: International Journal for Numerical Methods in Engineering
pp. 1-19, 2022

Status: Published

DOI: 10.1002/nme.7113

Abstract: For the numerical simulation of short fiber-reinforced composites and the correct analysis of the deformation, information about the plastic behavior and its spatial distribution is essential. When using purely deterministic modeling approaches information of the probabilistic microstructure is not included in the simulation process. One possible approach for the integration of stochastic information is the use of random fields, which requires information about the correlation structure of all material input parameters. In this study the correlation structure for finite strain elasto-plastic material behavior of short fiber-reinforced composites is analyzed. This approach combines the use of already established procedures for linear-elastic material behavior with a homogenization method for plasticity. The obtained results reveal a complex correlation structure, which is approximated with triangle and exponential correlation functions influenced by the window size. Due to the dependence of the hyperelastic and plastic material parameters on the fiber mass fraction, the strain-energy density function coefficients are cross-correlated with the yield strength of the composite. With this knowledge at hand, in a subsequent work numerical simulations of tensile tests are conducted that cover the elastic and plastic domain and include spatially distributed material properties.

IV.1 Introduction

Short fiber-reinforced composites (SFRC) are thermoplastic materials that are reinforced by short fibers or other particles. In contrast to the reinforcing elements, which usually show a brittle behavior, the thermoplastic matrix materials are characterized by a distinctive plastic deformation when allowing finite deformations [26, 152, 153]. Hence, the consideration of elasto-plastic material behavior is important for the modeling of SFRC to ensure an accurate prediction of the structural response under load. Furthermore, due to the spatial distribution and probabilistic characteristics of the reinforcing elements the material properties vary also over the spatial coordinates [57, 126, 141, 189]. Current modeling approaches address only one of these two aspects, either the local fluctuation of the material parameters of linear-elastic material behavior is investigated, or a modeling approach for the nonlinear material behavior is performed considering homogenization methods [1, 22, 85, 118]. A common approach for an elasto-plastic material model is the multiplicative decomposition of the deformation gradient as introduced by Lee [98] and Mandel [111]. Based on this approach, Simo et al. derived the framework of the finite strain elasto-plasticity by combining the multiplicative decomposition of the deformation gradient with hyperelastic strain-energy density functions [159, 160, 162]. Since then, this approach has been used widely, for example by Reina et al. [148, 149]. On the other hand, homogeneous second-order random fields are one possibility to model spatial distributed stochastic quantities like material properties of reinforced materials [57, 126, 141, 189]. Combining the finite strain elasto-plasticity with the use of random fields requires knowledge of the correlation structure of the strain-energy density function coefficients and the yield strength. When the correlation structure of the auto- and cross-correlation is established, random fields can be synthesized to represent the fluctuation of the nonlinear material properties on the component level without distinct modeling of the microstructure. Initial investigations of the correlation structure of material properties are provided by Sena et al. [157], which is limited to a checker board pattern. A second analysis is provided by Rauter et al. [144] focusing on the linear elastic domain.

Hence, the overall objective of this study is the numerical simulation of components made of SFRC including the spatial distribution of the plastic deformation described by the multiplicative decomposition of the deformation gradient in combination with hyperelastic material models for transversely isotropic symmetry. Therefore, the modeling approach presented in previous work by the author [141], which includes the spatial distribution of material properties but is limited to linear elasticity, will be extended to elasto-plastic material behavior. The work is divided into two parts. The first part, presented here, deals with the analysis of the correlation structure of the material properties. This knowledge is later used to generate second-order homogeneous random fields representing the spatial distribution of the material properties characterizing the elastic and plastic material behavior. Afterwards, these random fields are applied to a numerical model for the simulation of tensile tests covering the elastic and plastic domain. To validate the results, numerically obtained values are compared to experimental measurements in a subsequent work by the author [143].

Ensuing from this objective, the structure of the presented work is as follows. Section IV.2 holds the main aspects of the theoretical background including the fundamentals of the multi-scale and probabilistic modeling, finite strain elasto-plastic material behavior, and the homogenization of plastic material properties. In Section IV.3 the apparent overall material properties of the nonlinear material behavior are derived on the mesoscale by numerical simulations. The results of the correlation analysis are presented in Section IV.4. Finally, Section IV.5 gives a summary and conclusion.

IV.2 Theoretical background

This section comprises the basics concerning the stochastic framework, elasto-plastic material behavior and a homogenization method for plastic material properties.

IV.2.1 Stochastic framework

IV.2.1.1 Apparent material properties

All materials and especially reinforced materials show different characteristics when observed at different scales. Reinforced materials are strongly heterogeneous on the microscale. However, for numerical simulations on the component level, usually, homogeneous material properties are assumed. Therefore, the component is characterized by effective material properties that replace the spatially distributed by homogeneous material properties that are independent of the location. This scale transition from the microscale to the macroscale is achieved by homogenization. The main concept behind this homogenization is the representative volume element (RVE) [188], which was first introduced by Hill [70]. The RVE is a volume that consists of a statistically sufficient number of inclusions, and therefore, represents the effective behavior of the material. This implies that the size l of the inclusion or a microstructural characteristic must be much smaller than the size d of the RVE [64]. In addition, the RVE must be much smaller than the component with the dimension L . This separation of scales can be formulated as [28, 129, 190]

$$l \ll d \ll L, \quad (\text{IV.1})$$

where l is assigned to the microscale, L to the macroscale, and d to the edge length of the RVE.

To ensure the correct calculation of the effective material properties by numerical simulations Hill's condition [69] must be satisfied, given by

$$\langle \boldsymbol{\sigma} : \boldsymbol{\epsilon} \rangle = \langle \boldsymbol{\sigma} \rangle : \langle \boldsymbol{\epsilon} \rangle. \quad (\text{IV.2})$$

This condition expresses the equivalence between the local and global effective material properties of a heterogeneous material [69, 70]. The effective material properties for an RVE are written as

$$\langle \boldsymbol{\sigma} \rangle = \mathbb{C}^{\text{eff}} : \langle \boldsymbol{\epsilon} \rangle \quad (\text{IV.3})$$

and

$$\langle \boldsymbol{\epsilon} \rangle = \mathbb{S}^{\text{eff}} : \langle \boldsymbol{\sigma} \rangle, \quad (\text{IV.4})$$

where $\langle \cdot \rangle$ gives the volume average

$$\langle \cdot \rangle = \frac{1}{V} \int_V \cdot \, dV. \quad (\text{IV.5})$$

Hence, the strains $\boldsymbol{\epsilon}$ and stresses $\boldsymbol{\sigma}$ are microstructural quantities, whereas $\langle \boldsymbol{\epsilon} \rangle$ and $\langle \boldsymbol{\sigma} \rangle$ are related to the macroscopic scale. Furthermore, \mathbb{C}^{eff} and \mathbb{S}^{eff} are the effective stiffness and compliance tensor [190].

Suitable transformation of Eqs. (IV.3) and (IV.4) links the macroscopic quantities $\langle \boldsymbol{\epsilon} \rangle$ and $\langle \boldsymbol{\sigma} \rangle$ with the boundary values [190]. For the resulting boundary value problem, different types of boundary conditions can be established. Applying the average strain theorem and the average stress theorem to Eqs. (IV.3) and (IV.4) gives kinematic uniform boundary conditions of the kind $\boldsymbol{\epsilon}_0$ and static uniform boundary conditions of the kind $\boldsymbol{\sigma}_0$ [81].

Applying the boundary value problem on an RVE with simultaneous fulfillment of Hill's condition leads to three different kinds of boundary conditions [66, 67]

$$\mathbf{u} = \boldsymbol{\epsilon}_0 \cdot \mathbf{x} \quad \forall \mathbf{x} \in \partial V, \quad (\text{IV.6})$$

$$\mathbf{t} = \mathbf{t}_0 \cdot \mathbf{x} \quad \forall \mathbf{x} \in \partial V, \quad (\text{IV.7})$$

and

$$[\mathbf{t} - \mathbf{t}_0 \cdot \mathbf{x}] \cdot [\mathbf{u} - \boldsymbol{\epsilon}_0 \cdot \mathbf{x}] = 0 \quad \forall \mathbf{x} \in \partial V. \quad (\text{IV.8})$$

In the context of continuum mechanics Eq. (IV.6) gives a boundary condition of Dirichlet type, since pure kinematic boundary conditions with the constant macroscopic strain $\boldsymbol{\epsilon}_0$ are defined on the complete surface,

whereas Eq. (IV.7) is a boundary condition of Neumann type, because pure traction boundary conditions, with a constant macroscopic stress \mathbf{t}_0 are defined on the complete surface. A combination of these boundary condition types is given in Eq. (IV.8). For an RVE, the obtained material properties based on these boundary conditions are equal and hence, the material is assumed to be homogeneous. However, if the volume is smaller than the RVE one speaks of apparent overall properties [66, 67, 81]. In this case the extraction on the mesoscale is referred to as a statistical volume element (SVE) [130]. To determine the material properties for an SVE, the same procedure is used as for the effective material properties. However, now the results depend on the size of the extracted volume and the boundary conditions.

IV.2.1.2 Correlation

Combining the approach of apparent overall material properties with homogeneous second-order random fields on the component level enables one to model the structural behavior of inhomogeneous material properties induced by the probabilistic characteristics of the microstructure without the need of a scale transition [129]. To synthesize these homogeneous second-order random fields, the correlation structure must be known, which describes the point-to-point information of a stochastic quantity. For a continuous random field $Z(\omega, \mathbf{x})$ this is described by the covariance defined as

$$\text{Cov}[Z_1, Z_2] = E[Z_1 Z_2] - \mu_1 \mu_2. \quad (\text{IV.9})$$

Here, Z_1 and Z_2 are observations of the random field at different locations \mathbf{x}_i , E is the expectation operator, and μ_1 and μ_2 are the expected values of the random variables Z_1 and Z_2 , respectively. Usually, the dimensionless correlation parameter ρ_{12} is used, which is obtained by dividing Eq. (IV.9) by the standard deviations σ_i of the random variables. The standard deviation is defined as the square root of the variance, which is the second central moment

$$\sigma_{Z(\mathbf{x})} = \sqrt{\text{Var}[Z(\mathbf{x})]}. \quad (\text{IV.10})$$

Hence, the dimensionless correlation parameter reads

$$\rho_{12} = \rho_{Z_1, Z_2} = \frac{\text{Cov}[Z_1, Z_2]}{\sigma_1 \sigma_2}. \quad (\text{IV.11})$$

If the random variables Z_1 and Z_2 belong to the same random field Eqs. (IV.9) and (IV.11) give the auto-covariance and auto-correlation of the random field, otherwise it is referred to as the cross-covariance and cross-correlation, respectively. However, for most applications the random field is given by a discrete number of realizations ω_i , because the probability density function is unknown. In this case, instead of the expected value the spatial average is used

$$\overline{Z(\mathbf{x})} = \frac{1}{N} \sum_{i=1}^N Z(\omega_i, \mathbf{x}) \quad (\text{IV.12})$$

and rewriting the variance leads to

$$s^2(\mathbf{x}) = \overline{Z(\mathbf{x})^2} - \overline{Z(\mathbf{x})}^2. \quad (\text{IV.13})$$

Consequently, the dimensionless correlation parameter for a discrete number of realizations ω_i is calculated by evaluating

$$\rho_{12} = \rho_{Z_1, Z_2} = \frac{[\overline{Z_1 - \overline{Z_1}}][\overline{Z_2 - \overline{Z_2}}]}{s_1 s_2}. \quad (\text{IV.14})$$

For the synthesizing the random fields, the dimensionless correlation parameter is approximated by a correlation function. Examples for typically used correlation functions are the exponential correlation function [48, 128, 169]

$$\rho(\xi_1, \xi_2) = \exp^{-\frac{|\xi_1|}{b_1} - \frac{|\xi_2|}{b_2}}, \quad (\text{IV.15})$$

the triangle correlation function

$$\rho(\xi_1, \xi_2) = \begin{cases} \left(1 - \frac{|\xi_1|}{b_1}\right) \left(1 - \frac{|\xi_2|}{b_2}\right) & \text{if } |\xi_1| \leq b_1, |\xi_2| \leq b_2 \\ 0 & \text{else} \end{cases}, \quad (\text{IV.16})$$

and the Gaussian correlation function

$$\rho(\xi_1, \xi_2) = \exp\left(-\left(\frac{\xi_1}{b_1}\right)^2 - \left(\frac{\xi_2}{b_2}\right)^2\right). \quad (\text{IV.17})$$

Here, b_1 and b_2 are the correlation lengths with respect to the coordinate ξ_1 and ξ_2 , respectively. The functions given in Eqs. (IV.15) and (IV.16) have the advantage that they lead to analytical solutions for the eigenvalue problem, that needs to be solved when using the Karhunen-Loève expansion for the generation of random fields for a rectangular domain [48, 136, 169]. One technique to extract the relation between the information at different locations \mathbf{x}_i is the moving window method [8, 51, 156]. Within this method a window of predefined size is used to extract segments of a larger microstructure. Since the material parameters of an SVE are assigned to the spatial coordinates and are no longer identical at each material point, the local fluctuation of the material properties can be derived.

IV.2.2 Elasto-plastic material behavior

The modeling approach of plasticity in combination with finite deformation is based on the multiplicative decomposition of the deformation gradient, which is introduced by Lee [98] and Mandel [111]

$$\mathbf{F} = \mathbf{F}_{\text{el}} \cdot \mathbf{F}_{\text{pl}}. \quad (\text{IV.18})$$

Here, \mathbf{F}_{el} holds the elastic and \mathbf{F}_{pl} the plastic deformation, respectively. Based on this approach, Simo et al. derived the framework of the finite strain elasto-plasticity by combining the multiplicative decomposition of the deformation gradient with hyperelastic strain-energy density functions [159, 160, 162]. Hence, for the material modeling of SFRC a strain-energy density function is required that considers transversely-isotropic material behavior. Usually these potentials are divided into two parts, one representing the isotropic response Ψ_{iso} and a second part for the transversely-isotropic behavior Ψ_{trn}

$$\Psi = \Psi_{\text{iso}} + \Psi_{\text{trn}}. \quad (\text{IV.19})$$

In addition to the strain invariants for isotropic behavior I_1 , I_2 , and I_3 , for the description of transversely-isotropic material behavior the pseudo-invariants I_4 and I_5 are required. For a symmetric second-order tensor \mathbf{B} these two are defined by

$$I_4 = \mathbf{a} \cdot \mathbf{B} \cdot \mathbf{a} \quad \text{and} \quad I_5 = \mathbf{a} \cdot \mathbf{B}^2 \cdot \mathbf{a}, \quad (\text{IV.20})$$

where the vector \mathbf{a} gives the fiber orientation of the material.

The isotropic behavior is mostly given by well-known potentials of Neo-Hooke or Mooney-Rivlin [7, 10, 120, 151]. In this work, the Neo-Hooke potential in terms of the right Cauchy-Green tensor \mathbf{C} is used [10]

$$\Psi_{\text{Neo}}(\mathbf{C}) = \frac{1}{2} \Lambda (J - 1)^2 - \mu \ln(J) + \frac{1}{2} \mu (\text{tr } \mathbf{C} - 3). \quad (\text{IV.21})$$

Here, J is the Jacobian determinant and Λ and μ are the Lamé coefficients. This potential already leads to a strain-dependent elasticity tensor and therefore, induces nonlinear material behavior. The corresponding elasticity tensor reads

$$\mathbb{C}_{\text{Neo}} = \Lambda J (2J - 1) \mathbf{C}^{-1} \otimes \mathbf{C}^{-1} + 2 [\mu - \Lambda J (J - 1)] \mathbb{G}, \quad (\text{IV.22})$$

with

$$G_{ijkl} = (\mathbf{C}^{-1})_{ik}(\mathbf{C}^{-1})_{jl}. \quad (\text{IV.23})$$

For the representation of transversely-isotropic material behavior there exist several strain-energy density functions [87, 124, 140, 147]. However, most of these potentials are either not fully nonlinear, because the resulting stiffness tensor is independent of the deformation [87, 147] or include more than five independent material parameters [124, 140]. Therefore, in this study the potential given by Bonet et al. [16] is used, because it is fully nonlinear, but uses only five independent material parameters when combining the transversely-isotropic part with the isotropic potential given in Eq. (IV.21). The transversely-isotropic part of the potential reads

$$\Psi_{\text{tn}}(\mathbf{C}) = [\alpha + \beta(\text{tr } \mathbf{C} - 3) + \gamma(I_4 - 1)](I_4 - 1) - \frac{1}{2}\alpha(I_5 - 1), \quad (\text{IV.24})$$

where α , β , and γ are independent material parameters. The use of this strain-energy density function in combination with Eq. (IV.21) leads to a fully nonlinear representation of the material, since both parts of the potential result in a strain-dependent elasticity tensor. Based on the full potential the elasticity tensor for the transversely-isotropic material as a function of the deformation is given by

$$\begin{aligned} \mathbb{C}_{\text{full}} = & \Lambda J(2J - 1)\mathbf{C}^{-1} \otimes \mathbf{C}^{-1} + 2[\mu - \Lambda J(J - 1)]\mathbb{G} \\ & + 8\gamma \mathbf{a} \otimes \mathbf{a} \otimes \mathbf{a} \otimes \mathbf{a} + 4\beta(\mathbf{a} \otimes \mathbf{a} \otimes \mathbf{C}^{-1} + \mathbf{C}^{-1} \otimes \mathbf{a} \otimes \mathbf{a}) - \alpha \mathbb{A} - 4\beta(I_4 - 1)\mathbb{G}, \end{aligned} \quad (\text{IV.25})$$

where

$$A_{ijkl} = a_i a_l \delta_{jk} + \delta_{ik} a_j a_l. \quad (\text{IV.26})$$

To determine the five material parameters Λ , μ , α , β , and γ of the strain-energy density function the elasticity tensor is linearized by evaluating at zero strain for a fiber orientation in x -direction. In matrix notation this leads to

$$C_{\text{full}} = \begin{bmatrix} 8(\gamma + \beta) + \Lambda + 2\mu - 2\alpha & 4\beta + \Lambda & 4\beta + \Lambda & 0 & 0 & 0 \\ 4\beta + \Lambda & \Lambda + 2\mu & \Lambda & 0 & 0 & 0 \\ 4\beta + \Lambda & \Lambda & \Lambda + 2\mu & 0 & 0 & 0 \\ 0 & 0 & 0 & 2\mu & 0 & 0 \\ 0 & 0 & 0 & 0 & 2\mu - \alpha & 0 \\ 0 & 0 & 0 & 0 & 0 & 2\mu - \alpha \end{bmatrix}, \quad (\text{IV.27})$$

which holds the transversely-isotropic symmetry.

IV.2.3 Homogenization of plastic material properties

To derive the apparent overall plastic material properties a homogenization method is used, that allows one to determine, the yield function and subsequently the yield strength of a reinforced composite [102]. In this case the effective local potential of the phase r for a nonlinear composite is expressed as

$$u^{(r)}(\mathbf{x}, \boldsymbol{\sigma}) = \text{stat}_{\mu_0, k_0 \geq 0} \left\{ u_0(\mathbf{x}, \boldsymbol{\sigma}) - V^{(r)}(\mathbf{x}, \mu_0, k_0) \right\}. \quad (\text{IV.28})$$

Here, u_0 is the local potential of a linear comparison composite [138], which has the same microstructure as the nonlinear composite, and μ_0 and k_0 are the corresponding shear and bulk moduli, respectively. The functions $V^{(r)}(\mu_0, k_0)$ are so called error functions given by [139]

$$V^{(r)}(\mathbf{x}, \mu_0, k_0) = \text{stat}_{\boldsymbol{\sigma}} \left\{ u_0(\mathbf{x}, \boldsymbol{\sigma}) - u^{(r)}(\mathbf{x}, \boldsymbol{\sigma}) \right\}. \quad (\text{IV.29})$$

In a next step the macroscopic potential of the composite is obtained by

$$\tilde{U}(\bar{\sigma}) = \min_{\sigma \in S} \langle u(\mathbf{x}, \sigma) \rangle = \text{stat}_{\sigma \in S} \langle u(\mathbf{x}, \sigma) \rangle, \quad (\text{IV.30})$$

where

$$S = \{ \sigma, \text{div } \sigma = \mathbf{0} \text{ in } \Omega, \langle \sigma \rangle = \bar{\sigma} \}. \quad (\text{IV.31})$$

Introducing Eq. (IV.28) in Eq. (IV.30) and interchanging the stationary operators leads to the definition of the effective macroscopic potential of the nonlinear composite. Considering a composite consisting of two phases, with constant material properties and a volume fraction of $c^{(r)}$ results in

$$\tilde{U}(\bar{\sigma}) = \text{stat}_{\mu_0^{(s)}, k_0^{(s)} \geq 0} \left\{ \tilde{U}_0(\bar{\sigma}) - \sum_{r=1}^2 c^{(r)} V^{(r)}(\mu_0, k_0) \right\}, \quad (\text{IV.32})$$

with \tilde{U}_0 being the effective potential of the linear comparison composite.

Applying the procedure to SFRC both phases are assumed to be isotropic. Furthermore, the plastic deformation is exclusively assigned to the matrix material, since the reinforcing fibers show brittle fracture after linear elastic behavior. Therefore, first, the stress potential used for both phases, is given by

$$U^{(r)}(\sigma) = \frac{1}{2k^{(r)}} \sigma_m^2 + \phi^{(r)}(\tau_e), \quad (\text{IV.33})$$

where σ_m is the hydrostatic stress component and the function $\phi^{(r)}(\tau_e)$ gives the distortional response of the corresponding phase, which depends on the equivalent shear stress τ_e . For the linear-elastic inclusion phase ($r = 2$) a linear distortional response is assumed

$$\phi^{(2)}(\tau_e) = \frac{1}{2\mu^{(2)}} \tau_e^2. \quad (\text{IV.34})$$

In contrast to this the matrix material ($r = 1$) is characterized by a plastic deformation for stresses above the yield strength in shear $\tau_y^{(1)}$

$$\phi^{(1)}(\tau_e) = \frac{\tau_e^2}{2\mu^{(1)}} + \frac{(\tau_y^{(1)})^2}{2\mu^{(1)}} \left\{ \frac{2}{n+1} \left[\left(\frac{\tau_e}{\tau_y^{(1)}} \right)^{n+1} - 1 \right] - \left[\left(\frac{\tau_e}{\tau_y^{(1)}} \right)^2 - 1 \right] \right\} H(\tau_e - \tau_y^{(1)}). \quad (\text{IV.35})$$

Here, H is the Heaviside function and n gives the hardening exponent. The dilational response for both phases is assumed to be linear. In conclusion, the SFRC is modeled as a two-phase composite consisting of an elasto-plastic matrix material with power-law hardening behavior and linear-elastic inclusions. For the hardening coefficient $1 \leq n \leq \infty$ holds, where $n = 1$ indicates linear-elastic and $n = \infty$ rigid-ideally plastic behavior, respectively [82].

Following the procedure introduced by Li et al. [102] the error functions are bounded only in case $k_0^{(1)} = k^{(1)}$, $k_0^{(2)} = k^{(2)}$, and $\mu_0^{(2)} = \mu^{(2)}$ hold, which is simultaneously the best choice considering Eq. (IV.32). Selecting these values the error functions reduces to

$$V^{(1)}(\mathbf{x}, \mu_0^{(1)}, k_0^{(1)}) = \text{stat}_{\tau_e > 0} \left\{ \frac{\tau_e^2}{2\mu_0^{(1)}} - \phi^{(1)}(\tau_e) \right\} \quad (\text{IV.36})$$

and

$$V^{(2)} = 0, \quad (\text{IV.37})$$

respectively, which enables one to rewrite the effective potential from Eq. (IV.32)

$$\tilde{U}(\bar{\sigma}) = \text{stat}_{\mu_0^{(1)} \geq 0} \left\{ \tilde{U}_0(\bar{\sigma}) - c^{(1)} V^{(1)}(\mu_0^{(1)}) \right\}. \quad (\text{IV.38})$$

At this stage not only the distortional response $\phi^{(1)}(\tau_e)$ but also the error function $V^{(1)}$ can be separated for the linear ($\mu_0^{(1)} \geq \mu^{(1)}$) and the nonlinear case ($\mu_0^{(1)} < \mu^{(1)}$). With this, the convexity of $V^{(1)}$ in $1/\mu_0^{(1)}$, and the assumption of the monotone increasing behavior of \tilde{U}_0 with $1/\mu_0^{(1)}$ it can be shown that the effective potential is quadratic. Subsequently, the composite shows a linear response if

$$\left. \frac{\partial \tilde{U}_0}{\partial \mu_0^{(1)}}(\bar{\sigma}) \right|_{\mu_0^{(1)} = \mu^{(1)}} + \frac{c^{(1)}}{2} \left(\frac{\tau_y^{(1)}}{\mu^{(1)}} \right)^2 > 0 \quad (\text{IV.39})$$

is satisfied and in case

$$\left. \frac{\partial \tilde{U}_0}{\partial \mu_0^{(1)}}(\bar{\sigma}) \right|_{\mu_0^{(1)} = \mu^{(1)}} + \frac{c^{(1)}}{2} \left(\frac{\tau_y^{(1)}}{\mu^{(1)}} \right)^2 < 0 \quad (\text{IV.40})$$

holds the composite shows ductile deformation. Following these two conditions Li et al. [102] proposed a yield function given by

$$\Phi(\bar{\sigma}) = - \left[\left. \frac{\partial \tilde{U}_0}{\partial \mu_0^{(1)}}(\bar{\sigma}) \right|_{\mu_0^{(1)} = \mu^{(1)}} + \frac{c^{(1)}}{2} \left(\frac{\tau_y^{(1)}}{\mu^{(1)}} \right)^2 \right]. \quad (\text{IV.41})$$

Since the inclusions show linear-elastic material behavior, the yield function only depends on the material properties of the matrix material. Furthermore, it is independent of the hardening exponent. The initial yield strength is derived by solving $\Phi = 0$, which requires only linear-elastic simulations, because the derivative of the effect potential \tilde{U}_0 with respect to $\mu^{(1)}$ is based on the linear comparison composite. Beside this, the yield strength shows anisotropic behavior.

IV.3 Determination of the apparent material properties

IV.3.1 Methodology

To simulate the elasto-plastic behavior of a component made of SFRC the parameters of the strain-energy density function and the yield strength are required, since the matrix is assumed to show ideal-plastic behavior. Hence, the apparent values of these material properties are derived from artificial microstructures. This is done separately for the hyperelastic and plastic material properties. For the hyperelastic properties, the parameters of the strain-energy density function are determined based on numerically obtained stiffness matrices, which requires a linearization at zero strain. However, due to the reduction to a two-dimensional simulation, the stiffness matrix holds only four independent values. Therefore, an additional equation is required to receive unique solutions for all five independent coefficients of the strain-energy density function. Because of that, first, the engineering constants are calculated from the the compliance matrix obtained by numerical simulation. Due to the plane strain assumption the elements of the compliance matrix are a function of all five independent engineering constants E_1 , E_2 , ν_{12} , ν_{23} , and G_{12} of a transversely-isotropic material.

This problem is solved by utilizing the fiber volume fraction. Since, the artificial microstructures are based on a binary image [141] the fiber volume fraction of each extraction is derived by dividing the number of pixels representing fibers by the number of all pixels of the extraction. With this information at hand the fiber volume fraction of the numerical model is known and the Poisson's ratio ν_{23} can be approximated by using the Halpin-Tsai material model [61, 62]. Now it is possible to determine the remaining constants E_1 , E_2 , ν_{12} , and G_{12} . With all this information at hand, the stiffness matrix of transversely isotropic material behavior is established before using its elements to compute the parameters of the strain-energy density function by

Component	E GPa	ν -	ρ kg/m ³
Glass	72	0.22	2500
PBT	2.6	0.41	1300

Table IV.1: Material properties.

evaluating Eq. (IV.27). A detailed summary of the used framework is provided in Appendix IV.A.

For the determination of the yield strength, the homogenization procedure presented in Section IV.2.3 is used. To evaluate the yield condition

$$\left[\frac{\partial \tilde{U}_0}{\partial \mu_0^{(1)}}(\bar{\sigma}) \right]_{\mu_0^{(1)}=\mu^{(1)}} + \frac{c^{(1)}}{2} \left(\frac{\tau_y^{(1)}}{\mu^{(1)}} \right)^2 = 0 \quad (\text{IV.42})$$

a linear-elastic numerical model of the linear comparison composite is solved for different values of $\mu^{(1)}$, characterizing the matrix material. Based on the obtained derivative of the effective potential \tilde{U}_0 the apparent yield strength of the microstructure can be calculated. It is equal to the stress for which Eq. (IV.42) is valid.

IV.3.2 Numerical model

In the work of Rauter et al. [141] a modeling approach is introduced to determine the apparent material properties of SFRC for linear-elastic material behavior. This procedure is adapted to an elasto-plastic material response as shown below. As done by Rauter et al. [141] based on the probabilistic information of the fiber length, fiber diameter, and fiber orientation distribution 500 artificial microstructures with a size of $2500 \mu\text{m} \times 2500 \mu\text{m}$ are generated. The center coordinates of each fiber are provided by a Monte Carlo sampling, whereas the fiber properties are sampled with respect to their individual probability density function, which are taken from Günzel [58]. Next, for each microstructure 33 windows of the size $250 \mu\text{m} \times 250 \mu\text{m}$, $500 \mu\text{m} \times 500 \mu\text{m}$, and $750 \mu\text{m} \times 750 \mu\text{m}$ are extracted in accordance with Figure IV.1, see also previous work by the author [141]. The distance between the windows is equal to a quarter of the window size in vertical and horizontal direction. Along the diagonal, the distance is $\sqrt{2}/4$ times the window size. This ensures the ability to determine the two-dimensional correlation function accurately. Next, the microstructures are translated into an array, which contains the material properties for every point. Finally, the material properties of the microstructure are passed to the integration points of the numerical model. For both constituents, only linear-elastic material behavior is required. The corresponding material parameters of Polybutylene terephthalate (PBT) matrix material and of glass are given in Table IV.1. The fiber mass fraction is set to 30 % (PBT GF 30).

The numerical model is generated in accordance with the findings in Rauter et al. [141]. For the determination of the strain-energy density function coefficients and the yield strength, the same model is used. Since this two-dimensional model is a cross-section of a three-dimensional tensile test specimen, a plane strain state is assumed. This is reasonable, because the cross-section of SFRC manufactured by mold injection shows a layered structure [41, 43, 154]. In the middle is a core layer, which is characterized by an out-of-plane fiber orientation, that induces a resistance of the tensile test specimen against shrinking. To include this effect without an explicit modeling of this layer, the plane strain assumption is used. Therefore, only the shell layers are considered as shown by Rauter et al. [141].

IV.3.3 Results

In this section the results for the parameters of the strain-energy density function, the yield strength, and the correlation analysis are presented.

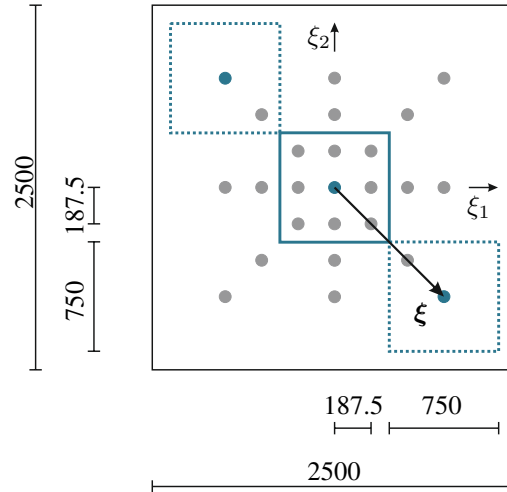


Figure IV.1: Moving window method applied to the artificial microstructure. All measures in μm .

	Sample	Λ GPa	μ GPa	α GPa	β GPa	γ GPa	E_{11} GPa
Mean	250 μm	5.62	1.34	1.16	-0.20	1.35	11.9
	500 μm	5.43	1.24	1.13	-0.14	1.19	10.5
	750 μm	5.38	1.20	1.10	-0.13	1.13	10.0
	Experiment	-	-	-	-	-	9.75
Standard-deviation	250 μm	0.492	0.192	0.239	0.081	0.475	3.85
	500 μm	0.224	0.097	0.131	0.033	0.244	1.96
	750 μm	0.140	0.064	0.090	0.020	0.148	1.26
	Experiment	-	-	-	-	-	0.27

Table IV.2: Mean values and standard deviations of the strain density function coefficients.

IV.3.3.1 Hyperelasticity

In Table IV.2 the mean value and the standard deviation for each parameter of the strain-energy density function is given. Since the numerical simulations are performed by applying pure displacement boundary conditions the mean of the absolute values show a decreasing tendency with increasing window size. Furthermore, the standard deviation increases with an decreasing window size, as expected. These observations meet the expectation of simulations on the mesoscale. In addition, the Young's modulus in horizontal direction is provided to validate the results with experimental investigations of tensile tests performed with specimens made of PBT GF 30. The experimentally obtained mean value based on 13 specimens is 9.75 GPa with a standard deviation of 0.27 GPa. A comparison with the numerically obtained values shows, that for all window sizes the numerical values cover the experimental results. Hence, the results for the parameters of the strain-energy density function appears to be reasonable.

IV.3.3.2 Plasticity

In Table IV.3 the mean value and standard deviation of the obtained yield strength is given for each window size. For a validation of the results, Figure IV.2 gives the strain-stress curve for a tensile test specimen made of PBT

Sample	Mean yield strength MPa	Standard deviation MPa
250 μm	151.7	57.1
500 μm	130.3	24.2
750 μm	125.7	14.7

Table IV.3: Results yield strength.

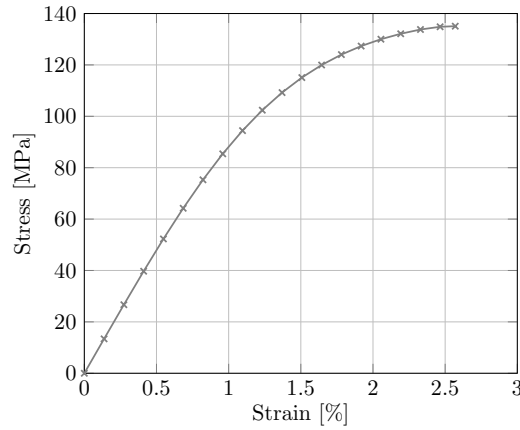


Figure IV.2: Stress strain curve for PBT GF 30 under uniaxial loading in melt flow direction, values taken from the data sheet of the manufacturer [21].

GF 30, taken from the data sheet of the manufacturer [21]. Assuming ideal plastic behavior, the experimentally obtained yield strength fits very well with the numerical results for the different window sizes.

Furthermore, in Figure IV.3 the spatial distribution of the yield strength is shown. First, Figure IV.3a gives an exemplary microstructure of the size $2500 \mu\text{m} \times 2500 \mu\text{m}$, where the center points of each extracted window with an edge length of $750 \mu\text{m}$ is indicated. In the context of SFRC the fiber mass fraction φ_m is commonly used. It can be computed from the fiber volume fraction by evaluating

$$\varphi_m = \frac{\rho_m \varphi}{\rho_f \varphi + \rho_m (1 - \varphi)}. \quad (\text{IV.43})$$

Subsequently, in Figure IV.3b and Figure IV.3c for each of these windows the fiber mass fraction and the resulting yield strength are provided, respectively. Since the reinforcing fibers are modeled with linear elastic material behavior and hence, they do not show any plastic deformation, it is expected that with an increasing amount of fibers in an extracted window the yield strength increases. This expectation can be validated by Figure IV.3b and Figure IV.3c. Windows with a higher fiber mass fraction show a significantly increasing yield strength. Based on the comparison with experimental results as well as the correlation between the fiber mass fraction and the obtained yield strength, the homogenization procedure appears to be applicable to SFRC.

IV.4 Correlation

IV.4.1 Overall behavior

For the analysis of the correlation between the coefficients of the strain-energy density function and the yield strength first, in Figure IV.4 the parameters for a window size of $750 \mu\text{m}$ are plotted against each other. If the two parameters of a plot are not correlated, the realizations give a random cloud of points. On the other hand,

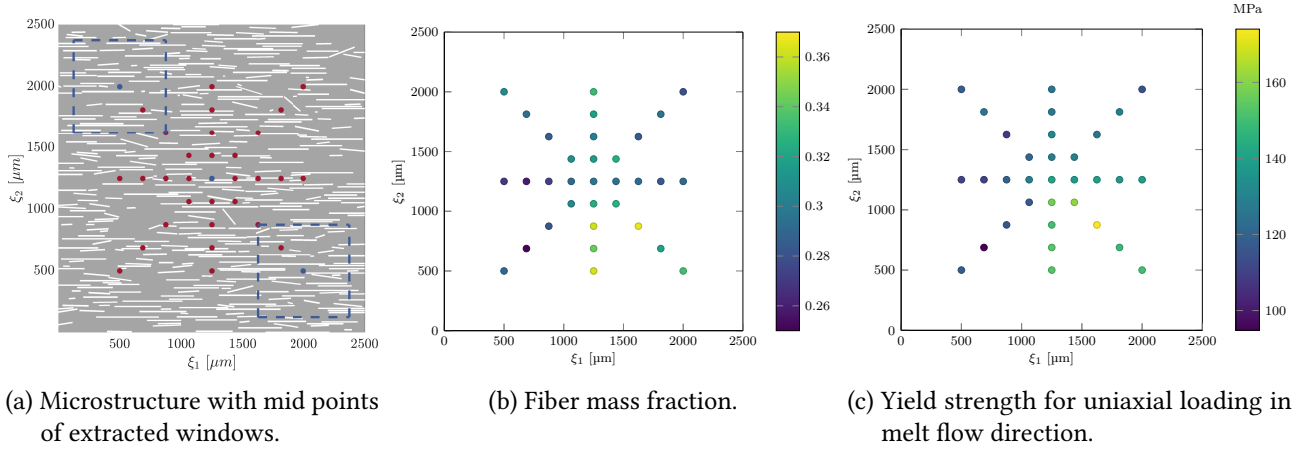


Figure IV.3: Example for the analysis of the yield strength for a window size of 750 μm .

the $\Lambda - \gamma$ parameter pair shows a distinct correlation, which is indicated by the alignment of the individual points on the diagonal. The stronger the correlation, the more pronounced is the concentration of the points, until they all lie on a straight line, as can be seen for the auto-correlations. One further example for a strong cross-correlation is the $\mu - \alpha$ parameter pair. This strong correlation meets the theoretical framework of the hyperelastic strain-energy density function. In Appendix IV.A the relation between the strain-energy density function coefficients and the components of the elasticity tensor is given. Following Eq. (IV.48), the parameters μ and α are directly linked to each other. The same holds for the parameter group of $\gamma, \mu, \Lambda, \alpha$, and β . Since γ is a function of μ, Λ, α , and β , these parameters should be significantly correlated to γ . This is confirmed in Figure IV.4. Finally, Figure IV.4 shows that the symmetry $\rho_{ij} = \rho_{ji}$ required by the definition is fulfilled and that the coefficients of the strain-energy density function and the yield strength are coupled by a complex correlation structure.

As already shown by Rauter et al. [141] for the linear elastic material parameters, the correlation depends on the window size. First, due to the definition of the different correlation functions, as given in Eqs. (IV.15) to (IV.17), the correlation length is bounded to the window size. However, not only the correlation length b_i but also the correlation strength given by the cross-correlation parameter a is influenced by the window size. In Figure IV.5 three different scenarios are depicted, that are obtained by evaluating Eq. (IV.11) for each window size. For better comparability, the coordinates ξ_1 and ξ_2 are normalized by the window size. The parameter pair $\gamma - \mu$ shows an independent cross-correlation strength with respect to the window size. Furthermore, the coefficient a is close to one for completely overlapping windows, which indicates a very pronounced cross-correlation. This also meets the distribution of the realizations in Figure IV.4, where the points are strongly aligned on the diagonal.

In the middle, the coefficient pair $\alpha - \mu$ is given. Here, the cross-correlation shows a significant influence of the window size on the parameter a . With an increasing window size, the parameter a also increases. In contrast to this, the parameter pair β and σ_y show the opposite behavior. With an increasing window size the parameter a decreases, which leads to a reduction of the correlation. This behavior is also observed for linear-elastic material properties, as shown in previous work [141]. Furthermore, in this case the value of the dimensionless correlation parameter is negative, which is induced by the different sign of the parameters β and σ_y . As given in Table IV.2 the values of β are negative, whereas the values of σ_y are positive.

IV.4.2 Correlation length

In a next step the correlation length is determined for each parameter pair. Therefore, first, the three different correlation functions given by Eqs. (IV.15) to (IV.17) are fitted with the calculated dimensionless correlation parameter. Based on the coefficient of determination R^2 , the best fit is selected to analyze the correlation

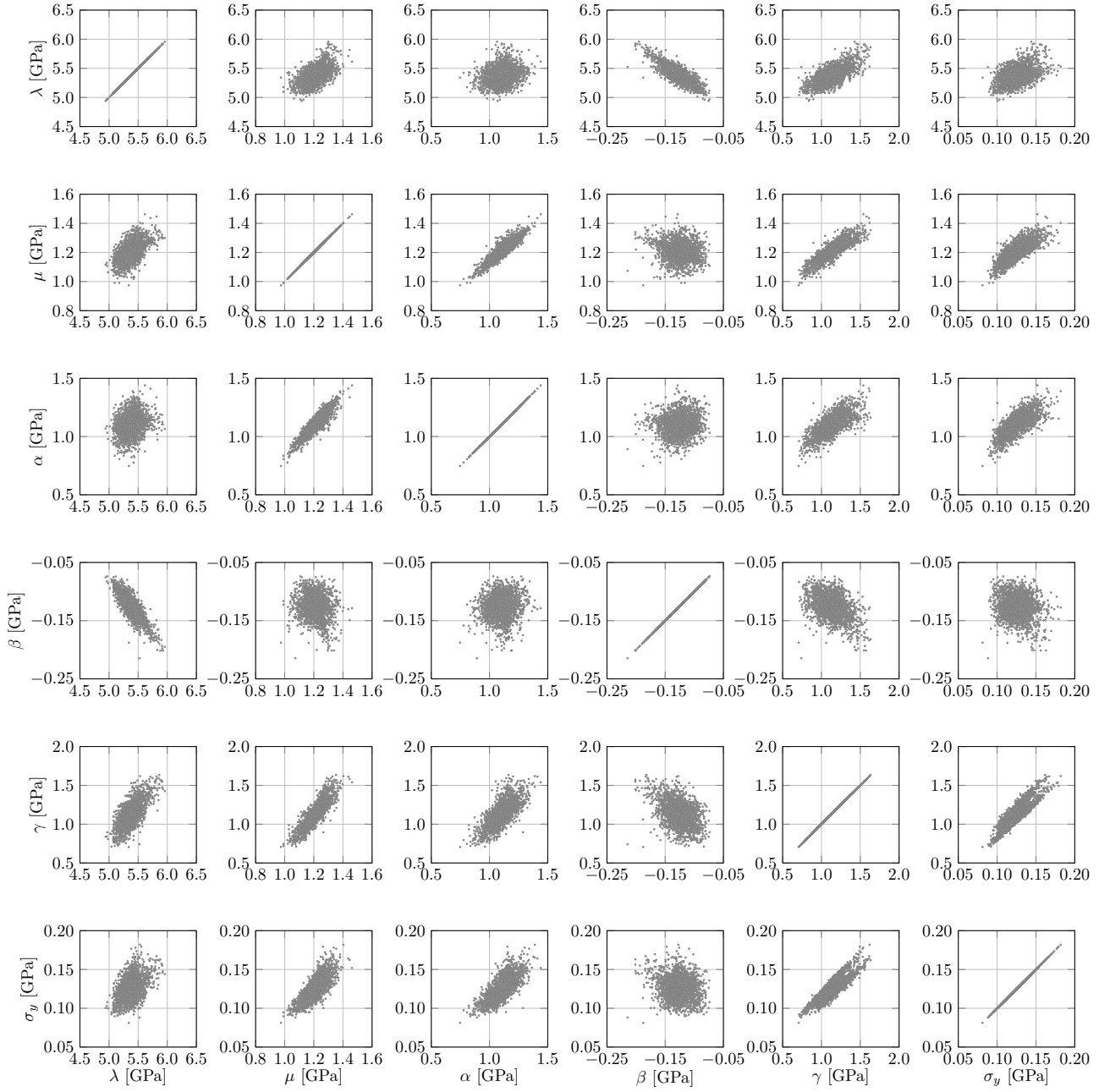


Figure IV.4: Correlation of the parameter pairs for a window size of 750 μm .

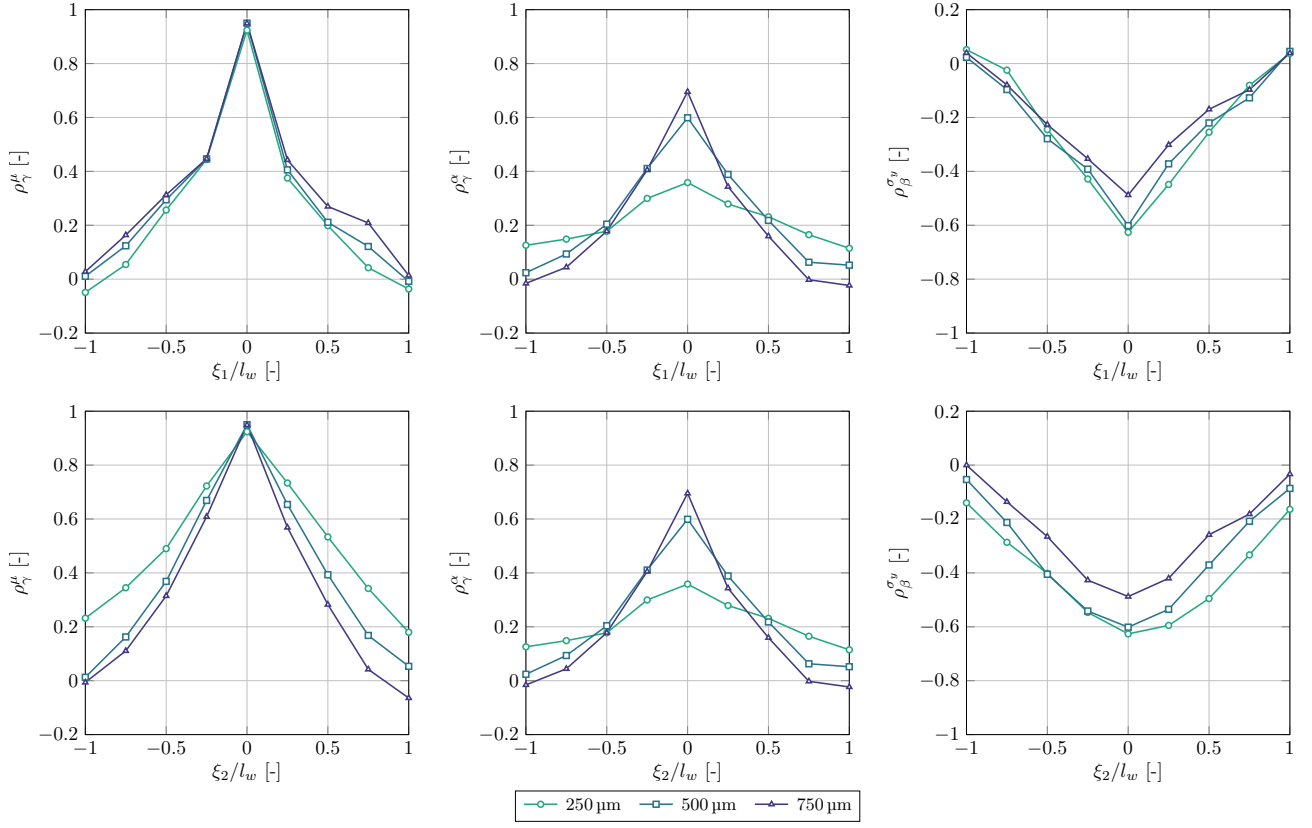


Figure IV.5: Dimensionless correlation parameters $\rho_{\gamma\mu}$, $\rho_{\gamma\alpha}$, and $\rho_{\beta\sigma_y}$ for each window size.

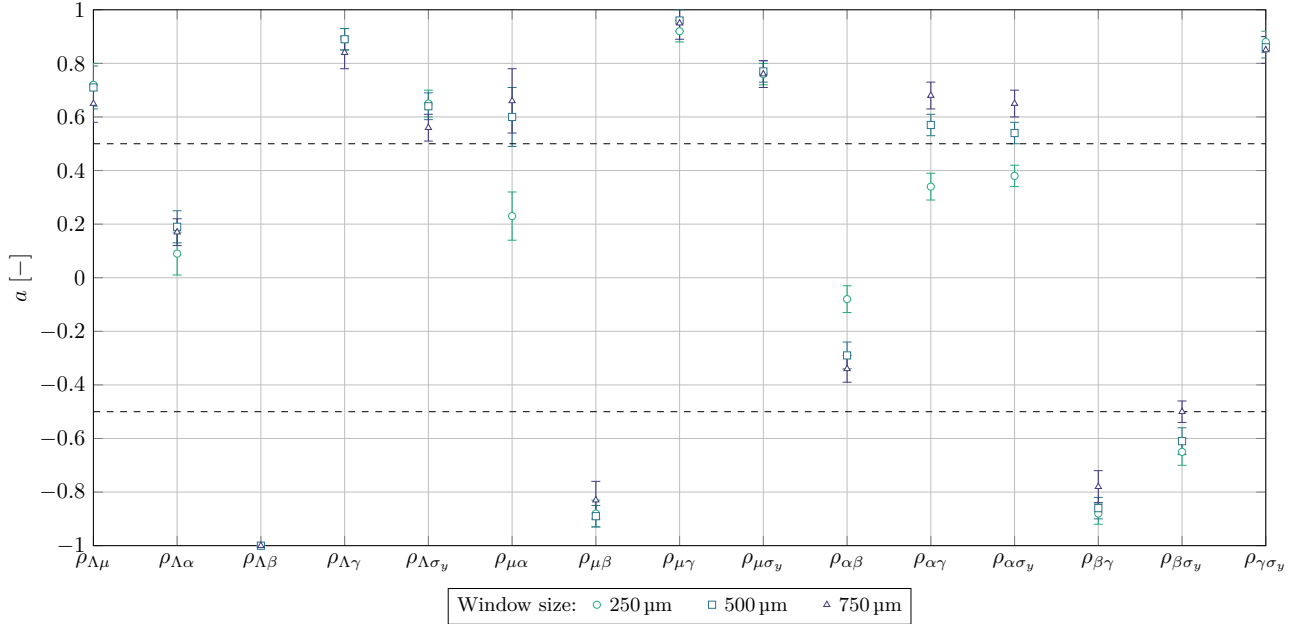


Figure IV.6: Cross-correlation coefficient a for all window sizes.

length in a second step. The results of R^2 for each window size and each correlation function are provided in Appendix IV.B. The results of the curve fit for the auto-correlation indicate that the triangle correlation function is the best fit for the parameters Λ , β , γ , and σ_y , whereas the exponential correlation function fits the

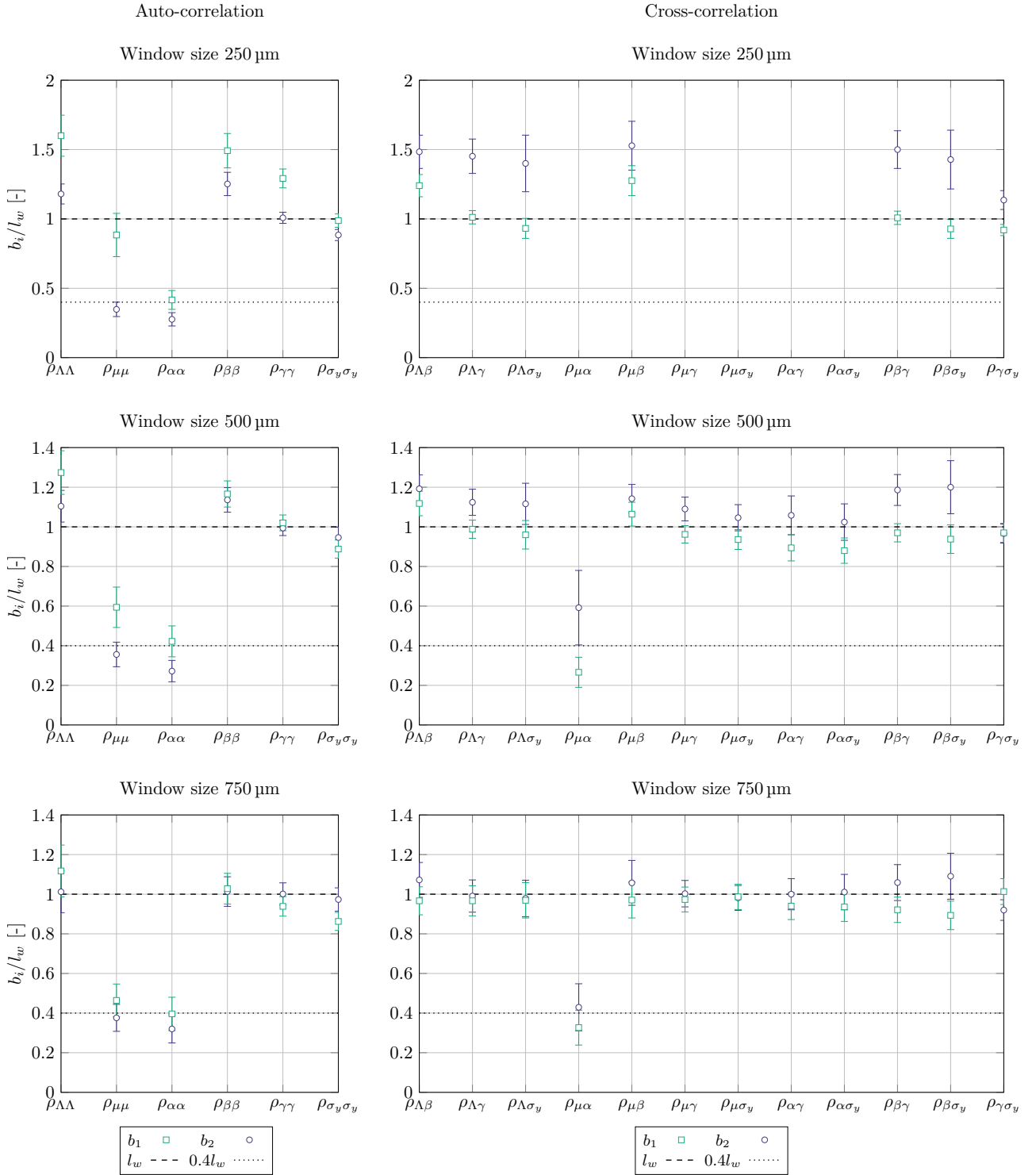


Figure IV.7: Analysis of the correlation length for each auto- and cross-correlation.

parameters μ and α best. Consequently it is expected that the exponential correlation function is the best option for the cross-correlation of these two parameters. The remaining parameter pairs should be approximated best by triangle cross-correlation function, because the corresponding auto-correlation functions of these parameters are given by a triangle correlation function, which is confirmed by the R^2 values of the performed curve fits given in Appendix IV.B.

For a detailed analysis of the auto- and cross-correlation, Figures IV.6 and IV.7 illustrate the results of the cross-correlation parameter a and the correlation lengths, respectively. The coefficient a describes the strength of the correlation between two parameters. Hence, for small absolute values of a the parameters are not correlated, which results in a random cloud of points in the corresponding diagram of Figure IV.4. For each window size and each parameter pair, the mean value and the 95% confidence interval is given. The dashed lines in Figure IV.6 indicate a cross correlation coefficient of $|a| = 0.5$. First, the dependence of a on the window size, as discussed before, is observable. Furthermore, the parameter pairs $\Lambda - \alpha$ and $\alpha - \beta$ are only very weakly cross-correlated, which is confirmed in Figure IV.4. For the remaining parameters, the correlation lengths b_1 and b_2 are calculated for both the auto- and cross-correlation, see Figure IV.7. Furthermore, dashed and dotted lines are added to indicate the window size l_w and a correlation length of $0.4l_w$. As done before, for each parameter pair the mean value and the 95% confidence interval are plotted. The results show, that with an increasing window size, the distance between b_1 and b_2 decreases. Furthermore, for an approximation with the triangle function the values converge to the edge length of the analyzed window. For the exponential function the value is $0.4l_w$. However, it is important to note that this correlation analysis gives only the behavior of the correlation with respect to the window size and hence, is a qualitative statement. Since the correlation length can be interpreted as an additional independent material parameter its value, which is required to synthesize random fields for the representation of the spatial distributed material parameters, needs to be derived from experimental investigations.

IV.5 Summary and Conclusion

In this work an approach is presented to extract the correlation structure of the finite strain elasto-plastic material properties of SFRC given by the five independent parameters of the transversely-isotropic strain-energy density function and the yield strength. Due to the linearization of the strain-energy density function at zero strain and the use of a homogenization procedure for the determination of the yield strength only linear-elastic simulations are required to obtain the apparent overall material properties for extractions of the microstructure at different locations. The obtained results are validated by experimental data, taken from literature. Furthermore, the expected link between the fiber mass fraction and the yield strength is confirmed.

With this data the dimensionless correlation parameter is calculated for the auto- and cross-correlation between the parameters of the strain-energy density function and the yield strength. It is shown, that the parameters are strongly correlated. Furthermore, the correlation shows a complex dependence on the window size. There are parameter pairs that are not influenced by the size of the microstructural extractions, others show a significant increasing and decreasing behavior, respectively. This is also supported by the results of the cross-correlation parameter a .

Analyzing the development of the correlation function and the corresponding correlation lengths, reveals that most correlations are described best by a triangle function, only two auto-correlation functions and the corresponding cross-correlation are assigned to exponential correlation functions. This influences also the results of the correlation lengths due to the different function definitions. The results show, that for an increasing window size the correlation lengths b_i converge to the window size l_w for a triangle function and to $0.4l_w$ for an exponential correlation function, respectively. Therefore, only one value needs to be determined based on experimental data to obtain the different correlation lengths for the generation of second-order random fields.

Summarizing, it can be concluded that the presented approach is suitable to derive the correlation structure for finite strain elasto-plastic material description of SFRC. The results of the correlation analysis are deployed in a subsequent study [143]. With the information about the correlation structure at hand second-order random fields are synthesized to represent the spatial distribution of the hyperelastic and plastic material properties of tensile tests specimens made of SFRC and hence, incorporate the probabilistic nature of the microstructure on the component level.

Acknowledgement

I want to acknowledge and extend my sincere thanks to Celia Reina from the University of Pennsylvania for the valuable ideas and tips during our discussions that significantly improved and shaped the work.

Funding

The financial support of the German Academic Exchange Service (Grant No. 91789376) is gratefully acknowledged.

Conflict of Interest

The author declares no conflict of interest. The funders had no role in the design of the study; in the collection, analyses, or interpretation of data; in the writing of the manuscript, or in the decision to publish the results.

IV.A Determination of the apparent hyperelastic material properties

Due to the five independent components of the elasticity tensor, a reduction of the material parameters automatically violates the symmetry properties induced by transversely isotropic behavior. Despite the fact, that the reduction of the elasticity tensor to a two-dimensional representation under plane strain assumption is independent of C_{44} , it is still a function of all five independent engineering constants. The compliance matrix for plane strain assumption is calculated from the three-dimensional representation by

$$\mathbf{S}_{\text{strain}} = \begin{bmatrix} S_{11} - \frac{S_{13}^2}{S_{22}} & S_{12} - \frac{S_{12}S_{13}}{S_{22}} & 0 \\ S_{12} - \frac{S_{12}S_{13}}{S_{22}} & S_{22} - \frac{S_{23}^2}{S_{22}} & 0 \\ 0 & 0 & S_{66} \end{bmatrix}, \quad (\text{IV.44})$$

where the elements of the three-dimensional compliance matrix can be derived directly from the engineering constants. As mentioned before, due to the plane strain assumption all five independent engineering constants are required to obtain the compliance matrix for a plane strain assumption. The following relations hold

$$\begin{aligned} S_{11} &= \frac{1}{E_1} & S_{12} &= -\frac{\nu_{21}}{E_2} = -\frac{\nu_{12}}{E_1} \\ S_{22} &= \frac{1}{E_2} & S_{23} &= -\frac{\nu_{23}}{E_2}. \end{aligned} \quad (\text{IV.45})$$

Since the two-dimensional modeling does not hold any information about the material properties in thickness direction, the out-of-plane Poisson's ratio ν_{23} is determined following the microstructural characteristics of the material by using the material model of Halpin-Tsai [61, 62]. If ν_{23} is known the remaining engineering constants can be calculated by evaluating

$$\begin{aligned} S_{11}^{\text{strain}} &= \frac{1}{E_1} - \frac{\nu_{21}^2}{E_2} & S_{12}^{\text{strain}} &= -\frac{\nu_{21}}{E_1} - \frac{\nu_{21}\nu_{23}}{E_2} \\ S_{22}^{\text{strain}} &= \frac{1}{E_2} - \frac{\nu_{23}^2}{E_2} & S_{66}^{\text{strain}} &= \frac{1}{G_{12}} \end{aligned} \quad (\text{IV.46})$$

Window size	Correlation function	Λ	μ	α	β	γ	σ_y
250 μm	Exponential	0.89	0.90	0.90	0.90	0.90	0.90
	Triangle	0.96	0.76	0.45	0.96	0.98	0.97
	Gaussian	0.95	0.80	0.82	0.92	0.96	0.93
500 μm	Exponential	0.84	0.89	0.87	0.88	0.87	0.91
	Triangle	0.96	0.74	0.36	0.98	0.98	0.96
	Gaussian	0.96	0.81	0.79	0.94	0.96	0.94
750 μm	Exponential	0.79	0.89	0.81	0.85	0.86	0.91
	Triangle	0.92	0.72	0.37	0.95	0.97	0.95
	Gaussian	0.92	0.81	0.71	0.92	0.94	0.94

Table IV.4: Results R^2 curve fit auto-correlation.

which leads to

$$\begin{aligned}
 E_1 &= \frac{1}{S_{11}^{\text{strain}} + \frac{\nu_{21}^2}{E_2}} & E_2 &= \frac{1 - \nu_{23}^2}{S_{22}^{\text{strain}}} \\
 G_{12} &= \frac{1}{S_{66}^{\text{strain}}} & \nu_{21} &= -\frac{S_{12}^{\text{strain}} E_2}{1 + \nu_{23}}.
 \end{aligned} \tag{IV.47}$$

To derive the coefficients of the strain-energy potential in a final step first the stiffness tensor for a three-dimensional representation is determined based on the known engineering constants. Afterwards the coefficients can be calculated by evaluating

$$\begin{aligned}
 \Lambda &= C_{23} & \mu &= \frac{1}{2}(C_{22} - \Lambda) \\
 \alpha &= C_{66} - 2\mu & \beta &= \frac{1}{4}(C_{12} - \Lambda) & \gamma &= \frac{C_{11} - 2\mu - \Lambda - 2\alpha}{8} - \beta.
 \end{aligned} \tag{IV.48}$$

IV.B Results of the coefficient of determination

In Tables IV.4 and IV.5 the results of R^2 for the auto-correlation and the cross-correlation curve fits are provided, respectively. There are no values of R^2 given for the cross-correlation of the parameter pair $\Lambda - \alpha$, because they are not connected by a cross-correlation.

Parameter		250 μm			500 μm			750 μm		
		Expo.	Tria.	Gaus.	Expo.	Tria.	Gaus.	Expo.	Tria.	Gaus.
Λ	μ	0.87	0.88	0.85	0.88	0.87	0.89	0.86	0.89	0.88
	β	0.90	0.96	0.95	0.87	0.97	0.96	0.84	0.95	0.92
	γ	0.91	0.97	0.97	0.88	0.98	0.96	0.85	0.95	0.93
	σ_y	0.84	0.92	0.93	0.86	0.94	0.93	0.83	0.93	0.92
μ	α	0.60	0.67	0.63	0.82	0.75	0.83	0.82	0.75	0.75
	β	0.91	0.95	0.91	0.90	0.97	0.94	0.85	0.93	0.89
	γ	0.93	0.97	0.96	0.90	0.98	0.95	0.88	0.96	0.94
	σ_y	0.89	0.97	0.96	0.88	0.97	0.95	0.88	0.96	0.95
α	β	0.12	0.10	0.11	0.73	0.76	0.74	0.75	0.84	0.82
	γ	0.75	0.81	0.78	0.89	0.94	0.93	0.88	0.95	0.93
	σ_y	0.83	0.86	0.83	0.88	0.94	0.92	0.87	0.93	0.92
β	γ	0.91	0.97	0.97	0.88	0.97	0.96	0.86	0.95	0.94
	σ_y	0.85	0.92	0.93	0.85	0.93	0.92	0.83	0.93	0.92
γ	σ_y	0.88	0.97	0.97	0.89	0.98	0.96	0.88	0.97	0.96

Table IV.5: Results R^2 curve fit cross-correlation.

Paper V

Numerical simulation of the elastic-ideal plastic material behavior of short fiber-reinforced composites including its spatial distribution with an experimental validation

Title: Numerical simulation of the elastic-ideal plastic material behavior of short fiber-reinforced composites including its spatial distribution with an experimental validation

Author: Natalie Rauter¹

Affiliation: ¹Helmut-Schmidt-University /
University of the Federal Armed Forces Hamburg
Holstenhofweg 85, 22043 Hamburg, Germany

Journal: Applied Science
pp. 10483, 2022

Status: Published

DOI: 10.3390/app122010483

Abstract: For the numerical simulation of components made of short fiber-reinforced composites the correct prediction of the deformation including the elastic and plastic behavior and its spatial distribution is essential. When using purely deterministic modeling approaches the information of the probabilistic microstructure is not included in the simulation process. One possible approach for the integration of stochastic information is the use of random fields. In this study numerical simulations of tensile test specimens are conducted utilizing a finite deformation elastic-ideal plastic material model. A selection of the material parameters covering the elastic and plastic domain are represented by cross-correlated second-order Gaussian random fields to incorporate the probabilistic nature of the material parameters. To validate the modeling approach tensile tests until failure are carried out experimentally, that confirm the assumption of spatially distributed material behavior in both the elastic and plastic domain. Since the correlation lengths of the random fields cannot be determined by pure analytic treatments, additionally numerical simulations are performed for different values of the correlation length. The numerical simulations endorse the influence of the correlation length on the overall behavior. For a correlation length of 5 mm a good conformity with the experimental results is obtained. Therefore, it is concluded, that the presented modeling approach is suitable to predict the elastic and plastic deformation of a set of tensile test specimens made of short fiber-reinforced composite sufficiently.

V.1 Introduction

The use of short fiber-reinforced composites (SFRC) has increased significantly over the years. Due to the specific strength and stiffness in comparison to conventional polymers and the applicability for mold injection production processes they are of special interest, e.g. in the automotive industry [38]. However, the mold injection process as well as the finite length of the reinforcing elements cause a microstructure of probabilistic nature that significantly affects the mechanical properties [141] and thus the structural response. Following this, a probabilistic modeling approach appears to be promising to exploit the lightweight potential in the best possible way.

To reduce the computational costs the main challenge here is the incorporation of microstructural information without its explicit modeling. One stochastic technique to model spatial data are random fields [75, 108, 176], that are also used in the context of material modeling. Soize and Guilleminot developed a comprehensive framework starting with non-Gaussian positive-definite matrix-valued random fields [163] and tensor-valued random fields for a meso-scale stochastic model of anisotropic elastic microstructures [164]. Based on this work by Soize the approach was extended by Guilleminot et al. covering the stochastic fluctuations in fiber-reinforced composites on the mesoscale [56, 57], random interphases from atomistic simulations of polymer nanocomposites [97] and a multiscale approach for heterogeneous materials with non-Gaussian random fields [55]. Beside this random fields are widely used, e.g. for geosystems [22], thin-walled composite cylinders [31], three-dimensional concrete microstructures [167], and the representation of the continuous mode conversion observed by the propagation of guided ultrasonic waves in thin-walled structures made of fiber-reinforced composite [189]. A first application of random fields in the context of nonlinear behavior for isotropic material is provided by Zheng et al. [185]. The application to SFRC is limited to the linear elastic domain so far [141]. However, SFRC show prominent nonlinear behavior, because the matrix material enters the plastic domain even at operation loads [77]. Hence, to predict the structural response correctly even at low stress levels information about the plastic deformation must be considered. Since the plastic deformation are localized initially the required nonlinear modeling approach needs to include information about the probabilistic nature of the microstructure causing spatially distributed material properties [146].

Beside the work on random fields for the probabilistic material modeling, the modeling of SFRC at the different scales mostly focuses on homogenization approaches and does not consider the spatial distribution of the material properties on the component level. The determination of a representative volume element (RVE) for random composites is discussed by Savvas et al. [156] by combining the extended finite element method with a Monte Carlo sampling. Breuer et al. [17, 18] applied the RVE to SFRC including artificial neural networks. Zhang et al. investigate the strain rate dependence of SFRC based on RVEs [184] and Jia et al. apply the RVE concept to cyclic mechanical and thermal loading [85].

Hence, the main objective of this research is the incorporation of the probabilistic material characteristics of SFRC into a modeling approach covering the elastic and plastic domain on the component level. The presented work is linked to a correlation structure study of the elastic-ideal plastic material behavior [142], where the moving window method [8, 51, 156] is utilized for the elastic domain and a homogenization method is used to derive the local apparent plastic material parameters [138, 139], respectively. Here, the obtained results are now employed for the numerical simulation of SFRC on the component level including an experimental validation. Therefore, first cross-correlated random fields are generated to describe the spatial distribution and the probabilistic nature of the material properties introduced by the stochastic attributes of the microstructure. In a second step a transversely-isotropic elastic-ideal plastic material model including finite deformation is established and implemented in COMSOL Multiphysics® to simulate tensile tests for specimens made of SFRC. For validation of the presented modeling approach incorporating the spatial distribution and probabilistic characteristics of elastic and plastic material properties uniaxial tensile tests are conducted experimentally.

Subsequently, the structure of the presented work is as follows. In Section V.2 the experimental investigation is given. This includes a detailed description of the specimens and the experimental setup and procedure, respectively. This is followed by the generation of cross-correlated random fields in Section V.3. After the

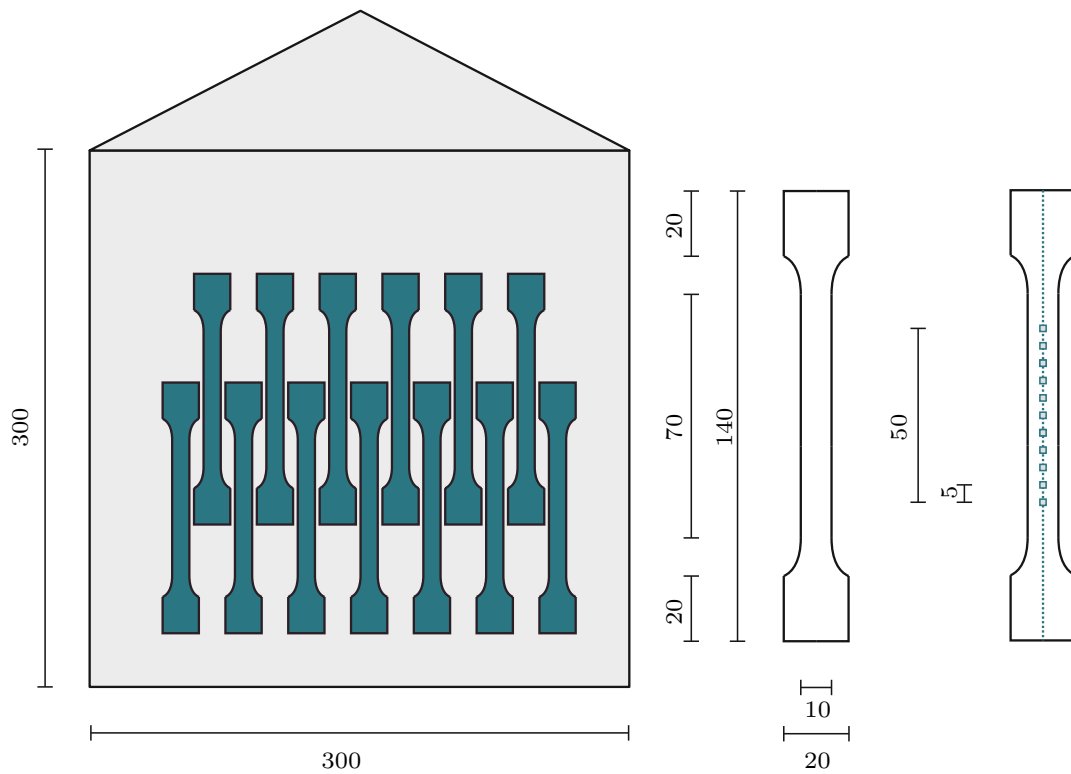


Figure V.1: Details of the specimens geometry and the measurement points. All measures in mm, $t = 3$ mm

implementation of an algorithm in Multiphysics® covering elasto-plastic material behavior in Section V.4, the random fields are used in Section V.4 to incorporate spatially distributed material properties into the numerical modeling procedure. Finally, Section V.6 gives a summary and conclusion.

V.2 Experiments

This section gives detailed information about the experimental investigation of the elastic and plastic properties of specimens made of SFRC by tensile tests. First, the specimen specifications are given before presenting the experimental setup and procedure. The section is concluded with an overview of the experimental results covering the elastic and plastic domain.

V.2.1 Specimens

In this work the elastic and plastic deformation for specimens made of Ultradur B 4300 G6 [21], a polybutylene terephthalate (PBT) matrix material filled with glass fibers, is investigated. The fiber mass fraction is set to 30%, which is equal to a fiber volume fraction of 18.2%. The specimens are cut out of a larger plate that was manufactured by mold injection. The size of this plate is 300 mm × 300 mm and has a thickness of 3 mm. The geometry of the tensile test specimens is defined in accordance with DIN-ISO-527-1 [84]. However, due to the plate dimensions the size of the specimen type 1B is slightly adapted. Figure V.1 gives an overview of the initial plate, the position of each specimen and its exact dimensions.

V.2.2 Experimental setup and procedure

For the tensile tests covering the elastic and plastic deformation until failure a Zwick-Roell Z050 tensile testing machine is used. With this testing machine a load of up to 50 kN can be applied. As suggested by DIN-ISO-527-1

	Number of specimens	E		σ_{failure}		$\epsilon_{\text{failure}}$	
		mean GPa	std GPa	mean MPa	std MPa	mean %	std %
Experiments	8	7.95	0.87	96.1	6.22	1.97	0.14
Data sheet	1	9.69	-	135	-	2.5	-

Table V.1: Experimental results obtained by tensile tests in the elastic and plastic domain.

for plastics the tensile test is performed displacement driven with a speed of 1 mm/min. The strain is captured by a contact-less laser extensometer with an initial measurement length of 50 mm. Furthermore, to analyze the spatial distribution of the material properties additional measurement points within the original measurement length are added. They have a distance of 5 mm, see Figure V.1.

For the elastic characterization of the material the Young's modulus is derived from the measured stress-strain data. It is determined by computing the slope of the curve between a strain level of 0.1% and 0.2%. For the plastic deformation the strain at failure and the maximum stress level are obtained from the measurement data. This is done based on the data for a measurement length of 50 mm for all specimens. In addition, to analyze the spatial distribution qualitatively the data is obtained for sections of 15 mm for one specimen. Hence, three non-overlapping different sections of the initial measurement length are examined individually.

V.2.3 Results

Figure V.2 summarizes the results of the conducted tensile tests in the elastic and plastic domain. On the left hand side the stress-strain curve for each specimen based on the measurement length 50 mm is plotted. Furthermore, the diagram holds data provided by the manufacturer [21]. The stress-strain curves clearly reveal the prominent plastic deformation of SFRC even at low stress levels. However, in comparison with the data sheet the experimentally obtained stress and strain level at failure are significantly lower. This also holds for the slope of the curve in the elastic domain. For a better overview the corresponding values of the Young's Modulus as well as the stress and strain level at failure are collected in Table V.1. For each parameter the mean value and the standard deviation are provided.

The differences between the experimental data and the data provided by the manufacturer are most likely related to the manufacturing process of the specimen. It significantly influences the microstructural characteristics like fiber length and fiber orientation of the specimen and the quality of the fiber-matrix bonding.

In the second diagram the focus is set on the spatial distribution of the material properties. For one specimen the stress-strain curve is not only determined for a measurement length of 50 mm but also for three sections of 15 mm length each. The sections don't overlap and are within the original measurement length. The different curves reveal that the plastic deformation is distributed over the specimen, confirming the assumption of spatially distributed material properties induced by the finite length of the reinforcing elements and the probabilistic characteristics of the microstructure.

V.3 Generation of cross-correlated random fields

V.3.1 Methodology

V.3.1.1 Random fields

Random fields $Z(\omega, \mathbf{x})$ represent spatially distributed random variables $Z(\omega)$. To describe a random field completely the function of the mean value $\mu(\mathbf{x})$, the variance $\sigma^2(\mathbf{x})$ and correlation coefficient $\rho(\mathbf{x}, \mathbf{x}')$ are required.

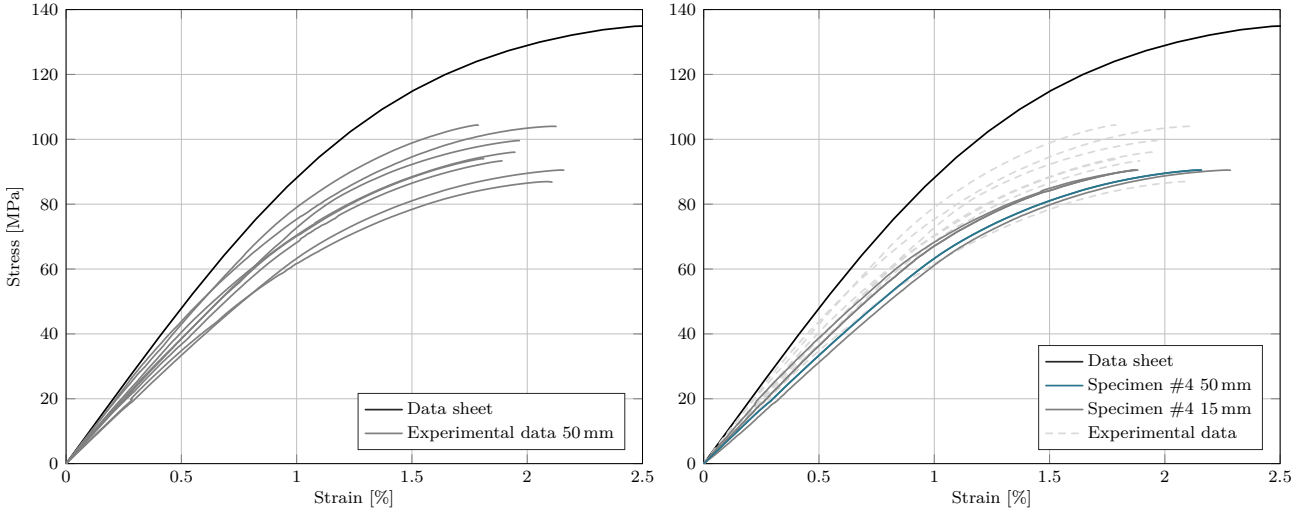


Figure V.2: Experimental results and comparison with data sheet.

Utilizing random fields in the context of material modeling it is important to note, that material parameters are of positive nature. This does not necessarily apply to the coefficients of strain-energy density functions. However, it is indispensable for the yield strength, which contradicts the found normal distribution of the yield strength [142]. Therefore, when using Gaussian random fields and hence, assume normal distributed underlying random variables, negative realizations are possible [47, 169]. In conclusion the use of Gaussian random fields for the representation of material properties in context of multi-scale modeling of heterogeneous material is controversial [163]. With non-Gaussian random fields negative realizations can be avoided and hence, a stochastic solution of second-order and the positive nature of the elasticity coefficient is guaranteed [27, 54, 55, 97, 110, 172].

Non-Gaussian random fields $M(\omega, \mathbf{x})$ are defined by

$$M(\omega, \mathbf{x}) = \mathcal{G}\{Z(\omega, \mathbf{x})\}, \quad (\text{V.1})$$

where \mathcal{G} is a non-linear mapping operator and $Z(\omega, \mathbf{x})$ a centered, homogeneous Gaussian random field[55]. With respect to the following work, where the concept of random fields is used within the finite element method framework only discretized random fields are used, requiring a finite sampling. Consequently, as long as negative values are excluded, the difference between the results based on non-Gaussian fields and Gaussian fields may not differ significantly. Therefore, the work presented here is based on homogeneous Gaussian random fields, which also allows one to use the well-known techniques presented below.

V.3.1.2 Generation of random fields by numerical methods

Initially, random fields are continuous functions with respect to the spatial coordinates. However, to be able to utilize this concept within the framework of material modeling and numerical simulations by the finite element method (FEM) a discrete representation is necessary. Over the years many different methods were developed for this purpose. Examples are the midpoint method [32, 182], the spatial averaging [177], and the shape function method [88, 104, 105]. Commonly used approaches are based on the series expansion technique [96]. Spanos et al. [165] extended the work by expressing random fields by a spatial decomposition of the correlation functions derived by the well-known Karhunen-L  ve expansion (KLE) [106]. The spatial decomposition obtained by the KLE for a mean free random field with a standard deviation equal to one is given by Cho et al. [25]

$$Z(\omega, \mathbf{x}) = \sum_{n=0}^{\infty} \sqrt{\lambda_n} \phi_n(\mathbf{x}) Z_n(\omega). \quad (\text{V.2})$$

Here, $Z_n(\omega)$ are uncorrelated, standard normal distributed random variables and λ_n and $\phi_n(\mathbf{x})$ are the eigenvalues and eigenfunctions of the correlation function kernel, that can be obtained by solving a Fredholm integral equation of second kind. Since the integral equation

$$\int_{\Omega} \text{Cov}[\mathbf{x}', \mathbf{x}] \phi_n(\mathbf{x}) d\mathbf{x} = \sum_{n=1}^{\infty} \lambda_n \phi_n(\mathbf{x}') \quad (\text{V.3})$$

has closed solutions only for a few types of correlation functions defined on a rectangular domain [14], e.g. the exponential correlation function [47, 128], numerical methods are often required. This is especially the case for multidimensional fields [101]. By deploying numerical integration methods the eigenfunctions $\phi_n(\mathbf{x})$ as a solution of the Fredholm integral is approximated by a set of functions h_i

$$\phi_n(\mathbf{x}') \approx \hat{\phi}_n(\mathbf{x}') = \sum_{i=1}^N d_i^n h_i(\mathbf{x}'), \quad (\text{V.4})$$

where the parameters d_i^n are unknown and need to be determined. One technique here is the expansion optimal linear estimate (EOLE) developed by Li et al. [101]. It is based on the linear estimation theory and belongs to the group of series expansion methods. Furthermore, it can be shown that the EOLE is equivalent to the Nyström method [6] with uniform distributed integration points [14]. Within the Nyström method the integral eigenvalue problem is written as

$$\sum_{i=1}^N w_i \text{Cov}[\mathbf{x}_n, \mathbf{x}_i] \hat{\phi}_j(\mathbf{x}_i) = \hat{\lambda}_j \hat{\phi}_j(\mathbf{x}_n), \quad (\text{V.5})$$

which can be reorganized in matrix notation as

$$\mathbf{C} \mathbf{W} \mathbf{y}_j = \hat{\lambda}_j \mathbf{y}_j. \quad (\text{V.6})$$

The $N \times N$ matrix \mathbf{C} is symmetric positive semi-definite and holds the elements $c_{n,i} = \text{Cov}[\mathbf{x}_n, \mathbf{x}_i]$, the integration weights w_i are stored in the diagonal matrix \mathbf{W} of the size $N \times N$ and \mathbf{y}_j is a column matrix with the entries $y_{j,n} = \hat{\phi}_j(\mathbf{x}_n)$. Assuming a uniform distribution of the points \mathbf{x}_i over the domain Ω and a equispaced structured grid, respectively, all integration weights w_i are the same. In this case the matrix \mathbf{W} reads

$$\mathbf{W} = w \mathbf{I}, \quad (\text{V.7})$$

with \mathbf{I} being the identity matrix and $w = |\Omega|/N$. This leads to

$$\mathbf{C} \mathbf{y}_j = \hat{\lambda}_j^* \mathbf{y}_j, \quad (\text{V.8})$$

giving the equivalent of Eq. (V.6) for the EOLE, with the eigenvalues $\hat{\lambda}_j^*$ and eigenfunctions \mathbf{y}_j of the covariance matrix \mathbf{C} . The eigenvalues of the EOLE are related to the eigenvalues of the Nyström method by

$$\hat{\lambda}_j^* = \frac{N}{|\Omega|} \hat{\lambda}_j. \quad (\text{V.9})$$

Finally, for normalized eigenvectors the truncated KLE approximated by the EOLE reads

$$Z(\omega, \mathbf{x}) = \sum_{j=1}^M \frac{Z_j(\omega)}{\sqrt{\hat{\lambda}_j^*}} \sum_{i=1}^N y_{j,i} \text{Cov}[\mathbf{x}, \mathbf{x}_i]. \quad (\text{V.10})$$

V.3.1.3 Cross-correlated random fields

In the context of nonlinear material modeling the correlation is of complex nature, because the individual parameters are approximated best by different correlation functions and the parameters are strongly cross-correlated [142, 144]. Therefore, to achieve a proper representation of the material properties, the generated random fields must include the information about the cross-correlation. Cho et al. introduce two different algorithms for the expansion of multi-correlated processes, namely the multiple uncorrelated Karhunen-Loève expansion (muKL) and the multiple correlated Karhunen-Loève expansion (mcKL) [25]. The main difference between these two procedures lays in the generation of the used random variables. In context of the muKL all correlated processes are described by a single set of uncorrelated random variables [25]. In contrast to this the mcKL provides multiple sets of mutually correlated random variables for the discretization of correlated processes. Since the modeling of nonlinear material behavior requires a set of random variables for each parameter the mcKL is applicable in this context.

Within this algorithm the same equations as for uncorrelated random fields are used and solved. However, in an additional step the uncorrelated random variables and eigenfunctions are transformed to obtain correlated random variables and eigenfunctions, respectively, that meet the given correlation structure. Here, first the matrix \mathbf{K} is introduced. The matrix is defined as

$$K_{km}^{ij} = E[Z_k^i Z_m^j], \quad (\text{V.11})$$

where Z_k^i and Z_m^j are a set of zero-mean uncorrelated random variables for processes i and j , respectively. Using Eq. (V.2) the cross-covariance between the processes i and j is written as [50]

$$\begin{aligned} C_{ij} &= E[f_i(\omega, \mathbf{x}) f_j(\omega, \mathbf{y})] \\ &= \sum_{k,m=1}^{\infty} K_{km}^{ij} \sqrt{\lambda_k^i \lambda_m^j} \phi_k^i(\mathbf{x}) \phi_m^j(\mathbf{y}). \end{aligned} \quad (\text{V.12})$$

The result is an integral equation similar to the one for the auto-correlation shown in Section V.3.1.2. Following Eq. (V.3) the elements of \mathbf{K} are obtained by solving

$$K_{km}^{ij} = \frac{1}{\sqrt{\lambda_k^i \lambda_m^j}} \int_{\Omega_1} \int_{\Omega_2} C_{ij}(\mathbf{x}, \mathbf{y}) \phi_k^i(\mathbf{x}) \phi_m^j(\mathbf{y}) d\mathbf{y} d\mathbf{x}. \quad (\text{V.13})$$

In a final step the matrix \mathbf{K} is used to determine sets of correlated random variables for each process. It is assumed that \mathbf{K} is positive definite, which allows a Cholesky decomposition given by [50]

$$\mathbf{K} = \mathbf{R}\mathbf{R}^T. \quad (\text{V.14})$$

Applying \mathbf{R} on a set of random variables leads to

$$\tilde{\mathbf{Z}} = \mathbf{R}^{-1}\mathbf{Z}, \quad (\text{V.15})$$

where

$$E[\tilde{\mathbf{Z}}\tilde{\mathbf{Z}}^T] = \mathbf{I}. \quad (\text{V.16})$$

This means that $\tilde{\mathbf{Z}}$ contains only uncorrelated random variables. In reverse by applying \mathbf{R} on a set of uncorrelated random variables $\tilde{\mathbf{Z}}$ gives a set of correlated random variables that represent cross-correlated random fields. The same procedure is also applicable to obtain cross-correlated eigenfunctions.

Parameter	Mean GPa	Standard deviation GPa	Correlation function	Correlation length ratio -
Λ	5.38	0.140	Triangle	1
μ	1.20	0.064	Exponential	0.4
α	1.10	0.090	Exponential	0.4
β	-0.13	0.020	Triangle	1
γ	1.13	0.148	Triangle	1
σ_y	0.126	0.015	Triangle	1

Table V.2: Mean values and standard deviations of the strain density function coefficients for a window size of 750 μm , taken from Rauter et al. [142].

V.3.2 Application to the elastic-ideal plastic material behavior of SFRC

In this section the presented framework for the generation of cross-correlated random fields is used to represent the material properties of elastic-ideal plastic material behavior of SFRC. The information of the correlation structure are derived and discussed in detail by Rauter et al. study [142]. It is shown, that the correlation structure of the material parameters is approximated best by a combination of the triangle correlation function, defined as

$$\rho(\xi_1, \xi_2) = \begin{cases} a \left(1 - \frac{|\xi_1|}{b_1}\right) \left(1 - \frac{|\xi_2|}{b_2}\right) & \text{if } |\xi_1| \leq b_1, |\xi_2| \leq b_2 \\ 0 & \text{else} \end{cases}, \quad (\text{V.17})$$

and an exponential correlation function [48, 128, 169]

$$\rho(\xi_1, \xi_2) = a \exp^{-\frac{|\xi_1|}{b_1} - \frac{|\xi_2|}{b_2}}. \quad (\text{V.18})$$

The parameter a indicates the strength of the correlation between two parameters, ξ_1 and ξ_2 hold the spatial coordinates and b_1 and b_2 are the corresponding correlation lengths, respectively. In case of an auto-correlation a is equal to one, in case of a cross-correlation a can take values between -1 and 1 .

The values of a are set in accordance with the results obtained by Rauter et al. [142]. In this initial study the numerical simulation of the elastic-ideal plastic material behavior of SFRC only two parameters are described by spatially distributed material properties to reduce the complexity of the nonlinear numerical simulations. To ensure that both the elastic and plastic domain are captured by the stochastic multiscale approach one parameter of the strain-energy density function, which is related to the elastic domain and the yield strength are represented by random fields. Based on this, the routine can be reduced to two parameters capturing the cross-correlation of Λ and σ_y . The matrix holding the factor a for each material parameter combination reads

$$\mathbf{a} = \begin{bmatrix} 1.00 & 0.53 \\ 0.53 & 1.00 \end{bmatrix}. \quad (\text{V.19})$$

In addition to the parameter a the required mean values, standard deviations and correlation lengths are provided in Table V.2. Since the correlation length cannot be determined solely on numerical data, the values are normalized to the correlation length of the parameter Λ . For more details about the material model and the provided data the reader is kindly referred to Section V.4.1 and the correlation analysis presented by the authors [142], respectively.

With this information at hand realizations of random fields for these two material parameters are generate using the numerical methods for two-dimensional cross-correlated homogeneous second-order random fields

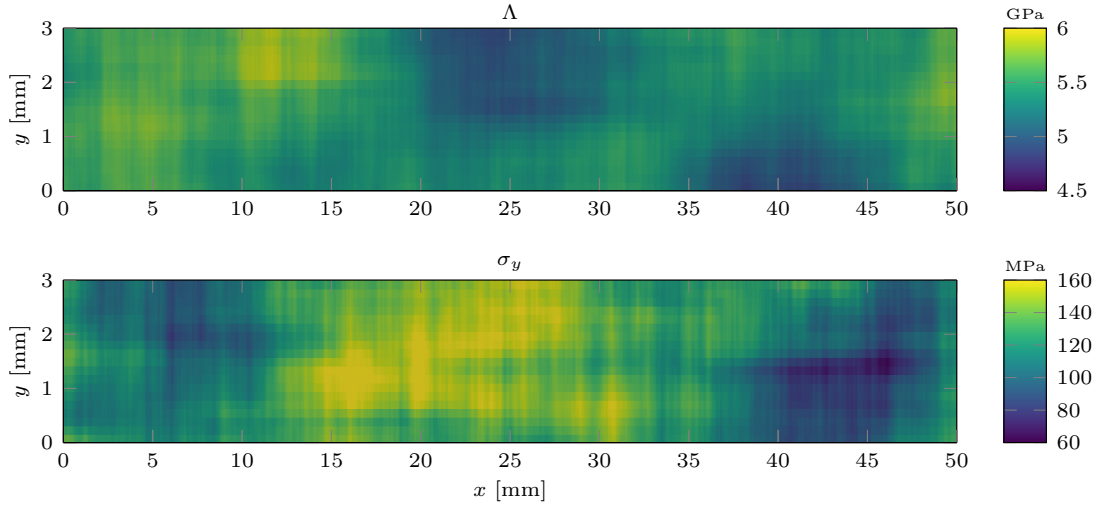


Figure V.3: Representation of the spatially distributed material parameters of elastic-ideal plastic material behavior by cross-correlated homogeneous second-order Gaussian random fields.

presented in Section V.3.1. In accordance with the numerical simulation of the tensile test in Section V.4 and the experimental procedure in Section V.2 the domain has a size of 50 mm \times 3 mm. One realization of the parameter set is presented in Figure V.3. The correlation length of Λ is set to $l_x = 20$ mm and $l_y = 3$ mm in horizontal and vertical direction, respectively.

In addition, the quality of the procedure is analyzed. Therefore, in total 1000 realizations for each parameter are generated. Based on the obtained data the correlation structure is derived and compared to the results presented in the former study by the author [142]. Figure V.4 holds the results for Λ and σ_y . The first two diagrams give the analytic auto-correlation functions of Λ and σ_y , based on the results obtained in a previous correlation analysis [142], and the correlation function based on the 1000 realizations, respectively. In the last diagram the cross-correlation function is plotted. For a better overview the correlation function plots are limited to the horizontal direction. In addition to this Figure V.5 gives histograms of these two parameters based on all 1000 realizations. As discussed before, in this work the material parameters are represented by Gaussian random fields. Since Gaussian random fields allow negative values in general the distribution of the sampled yield strength is analyzed more in detail. Based on the 1000 realizations and a discretization truncated after 2000 terms, in total $2e6$ values are sampled for the yield strength. The corresponding mean value and standard deviation are 125.6 MPa and 14.7 MPa, which meets the values provided in Table V.2. Furthermore, the minimal and maximal sampled values are 194.7 MPa and 64.0 MPa, respectively. Since the probability density function of the yield strength was not modified to avoid negative values, the moderate standard deviation of the Gaussian distribution results only in positive realizations of the random variable. Therefore, the use of second-order Gaussian random fields appears to be appropriate to incorporate spatially distributed material properties into the numerical simulation procedure.

Subsequently, the results for the correlation functions as well as the material parameter distributions show a very good agreement with the analytic values. Hence, the selected procedure is suitable to represent the locally varying material properties of elastic-ideal plastic material behavior of SFRC by random fields.

V.4 Numerical simulation

In this section the spatially distributed material properties described by cross-correlated second-order Gaussian random fields are combined with an algorithm for elastic-ideal plastic material behavior. The main objective is the integration of the locally varying material properties, which are observed during the experimental investigations in Section V.2, into a numerical modeling procedure. Therefore, first the framework and

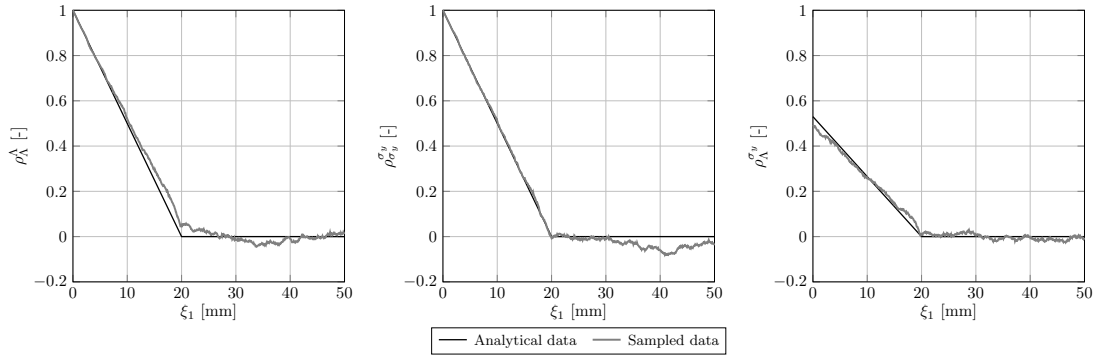


Figure V.4: Correlation analysis of the generated cross-correlated random fields.

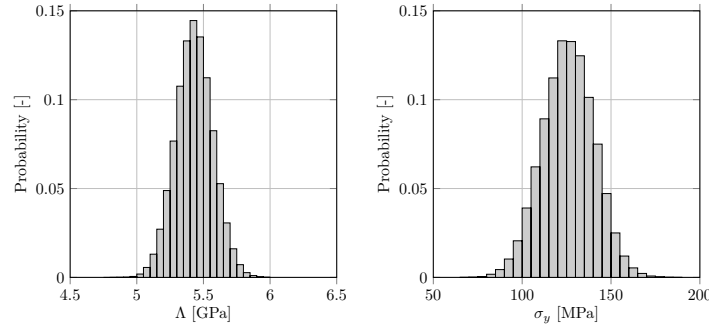


Figure V.5: Histograms of the sampled values of Λ and σ_y .

constitutive equations for transversely-isotropic elastic-ideal plastic material behavior and its implementation in COMSOL Multiphysics® is presented. The developed algorithm is then validated in detail before combining the algorithm with the material properties defined by random fields. In a last step the influence of the correlation length on the standard deviation of the obtained results is analyzed and an optimal value is selected for which the numerically obtained results and the experimental measurements coincided best.

V.4.1 Framework of elastic-ideal plastic material behavior

V.4.1.1 Constitutive equations

The constitutive model of elastic-ideal plastic material behavior comprises the following equations

- elastic constitutive equation,
- flow rule,
- and yield condition,

which need to satisfy the Kuhn-Tucker complementary conditions and the consistency condition [161]. The plastic constitutive model introduced here, is based on the work provided by Hashiguchi et al. [63] and Eidel et al. [39]. It is adapted to transversely-isotropic material by using the strain energy density function by Bonet et al. [16]. Furthermore, hardening is not considered. Hence, the material is assumed to show ideal plastic behavior [142].

Since the modeling approach covers finite deformation the constitutive model needs to be formulated with respect to the nonlinear continuum mechanical framework. Therefore, the deformation is described by the multiplicative decomposition of the deformation gradient, also known as Kröner-Lee decomposition. The

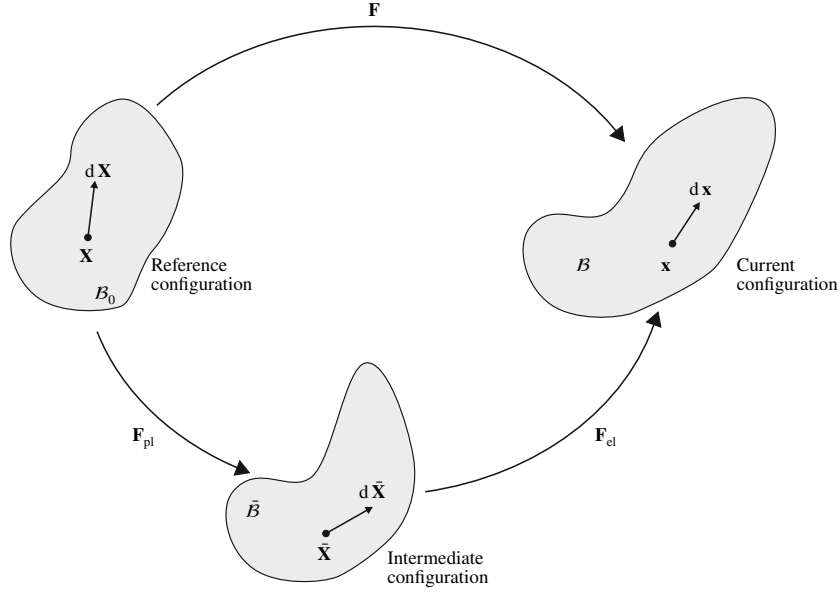


Figure V.6: Configuration definition within the nonlinear continuum mechanic framework.

decomposition is given by [94, 98, 99, 111]

$$\mathbf{F} = \mathbf{F}_{el} \cdot \mathbf{F}_{pl}. \quad (\text{V.20})$$

Here, \mathbf{F}_{el} holds the elastic and \mathbf{F}_{pl} the plastic deformation, respectively. Since the deformation gradient is used to map continuum mechanical quantities from the reference to the current configuration and vice versa, this decomposition reveals the definition of an additional configuration, the so called intermediate configuration [94, 98, 161]. As shown in Figure V.6, with \mathbf{F}_{pl} the quantities are mapped from the reference to the intermediate configuration and with \mathbf{F}_{el} from the intermediate to the current configuration. Accordingly

$$J = J_{el}J_{pl} \quad \text{with} \quad J = \det \mathbf{F} = \sqrt{\det \mathbf{C}} \quad (\text{V.21})$$

holds, with $\mathbf{C} = \mathbf{F}^T \cdot \mathbf{F}$ being the right Cauchy-Green tensor, defined in the reference configuration. It also splits into an elastic and a plastic part written by the decomposition [107]

$$\mathbf{C} = \mathbf{F}_{pl}^T \cdot \mathbf{C}_{el} \cdot \mathbf{F}_{pl}, \quad (\text{V.22})$$

where

$$\mathbf{C}_{el} = \mathbf{F}_{el}^T \cdot \mathbf{F}_{el}, \quad \mathbf{C}_{pl} = \mathbf{F}_{pl}^T \cdot \mathbf{F}_{pl} \quad (\text{V.23})$$

Assuming J_2 -plasticity and hence, plastic incompressibility, leads to

$$\det \mathbf{C}_{pl} = (J_{pl})^2 = 1 \quad (\text{V.24})$$

and

$$\det \mathbf{C} = J^2 = (J_{el})^2 = \det \bar{\mathbf{C}}_{el}, \quad (\text{V.25})$$

respectively. With respect to the introduced configurations, $\bar{\mathbf{C}}_{el}$, which is located in the intermediate configuration, contains the elastic deformation whereas \mathbf{C}_{pl} is assigned to the reference configuration and includes the plastic deformation.

A crucial part of the plasticity framework is the plastic flow rule providing information about the irreversible deformation of a body. The fundamental equation is the second law of thermodynamics provided by the

Clausian-Duhem-inequality for isothermal processes, which is written as [178]

$$-\dot{\Psi} + \mathbf{S} : \frac{1}{2}\dot{\mathbf{C}} \geq 0, \quad (\text{V.26})$$

where the dot indicates the derivative with respect to time, \mathbf{S} is the second Piola-Kirchhoff stress tensor and Ψ a Helmholtz free energy. Introducing a Helmholtz free energy as a function of \mathbf{C} the associate rate can be expressed by

$$\dot{\Psi} = \dot{\Psi}_{\text{el}} = \frac{\partial \Psi_{\text{el}}}{\partial \bar{\mathbf{C}}_{\text{el}}} : \dot{\bar{\mathbf{C}}}_{\text{el}}. \quad (\text{V.27})$$

Since in this case, both kinematic and isotropic hardening are omitted, only the part Ψ_{el} of the Helmholtz free energy Ψ , which is assigned to the elastic deformation, contributes to Eq. (V.26). Following the multiplicative decomposition of \mathbf{F} the derivative of the right Cauchy-Green tensor with respect to time is obtained by [39]

$$\dot{\mathbf{C}} = \mathbf{F}_{\text{pl}}^T \left[\dot{\mathbf{C}}_{\text{el}} + 2 \left(\mathbf{C}_{\text{el}} \cdot \mathbf{L}_{\text{pl}} \right)_s \right] \mathbf{F}_{\text{pl}} \quad (\text{V.28})$$

with the plastic velocity gradient in the intermediate configuration

$$\bar{\mathbf{L}}_{\text{pl}} = \dot{\mathbf{F}}_{\text{pl}} \cdot \mathbf{F}_{\text{pl}}^{-1}. \quad (\text{V.29})$$

Combining the inequality in Eq. (V.26) and the time derivative of \mathbf{C} , which must hold for arbitrary thermodynamic processes, one can derive first the constitutive equation for elastic deformation, which defines the second Piola-Kirchhoff stress tensor $\bar{\mathbf{S}}$ in the intermediate configuration

$$\bar{\mathbf{S}} = 2 \frac{\partial \Psi_{\text{el}}}{\partial \bar{\mathbf{C}}_{\text{el}}} \quad (\text{V.30})$$

and second the reduced form of the Clausian-Duhem inequality [39, 178]

$$\bar{\mathbf{M}} : \mathbf{L}_{\text{pl}} \geq 0, \quad (\text{V.31})$$

again omitting isotropic and kinematic hardening. In this formulation the Mandel stress tensor $\bar{\mathbf{M}}$ is introduced. It is defined as

$$\bar{\mathbf{M}} = \bar{\mathbf{C}}_{\text{el}} \cdot \bar{\mathbf{S}} \quad (\text{V.32})$$

and stands in the intermediate configuration.

The inequality in Eq. (V.26) is satisfied by the associate flow rule [39, 178]

$$\mathbf{L}_{\text{pl}} = \dot{\lambda} \frac{\partial \phi}{\partial \bar{\mathbf{M}}}, \quad (\text{V.33})$$

assuming an isotropic yield function ϕ [39]. In this work the framework of J_2 -plasticity is used. Therefore, the yield function is introduced as a von Mises criterion by [63]

$$f_{\text{yield}} = \sqrt{\frac{3}{2}} \|\bar{\mathbf{M}}_{\text{dev}}\| - \sigma_{\text{yield}}, \quad (\text{V.34})$$

where σ_{yield} is the reference yield stress for uniaxial loading and hence, an independent material parameter, and $\|\bar{\mathbf{M}}_{\text{dev}}\|$ denotes the norm of the deviatoric part of the Mandel stress. Substituting the von Mises yield function in Eq. (V.34) into Eq. (V.33) leads to [63, 178]

$$\mathbf{L}_{\text{pl}} = \dot{\lambda} \frac{\bar{\mathbf{M}}_{\text{dev}}}{\|\bar{\mathbf{M}}_{\text{dev}}\|}. \quad (\text{V.35})$$

With this framework at hand the flow rule is written as [39]

$$\dot{\mathbf{F}}_{\text{pl}} = \mathbf{L}_{\text{pl}} \cdot \mathbf{F}_{\text{pl}} = \dot{\lambda} \frac{\bar{\mathbf{M}}_{\text{dev}}}{\|\bar{\mathbf{M}}_{\text{dev}}\|} \cdot \mathbf{F}_{\text{pl}}. \quad (\text{V.36})$$

To solve this equation an implicit backward Euler-type tensor exponential based time integration scheme is used. Following this procedure the updated plastic part of the deformation gradient is obtained by [39, 116]

$$\mathbf{F}_{\text{pl},n+1} = \mathbf{Q}_{\text{pl},n+1} \mathbf{F}_{\text{pl},n} \quad (\text{V.37})$$

with the exponential function

$$\mathbf{Q}_{\text{pl},n+1} = \exp \left[\Delta \lambda \frac{\bar{\mathbf{M}}_{\text{dev},n+1}}{\|\bar{\mathbf{M}}_{\text{dev},n+1}\|} \right]. \quad (\text{V.38})$$

The subscripts n and $n + 1$ denote the corresponding steps, where n indicates the initial and $n + 1$ the updated values.

The presented framework of elastic-ideal plastic deformation is applied to transversely-isotropic material behavior characterizing SFRC in a next step. Therefore, the constitutive equations are used within the context of the finite element method. The resulting routine can be divided into four steps, which are presented in detail below.

V.4.1.2 Solution procedure

Elastic predictor In the initial step the deformation of the body is assumed to be purely elastic, which is described in the intermediate configuration, as shown before. Following the work of Simo et al., who derived the framework of the finite strain elasto-plasticity by combining the multiplicative decomposition of the deformation gradient with hyperelastic strain-energy density functions [159, 160, 162], the elastic deformation is obtained by evaluating the hyperelastic strain-energy density function Ψ_{el} with respect to the elastic part of the deformation.

In this study, the elastic material behavior of SFRC is described by the potential [16]

$$\Psi_{\text{el}}(\bar{\mathbf{C}}_{\text{el}}) = \frac{1}{2} \Lambda (J - 1)^2 - \mu \ln(J) + \frac{1}{2} \mu (\text{tr } \bar{\mathbf{C}}_{\text{el}} - 3) + [\alpha + \beta (\text{tr } \bar{\mathbf{C}}_{\text{el}} - 3) + \gamma (I_4 - 1)] (I_4 - 1) - \frac{1}{2} \alpha (I_5 - 1). \quad (\text{V.39})$$

Here, Λ , μ , α , β and γ are the independent material parameters characterizing the transversely-isotropic material behavior. In addition to the well-known invariants I_1 , I_2 , and I_3 for the description of isotropic material behavior [3, 109], the quantities I_4 and I_5 give the pseudo-invariants, which are defined for a symmetric second-order tensor \mathbf{B} by [74, 166]

$$I_4 = \mathbf{a} \cdot \mathbf{B} \cdot \mathbf{a} \quad \text{and} \quad I_5 = \mathbf{a} \cdot \mathbf{B}^2 \cdot \mathbf{a}. \quad (\text{V.40})$$

The vector \mathbf{a} gives the fiber orientation, and therefore, holds the transversely-isotropic characteristics of the material. In this case it is assumed, that the fibers are mainly orientated along the tensile test specimen. Hence, $a_1 = 1$ and $a_2 = a_3 = 0$ hold.

With respect to the used transversely-isotropic potential and the tensor derivatives, given by

$$\begin{aligned} \frac{\partial I_4}{\partial \mathbf{B}} &= \mathbf{a} \otimes \mathbf{a} & \frac{\partial I_5}{\partial \mathbf{B}} &= \mathbf{a} \cdot \mathbf{B} \otimes \mathbf{a} + \mathbf{a} \otimes \mathbf{B} \cdot \mathbf{a} \\ \frac{\partial \mathbf{B}}{\partial \mathbf{B}} &= \mathbb{I}^s = \frac{1}{2} (\delta_{ik} \delta_{lj} + \delta_{il} \delta_{jk}) & \frac{\partial \mathbf{B}^{-1}}{\partial \mathbf{B}} &= -\frac{1}{2} (B_{ik}^{-1} B_{lj}^{-1} + B_{il}^{-1} B_{jk}^{-1}), \end{aligned} \quad (\text{V.41})$$

the second Piola-Kirchhoff stress tensor in the intermediate configuration reads

$$\bar{\mathbf{S}} = \mu (\mathbf{I} - \bar{\mathbf{C}}_{\text{el}}^{-1}) + \lambda J (J - 1) \bar{\mathbf{C}}_{\text{el}}^{-1} + 2\beta (I_4 - 1) \mathbf{I} + 2[\alpha + \beta (\text{tr } \bar{\mathbf{C}}_{\text{el}} - 3) + 2\gamma (I_4 - 1)] \mathbf{a} \otimes \mathbf{a} - \alpha (\bar{\mathbf{C}}_{\text{el}} \cdot \mathbf{a} \otimes \mathbf{a} + \mathbf{a} \otimes \bar{\mathbf{C}}_{\text{el}} \cdot \mathbf{a}). \quad (\text{V.42})$$

Checking yield condition To be able to evaluate the yield condition, provided in Eq. (V.34), in the intermediate configuration, the deviatoric part of the Mandel stress must be computed to derive the corresponding von Mises stress.

If the resulting von Mises stress is lower than the yield strength of the material, the body shows only elastic deformation. Therefore, no further action is required. The stress measure can be updated with the trial value obtained by the elastic predictor step. If, however, the von Mises stress is larger than the yield strength, the body shows not only elastic but also plastic deformation. In this case the determination of the resulting plastic deformation is covered by the plastic corrector step.

Plastic corrector step (return mapping) Since the yield condition is given in the intermediate configuration, this also holds for the computation of the updated plastic part of the deformation gradient.

As shown before an associative plastic flow rule introduced by Eidel et al. [39] is used to describe the evaluation of the plastic deformation. With this framework at hand the return mapping procedure in case of plastic deformation leads to the following system of equations, cf. Eq. (V.37)

$$\begin{aligned} \mathbf{Y}_{\mathbf{F}_{\text{pl}}} &= \mathbf{F}_{\text{pl},n+1} - \mathbf{Q}_{\text{pl},n+1} \cdot \mathbf{F}_{\text{pl},n} = \mathbf{0}, \\ Y_{f_{\text{yield}}} &= \sqrt{\frac{3}{2} \bar{\mathbf{M}}_{\text{dev},n+1} : \bar{\mathbf{M}}_{\text{dev},n+1}^T} - F_{n+1} = 0, \end{aligned} \quad (\text{V.43})$$

which needs to be solved to obtain the updated quantities at the step $n + 1$ for the plastic deformation. Since the plastic part of the deformation gradient depends solely on the plastic multiplier $\Delta\lambda$, see Eqs. (V.37) and (V.38) a Newton-scheme algorithm is used to determine the updated components of the plastic deformation gradient. Therefore, the yield criterion is iteratively solved with respect to $\Delta\lambda$ and the procedure is stopped, when a maximum number of iterations or a converged solution is reached by satisfying the condition

$$\|Y_{f_{\text{yield}}}\| < \text{tol}. \quad (\text{V.44})$$

Furthermore, the required derivative is calculated numerically by deploying a one-sided difference scheme

$$f'(x) = \frac{f(x+h) - f(x)}{h}. \quad (\text{V.45})$$

Updating With the obtained value of $\Delta\lambda$ satisfying the yield condition the updated plastic deformation gradient $\mathbf{F}_{\text{pl},n+1}$ can be calculated by evaluating Eqs. (V.37) and (V.38). Next the resulting second Piola-Kirchhoff stress tensor in the intermediate configuration is derived. Therefore, the updated elastic part of the deformation gradient is computed and introduced in Eq. (V.42). COMSOL Multiphysics® requires the computation of the second Piola-Kirchhoff stress tensor and the consistent tangent modulus tensor with respect to the reference configuration. Hence, a pull-back operation

$$\mathbf{S} = \mathbf{F}_{\text{pl}}^{-1} \cdot \bar{\mathbf{S}} \cdot \mathbf{F}_{\text{pl}}^{-T}. \quad (\text{V.46})$$

is applied to obtain the second Piola-Kirchhoff stress tensor in the reference configuration. The last step is the computation of the consistent tangent modulus tensor. The corresponding procedure is provided in detail in the next section.

V.4.1.3 Variational formulation and consistent tangent modulus tensor

For a body \mathcal{B} the local form of the balance of momentum with respect to the reference configuration reads

$$\text{Div } \mathbf{P} + \rho_0 \mathbf{b} = \rho_0 \ddot{\mathbf{u}}. \quad (\text{V.47})$$

Here, \mathbf{P} is the first Piola-Kirchhoff stress tensor, ρ_0 is the density, \mathbf{b} are the volume forces and \mathbf{u} is the displacement field. To solve this differential equation Neumann and Dirichlet boundary conditions are used. They are given by

$$\mathbf{u} = \bar{\mathbf{u}} \text{ on } \partial\mathcal{B} \quad (\text{V.48})$$

$$\mathbf{P} \cdot \mathbf{N} = \bar{\mathbf{t}} \text{ on } \partial\mathcal{B}_\sigma, \quad (\text{V.49})$$

where $\partial\mathcal{B}$ is the boundary surface of \mathcal{B} and \mathbf{N} gives the normal to the boundary surface $\partial\mathcal{B}_\sigma$. To ensure, that the boundary conditions cover the complete surface of the body $\partial\mathcal{B} = \partial\mathcal{B} \cup \partial\mathcal{B}_\sigma$ and $\partial\mathcal{B} \cap \partial\mathcal{B}_\sigma = \emptyset$ hold. Applying standard variational calculus on Eq. (V.47) and $\mathbf{P} = \mathbf{F} \cdot \mathbf{S}$ leads to

$$F(\mathbf{u}, \delta\mathbf{u}) = \int_{\mathcal{B}} \frac{1}{2} \mathbf{S} : \delta\mathbf{C} dV + \int_{\mathcal{B}} \rho_0 (\ddot{\mathbf{u}} - \mathbf{b}) \cdot \delta\mathbf{u} dV - \int_{\partial\mathcal{B}_\sigma} \bar{\mathbf{t}} \cdot \delta\mathbf{u} dS = 0 \quad (\text{V.50})$$

for the equilibrium state of the body \mathcal{B} . Based on the definition

$$\mathbf{C} = \mathbf{F}^T \cdot \mathbf{F} \quad (\text{V.51})$$

the virtual right Cauchy-Green deformation tensor, expressed with respect to the virtual deformation gradient $\delta\mathbf{F} = \text{Grad } \delta\mathbf{u}$, is given by

$$\delta\mathbf{C} = (\delta\mathbf{F}^T \cdot \mathbf{F} + \mathbf{F}^T \cdot \delta\mathbf{F}) \quad (\text{V.52})$$

To solve this nonlinear equation within the FEM framework a standard Newton-Raphson iteration scheme is used. To ensure a quadratic convergence rate a consistent linearization of the principal of virtual displacement in Eq. (V.50) is crucial. Therefore, in this work the perturbation technique developed by Miehe [117] is used. This approach is widely in use and has been extensively investigated with respect to convergence properties and the application within the finite strain framework [39, 114, 115]. Due to the symmetry of \mathbf{S} the linear increment of F can be formulated as

$$\Delta F(\mathbf{u}, \delta\mathbf{u}, \Delta\mathbf{u}) = \frac{1}{2} \int_{\mathcal{B}} (\delta\mathbf{C} : \Delta\mathbf{S} + \Delta\delta\mathbf{C} : \mathbf{S}) dV, \quad (\text{V.53})$$

where $\Delta\delta\mathbf{C} = (\Delta\mathbf{F}^T \cdot \delta\mathbf{F} + \delta\mathbf{F}^T \cdot \Delta\mathbf{F})$ is the linearized virtual right Cauchy-Green deformation tensor given in terms of the incremental deformation gradient $\Delta\mathbf{F} = \text{Grad } \Delta\mathbf{u}$. To obtain the incremental second Piola-Kirchhoff stress tensor $\Delta\mathbf{S}$ the consistent tangent modulus tensor is required. In the reference configuration it is expressed by

$$\mathbf{C} = 2 \frac{\partial \mathbf{S}}{\partial \mathbf{C}}, \quad (\text{V.54})$$

which can be written as

$$\mathbf{C} = 2 \frac{\Delta\mathbf{S}}{\Delta\mathbf{C}} = \sum_{i,j,k,l=1}^3 2 \frac{\Delta S_{ij}}{\Delta C_{kl}} \mathbf{E}_i \otimes \mathbf{E}_j \otimes \mathbf{E}_k \otimes \mathbf{E}_l. \quad (\text{V.55})$$

The incremental change of the right Cauchy-Green tensor is obtained by applying a perturbation technique to the deformation gradient. Following this, the incremental change of the right Cauchy-Green tensor is given by

$$\Delta\mathbf{C} = \Delta(\mathbf{F}^T \cdot \mathbf{F}) = \mathbf{F}^T \cdot \Delta\mathbf{F} + (\Delta\mathbf{F})^T \cdot \mathbf{F} \quad (\text{V.56})$$

with

$$\Delta\mathbf{F}_{kl}(\epsilon) = \frac{\epsilon}{2} \left\{ (\mathbf{F}_{n+1}^{-T} \cdot \mathbf{E}_k) \otimes \mathbf{E}_l + (\mathbf{F}_{n+1}^{-T} \cdot \mathbf{E}_l) \otimes \mathbf{E}_k \right\}. \quad (\text{V.57})$$

Subsequently, the perturbed deformation gradient reads

$$\mathbf{F}_{n+1}(\epsilon) = \mathbf{F}_{n+1} + \Delta\mathbf{F}(\epsilon). \quad (\text{V.58})$$

Variable	Symbol	Description
F1Old	\mathbf{F}_n	Input: Deformation gradient at previous step
F1	\mathbf{F}_{n+1}	Input: Deformation gradient at current step
tempOld	T_n	Input: Temperature at previous step
temp	T_{n+1}	Input: Temperature at current step
K	\mathbf{e}	Input: Local material coordinate system
delta	–	Input: reserved for future use
nPar	n	Input: Number of material model parameters
par	–	Input: Array with the material model parameters
sPK	\mathbf{S}_{n+1}	Output: Second Piola-Kirchhoff stress tensor given in Voigt order
J	\mathbf{J}	Output: Jacobian of stress with respect to deformation gradient as a 6-by-9 matrix of partial derivatives of components of sPK with respect to components of F

Table V.3: List of input and output variables for a general stress deformation routine in COMSOL Multiphysics®.

Variable	Symbol	Description
nStates1	–	Input: Size of state array
states1	$\mathbf{F}_{pl,n}$	Input: Plastic part of deformation gradient at previous step

Table V.4: List of state variables used in the algorithm for the elastic-ideal plastic material behavior in COMSOL Multiphysics®.

With this the corresponding perturbed incremental right Cauchy-Green tensor can be calculated, which enables one to compute the stresses by applying the presented return mapping algorithm. This leads to the stress increment

$$\Delta \mathbf{S} = \mathbf{S}(\mathbf{F}_{n+1}(\epsilon)) - \mathbf{S}(\mathbf{F}_{n+1}) \quad (\text{V.59})$$

and hence, the consistent tangent modulus tensor by evaluating Eq. (V.55)

V.4.2 Implementation in COMSOL Multiphysics®

V.4.2.1 Algorithm

Using an external material option in COMSOL Multiphysics® requires the generation of a C-based dll, which can be loaded via the COMSOL Multiphysics® interface. With respect to the presented elastic-ideal plastic material behavior in Section V.4.1 the general stress deformation routine is used. The input and output parameter for a general stress deformation subroutine for the implementation in COMSOL Multiphysics® are provided in Table V.3. In addition to these variables optional variables can be stored utilizing state variables. Table V.4 gives an overview of the state variables used in the presented algorithm for the elastic-ideal plastic material behavior of SFRC.

With these definitions and the framework provided in Section V.4.1 an algorithm is established to compute the second Piola-Kirchhoff stress tensor and the Jacobian matrix of the second Piola-Kirchhoff stress tensor with respect to deformation gradient. The structure of the developed routine is depicted in Figure V.7. The main routine EVAL reads the input variables, calls the subroutine RETMAP, which is responsible for the return mapping procedure and updates all output and state variables. A detailed overview of the routine is provided by Algorithm 1. In addition Algorithm 2 and Table V.5 hold all information about the subroutine RETMAP.

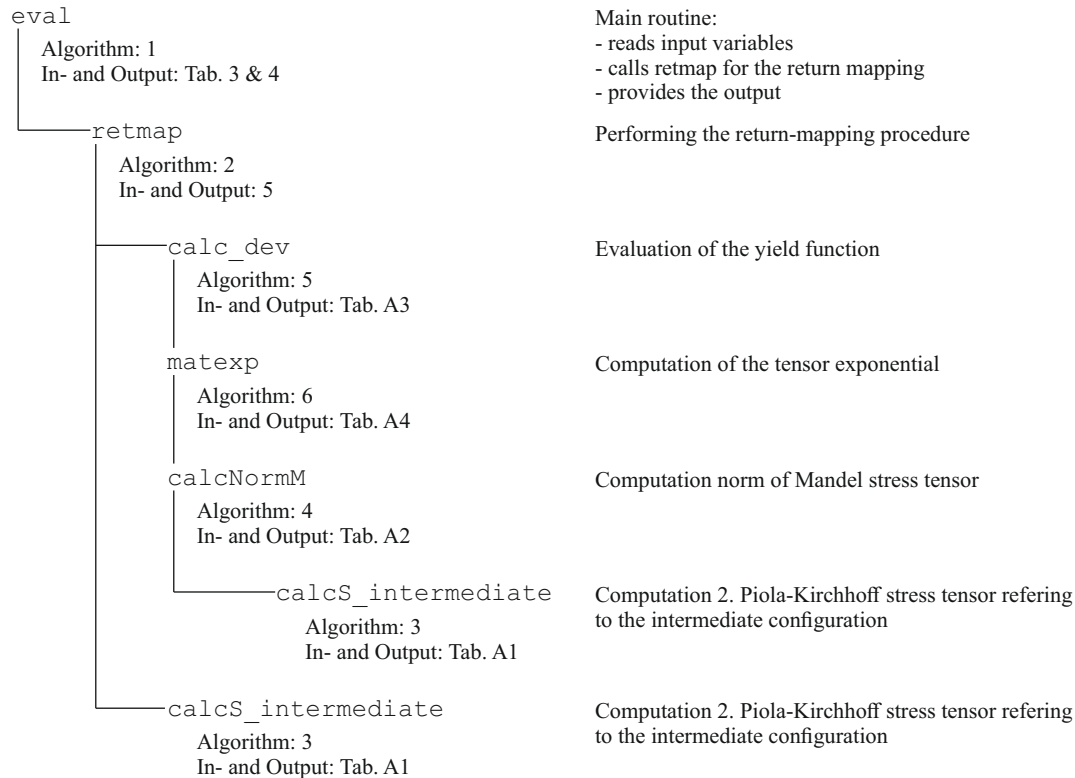


Figure V.7: Structure of the implemented algorithm

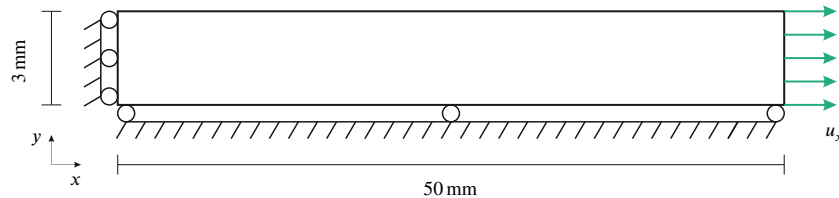


Figure V.8: Two-dimensional numerical model.

Details of all remaining routines indicated in Figure V.7 are given in Appendix V.A.

V.4.2.2 Validation of the algorithm

For the validation process a two-dimensional numerical model under plane strain assumption representing the cross-section of a tensile test specimen is used. The size of the numerical model is 50 mm \times 3 mm. In Figure V.8 the numerical model and the corresponding boundary conditions are depicted. To reduce convergence issues during the plastic deformation the simulation is displacement driven. Beside that, the numerical model is discretized by 4-node-elements with a size of 0.25 mm \times 0.25 mm. Hence over the thickness the cross-section is discretized with 12 and along the cross-section with 200 elements.

Due to the fact, that COMSOL Multiphysics® experiences some issues when combining a user defined hyperelastic strain energy density function with plasticity the provided algorithm is validated in two steps. In a first step the external material algorithm is validated based on the well-known hyperelastic Neo-Hookean material model [10]. Therefore, the strain-energy density function within the presented algorithm is adapted

Algorithm 1 Main routine implemented in COMSOL Multiphysics® for the calculation of \mathbf{S} and \mathbf{J}

```

1: procedure EVAL(see Tables V.3 and V.4)
2:   read material parameters
3:   read state variables
4:   initialize Jacobian and identity matrix
5:   compute  $\bar{\mathbf{S}}_{n+1}$  in intermediate configuration and  $\mathbf{F}_{pl,n+1}$  calling Algorithm 2           ▷ Eq. (V.42)
6:   compute  $\mathbf{S}_{n+1}$  by pull back of  $\bar{\mathbf{S}}_{n+1}$                                            ▷ Eq. (V.46)
7:   save  $\mathbf{S}_{n+1}$  in Voigt notation
8:   update state variable  $\mathbf{F}_{pl,n+1}$ 
9:   compute perturbed deformation gradient  $\Delta\mathbf{F}(\epsilon)$                              ▷ Eq. (V.57)
10:  compute  $\bar{\mathbf{S}}_{n+1}$  in intermediate configuration                                   ▷ Eq. (V.42)
11:  compute  $\mathbf{S}_{n+1}$  by pull back of  $\bar{\mathbf{S}}_{n+1}$                                        ▷ Eq. (V.46)
12:  compute Lagrangian constant tangent modulus tensor                             ▷ Eq. (V.55)
13:  reorganize  $\mathbf{C}$  in Voigt notation
14:  compute Jacobian by calling COMSOL Multiphysics® utilize function csext_jac_con
15:  return
16: end procedure

```

Algorithm 2 Return-mapping algorithm implemented in COMSOL Multiphysics® for the calculation of $\bar{\mathbf{S}}$ and \mathbf{F}_{pl}

```

1: procedure RETMAP(see Tables V.3 and V.4)
2:   compute  $\|\bar{\mathbf{M}}_{dev}\|$  by calling Algorithm 4
3:   evaluate yield condition by calling Algorithm 5           ▷ Eq. (V.34)
4:   if  $f_{yield} > 0$  then
5:     initialize Newton iteration
6:     evaluate yield condition for current value of  $\Delta\lambda$  by calling Algorithm 5           ▷ Eq. (V.34)
7:     while  $\|f_{yield}\| \geq 1e-4$  and  $n_{iter} \leq n_{max}$  do
8:       compute  $\Delta\lambda + \epsilon$ 
9:       evaluate yield condition for current value of  $\Delta\lambda + \epsilon$  by calling Algorithm 5       ▷ Eq. (V.34)
10:      compute  $\frac{\partial f_{yield}}{\partial \Delta\lambda}$  by numerical differentiation
11:      update  $\Delta\lambda$ 
12:      evaluate yield condition for updated value of  $\Delta\lambda$  by calling Algorithm 5           ▷ Eq. (V.34)
13:    end while
14:    compute  $\|\bar{\mathbf{M}}_{dev}\|$  by calling Algorithm 4 for final value of  $\Delta\lambda$ 
15:    compute directional tensor for plastic evolution
16:    compute tensor exponential by calling Algorithm 6           ▷ Eq. (V.38)
17:    update  $\mathbf{F}_{pl}$                                            ▷ Eq. (V.37)
18:  end if
19:  compute  $\mathbf{F}_{el}$                                            ▷ Eq. (V.20)
20:  compute  $\mathbf{C}$                                                ▷ Eq. (V.51)
21:  compute  $\bar{\mathbf{S}}_{n+1}$  in intermediate configuration by calling Algorithm 3           ▷ Eq. (V.42)
22:  return
23: end procedure

```

Variable	Symbol	Description
F	\mathbf{F}	Input: Deformation gradient
Fpl	$\mathbf{F}_{pl,n}$	Input: Plastic part of deformation gradient
Fpl	$\mathbf{F}_{pl,n+1}$	Output: Updated plastic part of deformation gradient
Sint	$\bar{\mathbf{S}}$	Output: Second Piola-Kirchhoff stress tensor with respect to the intermediate configuration
lam	Λ	Input: Material parameter
mu	μ	Input: Material parameter
alpha	α	Input: Material parameter
beta	β	Input: Material parameter
gamma	γ	Input: Material parameter
sigYs	σ_{yield}	Input: Yield stress

Table V.5: List of input and output variables for the subroutine RETMAP COMSOL Multiphysics®.

Table V.6: Material parameters validation with Neo-Hookean material model.

	Λ GPa	μ GPa	α GPa	β GPa	γ GPa	σ_Y MPa
Neo-Hookean	5.38	1.20	-	-	-	50
Transversely-isotropic	5.38	1.20	1.10	-0.13	1.13	-

to the one implemented in COMSOL Multiphysics® for the Neo-Hookean material model given by

$$\Psi_{Neo} = \frac{1}{2}\mu(I_1 - 3) - \mu \ln(J) + \frac{1}{2}\Lambda[\ln(J)]^2. \quad (V.60)$$

Subsequently two numerical simulations are performed. One with the implemented Neo-Hookean hyperelastic material model and a second one with the provided external material algorithm. In both cases ideal plasticity and a plain-strain state are assumed. The corresponding material properties are provided in Table V.6. Furthermore, a total displacement of $u_x = 1$ mm corresponding to a strain of 2% is applied to ensure plastic deformation. In a second step the strain-energy density function provided by Bonet[16] is passed to COMSOL Multiphysics® as an user-defined potential. Since this cannot be combined with ideal plastic behavior due to convergence issues, this is only simulated assuming elastic deformation. The results are compared again to the results provided by Algorithm 1. The corresponding material parameters are also provided in Table V.6.

The results are depicted in Figure V.9. The first row gives the result for the isotropic Neo-Hookean simulation, the second row holds the results for the transversely-isotropic simulations. The diagrams on the left hand side contain stress-strain curves. The von Mises stress is plotted in black and the horizontal component of the second Piola-Kirchhoff stress is plotted in gray, respectively. Following the theoretical framework provided in Section V.4.1 it is important to note, that the von Mises stress is given in the intermediate configuration where as the second Piola-Kirchhoff stress tensor stands in the reference configuration. The solid lines give the results of the implemented material model in COMSOL Multiphysics® and the small circles belong to the results obtained by the external material routine. As indicated by the diagrams on the right hand side, that provide the deviation of the external material routine to the implemented material model in percent, both validation steps show good agreement. Both comparisons experiences an increasing deviation at large

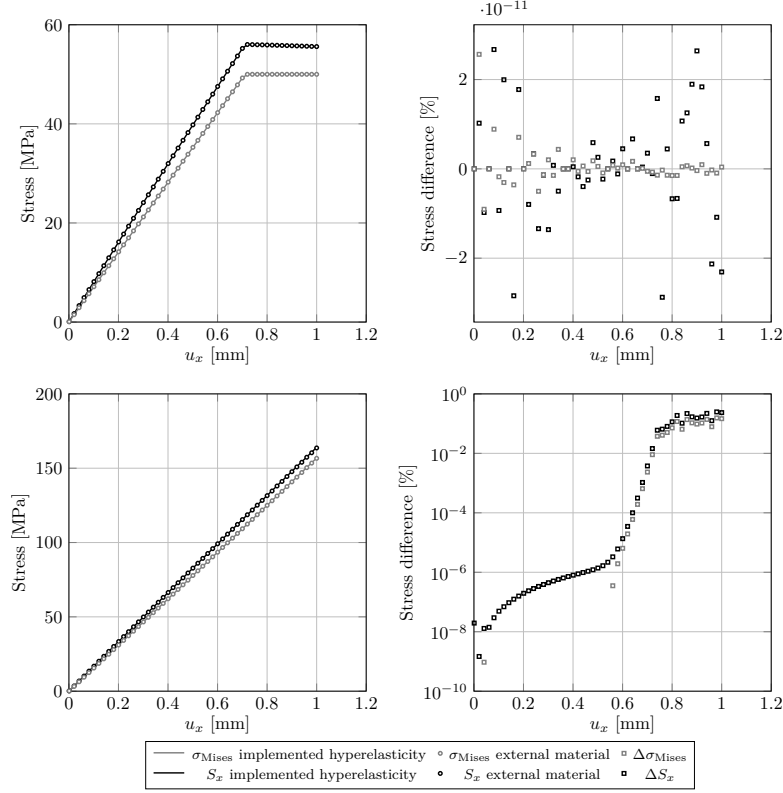


Figure V.9: Numerical validation of the implemented general stress-deformation algorithm in COMSOL Multiphysics®.

displacements, which is still very small.

V.5 Application to tensile test specimen

In this last step the presented modeling approach is used to incorporate the spatial distributed elastic-ideal plastic material behavior of SFRC into a numerical simulation of tensile tests. As mentioned before the probabilistic characteristics of the material parameters are analyzed in a former study of the authors [142]. The main results are summarized in Table V.2 for a window size of 750 μm , which show the best approximation for the simulation on the component level [145]. In this section the numerical model is briefly introduced, the numerical results are shown and corresponding results are discussed in detail including a comparison with the experimental data presented in Section V.2. This includes the analysis of the influence of the correlation length on the standard deviation of the obtained results and the selection of an optimal correlation length for which the numerical results and the experimental measurements coincide best.

V.5.1 Numerical model

The numerical model used to validate the novel modeling approach on the component level based on tensile test specimens is identical to the one used in Section V.4.2.2. As already discussed in Section V.3.2 only one parameter of the strain-energy density function and the yield strength are represented by cross-correlated second-order Gaussian random fields. This reduces the complexity at this state of the investigations. Since in this case the standard deviation of the material parameter Λ does not cover the total standard deviation of elasticity tensor element C_{11} , which is significantly related to the structural behavior under uniaxial tension, the corresponding value is set to 1.74 GPa. Furthermore, the experimental data clearly reveal that local plastic deformation occur even at low stress levels. This is related to the yield strength of the matrix material and to

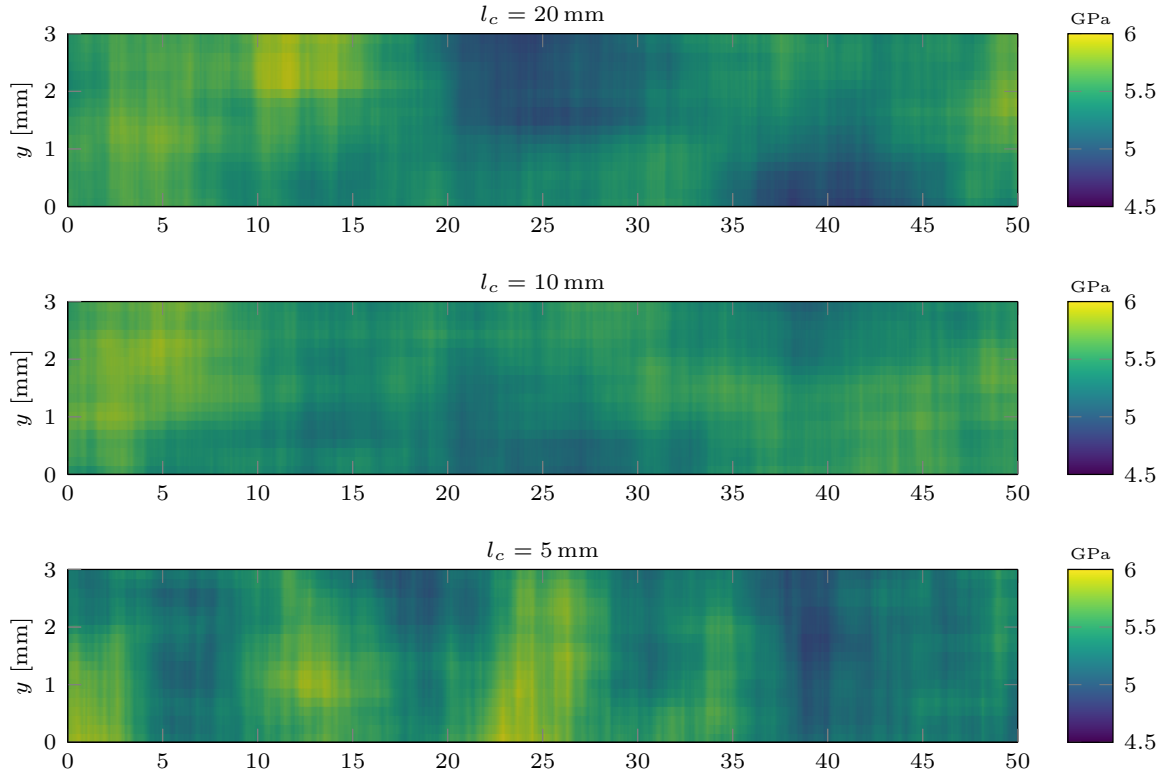


Figure V.10: Discretizations of cross-correlated homogeneous second-order Gaussian random fields to represent the spatially distributed material parameter Λ for different values of l_x .

plastic deformation induced by stress peaks at the edges of the reinforcing elements. In addition, the maximal stress level of the data sheet and hence, the results of the homogenization is not reached. Therefore, the mean value and the standard deviation are adjusted and set to 100 MPa and 31 MPa, respectively. The remaining parameters are assumed to be homogeneous and are set to the mean values obtained by a previous correlation analysis [142]. Furthermore, a plain strain state is employed. This is eligible because the microstructure of SFRC consists of layers with different main fiber orientation [46, 154]. The core layer, which is located in the center of the cross-section, is characterized by a fiber orientation perpendicular to the main flow direction of the injection mold process. With respect to the specimens used in this study the fibers within the small core layer are perpendicular to the load direction and hence, inhibit the out-of-plane deformation.

Further crucial parameters for the numerical simulation are the correlation lengths of the random fields. Since the correlation length significantly influences the local distribution of the material properties it is strongly linked to the standard deviation of the numerical results. Therefore, in this study different values are used to analyze the influence more in detail. In Figure V.10 realizations of for the strain-energy density function parameter Λ are depicted for a correlation length in horizontal direction of $l_x = 5$ mm, $l_x = 10$ mm, and $l_x = 20$ mm. In vertical direction the correlation length is set to $l_y = 3$ mm. The effect of the correlation length on the random field is clearly observable. In analogy to the description of oscillations the correlation length can be interpreted as the wavelength of the dominant eigenfunctions.

In this work the numerical simulation are performed for horizontal correlation length of $l_x = 5$ mm, $l_x = 10$ mm, and $l_x = 15$ mm. The correlation length in vertical direction is set to 0.3 mm for all simulations. The value is chosen to allow plastic deformation at different locations as it is observed during the experimental investigations. In combination with the ideal plastic modeling approach the resulting stress-strain relation approximates the experimental data for reinforced material. Would the correlation length be identical to the specimen's thickness of 3 mm the plastic deformation is limited to the region where the yield strength is

Strain level %	$l_x = 15 \text{ mm}$		$l_x = 10 \text{ mm}$		$l_x = 5 \text{ mm}$		Experimental data	
	mean	std	mean	std	mean	std	mean	std
	MPa	MPa	MPa	MPa	MPa	MPa	MPa	MPa
0.2	16.6	0.1	16.6	0.1	16.6	0.1	16.1	1.8
0.5	41.6	0.3	41.4	0.3	41.3	0.2	38.7	3.7
1.0	80.0	1.2	78.6	1.6	76.9	1.7	70.0	5.8
1.5	99.2	5.2	97.7	2.6	92.0	3.9	88.5	6.8
2.0	102.3	7.2	101.8	2.4	94.7	4.9	95.8	6.3

Table V.7: Deviation of the second Piola-Kirchhoff stress tensor component for the examined correlation lengths at different strain levels and comparison with the experimental data.

reached first, because the surrounding material cannot take higher stress levels. The obtained results would then be characterized purely by the ideal plastic behavior of the matrix material.

The numerical simulations are carried out for eight different realizations per correlation length. Hence, in total 24 simulations are conducted. The results are presented below.

V.5.2 Results

The results of the numerical simulations are summarized in Figure V.11. Furthermore, a comparison of the numerical data with the experimental results is included. The diagrams on the left hand side contain the stress-strain curve (black), taken from the data sheet [21], the experimental data (gray), see Section V.2, and the numerically obtained results (colored) for correlation lengths of $l_x = 5 \text{ mm}$, $l_x = 10 \text{ mm}$, and $l_x = 15 \text{ mm}$ from top to bottom. The diagrams on the right hold again the stress-strain curve (black), taken from the data sheet [21] and the numerical data (gray). One data set is highlighted. The corresponding stress-strain curve is based on a measurement length of 50 mm. For these specimens the spatial distribution of the material properties is qualitatively investigated by deriving the results for three sections of 15 mm each.

For a better comparability Table V.7 holds some additional information. For strain levels of 0.2 %, 0.5 %, 1.0 %, 1.5 %, and 2.0 % the mean stress as well as standard deviations are computed for the numerical and experimental data. For all numerical results the stress refers to the horizontal component of the second Piola-Kirchhoff stress tensor.

V.5.3 Discussion

The diagrams provided in Figure V.11 reveal that the numerical obtained stress-strain curves clearly show the expected elasto-plastic behavior. Despite the fact, that the material behavior is modeled based on the assumption of an elastic ideal-plastic material model, the resulting stress-strain curves show an overall good agreement with the experimental data. This is related to the localized plastic deformation and the rearrangement of the applied loading. In addition the diagrams disclose, that the numerical results show a better agreement with the experimental data for a decreasing correlation length. This is also indicated by the values provided in Table V.7. For a decreasing correlation length the mean stress state converges to the experimentally obtained values, for a correlation length of 5 mm the results show an overall good agreement. The deviation between the mean stress states at the different strain levels for the experimental and numerical results is covered by the standard deviation. However, despite the good overall conformity, the results indicate two shortcomings. First, the experimentally obtained stress range at strain levels up to 1 % is not covered by the numerical simulation. This might be due to reduction of parameters that are represented by random fields. Second, even though the composite material does not show explicitly ideal plasticity, the plastic deformation within the numerical

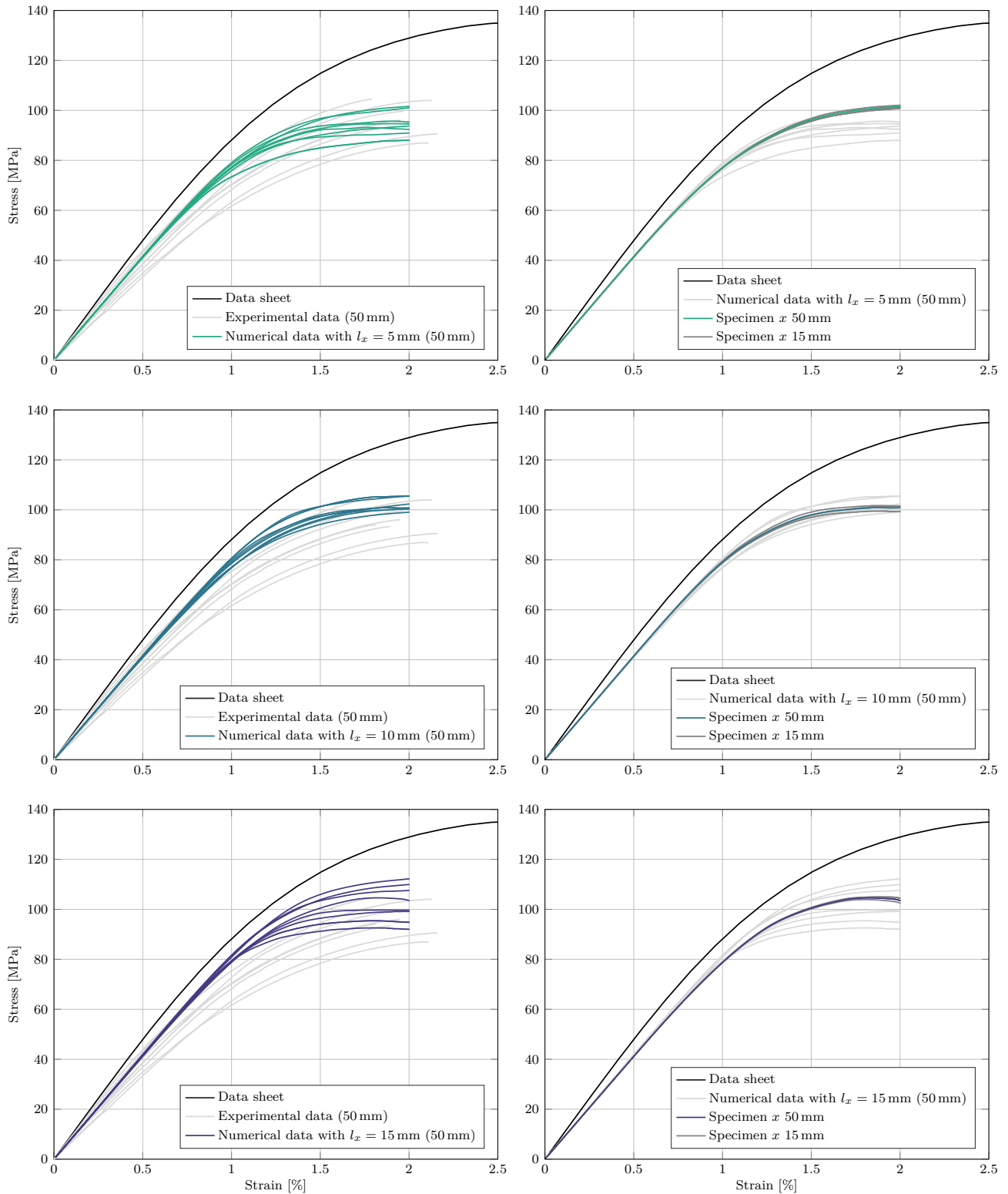


Figure V.11: Results of the numerical simulation in comparison with the experimentally obtained results and a stress-strain curve provided by the manufacturer [21].

simulations starts at higher strain levels as indicated by the experimental results. This might be resolved by reducing the yield strength locally or taking into account hardening effects.

The modeling approach is further endorsed by the results on the right hand side by two important aspects. First, the modeling approach leads to a plastic deformation covering the whole specimen and hence, does not show localized plastic deformation. Second, when dividing the measurement length into small sections, each section show a slightly different behavior. Both phenomena are confirmed by the experimental investigation.

All in all, it can be stated, that the presented modeling approach is a very appropriate method to incorporate the spatial distribution of the elastic and plastic material properties of SFRC.

V.6 Summary and conclusion

In this work a probabilistic modeling approach for the elasto-plastic material behavior at finite strain based on second-order Gaussian random fields is introduced. The description of the material behavior is based on the Kröner-Lee decomposition. Following this, the strain-energy density function introduced by Bonet et al. [16] is combined with a classical J_2 -plasticity formulation assuming ideal plastic behavior. Since this material model is not available in commercially available finite element codes, first an algorithm covering transversely-isotropic elastic-ideal plastic material behavior is developed and implemented in COMSOL Multiphysics®. The validation based on the well-known Neo-Hookean material model in the elastic and plastic domain as well as utilizing a user-defined strain-energy density function in the elastic domain show an excellent conformity.

Therefore, in a second step, based on the correlation analysis done in a previous study [142] cross-correlated second-order Gaussian random fields are generated to represent spatial distribution the strain-energy density function parameter Λ and the yield strength induced by the probabilistic characteristics of the microstructure. The remaining parameters are assumed to be homogeneous at this state of the study. With the spatially distributed material properties tensile tests for specimens made of PBT-GF-30 are simulated. Even though the initial modeling approach is based on elastic-ideal plastic material behavior the spatial distribution of two material parameters leads to localized plastic deformation covering the whole measurement length. This causes a strain dependent reduction of the material stiffness.

To validate the numerical results and the presented modeling approach uniaxial tensile tests are conducted to characterize the elastic and plastic deformation of PBT-GF-30. The obtained stress-strain curves are compared to the numerical results. It is shown that with an decreasing correlation length the numerical data matches the experimental results quite well. The deviation at large strain can be assigned to assumption of ideal plasticity. Furthermore, this initial investigation does not show a significant deviation between the results of different realizations at a low strain level. The reasons are the reduction of complexity by representing only one parameter of the strain-energy density function by a random field and the limitation of Gaussian random fields. To ensure only positive values for the yield strength low values are underestimated.

Summarizing, it can be concluded that the presented initial probabilistic approach is suitable for the numerical simulation of the elasto-plastic material behavior of SFRC at finite strain including its spatial distribution on the component level without the need of an explicit microstructural modeling. Future work will focus on the implementation of specimen unloading, hardening, non-Gaussian random fields and the representation of additional parameters by stochastic methods.

Funding

The financial support of the German Academic Exchange Service Grant No. 91789376 is gratefully acknowledged.

Acknowledgement

I want to acknowledge and extend my sincere thanks to Celia Reina for the valuable ideas and tips during our discussions that significantly improved and shaped the work.

Variable	Symbol	Description
Cel	$\bar{\mathbf{C}}_{\text{el}}$	Input: Elastic part of right Cauchy-Green tensor
lam	Λ	Input: Material parameter
mu	μ	Input: Material parameter
alpha	α	Input: Material parameter
beta	β	Input: Material parameter
gamma	γ	Input: Material parameter
tol_inv	–	Input: Tolerance for numerical matrix inversion
S	$\bar{\mathbf{S}}$	Output: Second Piola-Kirchhoff stress tensor with respect to the intermediate configuration

Table V.8: List of input and output arguments for Algorithm 3 (CALCS_INTERMEDIATE).

Variable	Symbol	Description
F	\mathbf{F}	Input: Deformation gradient
Fpl	\mathbf{F}_{pl}	Input: Plastic part of deformation gradient
Mdev	$\bar{\mathbf{M}}_{\text{dev}}$	Input: Deviatoric part of Mandel stress with respect to the intermediate configuration
lam	Λ	Input: Material parameter
mu	μ	Input: Material parameter
alpha	α	Input: Material parameter
beta	β	Input: Material parameter
gamma	γ	Input: Material parameter
tol_inv	–	Input: Tolerance for numerical matrix inversion
dnormx	$\ \bar{\mathbf{M}}_{\text{dev}}\ $	Output: Norm of deviatoric part of Mandel stress with respect to the intermediate configuration

Table V.9: List of input and output arguments for Algorithm 4 (CALCNORMM).

Conflict of Interest

The author declares no conflict of interest. The funders had no role in the design of the study; in the collection, analyses, or interpretation of data; in the writing of the manuscript, or in the decision to publish the results.

V.A Supporting routines

For the implementation of the elastic-ideal plastic routine in COMSOL Multiphysics® several subroutines are used to calculate the second Piola-Kirchhoff stress tensor in the intermediate and reference configuration, respectively. Furthermore, the subroutine to calculate the exponential functions `mat exp` provided by Hashiguchi et al. [63] written in Fortran is transferred into C. Beside this subroutines COMSOL Multiphysics® provides a library of utility functions for various tensor operations, computing principle and equivalent stresses. These routines are not explained here, a detailed overview is given in the documentation [168].

Variable	Symbol	Description
dp	$\Delta\lambda$	Input: Plastic multiplier
F	\mathbf{F}	Input: Deformation gradient
Fpl	\mathbf{F}_{pl}	Input: Plastic part of deformation gradient
lam	Λ	Input: Material parameter
mu	μ	Input: Material parameter
alpha	α	Input: Material parameter
beta	β	Input: Material parameter
gamma	γ	Input: Material parameter
sigYs	σ_{yield}	Input: Yield stress
dev	f_{yield}	Output: Value of yield function

Table V.10: List of input and output arguments for Algorithm 5 (CALC_DEV).

Algorithm 3 Subroutine implemented in COMSOL Multiphysics® for the calculation of $\bar{\mathbf{S}}$

- 1: **procedure** CALCS_INTERMEDIATE(see Table V.8)
 - 2: compute fiber orientation matrix $\mathbf{A} = \mathbf{a}\mathbf{a}^T$
 - 3: compute J , $\bar{\mathbf{C}}_{el}^{-1}$, $\det \bar{\mathbf{C}}_{el}$, $\text{tr } \bar{\mathbf{C}}_{el}$, and I_4 ▷ Eqs. (V.21), (V.22), and (V.40)
 - 4: compute $\bar{\mathbf{S}}$ ▷ Eq. (V.42)
 - 5: **end procedure**
-

Algorithm 4 Subroutine implemented in COMSOL Multiphysics® for the calculation of $\|\bar{\mathbf{M}}_{dev}\|$

- 1: **procedure** CALC_NORMM(see Table V.9)
 - 2: compute fiber orientation vector \mathbf{a} and matrix $\mathbf{A} = \mathbf{a}\mathbf{a}^T$
 - 3: compute \mathbf{F}_{pl}^{-1} , \mathbf{F}_{el} ▷ Eq. (V.20)
 - 4: compute \mathbf{C} ▷ Eq. (V.51)
 - 5: compute $\bar{\mathbf{S}}$ by calling Algorithm 3 ▷ Eq. (V.42)
 - 6: compute $\bar{\mathbf{M}}$ and $\bar{\mathbf{M}}_{dev}$ ▷ Eq. (V.32)
 - 7: compute $\|\bar{\mathbf{M}}_{dev}\|$
 - 8: **end procedure**
-

Algorithm 5 Subroutine implemented in COMSOL Multiphysics® for the evaluation of f_{yield}

- 1: **procedure** CALC_DEV(see Table V.9)
 - 2: compute $\|\bar{\mathbf{M}}_{dev}\|$ by calling Algorithm 4
 - 3: compute directional tensor of plastic evolution
 - 4: compute tensor exponential by calling Algorithm 6 ▷ Eq. (V.38)
 - 5: update \mathbf{F}_{pl} ▷ Eq. (V.37)
 - 6: compute $\|\bar{\mathbf{M}}_{dev}\|$ by calling Algorithm 4
 - 7: evaluate f_{yield} ▷ Eq. (V.34)
 - 8: **end procedure**
-

Variable	Symbol	Description
nmax	–	Input: Maximum number of terms of the series representation
etol	–	Input: Convergence tolerance
a	–	Input: Matrix
aexp	–	Output: Tensor exponential function

Table V.11: List of input and output arguments for Algorithm 6 (MATEXP).

Algorithm 6 Subroutine implemented in COMSOL Multiphysics® for the calculation of the tensor exponential function, adapted from Hashiguchi et al. [63]

```

1: procedure MATEXP(see Table V.10)
2:   initialize Identity matrix as first element of the series expansion
3:   initialize temp and A
4:   initialize factorial
5:   set temp to initial solution
6:   do
7:     compute  $T^n$  and its norm
8:     compute  $n!$ 
9:     add  $T^n$  to temp
10:    compute current solution by adding n-th order term to A
11:    check convergence
12:  while res > tol and n < nmax
13: end procedure

```

Bibliography

1. Adam, L. & Assaker, R. Integrated nonlinear multi-scale material modelling of fiber reinforced plastics with digimat: Application to short and continuous fiber composite. *Proceedings 11th World Congress on Computational Mechanics* (2014).
2. Advani, S. G. & Tucker, C. L. The Use of Tensors to Describe and Predict Fiber Orientation in Short Fiber Composites. *Journal of Rheology* **31**, 751–784 (1987).
3. Altenbach, H. *Kontinuumsmechanik* (Springer Berlin Heidelberg, Berlin, Heidelberg, 2015).
4. Altenbach, H., Altenbach, J. & Kissing, W. *Mechanics of composite structural elements* (Springer, Singapore, 2018).
5. Alzarrug, F. A., Dimitrijević, M. M., Jančić Heinemann, R. M., Radojević, V., Stojanović, D. B., Uskoković, P. S. & Aleksić, R. The use of different alumina fillers for improvement of the mechanical properties of hybrid PMMA composites. *Materials & Design* **86**, 575–581 (2015).
6. Atkinson, K. E. *The Numerical Solution of Integral Equations of the Second Kind* (Cambridge University Press, 2010).
7. Bathe, K.-J. *Finite element procedures* (Prentice-Hall, Englewood Cliffs, N.J, 2014).
8. Baxter, S. C. & Graham, L. L. Characterization of Random Composites Using Moving-Window Technique. *Journal of Engineering Mechanics* **126**, 389–397 (2000).
9. Behrens, B.-A., Rolfes, R., Vucetic, M., Reinoso, J., Vogler, M. & Grbic, N. Material Modelling of Short Fiber Reinforced Thermoplastic for the FEA of a Clinching Test. *Procedia CIRP* **18**, 250–255 (2014).
10. Belytschko, T., Liu, W. K. & Moran, B. *Nonlinear finite elements for continua and structures* (Wiley, Chichester, 2003).
11. Bendat, J. S. & Piersol, A. G. *Random data: Analysis and measurement procedures* (Wiley, Hoboken, NJ, 2010).
12. Berkovich, E. S. Three-Faceted Diamond Pyramid for Micro-hardness Testing. *Industrial Diamond Review* **11**, 129–132 (1951).
13. Bertein, J.-C. & Ceschi, R. *Discrete Stochastic Processes and Optimal Filtering* (John Wiley & Sons, 2007).
14. Betz, W., Papaioannou, I. & Straub, D. Numerical methods for the discretization of random fields by means of the Karhunen–Loève expansion. *Computer Methods in Applied Mechanics and Engineering* **271**, 109–129 (2014).
15. Bharat Bhushan & Manuel L. B. Palacio. in *Encyclopedia of Nanotechnology* 1576–1596 (Springer, Dordrecht, 2012).
16. Bonet, J. & Burton, A. J. A simple orthotropic, transversely isotropic hyperelastic constitutive equation for large strain computations. *Computer Methods in Applied Mechanics and Engineering* **162**, 151–164 (1998).
17. Breuer, K. & Stommel, M. RVE modelling of short fiber reinforced thermoplastics with discrete fiber orientation and fiber length distribution. *SN Applied Sciences* **2**, 140 (2020).
18. Breuer, K. & Stommel, M. Prediction of Short Fiber Composite Properties by an Artificial Neural Network Trained on an RVE Database. *Fibers* **9**, 8 (2021).
19. Brezinová, J. & Guzanová, A. Friction Conditions during the Wear of Injection Mold Functional Parts in Contact with Polymer Composites. *Journal of Reinforced Plastics and Composites* **29**, 1712–1726 (2010).

20. Budday, S., Nay, R., de Rooij, R., Steinmann, P., Wyrobek, T., Ovaert, T. C. & Kuhl, E. Mechanical properties of gray and white matter brain tissue by indentation. *Journal of the mechanical behavior of biomedical materials* **46**, 318–330 (2015).
21. CAMPUS®. *CAMPUS® Datasheet: Ultradur® B 4300 G6 - PBT-GF30* 11.03.2021.
22. Chen, G. & Suo, X. Constitutive modeling of nonlinear compressive behavior of fiber reinforced polymer composites. *Polymer Composites* **41**, 182–190 (2020).
23. Chicot, D., Yetna N’Jock, M., Puchhi-Cabrera, E. S., Iost, A., Staia, M. H., Louis, G., Bouscarrat, G. & Aumaitre, R. A contact area function for Berkovich nanoindentation : Application to hardness determination of a TiHfCN thin film. *Thin Solid Films* **558**, 259–266 (2014).
24. Chin, W.-K., Liu, H.-T. & Lee, Y.-D. Effects of fiber length and orientation distribution on the elastic modulus of short fiber reinforced thermoplastics. *Polymer Composites* **9**, 27–35 (1988).
25. Cho, H., Venturi, D. & Karniadakis, G. E. Karhunen–Loève expansion for multi-correlated stochastic processes. *Probabilistic Engineering Mechanics* **34**, 157–167 (2013).
26. Cho, H., Mayer, S., Pösel, E., Susoff, M., in ’t Veld, P. J., Rutledge, G. C. & Boyce, M. C. Deformation mechanisms of thermoplastic elastomers: Stress-strain behavior and constitutive modeling. *Polymer* **128**, 87–99 (2017).
27. Chu, S. & Guillemot, J. Stochastic multiscale modeling with random fields of material properties defined on nonconvex domains. *Mechanics Research Communications* **97**, 39–45 (2019).
28. Cowin, S. C. *Continuum Mechanics of Anisotropic Materials* (Springer New York, New York, NY, 2013).
29. Dean, A., Grbic, N., Rolfes, R. & Behrens, B. Macro-mechanical modeling and experimental validation of anisotropic, pressure- and temperature-dependent behavior of short fiber composites. *Composite Structures* **211**, 630–643 (2019).
30. Dean, A., Reinoso, J., Sahraee, S. & Rolfes, R. An invariant-based anisotropic material model for short fiber-reinforced thermoplastics: Coupled thermo-plastic formulation. *Composites Part A: Applied Science and Manufacturing* **90**, 186–199 (2016).
31. De Groof, V., Oberguggenberger, M., Haller, H., Degenhardt, R. & Kling, A. A case study of random field models applied to thin-walled composite cylinders in finite element analysis. *Proceedings 11th International Conference on Structural Safety & Reliability* (2013).
32. Der Kiureghian, A. & Ke, J.-B. The stochastic finite element method in structural reliability. *Probabilistic Engineering Mechanics* **3**, 83–91 (1988).
33. Dillenberger, F. *On the anisotropic plastic behaviour of short fibre reinforced thermoplastics and its description by phenomenological material modelling* Dissertation (Technische Universität Darmstadt, Darmstadt, 2019).
34. Diobet, M. in *Nanoindentation in Materials Science* (ed Nemecek, J.) (InTech, 2012).
35. Doerner, M. F. & Nix, W. D. A method for interpreting the data from depth-sensing indentation instruments. *Journal of Materials Research* **1**, 601–609 (1986).
36. Downey, R. H., Brewer, L. N. & Karunasiri, G. Determination of mechanical properties of a MEMS directional sound sensor using a nanoindenter. *Sensors and Actuators A: Physical* **191**, 27–33 (2013).
37. Dvorak, G. *Micromechanics of Composite Materials* (Springer Netherlands, Dordrecht, 2013).
38. Ebrahimi, F. & Dabbagh, A. A comprehensive review on modeling of nanocomposite materials and structures. *Journal of Computational Applied Mechanics* **50**, 197–209 (2019).
39. Eidel, B. & Gruttmann, F. Elastoplastic orthotropy at finite strains: multiplicative formulation and numerical implementation. *Computational Materials Science* **28**, 732–742 (2003).

40. Eshelby, J. D. The determination of the elastic field of an ellipsoidal inclusion, and related problems. *Proceedings of the Royal Society of London. Series A. Mathematical and Physical Sciences* **241**, 376–396 (1957).
41. Fiebig, I. & Schoeppner, V. Influence of the Initial Fiber Orientation on the Weld Strength in Welding of Glass Fiber Reinforced Thermoplastics. *International Journal of Polymer Science* **2016**, 1–16 (2016).
42. Folgar, F. & Tucker, C. L. Orientation Behavior of Fibers in Concentrated Suspensions. *Journal of Reinforced Plastics and Composites* **3**, 98–119 (1984).
43. Foss, P. H., Tseng, H.-C., Snawerdt, J., Chang, Y.-J., Yang, W.-H. & Hsu, C.-H. Prediction of fiber orientation distribution in injection molded parts using Moldex3D simulation. *Polymer Composites* **35**, 671–680 (2014).
44. Fu, S.-Y. Effects of fiber length and fiber orientation distributions on the tensile strength of short-fiber-reinforced polymers. *Composites Science and Technology* **56**, 1179–1190 (1996).
45. Fu, S.-Y. & Lauke, B. An analytical characterization of the anisotropy of the elastic modulus of misaligned short-fiber-reinforced polymers. *Composites Science and Technology* **58**, 1961–1972 (1998).
46. Gandhi, U. N., Goris, S., Osswald, T. A. & Song, Y.-Y. *Discontinuous fiber-reinforced composites: Fundamentals and applications* (Hanser Publishers and Hanser Publications, Munich and Cincinnati, OH, 2020).
47. Ghanem, R. G. *Stochastic finite elements: A spectral approach* (Springer, New York, 2012).
48. Ghanem, R. G. & Spanos, P. D. Polynomial Chaos in Stochastic Finite Elements. *Journal of Applied Mechanics* **57**, 197–202 (1990).
49. Gibson, R. F. A review of recent research on nanoindentation of polymer composites and their constituents. *Composites Science and Technology* **105**, 51–65 (2014).
50. Golub, G. H. & van Loan, C. F. *Matrix computations* (Johns Hopkins Univ. Press, Baltimore, 2007).
51. Graham-Brady, L. L., Siragy, E. F. & Baxter, S. C. Analysis of Heterogeneous Composites Based on Moving-Window Techniques. *Journal of Engineering Mechanics* **129**, 1054–1064 (2003).
52. Gross, T. S., Timoshchuk, N., Tsukrov, I. I., Piat, R. & Reznik, B. On the ability of nanoindentation to measure anisotropic elastic constants of pyrolytic carbon. *ZAMM - Zeitschrift für Angewandte Mathematik und Mechanik* **93**, 301–312 (2013).
53. Guan, X., Liu, X., Jia, X., Yuan, Y., Cui, J. & Mang, H. A. A stochastic multiscale model for predicting mechanical properties of fiber reinforced concrete. *International Journal of Solids and Structures* **56–57**, 280–289 (2015).
54. Guilleminot, J. in *Uncertainty Quantification in Multiscale Materials Modeling* (eds Wang, M. & McDowell, D. L.) 385–420 (Woodhead Publishing, 2020).
55. Guilleminot, J. & Soize, C. in *Encyclopedia of Continuum Mechanics* (eds Altenbach, H. & Öchsner, A.) 1–9 (Springer Berlin Heidelberg, Berlin, Heidelberg, 2017).
56. Guilleminot, J., Soize, C. & Kondo, D. Mesoscale probabilistic models for the elasticity tensor of fiber reinforced composites: Experimental identification and numerical aspects. *Mechanics of Materials* **41**, 1309–1322 (2009).
57. Guilleminot, J., Soize, C., Kondo, D. & Binetruy, C. Theoretical framework and experimental procedure for modelling mesoscopic volume fraction stochastic fluctuations in fiber reinforced composites. *International Journal of Solids and Structures* **45**, 5567–5583 (2008).
58. Günzel, S. *Analyse der Schädigungsprozesse in einem kurzglasfaserverstärkten Polyamid unter mechanischer Belastung mittels Röntgenrefraktometrie, Bruchmechanik und Fraktografie* Dissertation (Technische Universität Berlin, Berlin, 2013).

59. Gupta, M. & Wang, K. K. Fiber orientation and mechanical properties of short-fiber-reinforced injection-molded composites: Simulated and experimental results. *Polymer Composites* **14**, 367–382 (1993).
60. Gusev, A. A., Hine, P. J. & Ward, I. M. Fiber packing and elastic properties of a transversely random unidirectional glass/epoxy composite. *Composites Science and Technology* **60**, 535–541 (2000).
61. Halpin, J. C. Stiffness and Expansion Estimates for Oriented Short Fiber Composites. *Journal of Composite Materials* **3**, 732–734 (1969).
62. Halpin, J. C. & Kardos, J. L. The Halpin-Tsai equations: A review. *Polymer Engineering and Science* **16**, 344–352 (1976).
63. Hashiguchi, K. *Introduction to finite strain theory for continuum elasto-plasticity* (Wiley, Chichester, West Sussex, U.K, 2012).
64. Hashin, Z. Analysis of Composite Materials—A Survey. *Journal of Applied Mechanics* **50**, 481–505 (1983).
65. Hay, J. C., Bolshakov, A. & Pharr, G. M. A critical examination of the fundamental relations used in the analysis of nanoindentation data. *Journal of Materials Research* **14**, 2296–2305 (1999).
66. Hazanov, S. Hill condition and overall properties of composites. *Archive of Applied Mechanics (Ingenieur Archiv)* **68**, 385–394 (1998).
67. Hazanov, S. & Huet, C. Order relationships for boundary conditions effect in heterogeneous bodies smaller than the representative volume. *Journal of the Mechanics and Physics of Solids* **42**, 1995–2011 (1994).
68. Hickmann, M. A. & Basu, P. K. Stochastic Multiscale Characterization of Short-Fiber Reinforced Composites. *Technische Mechanik* **36**, 13–31 (2016).
69. Hill, R. The Elastic Behaviour of a Crystalline Aggregate. *Proceedings of the Royal Society of London. Series A. Mathematical and Physical Sciences* **A65**, 349–354 (1952).
70. Hill, R. Elastic properties of reinforced solids: Some theoretical principles. *Journal of the Mechanics and Physics of Solids* **11**, 357–372 (1963).
71. Hill, R. Theory of mechanical properties of fibre-strengthened materials: I. Elastic behaviour. *Journal of the Mechanics and Physics of Solids* **12**, 199–212 (1964).
72. Hine, P. J., Rudolf Lusti, H. & Gusev, A. A. Numerical simulation of the effects of volume fraction, aspect ratio and fibre length distribution on the elastic and thermoelastic properties of short fibre composites. *Composites Science and Technology* **62**, 1445–1453 (2002).
73. Hodzic, A., Kalyanasundaram, S., Kim, J., Lowe, A. & Stachurski, Z. Application of nano-indentation, nano-scratch and single fibre tests in investigation of interphases in composite materials. *Micron* **32**, 765–775 (2001).
74. Holzapfel, G. A. *Nonlinear solid mechanics: A continuum approach for engineering* (John Wiley & Sons LTD, Chichester et al., 2000).
75. Hristopulos, D. T. *Random fields for spatial data modeling: A primer for scientists and engineers* (Springer, Dordrecht, 2020).
76. Huang, C.-T., Chen, X.-W. & Fu, W.-W. Investigation on the Fiber Orientation Distributions and Their Influence on the Mechanical Property of the Co-Injection Molding Products. *Polymers* **12**, 24 (2019).
77. Huang, H.-B. & Huang, Z.-M. Micromechanical prediction of elastic-plastic behavior of a short fiber or particle reinforced composite. *Composites Part A: Applied Science and Manufacturing* **134**, 105889 (2020).
78. Huang, S. P., Quek, S. T. & Phoon, K. K. Convergence study of the truncated Karhunen–Loeve expansion for simulation of stochastic processes. *International Journal for Numerical Methods in Engineering* **52**, 1029–1043 (2001).

79. Huet, C. Universal conditions for assimilation of a heterogeneous material to an effective continuum. *Mechanics Research Communications* **9**, 165–170 (1982).
80. Huet, C. On the definition and experimental determination of effective constitutive equations for assimilating heterogeneous materials. *Mechanics Research Communications* **11**, 195–200 (1984).
81. Huet, C. Application of variational concepts to size effects in elastic heterogeneous bodies. *Journal of the Mechanics and Physics of Solids* **38**, 813–841 (1990).
82. Idiart, M. I. & Ponte Castañeda, P. Field statistics in nonlinear composites. I. Theory. *Proceedings of the Royal Society A: Mathematical, Physical and Engineering Sciences* **463**, 183–202 (2007).
83. Idiart, M. I. & Ponte Castañeda, P. Field statistics in nonlinear composites. II. Applications. *Proceedings of the Royal Society A: Mathematical, Physical and Engineering Sciences* **463**, 203–222 (2007).
84. International Organization for Standardization. *Plastics - Determination of tensile properties: Part 1: General principles* Berlin, 2019.
85. Jia, D., Shi, H. & Cheng, L. Multiscale thermomechanical modeling of short fiber-reinforced composites. *Science and Engineering of Composite Materials* **24**, 765–772 (2017).
86. Kabele, P. Stochastic Finite Element Modeling of Multiple Cracking in Fiber Reinforced Cementitious Composites. *Fracture and Damage Advanced Fibre-reinforced Cement-based Materials Proceedings*, 155–163 (2010).
87. Kaliske, M. A formulation of elasticity and viscoelasticity for fibre reinforced material at small and finite strains. *Computer Methods in Applied Mechanics and Engineering* **185**, 225–243 (2000).
88. Kamiński, M. & Kleiber, M. Stochastic structural interface defects in fiber composites. *International Journal of Solids and Structures* **33**, 3035–3056 (1996).
89. Karimzadeh, A., R Koloor, S. S., Ayatollahi, M. R., Bushroa, A. R. & Yahya, M. Y. Assessment of Nano-Indentation Method in Mechanical Characterization of Heterogeneous Nanocomposite Materials Using Experimental and Computational Approaches. *Scientific Reports* **9**, 15763 (2019).
90. Khanna, S. K., Ranganathan, P., Yedla, S. B., Winter, R. M. & Paruchuri, K. Investigation of Nanomechanical Properties of the Interphase in a Glass Fiber Reinforced Polyester Composite Using Nanoindentation. *Journal of Engineering Materials and Technology* **125**, 90–96 (2003).
91. Klein, C. A. & Cardinale, G. F. *Young's modulus and Poisson's ratio of CVD diamond* in *Diamond Optics V* (eds Feldman, A. & Holly, S.) (SPIE, 1992), 178–193.
92. Koumoulos, E. P., Jagdale, P., Lorenzi, A., Tagliaferro, A. & Charitidis, C. A. Evaluation of surface properties of epoxy–nanodiamonds composites. *Composites Part B: Engineering* **80**, 27–36 (2015).
93. Krier, J., Breuils, J., Jacomine, L. & Pelletier, H. Introduction of the real tip defect of Berkovich indenter to reproduce with FEM nanoindentation test at shallow penetration depth. *Journal of Materials Research* **27**, 28–38 (2012).
94. Kröner, E. Allgemeine Kontinuumstheorie der Versetzungen und Eigenspannungen. *Archive for Rational Mechanics and Analysis* **4**, 273–334 (1959).
95. Lambi, M. *Predicting Performance of Thermoplastic Composites Taking Into Account the Fiber Orientation Effects Utilizing ULTRASIM Technology: Part I: Methodology* Michigan, 2011.
96. Lawrence, M. A. Basis random variables in finite element analysis. *International Journal for Numerical Methods in Engineering* **24**, 1849–1863 (1987).
97. Le, T. T., Guilleminot, J. & Soize, C. Stochastic continuum modeling of random interphases from atomistic simulations. Application to a polymer nanocomposite. *Computer Methods in Applied Mechanics and Engineering* **303**, 430–449 (2016).

98. Lee, E. H. Elastic-Plastic Deformation at Finite Strains. *Journal of Applied Mechanics* **36**, 1–6 (1969).
99. Lee, E. H. & Liu, D. T. Finite-Strain Elastic-Plastic Theory with Application to Plane-Wave Analysis. *Journal of Applied Physics* **38**, 19–27 (1967).
100. Lee, Y. H., Lee, S. W., Youn, J. R., Chung, K. & Kang, T. J. Characterization of fiber orientation in short fiber reinforced composites with an image processing technique. *Materials Research Innovations* **6**, 65–72 (2002).
101. Li, C.-C. & Der Kiureghian, A. Optimal Discretization of Random Fields. *Journal of Engineering Mechanics* **119**, 1136–1154 (1993).
102. Li, G. & Ponte Castañeda, P. Variational Estimates for the Elastoplastic Response of Particle-Reinforced Metal-Matrix Composites. *Applied Mechanics Reviews* **47**, S77–S94 (1994).
103. Liu, K., Ostadhassan, M., Bubach, B., Dietrich, R. & Rasouli, V. Nano-dynamic mechanical analysis (nano-DMA) of creep behavior of shales: Bakken case study. *Journal of Materials Science* **53**, 4417–4432 (2018).
104. Liu, P.-L. & Kiureghian, A. D. Finite Element Reliability of Geometrically Nonlinear Uncertain Structures. *Journal of Engineering Mechanics* **117**, 1806–1825 (1991).
105. Liu, W. K., Belytschko, T. & Mani, A. Random field finite elements. *International Journal for Numerical Methods in Engineering* **23**, 1831–1845 (1986).
106. Loève, M. *Probability theory* (Springer, New York, 1977).
107. Lubarda, V. A. *Elastoplasticity Theory* (CRC Press, Boca Raton, 2019).
108. Maccone, C. *Deep Space Flight and Communications: Exploiting the Sun as a Gravitational Lens* (Springer Berlin Heidelberg, Berlin, Heidelberg, 2009).
109. Malvern, L. E. *Introduction to the mechanics of a continuous medium* (Prentice-Hall, Englewood Cliffs, NJ, 1969).
110. Malyarenko, A. & Ostoja-Starzewski, M. A Random Field Formulation of Hooke's Law in All Elasticity Classes. *Journal of Elasticity* **127**, 269–302 (2017).
111. Mandel, J. in *Problems of Plasticity* (ed Sawczuk, A.) 135–143 (Springer Netherlands, Dordrecht, 1974).
112. Matthies, H. G. & Bucher, C. Finite elements for stochastic media problems. *Computer Methods in Applied Mechanics and Engineering* **168**, 3–17 (1999).
113. Menges, G. & Geisbüsch, P. Die Glasfaserorientierung und ihr Einfluss auf die mechanischen Eigenschaften thermoplastischer Spritzgießteile - Eine Abschätzmethode. *Colloid & Polymer Science* **260**, 73–81 (1982).
114. Menzel, A., Ekh, M., Runesson, K. & Steinmann, P. A framework for multiplicative elastoplasticity with kinematic hardening coupled to anisotropic damage. *International Journal of Plasticity* **21**, 397–434 (2005).
115. Menzel, A. & Steinmann, P. On the spatial formulation of anisotropic multiplicative elasto-plasticity. *Computer Methods in Applied Mechanics and Engineering* **192**, 3431–3470 (2003).
116. Miehe, C. Exponential map algorithm for stress updates in anisotropic multiplicative elastoplasticity for single crystals. *International Journal for Numerical Methods in Engineering* **39**, 3367–3390 (1996).
117. Miehe, C. Numerical computation of algorithmic (consistent) tangent moduli in large-strain computational inelasticity. *Computer Methods in Applied Mechanics and Engineering* **134**, 223–240 (1996).
118. Modniks, J. & Andersons, J. Modeling the non-linear deformation of a short-flax-fiber-reinforced polymer composite by orientation averaging. *Composites Part B: Engineering* **54**, 188–193 (2013).

119. Molazemhosseini, A., Tourani, H., Naimi-Jamal, M. R. & Khavandi, A. Nanoindentation and nanoscratching responses of PEEK based hybrid composites reinforced with short carbon fibers and nano-silica. *Polymer Testing* **32**, 525–534 (2013).
120. Mooney, M. A Theory of Large Elastic Deformation. *Journal of Applied Physics* **11**, 582–592 (1940).
121. Mori, T. & Tanaka, K. Average stress in matrix and average elastic energy of materials with misfitting inclusions. *Acta Metallurgica* **21**, 571–574 (1973).
122. Mos, N., Dolbow, J. & Belytschko, T. A finite element method for crack growth without remeshing. *International Journal for Numerical Methods in Engineering* **46**, 131–150 (1999).
123. Müller, V. *Micromechanical modeling of short-fiber reinforced composites* PhD thesis (Karlsruher Institute für Technologie, Karlsruhe, 2016).
124. Murnaghan, F. D. Finite Deformations of an Elastic Solid. *American Journal of Mathematics* **59**, 235 (1937).
125. Oliver, W. C. & Pharr, G. M. An improved technique for determining hardness and elastic modulus using load and displacement sensing indentation experiments. *Journal of Materials Research* **7**, 1564–1583 (1992).
126. Ostoja-Starzewski, M. Scale effects in materials with random distributions of needles and cracks. *Mechanics of Materials* **31**, 883–893 (1999).
127. Ostoja-Starzewski, M. Material spatial randomness: From statistical to representative volume element. *Probabilistic Engineering Mechanics* **21**, 112–132 (2006).
128. Ostoja-Starzewski, M. *Microstructural Randomness and Scaling in Mechanics of Materials* (Chapman and Hall/CRC, 2007).
129. Ostoja-Starzewski, M. *Microstructural randomness and scaling in mechanics of materials* (Chapman & Hall/CRC, Boca Raton, 2008).
130. Ostoja-Starzewski, M. Stochastic finite elements: Where is the physics? *Theoretical and Applied Mechanics* **38**, 379–396 (2011).
131. Papadopoulos, V. & Giovanis, D. G. *Stochastic Finite Element Methods: An Introduction* (Springer International Publishing, Cham, 2018).
132. Papoulis, A. & Pillai, S. U. *Probability, random variables, and stochastic processes* (McGraw-Hill, Boston, 1991).
133. Peskersoy, C. & Culha, O. Comparative Evaluation of Mechanical Properties of Dental Nanomaterials. *Journal of Nanomaterials* **2017**, 1–8 (2017).
134. Pflamm-Jonas, T. *Auslegung und Dimensionierung von kurzfaserverstärkten Spritzgussbauteilen* Dissertation (Technische Universität Darmstadt, Darmstadt, 2001).
135. Pharr, G. M., Oliver, W. C. & Brotzen, F. R. On the generality of the relationship among contact stiffness, contact area, and elastic modulus during indentation. *Journal of Materials Research* **7**, 613–617 (1992).
136. Phoon, K. K., Huang, S. P. & Quek, S. T. Simulation of second-order processes using Karhunen–Loeve expansion. *Computers & Structures* **80**, 1049–1060 (2002).
137. Pike, M. G. *Mechanical Modeling of Short Fiber Reinforced Composites Using the Extended Finite Element Method* Dissertation (Vanderbilt University, Tennessee, 2015).
138. Ponte Castañeda, P. The effective mechanical properties of nonlinear isotropic composites. *Journal of the Mechanics and Physics of Solids* **39**, 45–71 (1991).
139. Ponte Castañeda, P. Stationary variational estimates for the effective response and field fluctuations in nonlinear composites. *Journal of the Mechanics and Physics of Solids* **96**, 660–682 (2016).

140. Rauter, N., Hennings, B., Neumann, M. N., Asmus, A. & Lammering, R. in *Lamb-Wave Based Structural Health Monitoring in Polymer Composites* (eds Lammering, R., Gabbert, U., Sinapius, M., Schuster, T. & Wierach, P.) 17–62 (Springer International Publishing, Cham, 2018).
141. Rauter, N. A computational modeling approach based on random fields for short fiber-reinforced composites with experimental verification by nanoindentation and tensile tests. *Computational Mechanics* **67**, 699–722 (2021).
142. Rauter, N. Correlation analysis of the elastic-ideal plastic material behavior of short fiber-reinforced composites. *International Journal of Numerical Methods in Engineering*, 1–19 (2022).
143. Rauter, N. Numerical simulation of the elastic-ideal plastic material behavior of short fiber-reinforced composites including its spatial distribution with an experimental validation. *Applied Science*, in Revision (2022).
144. Rauter, N. & Lammering, R. Correlation structure in the elasticity tensor for short fiber-reinforced composites. *Probabilistic Engineering Mechanics* **62**, 103100 (2020).
145. Rauter, N. & Lammering, R. The impact of fiber properties on the material coefficients of short fiber-reinforced composites. *PAMM* **20**, e202000019 (2020).
146. Rauter, N. & Lammering, R. Experimental Characterization of Short Fiber-Reinforced Composites on the Mesoscale by Indentation Tests. *Applied Composite Materials* (2021).
147. Reese, S., Raible, T. & Wriggers, P. Finite element modelling of orthotropic material behaviour in pneumatic membranes. *International Journal of Solids and Structures* **38**, 9525–9544 (2001).
148. Reina, C., Fokoua Djodom, L., Ortiz, M. & Conti, S. Kinematics of elasto-plasticity: Validity and limits of applicability of $F=FeFp$ for general three-dimensional deformations. *Journal of the Mechanics and Physics of Solids* **121**, 99–113 (2018).
149. Reina, C., Schlömerkemper, A. & Conti, S. Derivation of $F=FeFp$ as the continuum limit of crystalline slip. *Journal of the Mechanics and Physics of Solids* **89**, 231–254 (2016).
150. Reuss, A. Berechnung der Fließgrenze von Mischkristallen auf Grund der Plastizitätsbedingung für Einkristalle. *ZAMM - Zeitschrift für Angewandte Mathematik und Mechanik* **9**, 49–58 (1929).
151. Rivlin, R. S. & Saunders, D. W. Large elastic deformations of isotropic materials VII. Experiments on the deformation of rubber. *Philosophical Transactions of the Royal Society of London. Series A, Mathematical and Physical Sciences* **243**, 251–288 (1951).
152. Röhrig, C., Scheffer, T. & Diebels, S. Mechanical characterization of a short fiber-reinforced polymer at room temperature: experimental setups evaluated by an optical measurement system. *Continuum Mechanics and Thermodynamics* **29**, 1093–1111 (2017).
153. Röhrig, C. & Diebels, S. in *Multi-scale Simulation of Composite Materials* (eds Diebels, S. & Rjasanow, S.) 143–175 (Springer Berlin Heidelberg, Berlin, Heidelberg, 2019).
154. Rolland, H., Saintier, N. & Robert, G. Fatigue Mechanisms Description in Short Glass Fiber Reinforced Thermoplastic by Microtomographic Observation. *Proceedings 20th International Conference on Composite Material* (2015).
155. El-Safty, S., Akhtar, R., Silikas, N. & Watts, D. C. Nanomechanical properties of dental resin-composites. *Dental materials: official publication of the Academy of Dental Materials* **28**, 1292–1300 (2012).
156. Savvas, D., Stefanou, G. & Papadarakakis, M. Determination of RVE size for random composites with local volume fraction variation. *Computer Methods in Applied Mechanics and Engineering* **305**, 340–358 (2016).
157. Sena, M. P., Ostoja-Starzewski, M. & Costa, L. Stiffness tensor random fields through upscaling of planar random materials. *Probabilistic Engineering Mechanics* **34**, 131–156 (2013).

158. Sharma, B. N., Naragani, D., Nguyen, B. N., Tucker, C. L. & Sangid, M. D. Uncertainty quantification of fiber orientation distribution measurements for long-fiber-reinforced thermoplastic composites. *Journal of Composite Materials* **52**, 1781–1797 (2018).
159. Simo, J. C. A framework for finite strain elastoplasticity based on maximum plastic dissipation and the multiplicative decomposition: Part I. Continuum formulation. *Computer Methods in Applied Mechanics and Engineering* **66**, 199–219 (1988).
160. Simo, J. C. A framework for finite strain elastoplasticity based on maximum plastic dissipation and the multiplicative decomposition. Part II: Computational aspects. *Computer Methods in Applied Mechanics and Engineering* **68**, 1–31 (1988).
161. Simo, J. C. & Hughes, T. J. R. *Computational inelasticity* (Springer, New York, 1998).
162. Simo, J. C. & Ortiz, M. A unified approach to finite deformation elastoplastic analysis based on the use of hyperelastic constitutive equations. *Computer Methods in Applied Mechanics and Engineering* **49**, 221–245 (1985).
163. Soize, C. Non-Gaussian positive-definite matrix-valued random fields for elliptic stochastic partial differential operators. *Computer Methods in Applied Mechanics and Engineering* **195**, 26–64 (2006).
164. Soize, C. Tensor-valued random fields for meso-scale stochastic model of anisotropic elastic microstructure and probabilistic analysis of representative volume element size. *Probabilistic Engineering Mechanics* **23**, 307–323 (2008).
165. Spanos, P. D. & Ghanem, R. Stochastic Finite Element Expansion for Random Media. *Journal of Engineering Mechanics* **115**, 1035–1053 (1989).
166. Spencer, A. J. M. *Deformations of fibre-reinforced materials* (Clarendon Press, Oxford, 1972).
167. Stefanou, G., Savvas, D. & Metsis, P. Random Material Property Fields of 3D Concrete Microstructures Based on CT Image Reconstruction. *Materials (Basel, Switzerland)* **14** (2021).
168. *Structural Mechanics Module User's Guide* (COMSOL Multiphysics® v. 5.5. COMSOL AB, Stockholm, Sweden, 2019).
169. Sudret, B. & Der Kiureghian, A. *Stochastic Finite Element Methods and Reliability: A State-of-the-Art Report* Report No. UCB/SEMM-2000/08 (University of California, Berkeley, November 2000).
170. Tandon, G. P. & Weng, G. J. The Effect of Aspect Ratio of Inclusions on the Elastic Properties of Unidirectional Aligned Composites. *Polymer Composites* **5**, 327–333 (1984).
171. Tiwari, A. Nanomechanical Analysis of Hybrid Silicones and Hybrid Epoxy Coatings—A Brief Review. *Advances in Chemical Engineering and Science* **02**, 34–44 (2012).
172. Tran, V. P. *Stochastic modeling of random heterogeneous materials* Dissertation (Université Paris-Est, Paris, 2016).
173. Troyon, M. & Lafaye, S. About the importance of introducing a correction factor in the Sneddon relationship for nanoindentation measurements. *Philosophical Magazine* **86**, 5299–5307 (2006).
174. Tucker III, C. L. & Liang, E. Stiffness predictions for unidirectional short-fiber composites: Review and evaluation. *Composites Science and Technology* **59**, 655–671 (1999).
175. van Dommelen, J. A. W., van der Sande, T. P. J., Hrapko, M. & Peters, G. W. M. Mechanical properties of brain tissue by indentation: interregional variation. *Journal of the mechanical behavior of biomedical materials* **3**, 158–166 (2010).
176. Vanmarcke, E. *Random fields: Analysis and synthesis* (World Scientific Publ, Singapore, 2010).
177. Vanmarcke, E. & Grigoriu, M. Stochastic Finite Element Analysis of Simple Beams. *Journal of Engineering Mechanics* **109**, 1203–1214 (1983).

178. Vladimirov, I. N., Pietryga, M. P. & Reese, S. On the modelling of non-linear kinematic hardening at finite strains with application to springback—Comparison of time integration algorithms. *International Journal for Numerical Methods in Engineering* **75**, 1–28 (2008).
179. Voigt, W. Über die Beziehung zwischen den beiden Elasticitätsconstanten isotroper Körper. *Annalen der Physik* **274**, 573–587 (1889).
180. Wong, E. & Hajek, B. *Stochastic Processes in Engineering Systems* (Springer New York, NY, New York, NY, 1985).
181. Yaglom, A. M. *An introduction to the theory of stationary random functions* (Martino Publ, Mansfield Centre, CT, 2014).
182. Yamazaki, F., Member, A., Shinozuka, M. & Dasgupta, G. Neumann Expansion for Stochastic Finite Element Analysis. *Journal of Engineering Mechanics* **114**, 1335–1354 (1988).
183. Zaïri, F., Naït-Abdelaziz, M., Gloaguen, J. M., Bouaziz, A. & Lefebvre, J. M. Micromechanical modelling and simulation of chopped random fiber reinforced polymer composites with progressive debonding damage. *International Journal of Solids and Structures* **45**, 5220–5236 (2008).
184. Zhang, S., van Dommelen, J. A. W. & Govaert, L. E. Micromechanical Modeling of Anisotropy and Strain Rate Dependence of Short-Fiber-Reinforced Thermoplastics. *Fibers* **9**, 44 (2021).
185. Zheng, K., Yang, K., Shi, J., Yuan, J. & Zhou, G. Innovative methods for random field establishment and statistical parameter inversion exemplified with 6082-T6 aluminum alloy. *Scientific Reports* **9**, 17788 (2019).
186. Zhou, H., Liu, H., Jiang, Q., Kuang, T., Chen, Z. & Li, W. Effect of Process Parameters on Short Fiber Orientation along the Melt Flow Direction in Water-Assisted Injection Molded Part. *Advances in Materials Science and Engineering* **2019**, 1–10 (2019).
187. Zienkiewicz, O. C. & Taylor, R. L. *The Finite Element Method: Volume 1: The Basis* (Butterworth-Heinemann, Oxford [u.a.], 2002).
188. Zimmermann, E. *Stochastische Materialmodellierung mit einer Anwendung auf die Wellenausbreitung in unidirektionalen Kompositen* Dissertation (Helmut-Schmidt-Universität / Universität der Bundeswehr Hamburg, Hamburg, 2019).
189. Zimmermann, E., Eremin, A. & Lammering, R. Analysis of the continuous mode conversion of Lamb waves in fiber composites by a stochastic material model and laser vibrometer experiments. *GAMM-Mitteilungen* **41**, e201800001 (2018).
190. Zohdi, T. I. & Wriggers, P. *An Introduction to Computational Micromechanics: Reprinted with corrections* (Springer Berlin Heidelberg, Berlin, Heidelberg, 2010).

List of Figures

1.1	Contribution of the Papers to the overall objective of the cumulative Habilitation thesis. . . .	4
2.1	Scale definition based on a tensile test specimen made of SFRC, taken from Paper III [146]. . .	6
3.1	Specimen definition for the tensile and nanoindentation tests, cf. Paper II and Paper III [141, 146].	9
3.2	Different stages of image processing, taken from Paper II [141].	9
3.3	Results of the microstructural characteristics, cf. Paper II [141].	10
3.4	Histograms of the microstructural characteristics, cf. Paper II [141].	10
3.5	PDFs of the fiber length, fiber diameter, and orientation derived by μ CT, cf. Paper I [144]. Data taken from [58].	11
3.6	Results for the distribution of E_1 and C_{11} for a varying fiber length, diameter, and orientation based on the material model by Tandon and Weng, cf. Paper I [144].	12
3.7	Moving window method applied to the artificial microstructure. All measures in μm . Taken from Paper IV [142], see also Papers I and II [141, 144].	13
3.8	Distribution of the values for the elasticity tensor element C_{11} with respect to the boundary condition and the window size, cf. Paper I [144].	14
4.1	Scheme of a nanoindentation load cycle and a micrograph of the indentation area after unloading, taken from Paper II [141]. See also [103, 146, 171].	16
4.2	Spatial distribution of the indentation modulus for each load case and loading direction, taken from Paper III [146].	17
4.3	Results of the numerical simulation and comparison with the experimental results, taken from Paper III [146].	19
5.1	Experimental results and comparison with data sheet, Paper V [143].	22
5.2	Analysis of the correlation length for each auto- and cross-correlation, taken from Paper IV [142].	25
5.3	Cross-correlation coefficient a for all window sizes, taken from Paper IV [142].	26
5.4	Discretizations of cross-correlated homogeneous second-order Gaussian random fields to represent the spatially distributed material parameter Λ for different values of l_x , taken from Paper V [143].	27
5.5	Results of the numerical simulation in comparison with the experimentally obtained results and a stress-strain curve provided by the manufacturer [21], taken from Paper V [143].	28
I.1	Probability density functions.	43
I.2	Engineering constants due to a varying fiber length for the material model by Tandon and Weng.	45
I.3	Elasticity coefficients due to a varying fiber length for the material model by Tandon and Weng.	45
I.4	Results for the distribution of E_1 and C_{11} with respect to a varying fiber length, diameter, and orientation based on the material model by Tandon and Weng.	46
I.5	Results for the distribution of E_1 and C_{11} with respect to a varying fiber length, diameter, and orientation based on the material model by Halpin and Tsai.	46
I.6	Influence of the fiber volume fraction on the material properties of SFRC.	47
I.7	SFRC microstructure of $2500\text{ }\mu\text{m} \times 2500\text{ }\mu\text{m}$ with a over all fiber volume fraction of 18.2%. . . .	48
I.8	Procedure to generate a numerical model representing a SFRC microstructure.	49
I.9	Symmetry analysis of the elasticity tensor.	51

I.10	Distribution of the elasticity coefficients under pure displacement boundary conditions with respect to a 250 μm window size.	52
I.11	Distribution of the values for the elasticity tensor element C_{11} with respect to the boundary conditions and the window size.	53
I.12	Mean values of the elasticity coefficients in dependence of the geometrical fiber properties as well as the fiber volume fraction and fiber orientation on the elasticity coefficients.	55
I.13	Standard deviation of the elasticity coefficients in dependence of the geometrical fiber properties as well as the fiber volume fraction and fiber orientation on the elasticity coefficients.	56
I.14	Moving window procedure	57
I.15	Symmetry analysis of the elasticity tensor.	58
I.16	Correlation analysis of the elasticity tensor based on the element C_{16} for a window size of 250 μm	59
I.17	Comparison of ρ_{16}^{26} and ρ_{26}^{16}	60
I.18	Dimensionless correlation parameters that are independent of the window size.	61
I.19	Dimensionless correlation parameters that depend on the window size.	62
I.20	Engineering constants due to a varying fiber diameter calculated with the Tandon-Weng material model.	64
I.21	Elasticity coefficients due to a varying fiber diameter calculated with the Tandon-Weng material model.	64
I.22	Engineering constants due to a varying fiber orientation calculated with the Tandon-Weng material model.	65
I.23	Elasticity coefficients due to a varying fiber orientation calculated with the Tandon-Weng material model.	65
I.24	Engineering constants due to a varying fiber orientation calculated with the Halpin-Tsai material model.	66
I.25	Elasticity coefficients due to a varying fiber orientation calculated with the Halpin-Tsai material model.	66
I.26	Comparison of the dimensionless correlation parameters based on C_{16} assuming plane strain and plane stress states for a window size of 250 μm at $x = 1250 \mu\text{m}$	68
I.27	Comparison of ρ_{16}^{26} and ρ_{26}^{16} assuming plane strain and plane stress states at $x = 1250 \mu\text{m}$	69
I.28	Comparison of the dimensionless correlation parameters that are independent of the window size assuming plane strain and plane stress states at $x = 1250 \mu\text{m}$	69
I.29	Comparison of the dimensionless correlation parameters that depend on the window size assuming plane strain and plane stress states at $x = 1250 \mu\text{m}$	70
II.1	Evaluation of the transcendental equation for ω_i	77
II.2	Specification of the experimental and numerical specimens.	80
II.3	Angle and cross-section definition for the description of the fiber orientation and fiber length, see also [59, 100, 158].	82
II.4	Different stages of the image processing routine.	82
II.5	Results of the fiber length, fiber orientation, as well as correlation between fiber length and fiber orientation based on the micrograph.	83
II.6	PDF fiber diameter.	84
II.7	Fiber orientation schemes due to mold injection process, compare [154].	84
II.8	Results for the elements A_{11} and A_{33} of the orientation tensor based on the micrograph.	85
II.9	Histogram of the fiber length for the shell and core layers.	85
II.10	Comparison of shell layers of the micrograph (upper two images) and an artificial microstructure (lower image). All measures in μm	88
II.11	Scheme load cycle nanoindentation [103, 171] (left), micrograph of the indentation location after unloading (right).	90
II.12	Auto- and cross-correlation of the elasticity tensor elements.	93

II.13	A realization for the four independent elasticity coefficients for the modeling of the material properties of SFRC based on the correlation length derived from a window size of 250 μm and an exponential correlation functions. All values in GPa.	94
III.1	Multiscale approach, [127].	104
III.2	Scheme load cycle indentation test, [103, 171].	104
III.3	Spatial distribution of the numerically obtained indentation modulus for each load case and direction.	106
III.4	Specimens for experimental investigation and numerical validation.	106
III.5	Spatial distribution of the indentation modulus for each load case and direction.	108
III.6	Fiber orientation schemes consisting of five different layers due to injection molding process, compare [154].	109
III.7	Numerical models used for the determination of the Young's Modulus by tensile tests.	111
III.8	Results of the numerical simulation in x - and y -direction and comparison with experimental results.	113
IV.1	Moving window method applied to the artificial microstructure. All measures in μm	127
IV.2	Stress strain curve for PBT GF 30 under uniaxial loading in melt flow direction, values taken from the data sheet of the manufacturer [21].	128
IV.3	Example for the analysis of the yield strength for a window size of 750 μm	129
IV.4	Correlation of the parameter pairs for a window size of 750 μm	130
IV.5	Dimensionless correlation parameters $\rho_{\gamma\mu}$, $\rho_{\gamma\alpha}$, and $\rho_{\beta\sigma_y}$ for each window size.	131
IV.6	Cross-correlation coefficient a for all window sizes.	131
IV.7	Analysis of the correlation length for each auto- and cross-correlation.	132
V.1	Details of the specimens geometry and the measurement points. All measures in mm, $t = 3 \text{ mm}$	139
V.2	Experimental results and comparison with data sheet.	141
V.3	Representation of the spatially distributed material parameters of elastic-ideal plastic material behavior by cross-correlated homogeneous second-order Gaussian random fields.	145
V.4	Correlation analysis of the generated cross-correlated random fields.	146
V.5	Histograms of the sampled values of Λ and σ_y	146
V.6	Configuration definition within the nonlinear continuum mechanic framework.	147
V.7	Structure of the implemented algorithm	153
V.8	Two-dimensional numerical model.	153
V.9	Numerical validation of the implemented general stress-deformation algorithm in COMSOL Multiphysics®.	156
V.10	Discretizations of cross-correlated homogeneous second-order Gaussian random fields to represent the spatially distributed material parameter Λ for different values of l_x	157
V.11	Results of the numerical simulation in comparison with the experimentally obtained results and a stress-strain curve provided by the manufacturer [21].	159

List of Tables

3.1	Linear elastic material properties of the fiber and matrix material.	8
3.2	Comparison of the mean values for the engineering constants based on the analytical and numerical analysis, cf. Paper I [144].	13
4.1	Results of the cross section analysis, cf. Paper II [141].	16
4.2	Results of the experimentally obtained indentation modulus, cf. Papers II and III [141, 146]. . .	18
4.3	Comparison of the experimentally and numerically obtained values, cf. Papers II and III [141, 146].	18
5.1	Experimental results obtained by tensile tests in the elastic and plastic domain, compare Paper IV [142].	21
5.2	Mean values and standard deviations of the strain energy density function coefficients as well as the yield strength, cf. Paper IV [142].	24
5.3	Material properties of numerical simulation.	26
5.4	Deviation of the single simulations at different strain levels and comparison with experimental data.	29
I.1	Material properties of PBT and Glass fibers.	41
I.2	Results of the engineering constants for Tandon-Weng and Halpin-Tsai.	43
I.3	Load cases for the determination of the elasticity coefficients in accordance with the Hill condition [188].	49
I.4	Results of the elasticity coefficients with respect to the element size.	50
I.5	Comparison of the mean values for the engineering constants based on the analytical and numerical analysis.	57
II.1	Material properties of the fiber and matrix material.	80
II.2	Results of the numerical simulation based on the micrograph.	87
II.3	Fiber mass fraction for each layer of the artificial microstructure.	87
II.4	Results of the numerical simulation based on the artificial microstructures.	89
II.5	Results of the indentation tests.	91
II.6	Comparison of the experimental and numerical obtained results.	91
II.7	Results of the auto-correlation lengths of the elasticity tensor coefficients using different correlation functions and a window size of 250 μm	93
II.8	Results of the analysis of the exemplary random fields with respect to possible negative realizations due to the underlying Gaussian distribution.	95
II.9	Results of the convergence study for the element size of the numerical model on the component level.	96
II.10	Results of the experimentally obtained Young's modulus and deviation to the previous observations.	96
II.11	Material properties of the matrix and fiber material of PA 6 GF 30 dry as molded.	98
II.12	Results of the auto-correlation lengths of the elasticity tensor coefficients using an exponential correlation functions and a window size of 250 μm based on the microstructure characteristics provided in [58] and the material properties of PA 6 GF 30.	98

II.13	Results of the numerically obtained Young's modulus based on the microstructural characteristics of PA 6 given in [58] and deviation to the experimentally obtained Young's modulus. . .	98
II.14	Results of the auto-correlation lengths of the elasticity tensor coefficients using an exponential correlation functions and a window size of 250 μm based on the microstructure characteristics provided in [58] and the material properties of PBT GF 30.	99
II.15	Results of the numerically obtained Young's modulus based on the microstructural characteristics of PA 6 given in [58] in combination with the material properties of PBT GF 30 and deviation to the experimentally obtained Young's modulus.	100
II.16	Local distribution of the material properties based on numerical simulations and experiments. All values in GPa	100
III.1	Material properties of the fiber and matrix material.	105
III.2	Results of the experimentally obtained indentation modulus.	107
III.3	Microstructural characteristics of the specimen taken from [145].	109
III.4	Mean values of the indentation modulus.	110
III.5	Summary indentation characteristics.	111
III.6	Results of the experimentally obtained Young's modulus in x -direction.	112
III.7	Results of the numerically obtained Young's modulus.	116
IV.1	Material properties.	126
IV.2	Mean values and standard deviations of the strain density function coefficients.	127
IV.3	Results yield strength.	128
IV.4	Results R^2 curve fit auto-correlation.	135
IV.5	Results R^2 curve fit cross-correlation.	136
V.1	Experimental results obtained by tensile tests in the elastic and plastic domain.	140
V.2	Mean values and standard deviations of the strain density function coefficients for a window size of 750 μm , taken from Rauter et al. [142].	144
V.3	List of input and output variables for a general stress deformation routine in COMSOL Multiphysics®.	152
V.4	List of state variables used in the algorithm for the elastic-ideal plastic material behavior in COMSOL Multiphysics®.	152
V.5	List of input and output variables for the subroutine RETMAP COMSOL Multiphysics®.	155
V.6	Material parameters validation with Neo-Hookean material model.	155
V.7	Deviation of the second Piola-Kirchhoff stress tensor component for the examined correlation lengths at different strain levels and comparison with the experimental data.	158
V.8	List of input and output arguments for Algorithm 3 (CALCS_INTERMEDIATE).	161
V.9	List of input and output arguments for Algorithm 4 (CALCNORMM).	161
V.10	List of input and output arguments for Algorithm 5 (CALC_DEV).	162
V.11	List of input and output arguments for Algorithm 6 (MATEXP).	163